

ETD Archive

2019

Measurement of Red Blood Cell Oxygenation State by Magnetophoresis

Nina A. Smith
Cleveland State University

Follow this and additional works at: <https://engagedscholarship.csuohio.edu/etdarchive>

 Part of the [Biomedical Engineering and Bioengineering Commons](#), and the [Chemical Engineering Commons](#)

[How does access to this work benefit you? Let us know!](#)

Recommended Citation

Smith, Nina A., "Measurement of Red Blood Cell Oxygenation State by Magnetophoresis" (2019). *ETD Archive*. 1171.
<https://engagedscholarship.csuohio.edu/etdarchive/1171>

This Thesis is brought to you for free and open access by EngagedScholarship@CSU. It has been accepted for inclusion in ETD Archive by an authorized administrator of EngagedScholarship@CSU. For more information, please contact library.es@csuohio.edu.

MEASUREMENT OF RED BLOOD CELL OXYGENATION STATE BY MAGNETOPHORESIS

NINA A. SMITH

Bachelor of Science in Chemical Engineering

Cleveland State University

May 2018

Submitted in partial fulfillment of requirements for the degree

MASTER OF SCIENCE IN CHEMICAL ENGINEERING

at the

CLEVELAND STATE UNIVERSITY

AUGUST 2019

©COPYRIGHT BY NINA A. SMITH 2019

We hereby approve this thesis

For

NINA A. SMITH

Candidate for the Master's degree

For the Department of

Chemical and Biomedical Engineering

And

CLEVELAND STATE UNIVERSITY'S

College of Graduate Studies by

Maciej Zborowski

Department & Date

Joanne Belovich

Department & Date

Jeffrey Chalmers

Department & Date

August 1, 2019

Date of Defense

DEDICATION

This thesis is dedicated to my parents, Tanya and Anthony Vinci, my sister, Tia Vinci, my husband, Adam Smith/Sminci, and to our cat and dog, Mia and Boots. Thank you for all your love and support throughout these amazing years of college. I could not have accomplished any of this without you all.

ACKNOWLEDGEMENTS

First and foremost, I would like to acknowledge Dr. Joanne Belovich for all the support she has given me throughout my college career at Cleveland State University. You have helped me make difficult decisions in my internships, pushed me in the courses I took with you, and helped me determine what I wanted to do in the next chapter of my life. You have helped me become the engineer I am today. Thank you for all your continued support and mentorship.

I would also like to thank Dr. Maciej Zborowski for welcoming me into his lab to research the topic of characterizing red blood cells based on their magnetic properties in varied deoxygenated states and determining the magnetic characteristics of glioma and glioblastoma brain cancer cells. I am grateful to have had this opportunity.

Thank you, Lee Moore, for all the help you provided me to succeed in my experiments. I appreciate everything you did for me, from helping me understand magnetics, to guiding me through experiments, and making sure my deoxygenation set up was working correctly, to helping me locate cells in CTV when I was not able to. I am thankful to have had your assistance and support throughout my master's career.

Naru, thank you for all the training you helped me with when I was beginning in the lab. Bo, thank you for your contributions during lab meetings, helping me with MATLAB coding, helping set up my system, and keeping me informed about the Cavs.

Last, but not least, I would again like to thank my family and friends for all their love and support through this journey of not understanding what I am talking about when you ask about school. You will just have to listen to me talk about work from now on!

MEASUREMENT OF RED BLOOD CELL OXYGENATION STATE BY MAGNETOPHORESIS

NINA A. SMITH

ABSTRACT

Magnetophoresis of red blood cells (RBCs) at varying partial pressures of oxygen (pO_2) is hypothesized to rejuvenate stored blood to be utilized beyond the FDA regulated 42-day storage time. Magnetophoresis is a particle or cells motion induced by an applied magnetic field in a viscous media. The average magnetophoretic mobility of an oxygenated RBC is $-0.126 \times 10^{-6} \text{ mm}^3\text{-s/kg}$, and a deoxygenated RBC is $3.66 \times 10^{-6} \text{ mm}^3\text{-s/kg}$, presenting magnetophoresis as a resource for RBC rejuvenation in hopes of storing it longer than 42 days. The main objective of this paper was to determine if controlling the pO_2 within an RBC suspension, can singly- doubly- triply- or fully deoxygenated RBCs be identified by means of cell tracking velocimetry (CTV). These results agreed with the cooperative binding scheme developed by Hill, especially from $\sim 30\text{-}40$ to 160 mmHg . From 0 to 30 mmHg , further research must be completed to characterize the binding behavior of oxygen and hemoglobin. The validation of the magnetic energy density gradient value (S_m , currently at 365 T-A/mm^2) utilized within CTV, and the exact location for the field of view (FOV, currently set to 4.5 mm from the edge of the magnet assembly) were needed to state particle motion was independent of location within the CTV channel. The FOV location was successfully verified 4.5 mm from the edge of the magnet assembly, however, the S_m value, 880 T-A/mm^2 , was 140% higher than the original. Spectrophotometry was utilized to validate the oxygenation state of RBCs. Results confirmed spectrophotometry was a reliable model for RBC magnetophoresis. CTV post-processing was tested with glioma

progenitor cells. Scatter plots generated for these experiments demonstrated cells with different magnetic mobilities in a sample can be detected. To fully characterize the glioma progenitor cells, more experiments must be completed. Lastly, applying a temperature gradient to the magnetic deposition microscopy (MDM) assembly to enhance the separation of RBCs was explored. Preliminary results determined, introducing a temperature gradient of 40°C was large enough to affect the RBC sedimentation rate in the channel. After, modeling within COMSOL was completed, however, more time and knowledge of COMSOL is needed to generate practical results.

TABLE OF CONTENTS

	Page
ABSTRACT.....	vi
LIST OF TABLES	xii
LIST OF FIGURES	xiiv
 CHAPTER	
I. INTRODUCTION	1
1.1 Introduction.....	1
1.2 Hypothesis.....	2
1.3 Specific Aims.....	3
1.4 Significance of Research.....	5
II. BACKGROUND	6
2.1 Red Blood Cell Properties	6
2.2 General Magnetic Properties.....	8
2.3 Magnetic Susceptibility Balance.....	15
2.4 Magnetic Separation of Labeled versus Unlabeled Cells	18
2.5 Separation Devices.....	19
2.6 Analytical Devices	19
2.6.1 Cell Tracking Velocimetry	20
2.6.2 Magnetic Deposition Microscopy	25
2.7 Cooperative Binding of Oxygen and Hemoglobin: Adair and Hill Equations	30
2.8 Spectrophotometry	33
2.9 Glioblastoma	36
2.10 Giddings Velocity Profile	38

III.	MATERIALS AND METHODS.....	41
3.1	Determination of the Magnetophoretic Driving Force for the Cell Tracking	
	Velocimetry Magnet Assembly	41
3.1.1	Materials	41
3.1.2	Methods	44
3.1.3	MSB-Auto Methods to Measure the Magnetic Susceptibility of the	
	MDM Buffer and Magnevist Solution	46
3.2	Spectrophotometry	47
3.2.1	Materials	47
3.2.2	Methods	48
3.3	Modifications made to the Cell Tracking Velocimetry System for the	
	Deoxygenation of Red Blood Cells	49
3.4	Red Blood Cell Deoxygenation	54
3.4.1	Materials	54
3.4.2	Methods for Calibrating the Dissolved Oxygen Probe and Meter	55
3.4.3	Methods for Deoxygenation Experiments.....	56
3.4.4	Methods of Analysis.....	60
3.4.5	Analysis of S_m Verification Experiments.....	62
3.4.6	Analysis of RBC Deoxygenation Experiments	62
3.5	Glioma Progenitor Cell Experiments.....	67

3.5.1 Materials	67
3.5.2 Methods	70
3.6 Exploration of the Effects of a Temperature Gradient on the Separation of Red Blood Cells	75
IV. RESULTS AND DISCUSSION	79
4.1 S_m Verification Results	79
4.2 Spectrophotometry Results	80
4.3 Deoxygenation of Red Blood Cell Results	82
4.3.1 Results Generated through the MATLAB Code for Experiment #1	83
4.3.2 Gaussian Fit Results Compared to the Hill Equation	115
4.4 Results for Glioma Experiments	122
4.5 Results for Temperature Gradient Exploration	128
4.6 Discussion for S_m Verification	131
4.7 Discussion for the Spectrophotometer Experiments	132
4.8 Discussion for the Deoxygenation of Red Blood Cells	132
4.9 Discussion for the Glioma Experiments	134
4.10 Discussion for the Temperature Gradient Exploration	135
V. CONCLUSION AND RECOMMENDATIONS	136
5.1 Conclusions and Recommendations: S_m Verification Experiments	136
5.2 Conclusions and Recommendations: Spectrophotometry	137
5.3 Conclusions and Recommendations: Red Blood Cell Deoxygenation Experiments	137
5.4 Conclusions and Recommendations: Glioma Experiments	138

5.5 Conclusions and Recommendations: Temperature Gradient Exploration....	139
REFERENCES	140
APPENDIX	
A: RELEVANT GRAPHS AND TABLES.....	151
B: MATLAB CODE FOR ANALYZING CTV RESULTS – 4/17/2019	154
C: RESULTS GENERATED BY THE MATLAB CODE FOR THE GLIOMA EXPERIMENTS	167

LIST OF TABLES

Table	Page
I: Form-specific Adair's Coefficients (Matejak, Kulhanek, & Matousek, 2015).	32
II: Dimensions of the deoxygenation vessel designed in collaboration with Lee Moore.....	53
III: Theoretical oxygenation levels for one experiment to determine if CTV is capable to detect differences in the magnetic mobility of RBCs.....	59
IV: Pump programs implemented by Nina Smith.....	72
V: Constants utilized to create Figure 74 Giddings velocity profile.	76
VI: Concentrations calculated from Equations 2.32-2.34 to obtain the concentration of oxyHb, metHb, and hemichromes within the samples analyzed by spectrophotometry.....	82
VII: Regression line information for both Gaussians in Experiments 1 and 2.	122
VIII: Results of the t-Test between RPMI media and MilliQ water to determine how similar the magnetic susceptibilities are between the two.	123
IX: Results of the t-Test between RPMI media and distilled water to determine how similar the magnetic susceptibilities are between the two.	123
X: Common forms of magnetic susceptibility designation, units, and conversion factors (Zborowski, Chalmers, & Lowrie, Magnetic cell manipulation and sorting, 2016).	151
XI: Specifications for the Beckman Coulter spectrophotometer (User's guide: DU series 700 UV/Vis scanning spectrophotometer, 2012).....	151

XII:	Specifications for the Oakton™ Gilmont™ Shielded laboratory Direct-Reading Flowmeter (Oakton™ Gilmont™ shielded laboratory direct-reading flowmeters, 2006).	151
XIII:	Specifications for the Bel-Art™ SP Scienceware™ Riteflow™ Mounted Flowmeter (Bel-Art riteflow aluminum mounted flowmeter; 150mm scale, size 4, 1998).	152
XIV:	Specifications for the RDO® Rugged DO sensor operated in the deoxygenation vessel for the deoxygenation of RBCs experiments (Orion™ RDO™ dissolved oxygen probe, 2008).	152
XV:	Dimensions for the RDO® Rugged DO sensor used in the deoxygenation vessel for the deoxygenation of RBCs experiments (Orion™ RDO™ dissolved oxygen probe, 2008).	152
XVI:	Specifications for the Orion Star A213 DO Benchtop meter utilized for the deoxygenation of RBCs experiments (Orion star™ A213 dissolved oxygen benchtop meter, 2015).	153
XVII:	Specifications and dimensions of the Shandon Cytospin 3 (Cytospin: Cell Preparation System Operator Guide, 1997).	153
XVIII:	Specifications of the Legato 210P multi-syringe pump (Legato 210/210P Syringe Pump, 2016).	153

LIST OF FIGURES

Figure	Page
1: Structure of a single hemoglobin molecule within an RBC.	7
2: Schematic representation of cooperative mechanism of O ₂ binding to Fe ²⁺ within hemoglobin (Hemoglobin: portrait of a protein in action , 2012).	7
3: Left: Shows the ionic bonds between the ferrous molecule and globin protein.	8
4: Imbalance of electrons within an iron atom's electron shells (Understanding permanent magnets, 2015).	9
5: Current flow within a coil resulting in a magnetic field (Understanding permanent magnets, 2015).	10
6: Normal and intrinsic hysteresis loops with key properties marked (What is the magnetic hysteresis loop, 2015).	12
7: Schematic of Faraday's magnetic balance used to determine the magnetic susceptibility of different materials (Zborowski & Chalmers, 2007).	14
8: Adapted schematic of a traditional Gouy balance (Magnetic susceptibility balances, 1930).	15
9: Above: Schematic of the inside of an MSB (Magnetic susceptibility balances (MSB), 2005).	17
10: Image of the CTV magnet with explanations.	24
11: Key CTV magnetostatic field parameters (Xue, et al., 2019).	25
12: (A) Color map of the magnetic field with color graduations of 0.08 T,	28
13: 1) 1 mL vials containing sample solutions.	29
14: Graph of the oxygen-hemoglobin equilibrium curve generated in Maple by Dr. Zborowski.	30

15: Magnetophoretic mobility of oxygenated and deoxygenated RBCs.	31
16: Adapted schematic of what occurs within a spectrophotometer (Bostick, 2018).....	33
17: OxyHb and metHb absorbance curves from 450 - 700 nm (Giangreco, et al., 2013).35	
18: Representation of the Giddings velocity profile with a temperature gradient within the fluid (Giddings, 1991).....	39
19: Picture of the CTV system utilized for the S_m verification experiments.	43
20: Schematic of the empty syringe on the left and full syringe on the right attached to the Hamilton valves.	45
21: Edge of the CTV magnet in the center of the FOV within Video Savant.	46
22: Spectrophotometer by Beckman Coulter and cuvettes by VWR utilized for the spectrophotometer experiments.	48
23: Adapted schematic of original CTV setup (Xue, et al., 2019).....	50
24: Modified CTV setup for the deoxygenation of RBC experiments (Xue, et al., 2019).	50
25: Full CTV setup for deoxygenation experiments.....	51
26: Magnet assembly with glass syringes, and Hamilton valves.....	51
27: Left: Orion Star A213 dissolved oxygen meter from Thermo Scientific. (Component number 7 in Figure 25)	52
28: A schematic (left) and image (right) of the 3-D printed deoxygenation vessel (part of component numbers 3, 4, 5, and 6 in Figure 25).	53
29: Flow meters utilized within the deoxygenation system. (Components 1 from Figure 25).....	55
30: Deoxygenation system set up labeling the three three-way Hamilton valves.	58

31: Parameters changed in ImageView to ensure particles are tracked accurately.	61
32: Shandon Cytospin 3 (Thermo Fisher Scientific, San Francisco, CA) used to create cytospins of glioma cultures (Cytospin: Cell Preparation System Operator Guide, 1997).	68
33: Magnet assembly (Buck, et al., 2014).	69
34: Legato 210P multi-syringe pump adaptor from kd Scientific (Hollison, MA) utilized in MDM (Legato 210/210P Syringe Pump, 2016).....	70
35: Schematic of a Mylar slide, 25 mm × 75 mm, used within MDM as a microscope slide, cut on the bottom right corner to determine the locations of the channels.	72
36: Schematic of how the Cytoclip™ slide clip, the microscope slide, and the disposable Cytotunnel® are put together to be placed into the cytospin (Cytospin: Cell Preparation System Operator Guide, 1997).	73
37: Above: Full MDM magnet assembly. Below: One channel of the assembly.....	78
38: Results to determine the FOV location and the value of S_m	80
39: Results from running spectrophotometry on the oxyHb and metHb samples over a range of 500 - 700 nm.	81
40: Magnetic mobility versus the pO ₂ level for Experiment #1.	82
41: Magnetic mobility versus the pO ₂ level for Experiment #2.	83
42: MATLAB graphs generated for the 160-mmHg oxygenation level in Experiment #1.....	84
43: Above: Gaussian curves for the k-mean clusters for Experiment #1 at 160 mmHg. .	85
44: MATLAB graphs generated for the 60-mmHg oxygenation level in Experiment #1.	86
45: Above: Gaussian curves for the k-mean clusters for Experiment #1 at 60 mmHg. ...	87

46: MATLAB graphs generated for the 40-mmHg oxygenation level in Experiment #1.	88
47: Above: Gaussian curves for the k-mean clusters for Experiment #1 at 40 mmHg. ...	89
48: MATLAB graphs generated for the 30-mmHg oxygenation level in Experiment #1.	90
49: Above: Gaussian curves for the k-mean clusters for Experiment #1 at 30 mmHg. ...	91
50: MATLAB graphs generated for the 25-mmHg oxygenation level in Experiment #1.	92
51: Above: Gaussian curves for the k-mean clusters for Experiment #1 at 25 mmHg. ...	93
52: MATLAB graphs generated for the 20-mmHg oxygenation level in Experiment #1.	94
53: Above: Gaussian curves for the k-mean clusters for Experiment #1 at 20 mmHg. ...	95
54: MATLAB graphs generated for the 15-mmHg oxygenation level in Experiment #1.	96
55: Above: Gaussian curves for the k-mean clusters for Experiment #1 at 15 mmHg. ...	97
56: MATLAB graphs generated for the 10-mmHg oxygenation level in Experiment #1.	98
57: Above: Gaussian curves for the k-mean clusters for Experiment #1 at 10 mmHg. ...	99
58: MATLAB graphs generated for the 5-mmHg oxygenation level in Experiment #1.	100
59: Above: Gaussian curves for the k-mean clusters for Experiment #1 at 5 mmHg. ...	101
60: MATLAB graphs generated for 0.1% O ₂ saturation level in Experiment #1.	102
61: Above: Gaussian curves for the k-mean clusters for Experiment #1 at 0.1% O ₂ saturation level.	103
62: MATLAB graphs generated for 160 mmHg oxygenation level in Experiment #2. .	105
63: MATLAB graphs generated for 60 mmHg oxygenation level in Experiment #2. ...	106
64: MATLAB graphs generated for 40 mmHg oxygenation level in Experiment #2. ...	107
65: MATLAB graphs generated for 30 mmHg oxygenation level in Experiment #2. ...	108

66: MATLAB graphs generated for 25 mmHg oxygenation level in Experiment #2. ...	109
67: MATLAB graphs generated for 20 mmHg oxygenation level in Experiment #2. ...	110
68: MATLAB graphs generated for 15 mmHg oxygenation level in Experiment #2. ...	111
69: MATLAB graphs generated for 10 mmHg oxygenation level in Experiment #2. ...	112
70: MATLAB graphs generated for 5 mmHg oxygenation level in Experiment #2.	113
71: MATLAB graphs generated for 0.1% O ₂ oxygenation level in Experiment #2.	114
72: Gaussian 1 magnetophoretic velocity mode for Experiment #1.	115
73: Gaussian 2 magnetophoretic velocity mode for Experiment #1.	116
74: Gaussian 1 magnetophoretic velocity mode for Experiment #2.	116
75: Gaussian 2 magnetophoretic velocity mode for Experiment #2.	117
76: Hill curve for the Gauss 1 data for Experiment #1.	118
77: Linear regression of Gauss 1 data for Experiment #1.	118
78: Hill curve for the Gauss 2 data for Experiment #1.	119
79: Linear regression of Gauss 2 data for Experiment #1.	119
80: Hill curve for the Gauss 1 data for Experiment #2.	120
81: Linear regression of Gauss 1 data for Experiment #2.	120
82: Hill curve for the Gauss 2 data for Experiment #2.	121
83: Linear regression of Gauss 2 data for Experiment #2.	121
84: Image of GL261 fixed with HEMA solution, imaged at 40× magnification on November 19, 2018.	124
85: Image of GL261 fixed with HEMA solution, imaged at 40× magnification on November 30, 2018.	124

86: Image of GL261 fixed with HEMA solution, imaged at 40× magnification on December 5, 2018.	125
87: Image of GL261 fixed with HEMA solution, imaged at 40× magnification on December 14, 2018.	125
88: Left: Scatter plot of original data obtained December 5, 2018.....	126
89: Gaussian plot of the two clusters presented in Figure 88.	127
90: Left: Scatter plot of original data obtained December 20, 2018.....	127
91: Gaussian plot of the two clusters presented in Figure 90.	128
92: Giddings velocity profile calculated within Excel.....	129
93: Above: Velocity profile through the manifold generated with COMSOL.	130
94: Model of Adair’s equation generated in Maple by Dr. Zborowski.	133
95: MATLAB results generated for 2 clusters the experiment completed by Matt Nagy for a GL261 on August 21, 2018.....	167
96: MATLAB results generated for 2 clusters the experiment completed by Matt Nagy for a GL261 on August 28, 2018.....	168
97: MATLAB results generated for 3 clusters the experiment completed by Matt Nagy for a GL261 on August 28, 2018.....	169
98: MATLAB results generated for 2 clusters the experiment completed for a GL261 on October 15, 2018.	170
99: MATLAB results generated for 2 clusters the experiment completed for a GL261 on November 19, 2018.	171
100: MATLAB results generated for 2 clusters the experiment completed for a GL261 on November 30, 2018.	172

101: MATLAB results generated for 3 clusters the experiment completed for a GL261 on November 30, 2018.	173
102: MATLAB results generated for 2 clusters the experiment completed for a GL261 on December 14, 2018.....	174
103: MATLAB results generated for 2 clusters the experiment completed for a GL261 on January 15, 2019.....	175

CHAPTER I

INTRODUCTION

1.1 Introduction

Red blood cell (RBC) transfusions are needed by patients for a variety of reasons, such as to replace blood loss during a surgical procedure or trauma, or an illness which may cause anemia like liver disease, a hematological disease, or cancer (Why patients receive blood transfusions, 2019). A unit of RBCs is only able to be preserved and stored in a refrigerator for 42 days (Sparrow, 2010). The preservation solution most commonly utilized is saline-adenine-glucose-mannitol (SAG-M), which also extends the shelf-life of the RBCs (Sparrow, 2010). While stored, RBCs undergo physicochemical changes, which decreases the quality, function, and *in vivo* survival, due to being out of their natural environment (Sparrow, 2010). Depending on the storage duration of an RBC unit, there is a possibility that up to 25% of transfused RBCs clear from a recipient's circulation within 24 hours (Moore, et al., 2018). As the need for a technique to separate fresh RBCs from aged RBCs arises, a possible solution is magnetic separation.

As of 2002, magnetic separation has grown in the life sciences, particularly for cell separation (Zborowski, et al., 1995). As an RBC ages, it loses its ability to release oxygen (Haidas, et al., 1971), which in turn causes its magnetic properties to change (Pauling &

Coryell, 1936b), and it becomes more diamagnetic relative to water (Jin, et al., 2012). This will be described further in Section 2.1. This results in a difference in the magnetophoresis of aged RBCs compared to fresh RBCs, where magnetophoresis is defined as the particle motion created by an applied magnetic field within a viscous media (Zborowski, et al., 2016). This magnetophoretic difference allows magnetic separation to be a feasible technique for isolating oxygen functional RBCs in stored blood from non-oxygen functional RBCs, to be utilized for transfusions.

1.2 Hypothesis

Based on previous studies, it is known that the magnetic susceptibility of RBCs changes at two oxygen partial pressure (pO_2) extrema values of ~ 0 mmHg (high susceptibility) and ~ 160 mmHg (in ambient air, low susceptibility). Magnetic susceptibility of a material is defined as the response the material has to an applied magnetic field. However, the dependence of the RBC susceptibility on pO_2 values between these two extremes was never studied. It is also known that the chemical kinetics of the oxygen binding to hemoglobin follows a cooperative binding model characterized by the Adair and Hill equations. With this information, it was hypothesized that the magnetic susceptibility of RBCs follows the same cooperative binding dependence on pO_2 . This hypothesis was made because it is known that the magnetic susceptibility of hemoglobin decreases linearly when the number of bound oxygen (O_2) molecules to hemoglobin increases. In other words, we expect that RBC magnetophoresis depends on the oxygenation state of intracellular hemoglobin in a manner that is well understood theoretically, but has never been examined in detail experimentally. Therefore, under carefully controlled oxygenation conditions, the hypothesis was tested to determine if cell tracking velocimetry (CTV) is capable of

differentiating RBC subfractions differing in oxygenation state with sufficient accuracy. In turn, this would also determine if the dependence of RBC susceptibility on pO_2 follows the cooperative binding model of Adair and Hill.

1.3 Specific Aims

To prove this hypothesis, a variety of experiments were performed.

1. To determine the optimal magnetophoretic driving force vector, S_m , and the optimal field of view (FOV) location for cell tracking velocimetry (CTV) applications to study the magnetophoresis of red blood cells (RBCs). The optimal location of the FOV is where the S_m magnitude and the magnetic field-induced particle velocity does not depend on position inside the FOV. This will ensure the most accurate measurement of RBC velocities during deoxygenation experiments. These experiments were completed utilizing polystyrene (PS) particles within a 50/50 mixture of Magnevist, which is a chelated and stabilized form of gadolinium, and a special buffer formulation with a defined magnetic susceptibility.
2. To measure the absorbance of a blood sample to determine the methemoglobin (metHb) and oxyhemoglobin (oxyHb) concentration levels within it through spectrophotometry as a means to validate RBC deoxygenation. This technique was used to measure intraerythrocytic metHb concentration as the surrogate of deoxygenated RBCs. The data were analyzed with the equations stated in Winterbourne's paper (Winterbourn, 1990) to determine the oxyHb, metHb, and hemichrome concentration levels within a metHb and oxyHb sample.
3. To modify the CTV system to facilitate the deoxygenation of RBCs for magnetophoresis experiments. The system modifications allowed for precisely

controlled deoxygenation of RBCs while their magnetophoretic motion was analyzed by CTV.

4. To measure the magnetophoretic mobility of RBCs at varying oxygenation levels, to study the effect of O_2 binding to hemoglobin ($Hb-O_2$) on red blood cell magnetization. The $Hb-O_2$ reaction kinetics is known from $Hb-O_2$ equilibrium curves determined spectrophotometrically, however, spectrophotometry of the bulk sample does not provide details about the cooperative binding process. The purpose of this study was to determine if RBC magnetophoresis as a function of $Hb-O_2$ binding could provide details about individual stages of a cooperative binding.
5. To validate CTV data post-processing capabilities using the model of glioma progenitor cells known for atypical iron metabolism and to compare their magnetic velocities with the magnetic velocities of oxygenated and deoxygenated RBCs. These experiments were used to validate the sensitivity of CTV to distinguish differences in magnetic velocities of different cell types other than RBCs, such as 3T3, GL26, and GL261 cell lines. The CTV data was analyzed by a newly developed MATLAB code.
6. To model and explore the effects of convective transport with a temperature gradient as a possible option to enhance RBC magnetic separation. This would determine if convective transport heightened by a temperature gradient is a feasible approach to high throughput RBC separation. Modeling within COMSOL was briefly explored to determine if cooling the MDM magnet to 0°C and heating the opposite wall to 40 or 60°C would allow for faster and higher recovery of fresh (magnetic) RBCs.

1.4 Significance of Research

The significance of this research is in its contribution to understanding the physical processes associated with stored blood aging, with potential applications to stored blood “rejuvenation,” so that blood could be safely used beyond the current limit of 42 days. Specifically, this study investigates how the oxygen concentration in solution influences the magnetic field-induced velocity of an RBC in suspension. The accumulation of oxygen binding defects in RBCs over the blood storage time contributes to the current limit of 42 days. Such defects have been shown within Dr. Maciej Zborowski’s laboratory at the Cleveland Clinic, the site of this research, and by collaborators, to affect the magnetically induced RBC velocity, which therefore could provide a basis for selective depletion of the non-functional RBCs. This research contributes to the future design of a magnetic RBC sorter that could improve the quality of stored blood and therefore extend the storage time for banked blood.

CHAPTER II

BACKGROUND

2.1 Red Blood Cell Properties

A general understanding of the biology of an RBC is needed before proceeding with the experiments described in Chapter I. About 270 million hemoglobin molecules are present within a mature RBC, accounting for approximately 90% of an RBC's dry weight (D'Alessandro, et al., 2017). For every hemoglobin molecule there are four folded globin proteins, two beta chains and two alpha chains, each containing its own heme group, which is a red pigmented molecule with the capabilities of binding to an iron ion (Fe^{2+} , ferrous) (Erythrocytes, 2013). Figure 1 represents what a single hemoglobin molecule looks like within an RBC. Every Fe^{2+} is able to bind to one oxygen (O_2) molecule, therefore, each hemoglobin has the capacity to carry four O_2 molecules. The binding sequence of O_2 to hemoglobin is displayed in Figure 2.

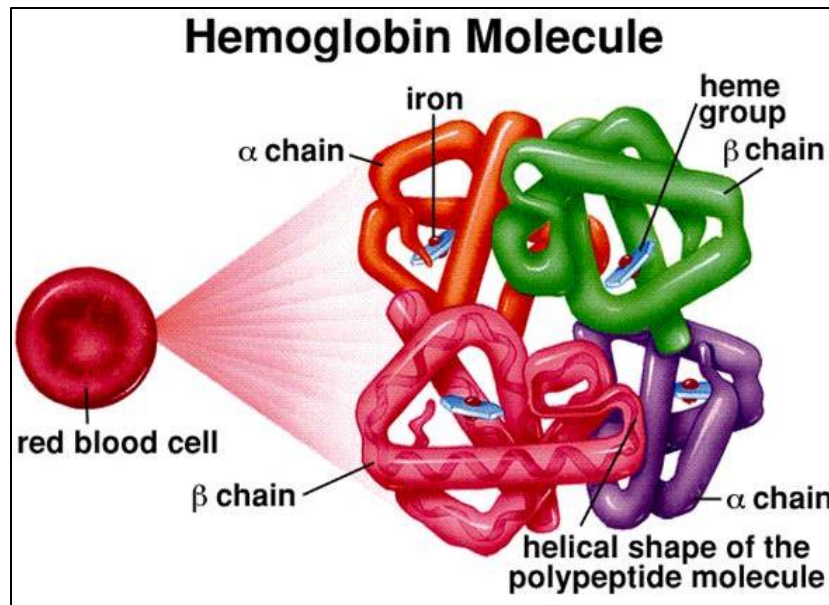


Figure 1: Structure of a single hemoglobin molecule within an RBC containing four folded globin proteins, two alpha and two beta chains, each connected to heme groups which carry an iron ion (Mader, 1997).

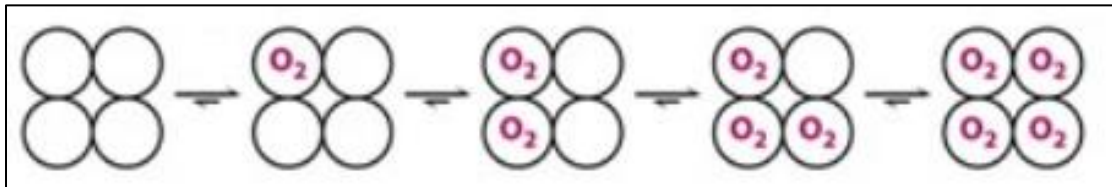


Figure 2: Schematic representation of cooperative mechanism of O_2 binding to Fe^{2+} within hemoglobin (Hemoglobin: portrait of a protein in action , 2012). The open circles illustrate the tetrameric structure of the hemoglobin molecule. Each monomer binds one O_2 molecule sequentially when the pO_2 increases from zero on the left to fully saturated at the ambient pO_2 of approximately 160 mmHg, on the right. The arrows indicate that the bound O_2 increases the hemoglobin tetramer affinity to bind to O_2 , a mechanism known as “cooperative binding”.

The electron configuration of the Fe^{2+} bound to the hemoglobin causes an RBC to be paramagnetic. When an O_2 molecule is bound to a Fe^{2+} ion the hemoglobin is diamagnetic. Unpaired electrons within the four heme groups of a deoxyhemoglobin (deoxyHb) is what causes the RBC to present paramagnetic properties as contrasted by the diamagnetic character of oxyhemoglobin (Zborowski, et al., 2003). As presented in Figure 3, the ferrous molecule contains two free electrons due to the ionic bonding, and when O_2 is bound to the globin protein, the unpaired electrons are bound, creating a covalent bond (Zborowski, et al., 2003).

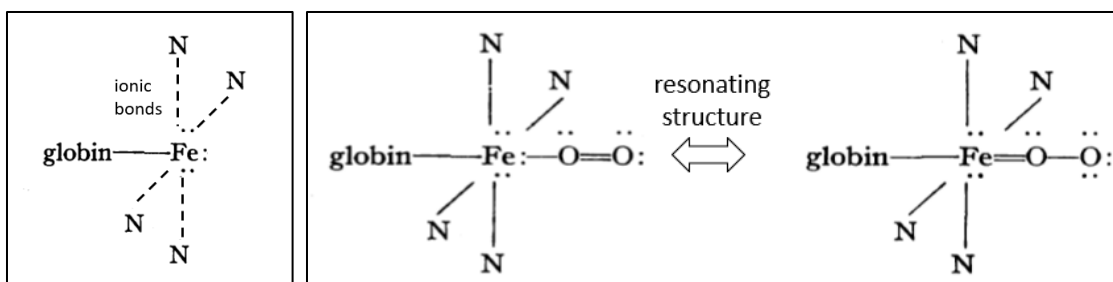


Figure 3: Left: Shows the ionic bonds between the ferrous molecule and globin protein. Right: Demonstrates the configuration change when O₂ is bound in resonating structures (Pauling & Coryell, 1936a).

2.2 General Magnetic Properties

There are four types of magnetization: diamagnetism, paramagnetism, ferromagnetism, and superparamagnetism. For the scope of this paper, only diamagnetism and paramagnetism will be analyzed for experiments, and ferromagnetism will be used to understand how permanent magnets are utilized. For more information on superparamagnetism, refer to ‘Introduction to Magnetic Materials’ (Cullity & Graham, 2008), ‘Four Different Types of Magnetism’ (Four different kinds of magnetism, 2016), and ‘Magnetic Cell Separation’ (Zborowski & Chalmers, 2007). When a particle is diamagnetic, it is repelled from a magnetic field source. It is an extremely weak form of magnetism that is only observed when an external magnetic field is present. However, a paramagnetic particle is weakly attracted to a magnetic field source. For example, the four heme groups of deoxy and methHb (chemically reduced red blood cell, surrogate for deoxy red blood cells) have unpaired electrons, which gives them paramagnetic properties (Zborowski, et al., 2003).

To appreciate how permanent magnets in devices perform, the fundamental theory and equations of magnetics and ferromagnetism is needed. The first property which is vital to recognize is that all magnetic fields are the result of electrons in motion (Understanding permanent magnets, 2015). For example, Figure 4 displays an iron atom that has an

imbalance in the spin direction of electrons, allowing them to be transferred to and from the atom, or to and from a spin direction, which creates an atomic magnetic dipole moment (p_m) within the atom (Understanding permanent magnets, 2015). The magnetic dipole moment is a microscopic property of the material measured in A-m². (Campbell, 1999). Within a current loop, it can be calculated from the following equation:

$$p_m = IA \quad (2.1)$$

where I is the current within the loop and A is the surface area bounded by the current I, which is coincident with the path of I. Vector quantities within equations are represented by bold notation.

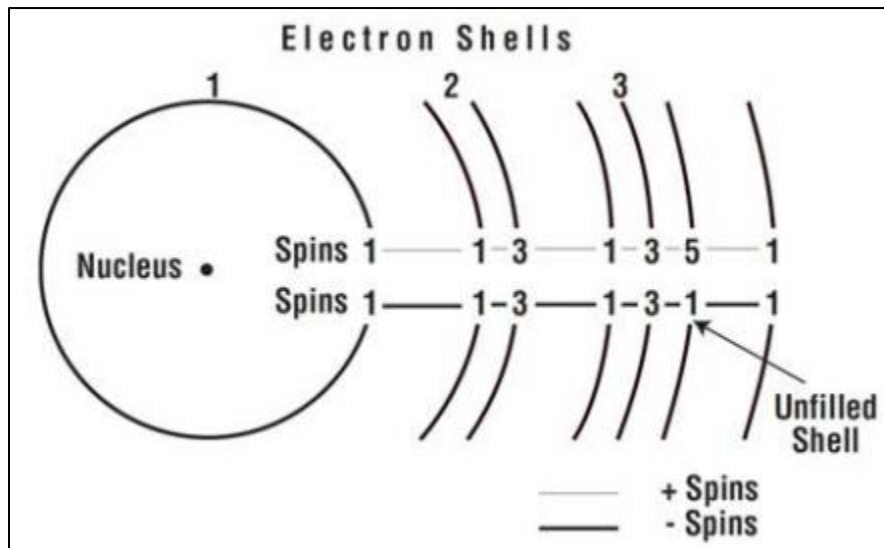


Figure 4: Imbalance of electrons within an iron atom's electron shells (Understanding permanent magnets, 2015).

The magnetic dipole moment vector produced when electrons are coordinated between neighboring atoms through cooperative interatomic exchange forces, determines the ability of a material to create spontaneous magnetization and become a source of the magnetic field in space around that material (known as a permanent magnet). The magnetic field strength, denoted as **H**, and is measured in ampere-turns per meter in the International System (SI), or in oersteds (Oe) in the gram-centimeter-second (CGS) system (Permanent

magnet guidelines, 1998). Another description of **H** is depicted in Figure 5, where a current, **I**, was produced by a DC battery to flow through wires to a load. The movement of electrons in the conductor, also known as the current flow, causes a magnetic field to be established around the wire (Understanding permanent magnets, 2015). For example, an infinitely long solenoid produces an **H** field inside the solenoid, which can be calculated by Equation 2.2 (Cullity & Graham, 2008).

$$H = nI_1 \quad (2.2)$$

Here **n** is the number of turns per unit length (in units of 1/m) and **I₁** is the current in the conductor (measured in amperes, A).

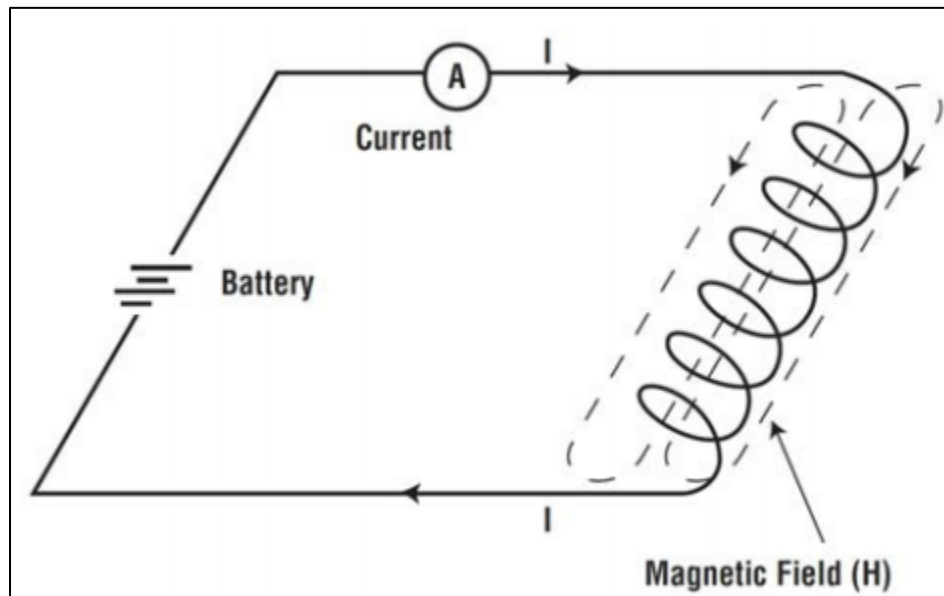


Figure 5: Current flow within a coil resulting in a magnetic field (Understanding permanent magnets, 2015).

When a paramagnetic substance is placed inside the coil, a magnetic field is induced, which increases the total observed field. The magnitude of the magnetic field per unit area is known as the flux density and is measured normal to the direction of magnetization (Permanent magnet guidelines, 1998). The flux density is denoted as **B** and is measured in the CGS system as “lines” of magnetic flux, or maxwells per square

centimeter, (one maxwell per square centimeter is equal to one gauss), while in the SI system, it is measured in tesla (one tesla, T is equal to one weber per square meter, Wb/m²) (Understanding permanent magnets, 2015). Equation 2.3 demonstrates that **B** is directly proportional to **H** within a vacuum (free space).

$$\mathbf{B} = \mu_0 \mathbf{H} \quad (2.3)$$

Magnetic permeability of free space is represented by μ_0 . It is a constant fixed by the definition of the electric current unit, $\mu_0 = 4\pi \times 10^{-7}$ T-m/A (Zborowski & Chalmers, 2007).

Once **H** and **B** are known for a magnetic material, a normal magnetization curve and a hysteresis loop can be generated. The normal magnetization curve is simply the induced flux density, **B**, versus the magnetizing field, **H**. A hysteresis loop is a more complex curve because it demonstrates how a magnetic material reacts when an external magnetic field is applied to it. To produce the loop, a sample material is placed between the poles of an electromagnet, leaving a minimal air gap between the sample and the poles (Understanding permanent magnets, 2015). Figure 6 depicts a normal hysteresis loop and an intrinsic hysteresis loop. The difference between a normal and an intrinsic hysteresis loop is the normal hysteresis loop compares **B** versus **H**, while the intrinsic loop compares magnetization (**J**, which is described below) versus **H**. For permanent magnets, the first quadrant is analyzed to learn how difficult it might be to magnetize a material to saturation (What is the magnetic hysteresis loop, 2015). The first quadrant also corresponds to the normal magnetization curve of a magnetic material; however, it would begin at the origin.

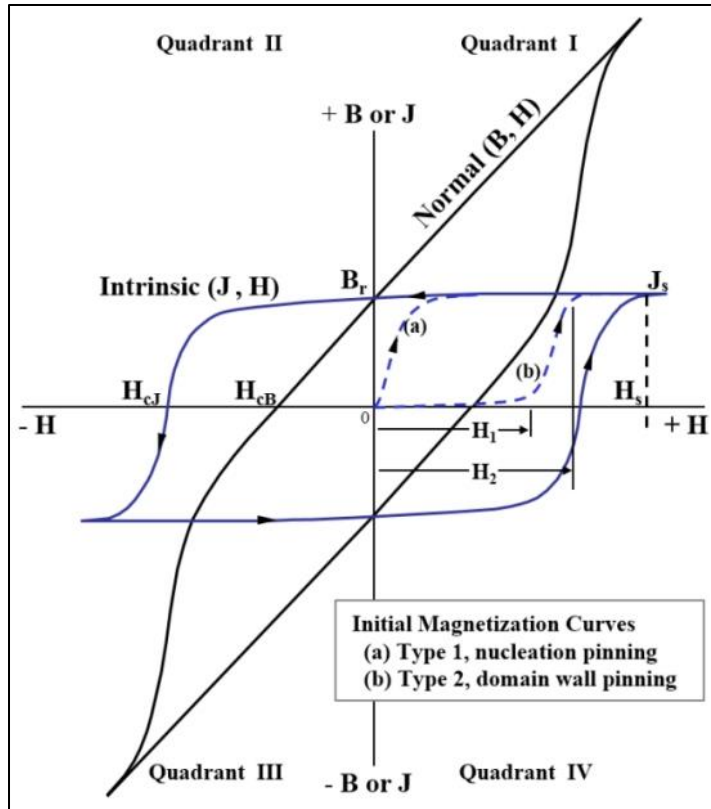


Figure 6: Normal and intrinsic hysteresis loops with key properties marked (What is the magnetic hysteresis loop, 2015).

To obtain a permanent magnet, a magnetic material must be able to sustain a magnetic flux without the presence of a coil, or outside source, which is known as a ferrimagnet. To achieve this, exchange interaction must occur, which is the alignment of the magnetic dipole's axes due to the materials own internal field (Campbell, 1999). Because an internal field exists without the presence of an applied external field, the material is spontaneously magnetized (Campbell, 1999). When a flux density is produced by a magnet alone it is called an intrinsic induction, magnetization (\mathbf{M}), or magnetic polarization (\mathbf{J}) (units of A/m) (Understanding permanent magnets, 2015).

Magnetization yields a specific value in a designated volume of a magnet, however, it is not likely the entire magnet will present the same, unique \mathbf{M} throughout the material (Campbell, 1999). Magnetization is the sum of the magnetic dipoles, p_m , over the volume,

V , shown in Equation 2.4. The description provided thus far neglects the practical conditions which occur, such as temperature variation which would disrupt the alignment of the moments and reduce the materials magnetization (Campbell, 1999). By rearranging Equation 2.4, the overall magnetic dipole moment, \mathbf{P} , is equivalent to the magnetization multiplied by the volume of the substance being measured, shown in Equation 2.5. From the magnetic dipole moment, the magnetic force exerted, denoted by \mathbf{F} , is able to be calculated from Equation 2.6. Here $d\mathbf{B}_0/dx$ is the derivative of the flux density over the distance at a specific point of interest.

$$\mathbf{M} \equiv \frac{\sum \mathbf{p}_m}{V} \quad (2.4)$$

$$\mathbf{P} = \sum \mathbf{p}_m = \mathbf{M}V \quad (2.5)$$

$$\mathbf{F} = P \frac{d\mathbf{B}_0}{dx} = MV \frac{d\mathbf{B}_0}{dx} \quad (2.6)$$

One way to characterize a material within a magnetic field would be to determine the magnetic susceptibility of the material. Volumetric, magnetic susceptibility, denoted as χ , is a dimensionless material property, which measures the response of a material to an applied magnetic field (Borradaile, 1998), defined by Equation 2.7. To convert χ from CGS units to SI units, it must be multiplied by 4π as shown in Equation 2.8. The conversion factors from CGS to SI units for the mass, specific, molar, and one-gram-formula-weight susceptibilities with their units in CGS and SI are included in Appendix A, Table X. The magnetic susceptibility is determined experimentally by measuring the amount of force exerted by a well-defined magnetic field on an established volume of a substance (Zborowski & Chalmers, 2007). The magnetic force exerted can also be calculated from

Equation 2.9, by rearranging Equation 2.7 to replace M , where H is the magnetic field strength described above.

$$\chi \equiv \frac{M}{H} \quad (2.7)$$

$$\chi(\text{SI}) = 4\pi\chi(\text{CGS}) \quad (2.8)$$

$$\mathbf{F} = \chi V H \frac{d\mathbf{B}_0}{dx} \quad (2.9)$$

Faraday designed an experiment utilizing a balance to measure the magnetic susceptibility of different materials, which is shown in Figure 7. Part A in Figure 7 demonstrates how a paramagnetic, or ferromagnetic, material would react when placed on the left side of the balance. Due to the magnetic field, the material would be attracted to the field, which would mean the magnetic susceptibility of that material was greater than zero ($\chi > 0$). Therefore, weight would need to be added to the opposite side to keep the balance at equilibrium, and to keep the material from being pulled into the magnetic field. However, for a diamagnetic material, it would repel out of the magnetic field causing the magnetic susceptibility to be less than zero ($\chi < 0$). Therefore, as shown in Part B of Figure 7, weight would be added to the side with the material being tested to keep the balance at equilibrium.

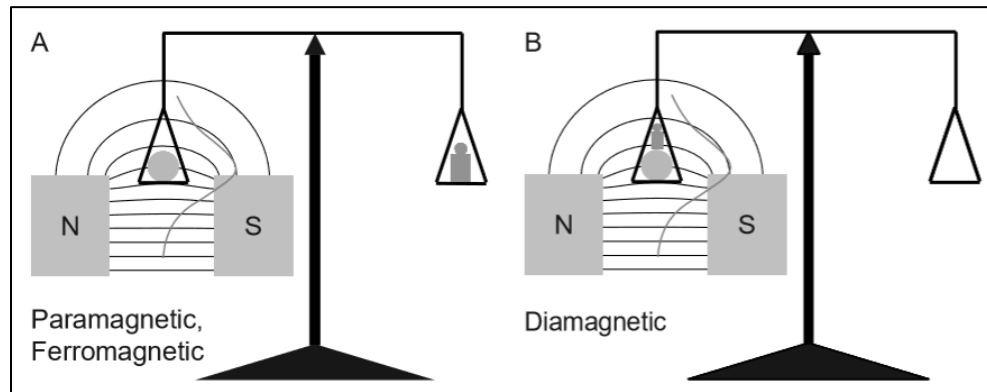


Figure 7: Schematic of Faraday's magnetic balance used to determine the magnetic susceptibility of different materials (Zborowski & Chalmers, 2007).

2.3 Magnetic Susceptibility Balance

The modern-day Faraday balance, which employs the Gouy technique, is known as a magnetic susceptibility balance (MSB). A schematic of the Gouy balance is shown in Figure 8. This technique utilizes an electromagnet and a conventional balance. When a sample is placed between the magnet poles, it will appear to gain weight (be attracted to the magnet) or lose weight (be repelled from the magnet) (Magnetic susceptibility balances, 1930). As described by the Faraday balance, weight gain indicates the sample would be ferro- or paramagnetic, while weight loss indicates a diamagnetic sample.

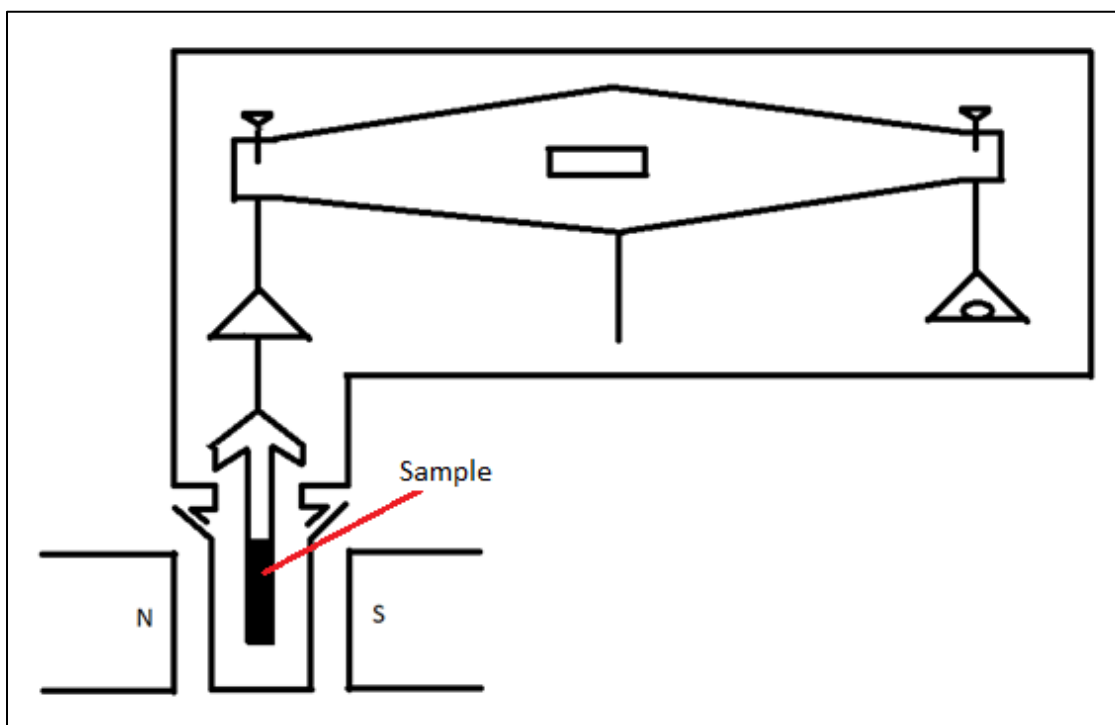


Figure 8: Adapted schematic of a traditional Gouy balance (Magnetic susceptibility balances, 1930).

An MSB operates with similar techniques to the Gouy balance, however, the sample remains stationary while the magnets within the system move. Figure 9 displays a schematic of the inside of an MSB with an image of an actual balance below it. A pair of magnets are on opposite sides of the beam, which creates a balanced system with a

magnetic field on each end (Magnetic susceptibility balances (MSB), 2005). Once the sample is introduced into the magnetic field, it attempts to deflect the set of magnets closest to it on the beam (Magnetic susceptibility balances, 1930). This movement is detected by the optical sensors, which passes a current through a coil between the other pair of magnet poles to produce an equal and opposite force that was exerted by the sample to return the system to an equilibrium position (Magnetic susceptibility balances (MSB), 2005). Thus, the current through the coil is proportional to the force exerted by the sample, and the direction in which the beam moves indicates if the sample is paramagnetic (shown by a plus sign on the display) or diamagnetic (shown by a minus sign on the display) (Magnetic susceptibility balances, 1930).

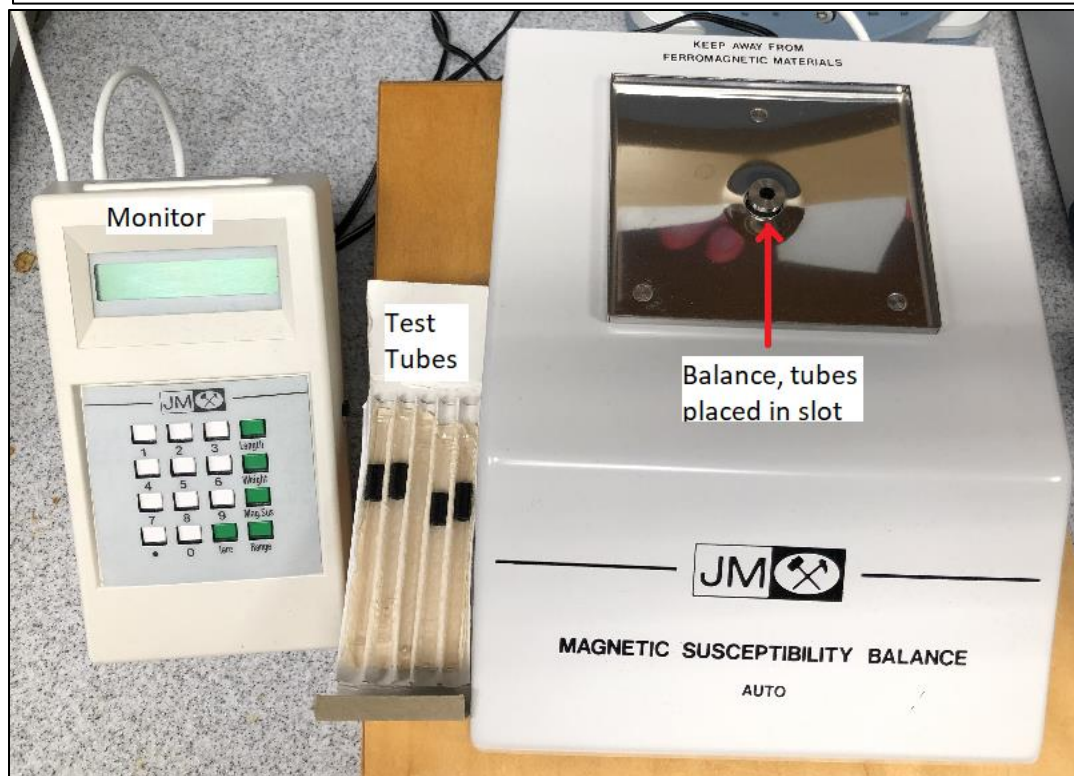
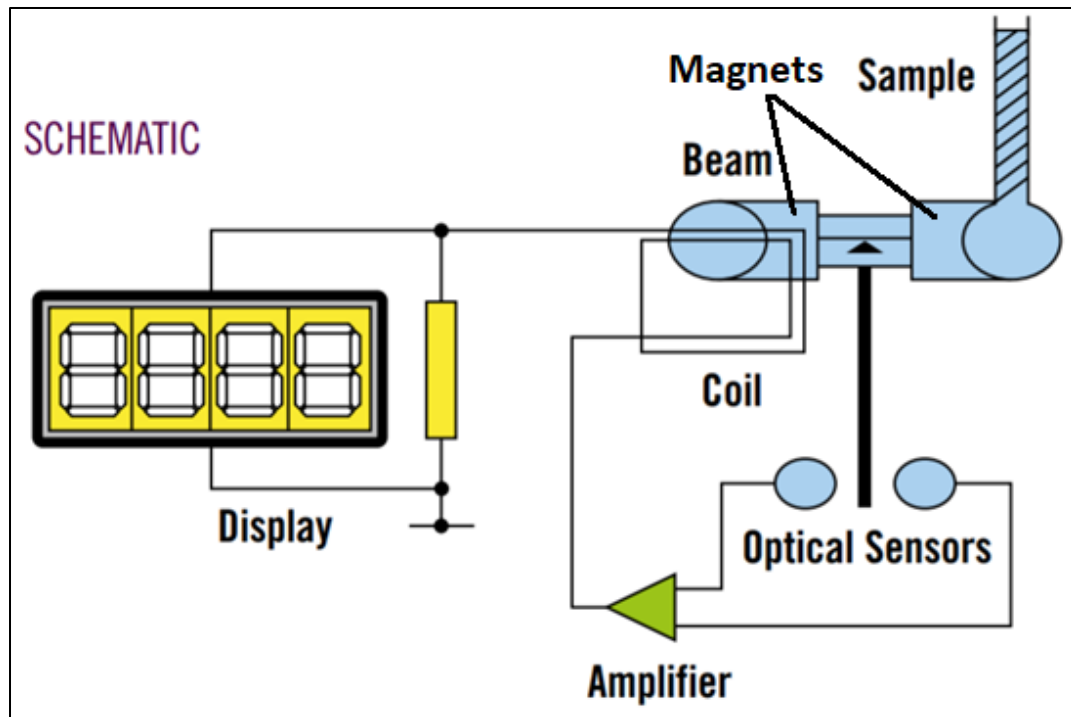


Figure 9: Above: Schematic of the inside of an MSB (Magnetic susceptibility balances (MSB), 2005). Below: Image of the actual MSB-Auto from Dr. Zborowski's lab at the Cleveland Clinic.

2.4 Magnetic Separation of Labeled versus Unlabeled Cells

Magnetically labeling cells is one way magnetics is employed to separate specific cells to be utilized for treatments and/or analyzed for a prognosis of a disease (Joshi, et al., 2014). Biological materials have low magnetic susceptibility. To increase the highly selective magnetostatic forces, cells are tagged with magnetic nanoparticles, which do not interfere with the physiological electrolyte solutions used for cell suspensions and with other cells (Zborowski, et al., 2016). However, based on a biological cell's intrinsic magnetic properties, labeling with magnetic nanoparticles may not be necessary, provided the magnetic device yields a high enough magnetic field. This is an attractive alternative to techniques which rely on immunomagnetic labeling because it eliminates the cost of reagents and the arduous sample preparation steps of labeling the particles (Jin, et al., 2012). Intraerythrocytic malaria parasites (Zimmerman, et al., 2006) and select cancer cell lines have been tested and used to demonstrate the feasibility of magnetophoresis and magnetic separation by the means of only their intrinsic magnetic susceptibility (Joshi, et al., 2015). These types of cell separation were quantified by enrichment upon separation. For example, *Plasmodium malariae* infected erythrocytes were enriched from 0.4% to 100% by means of magnetic deposition microscopy (MDM) (Zimmerman, et al., 2006). Other examples are RBCs, which do not require magnetic nanoparticle labeling due to the presence of unbound electrons (Zborowski, et al., 2003) creating a magnetic dipole moment, and glioma brain cancer progenitor cells because of the increased ferritin uptake which takes place by these cells (Kawabata, et al., 1999). In the following sections, separation and analytical devices are presented to demonstrate how to evaluate the magnetic susceptibility of labeled or unlabeled cells.

2.5 Separation Devices

Magnetic cell separation and manipulation has a large impact on the development of biotechnology engineering and is one of the fastest growing segments of cell separation (Zborowski, et al., 2016). Two examples of high-gradient magnetic separation (HGMS) devices are the quadrupole magnetic cell sorter (QMS) and the circular Halbach array. These magnet arrangements are excellent tools for quantifying purity, recovery, and throughput of sorted cell fractions. They can be utilized to separate red blood cells from whole blood and separating cells which were magnetically labeled. ‘Continuous, intrinsic magnetic depletion of erythrocytes from whole blood with a quadrupole magnet and annular flow channel; pilot scale study’ (Moore, et al., 2018) and ‘Circular Halbach array for fast magnetic separation of hyaluronan-expressing tissue progenitors’ (Joshi, et al., 2015) provide more information on these devices.

2.6 Analytical Devices

There are numerous magnetic devices which are used to quantify the magnetophoretic mobility (described further in Section 2.6.1) of cells, such as cell tracking velocimetry (CTV), magnetic deposition microscopy (MDM), and magnetic flow-field fractionation (MgFFF). Through CTV, cells are tracked with the computer program, ImageView (described further in Section 3.4.4), to determine the average magnetic and average sedimentation velocities of a sample. With MDM, a sample is infused into a channel, which is placed on to a magnetic assembly, allowing the magnetic cells to deposit on a Mylar slide and the nonmagnetic cells continue to the outlet of the channel. Lastly, MgFFF separates cells based on different levels of magnetic material on, or within them, and passes the fractions to an analytical device, such as a mass spectrometer. For more

information on MgFFF refer to ‘Characterization of magnetic nanoparticles using programmed quadrupole magnetic field-flow fractionation’ (Williams, et al., 2010).

2.6.1 Cell Tracking Velocimetry

An increasingly important technique for the diagnosis and treatment of various cancers and diseases is cell analysis and separation (Zborowski, M., Chalmers, J., & Moore, L. R., 2003). To help with analysis, cell tracking velocimetry (CTV) was patented by Dr. Maciej Zborowski, Dr. Jeffrey J. Chalmers, and Lee Moore in July of 2003 (Zborowski, M., Chalmers, J., & Moore, L. R., 2003). The technique measures a labeled or unlabeled particle’s magnetically induced velocity when placed in a magnetic field and its settling velocity, by means of video imaging through CTV. From the settling velocity, the size of the particle can be calculated.

There are three fundamental components along with theoretical concepts needed for CTV. The three characteristics are a well-characterized magnetic field energy gradient, a microscopic image acquisition system, and a computer algorithm particle tracking velocimetry (PTV). With PTV the location and velocity of a particle can be determined in the region of image analysis (Nakamura, et al., 2001). To begin the theoretical analysis, the forces which act on the particle during CTV must be identified: the magnetic force (F_m), the buoyant force (F_b), the viscous drag force (F_d), and force by gravity (F_g). From these forces, the magnetic velocity, settling velocity, and the hydrodynamic diameter of the particle can be determined.

Equation 2.10 demonstrates the magnetic force, F_m , depends upon three variables: S_m (calculated from measured data), $\Delta\chi$ (determined from previous experiments or

literature), and V_p , which is the volume of the particle within the sample (known by researcher making sample) (Nakamura, et al., 2001).

$$F_m = \Delta\chi V_p S_m \quad (2.10)$$

The magnetophoretic driving force, S_m , is defined by Equation 2.11, where H and B are known from the calibration of the CTV magnet, and μ_0 is the magnetic permeability constant.

$$S_m \equiv H \frac{dB}{dx} = \frac{B}{\mu_0} \frac{dB}{dx} = \frac{d}{dx} \left(\frac{B^2}{2\mu_0} \right) \quad (2.11)$$

The $\Delta\chi$ (dimensionless) is the difference between two solutions volumetric, magnetic susceptibility calculated by Equation 2.12, which is written for the two solutions utilized in the S_m verification experiments. This equation could also be used to determine the magnetic susceptibility difference between a particle and a solution, where the solution susceptibility would be subtracted from the particle's susceptibility.

$$\Delta\chi = \phi_{Magnevist} \chi_{Magnevist} - \phi_{H_2O} \chi_{H_2O} \quad (2.12)$$

The $\phi_{Magnevist}$ is the volume fraction of Magnevist (known by researcher creating the solution), $\chi_{Magnevist}$ is the volumetric, magnetic susceptibility of the Magnevist (physical property of substance), ϕ_{H_2O} is the volume fraction of water (known by researcher creating the solution), and χ_{H_2O} is the volumetric, magnetic susceptibility of water (physical property of substance). The difference between the magnitude of the buoyant force, F_b , and the gravity force, F_g , is defined as follows (Nakamura, et al., 2001):

$$F_g - F_b = \frac{(\rho_p - \rho_f)\pi D_p^3 g}{6} \quad (2.13)$$

where ρ_p is the density of the particle, ρ_f is the density of the fluid, D_p is the particle diameter, and g is the gravity constant, which are all known from literature. Lastly, when the Reynold's number is less than 0.1 the viscous drag force can be assumed to be the Stokes drag (Nakamura, et al., 2001).

$$F_{d,x} = 3\pi D_p \eta u_m \quad (2.14)$$

Here $F_{d,x}$ is the drag force component opposing the particle motion in the u_m direction, where u_m is the terminal magnetic velocity component in the horizontal direction (directly measured), D_p is the particle diameter, and η is the viscosity of the fluid (known from literature). When setting Equations 2.10 and 2.14 equal to each other, another equation for S_m arises.

$$S_m = \frac{18\eta u_m}{\Delta\chi D_p^2} \quad (2.15)$$

where Equation 2.12 was used to calculate $\Delta\chi$ between two materials.

The particle terminal velocity is calculated by equating the total force, F , with the viscous drag force (Xue, et al., 2019):

$$F = F_d \quad (2.16)$$

where F is also the vector sum of the magnetic component, F_m , (acting in the horizontal, x-axis direction) and the $F_g - F_b$ component (acting in the vertical, y-axis direction), so that in the vertical direction the following expression for the drag force applies:

$$F_{d,y} = 3\pi D_p \eta v \quad (2.17)$$

The particle terminal velocity vector has two components, in the horizontal (x-axis) direction and vertical (y-axis) direction. From the foregoing equations, terminal velocity magnetic and sedimentation components are, respectively (Xue, et al., 2019):

$$u_m = \frac{\chi_{cell} - \chi_{solution}}{3\pi\eta} \frac{V_{cell}}{D_{cell}} S_m \quad (2.18)$$

$$v = \frac{\rho_{cell} - \rho_{solution}}{18\eta} D_{cell}^2 g \quad (2.19)$$

where u_m is the experimentally determined mean magnetic velocity in units of m/s, v is the experimentally determined sedimentation velocity in units of m/s, and the other variables follow the same notation stated within this section. The particle magnetophoretic mobility, m , is defined as the ratio of its magnetic field-induced velocity, u_m , and the magnetophoretic driving force, S_m :

$$m = \frac{u_m}{S_m} \quad (2.20)$$

These equations provide the theoretical foundation for CTV.

The well-defined magnet assembly, Mk V, which has been utilized in many other experiments, is the strongest magnet created for CTV research (Xue, et al., 2019). Within the FOV, the magnetostatic potential energy gradient, S_m , is horizontal, nearly constant, and well-characterized due to the hyperbolic pole pieces within the system, which occurs in the microscopes FOV (Xue, et al., 2019). Figure 10 Part A represents the section of the CTV system where the cell suspension is contained by a glass channel, which is located inside the magnet assembly (Xue, et al., 2019). The magnetostatic potential energy density gradient should be as constant as possible to avoid any variation in the magnetic field

presented to the particles within the FOV. Figure 11 represents a predicted model of the Mk V magnet flux density field \mathbf{B} in units of Tesla (T) (blue dotted line), with a best fit line corresponding to the flux density (black line), the gradient of the \mathbf{B} field (red line), and twice the product of the magnetic flux density field and the gradient of the flux density, $d\mathbf{B}^2/dy$ (green line), which is proportional to S_m . Here the S_m graph is nearly constant within the FOV, which would allow for the particles to be exposed to the most uniform magnetic field possible. This is important in order to characterize the magnetic properties of the particles appropriately within the CTV system. If the magnetic field within the FOV is constant, or nearly constant, the particles will have a magnetic velocity which is independent of the particle location within the system.

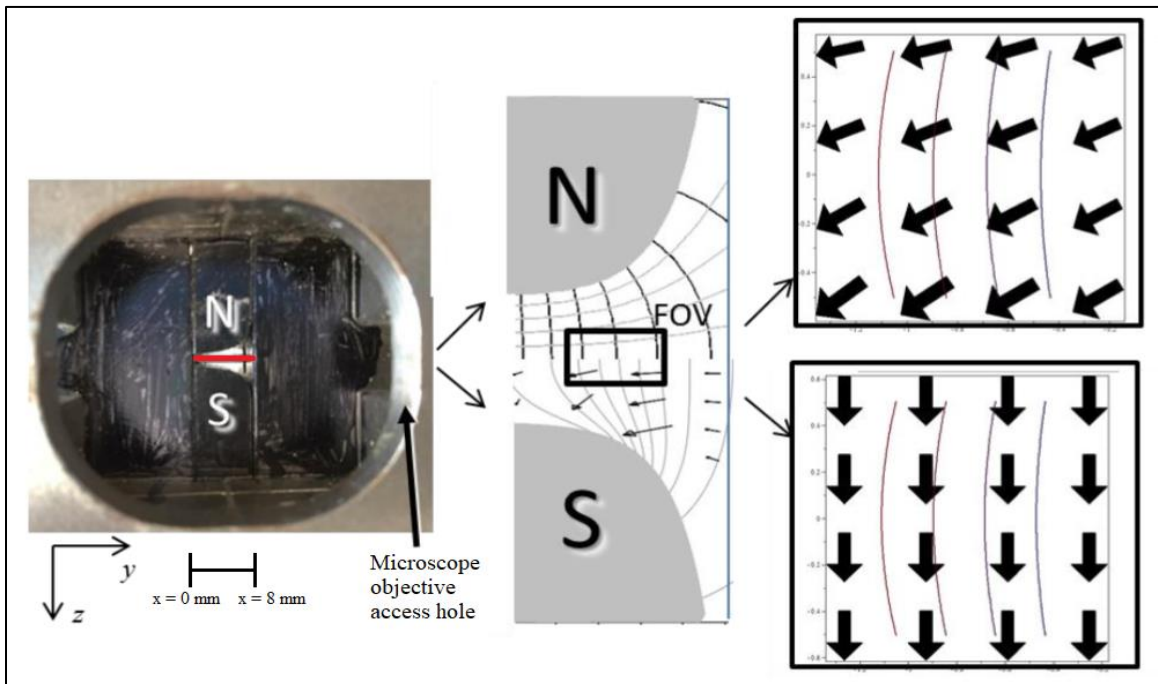


Figure 10: Image of the CTV magnet with explanations. A) Photograph of portion of permanent magnet showing hyperbolic shape of pole pieces with the glass channel colored red, B) Composite diagram of equipotential and field lines (top) and magnetostatic potential isolines and force vectors (bottom) C) Expected outcomes for deoxygenated RBCs (top) and oxygenated RBCs (bottom) (Xue, et al., 2019).

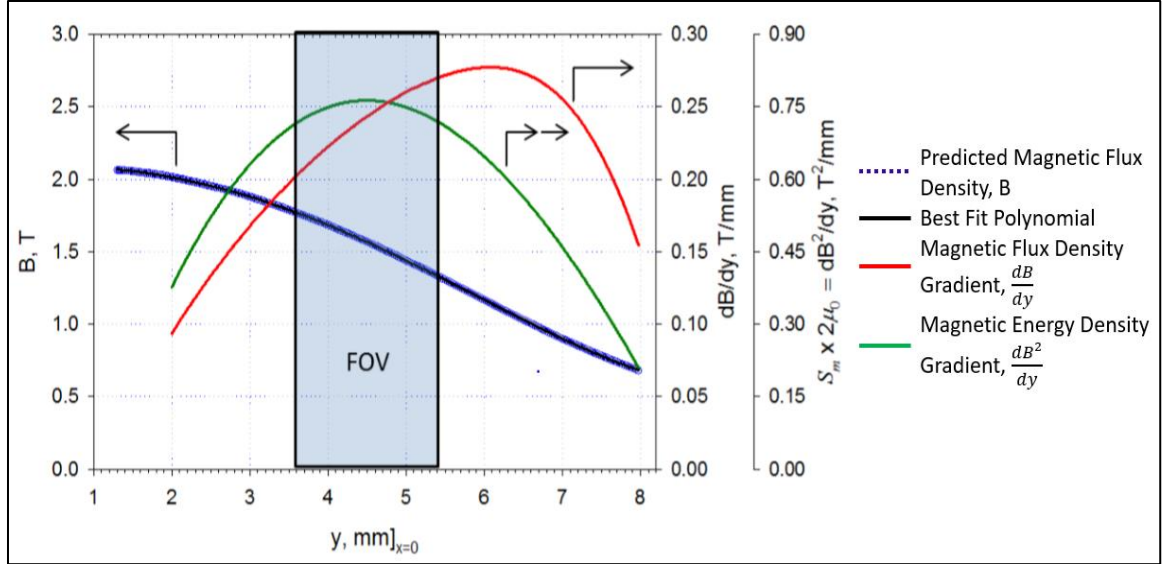


Figure 11: Key CTV magnetostatic field parameters (Xue, et al., 2019).

The computer algorithm needed to perform CTV mentioned above originated from a 3-D version of particle tracking code, known as particle tracking velocimetry (PTV) (Nakamura, et al., 2001). PTV utilized five successive images to predict the most probable pathway for a specific particle (Nakamura, et al., 2001). The original PTV algorithm was developed for 3-D flow visualization studies of complex hydrodynamic flow where hundreds of instantaneous velocities at different locations were wanted, and does not report particles tracked from frame to frame (Nakamura, et al., 2001). For CTV, the algorithm was modified to provide these reports in which the location and velocities of specific particles are presented for a series of frames, which is determined by the user (Nakamura, et al., 2001). This algorithm will be described in length in Chapter III – Materials and Methods.

2.6.2 Magnetic Deposition Microscopy

Magnetic cell separation was propelled to the forefront of separation techniques due to the rapidly growing demands in cell biology and clinical laboratories (Zborowski,

et al., 2016). The prototype of MDM was known as the Bio-Ferrograph, which was developed in collaboration with the Institute Guilfoyle in Belmont, MA and Bingbing Fang, Dr. Maciej Zborowski, and Lee Moore from the Department of Biomedical Engineering at the Cleveland Clinic (Fang, et al., 1999). A few of the first cell-types separated utilizing MDM (Bio-Ferrograph) were MCF-7 breast cancer cells and malaria cells from whole blood.

Applications of MDM are known to pull weakly magnetic cells from a flowing cell suspension due to the high magnetic gradient generated by the magnets within the assembly. The magnetic cells are deposited onto a transparent, thin sheet of Mylar, which can be analyzed under a microscope. More information about the magnet assembly can be found in ‘Magnetic separation of algae genetically modified for increased intracellular iron uptake’ (Buck, et al., 2014).

A theoretical analysis of the MDM is similar to CTV because the magnetic force, the viscous drag force, and the magnetic velocity are calculated from the same equations, Equation 2.10, 2.14, and 2.18, respectively (Moore L. R., et al., 1998). However, the microfluidic fluid velocity profile between CTV and MDM are different. The following equation approximates the velocity profile given by Purday (Moore L. R., et al., 1998):

$$w = w_{max} \left(1 - \left(\frac{x}{a}\right)^2\right) \left(1 - \left(\frac{|y|}{b}\right)^n\right); \quad |x| \leq a, |y| \leq b \quad (2.21)$$

The cell velocity is represented by w , w_{max} is the maximum cell velocity, x and y are distances from the channel center, a is the half-depth of the channel, b is the half-width of the channel, and n is a constant that depends on the aspect ratio of the channel, b/a . It can be calculated by Equation 2.22 (Moore L. R., et al., 1998).

$$n(n + 1) = \frac{2b^2}{a^2} \quad (2.22)$$

Once n is known, the relationship between w_{mean} and w_{max} can be determined by Equation 2.23 and w_{mean} is given by Equation 2.24 (Moore L. R., et al., 1998).

$$\frac{w_{\text{max}}}{w_{\text{mean}}} = \frac{3(n + 1)}{2n} \quad (2.23)$$

$$w_{\text{mean}} = \frac{Q^o}{A} \quad (2.24)$$

Here Q^o is the volumetric flow rate entering the channel and A is the surface area of the channel.

Below, Figure 12 provides three important aspects to the MDM setup. Part A displays a color map, with graduations of 0.08 T, of the magnetic field generated by the magnetic assembly (Buck, et al., 2014). At the edges of the two interpolar gaps, the blue rectangles, there are four spots where the magnetic field exceeds 1.4 T and the gradient exceeds 1,000 T/m, at the corners of the interpolar gaps (Buck, et al., 2014). Part B presents a graph which verified the field map compared to the magnitude of the magnetic field along the y-axis at $x=0$ (Buck, et al., 2014). The last part of Figure 12 is Part C, which represents all the components of the experimental setup. The magnet assembly is labeled 1, the Mylar slide is denoted as 2, while 3 is the silicon rubber gasket with five flow channel cutouts, 4 is the manifold with the inlet at the bottom connected to the sample vial by tubing and the outlet at the top linked to the syringe pump also by tubing, and lastly 5 is the platen which holds all of the parts together against the magnet (Buck, et al., 2014). Figure 13 is an image of the fully assembled MDM system displayed in Part C of Figure 12.

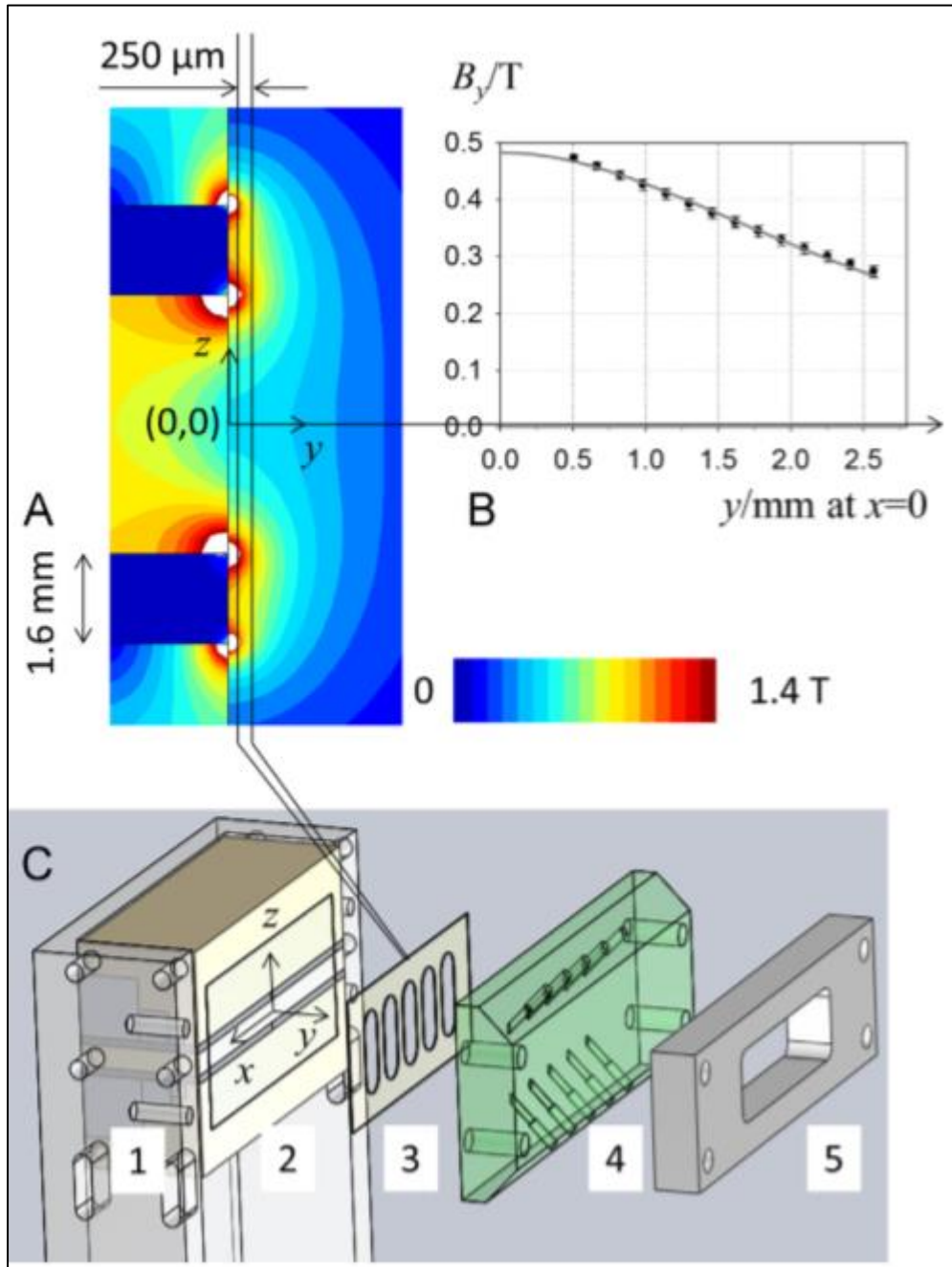


Figure 12: (A) Color map of the magnetic field with color graduations of 0.08 T, (B) Verified the magnitude of the magnetic field represented by the color map in A along the y-axis with $x=0$, (C) Represents all of the parts used to assemble the MDM to complete an experiment (Buck, et al., 2014).

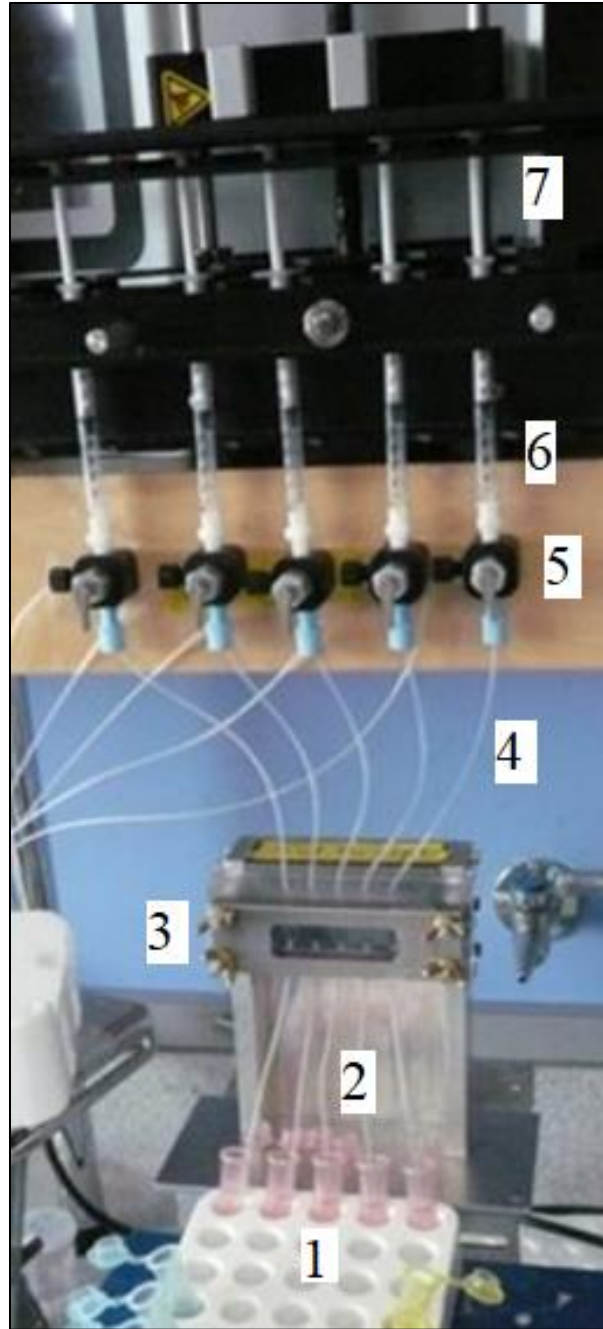


Figure 13: 1) 1 mL vials containing sample solutions. 2) Microfluidic tubing connecting the sample to the channel against the magnet. 3) Fully assembled MDM system presented in Part C in Figure 12 along the y-axis. 4) Second set of microfluidic tubing connecting the channel to the syringes. 5) Three-way Hamilton valves allowing the sample to move from the channel to the syringes. 6) 1 mL syringes collecting the sample solution. 7) Legato 210P multi-syringe kd Scientific syringe pump, withdrawing the sample into the syringe and infusing the sample back into the sample vial.

2.7 Cooperative Binding of Oxygen and Hemoglobin: Adair and Hill Equations

Red blood cell saturation by oxygen depends on the pO_2 in the solution and is described by Adair's equation illustrated by the oxygen-hemoglobin equilibrium curve in Figure 14. This is also demonstrated in Figure 15, where fully oxygenated RBCs (low spin) present a diamagnetic magnetic mobility, whereas fully deoxygenated RBCs (high spin) display a more paramagnetic response in the presence of a magnetic field (Zborowski, et al., 2003). The number of cells tracked is denoted by n , and magnetic mobility is denoted by m .

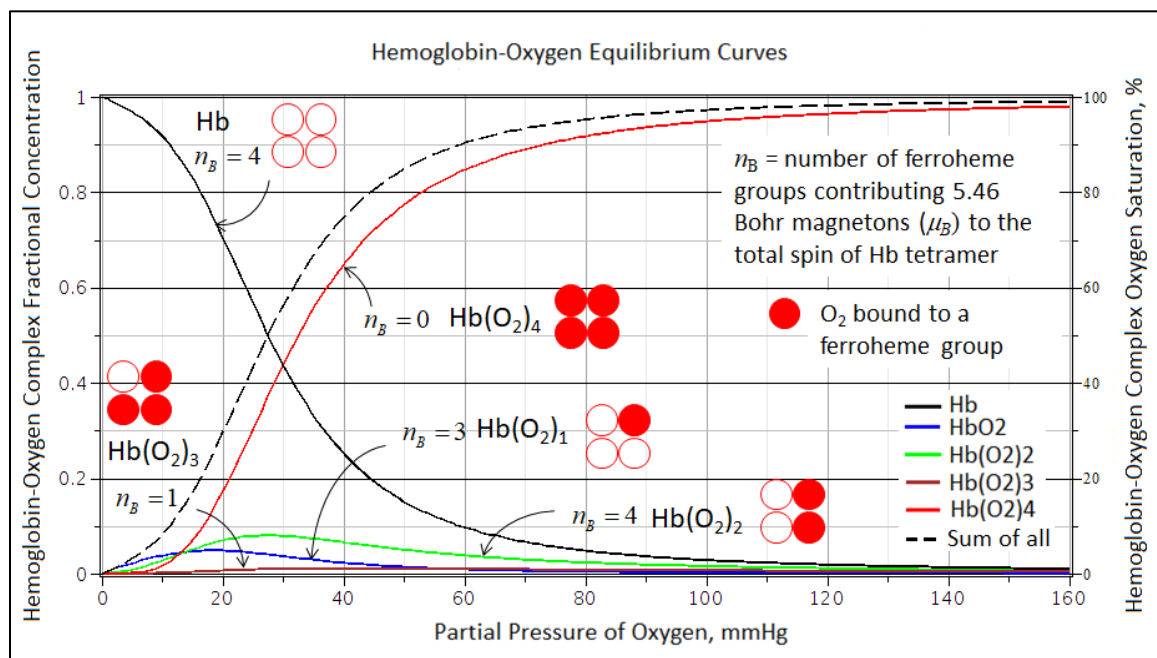


Figure 14: Graph of the oxygen-hemoglobin equilibrium curve generated in Maple by Dr. Zborowski. Graph of the fractional concentrations of five hemoglobin-O₂ complexes (left axis), and the corresponding hemoglobin-O₂ equilibrium curve (right axis) as a function of pO_2 calculated from the Adair equation. Symbols n_B describe the number of heme groups that contribute to the paramagnetic dipole moment of the hemoglobin-O₂ complex.

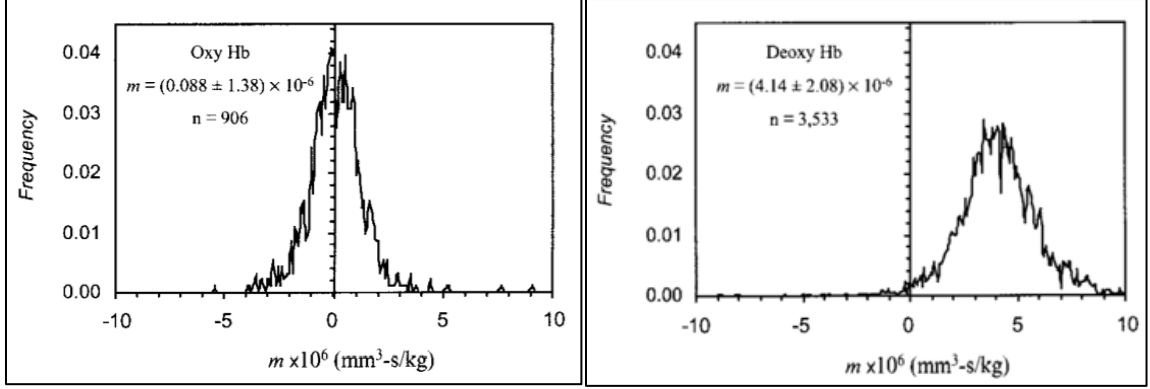


Figure 15: Magnetophoretic mobility of oxygenated and deoxygenated RBCs. The graph on the left represents fully oxygenated RBCs, while the graph on the right displays fully deoxygenated RBCs (Zborowski, et al., 2003).

Adair's generalized equation is stated in Equation 2.25, where S is the fractional saturation, p is the oxygen pressure, a_n are the overall Adair parameters, which are determined experimentally, and n corresponds to the number of oxygen molecules bound to the hemoglobin within the RBCs (Winslow, et al., 1977). The K_n parameters are the stepwise Adair constants, which refer to a specific binding scheme of oxygen to hemoglobin and the simplest way to describe the binding scheme (Imai, 1994). Theoretical values for the stepwise Adair's coefficients are found in Table I.

$$\begin{aligned}
 S &= \frac{a_1 p + 2a_2 p^2 + 3a_3 p^3 + 4a_4 p^4}{4(1 + a_1 p + a_2 p^2 + a_3 p^3 + a_4 p^4)} \\
 &= \frac{K_1 p + 3K_1 K_2 p^2 + 3K_1 K_2 K_3 p^3 + 3K_1 K_2 K_3 K_4 p^4}{1 + 4K_1 p + 6K_1 K_2 p^2 + 4K_1 K_2 K_3 p^3 + K_1 K_2 K_3 K_4 p^4}
 \end{aligned} \tag{2.25}$$

Also, S is the fractional saturation of oxyhemoglobin, which influences RBC magnetophoresis by determining the magnetic susceptibility of an RBC. Equation 2.26 demonstrates how the fractional saturation levels influence the susceptibility of an RBC.

$$\chi_{RBC} = \phi_{H_2O} \chi_{H_2O} + (1 - S) \phi_{Hb} \chi_{deoxyHb} + \phi_{globin} \chi_{globin} \tag{2.26}$$

The volume fraction of water, deoxyhemoglobin, and the globin protein are denoted as ϕ_{H_2O} , ϕ_{Hb} , and ϕ_{globin} , respectively. The volumetric, magnetic susceptibility of these species

are χ_{H_2O} for water, $\chi_{deoxyHb}$ for deoxyhemoglobin, and χ_{globin} for the globin protein. Utilizing these definitions, varying the fractional saturation of the RBC solution, and evaluating the volumetric, magnetic susceptibility at those fractional saturation values by means of the CTV deoxygenation system, it will be determined if the oxygenation level of an RBC can be measured through magnetophoresis.

Table I: Form-specific Adair's Coefficients (Matejak, et al., 2015).

Estimated Form-Specific Adair's Coefficients		
Coefficient	Value	Units
K_1	0.0121	mol/m ³
K_2	0.0117	mol/m ³
K_3	0.0871	mol/m ³
K_4	3.86×10^{-4}	mol/m ³

The Hill equation, stated in Equation 2.27, was originally formulated by Archibald Hill in 1910 to describe the sigmoidal curve of oxygen binding to hemoglobin (Hill, 1910). Here Y is the fractional saturation of oxygen bound to the hemoglobin, x corresponds to the log of the Gaussian b-value, k is 10 raised to the negative value of the y-intercept from the regression line of the linearized Hill equation, and n is the Hill coefficient, also known as the slope of the regression line of the linearized Hill equation. This will be discussed further in Section 3.4.6. For the purpose of this study, the Hill equation was considered a satisfactory approximation of a more complex Adair equation in applications to analyze the RBC magnetophoresis data.

$$Y = \frac{x^n}{k + x^n} \quad (2.27)$$

2.8 Spectrophotometry

There are many applications within the life sciences for spectrophotometry outside of a classroom. For example, it could be used to determine the number of cells within a suspension. For the interest of the research being presented in this paper, it was utilized to determine the concentration of oxyhemoglobin and methemoglobin within a blood sample. This is done by measuring the amount of light which passes through or is absorbed by a sample (Bostick, 2018). Spectrophotometry follows two basic principles. First, every substance transmits or absorbs specific wavelengths of energy (Bostick, 2018). Second, depending on the amount of material dissolved within the sample solution (known as an analyte), the measured intensity of the color will vary, allowing the concentration of a substance to be determined within the sample (Bostick, 2018). Figure 16 represents a general overview of what occurs within a spectrophotometer. An initial known intensity of light, I_0 , is passed through the sample, and a different intensity, I , is measured by the photocell on the opposite side of where the initial light entered the sample. Equation 2.28 is then utilized to calculate the transmittance of the sample, T .

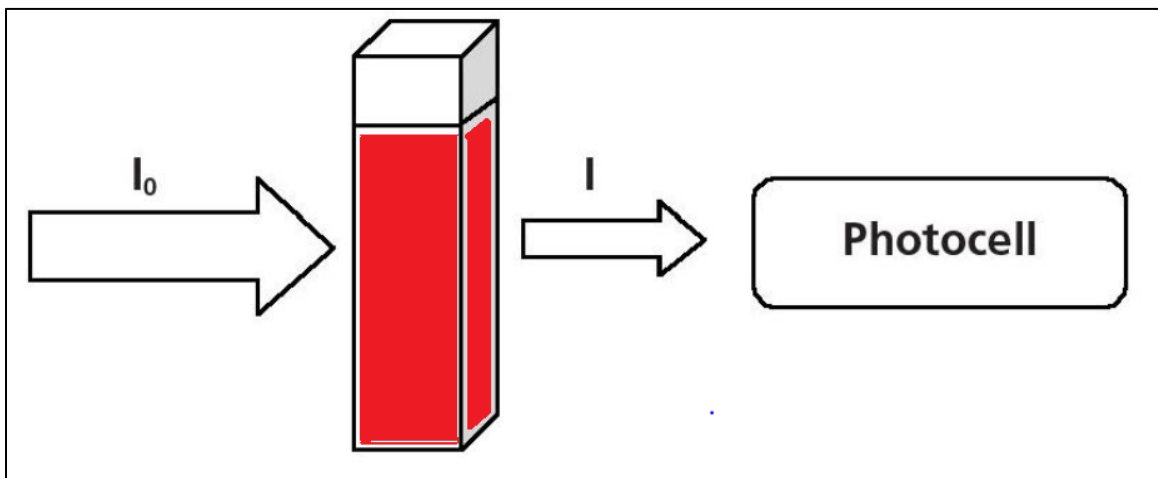


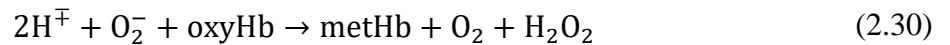
Figure 16: Adapted schematic of what occurs within a spectrophotometer (Bostick, 2018).

$$T = \frac{I}{I_0} \quad (2.28)$$

Another way to interpret the intensity of light within a sample is with the absorbance, A . This value can be calculated with Equation 2.29.

$$A = -\log T \quad (2.29)$$

Christine Winterbourn determined that different forms of oxygen-hemoglobin compounds present different absorbance levels when a spectrum of 500 – 700 nm wavelengths are passed through the sample (Winterbourn, 1990). Specifically, Winterbourn focused on oxyhemoglobin, methemoglobin, and hemichrome. Oxyhemoglobin (oxyHb) is the form of hemoglobin where all eligible binding sites of the hemoglobin molecule have an O_2 molecule bound, therefore, there are no unpaired electrons. Methemoglobin (metHb) is formed by chemically reducing oxyHb with sodium nitrite ($NaNO_2$). Hemichromes form by methemoglobin having an unstable globin structure, which allows for the distal histidine or an external ligand to bind to heme (Winterbourn, 1990). Chemical reactions presented in Equations 2.30 and 2.31 represent how oxyHb turn into metHb and metHb revert to oxyHb, respectively.



It is known that reactions can be followed spectrally, and with this information Winterbourn developed equations to calculate the concentration, in units of μM , of oxyhemoglobin, methemoglobin, and hemichrome within a blood sample, presented in Equations 2.32, 2.33, and 2.34, respectively. The A_i variables denote the absorbance value at the i wavelength.

$$[\text{Oxyhemoglobin}] = 119A_{577} - 39A_{630} - 89A_{560} \quad (2.32)$$

$$[\text{Methemoglobin}] = 28A_{577} + 307A_{630} - 55A_{560} \quad (2.33)$$

$$[\text{Hemichrome}] = -133A_{577} - 114A_{630} + 233A_{560} \quad (2.34)$$

At each of these absorbance levels there are certain attributes which allowed for a distinction between the different hemoglobin types. For wavelength 577 nm, oxyHb presents a sharp rise to a second peak (Winterbourn, 1990). MetHb presents a characteristic peak or shoulder at wavelength 630 nm (Winterbourn, 1990). Lastly, hemichrome is shown by a shallower trough at 560 nm within oxyHb-metHb mixtures (Winterbourn, 1990).

Figure 17 displays the spectra of Hb, oxyHb, and metHb from 450 – 700 nm.

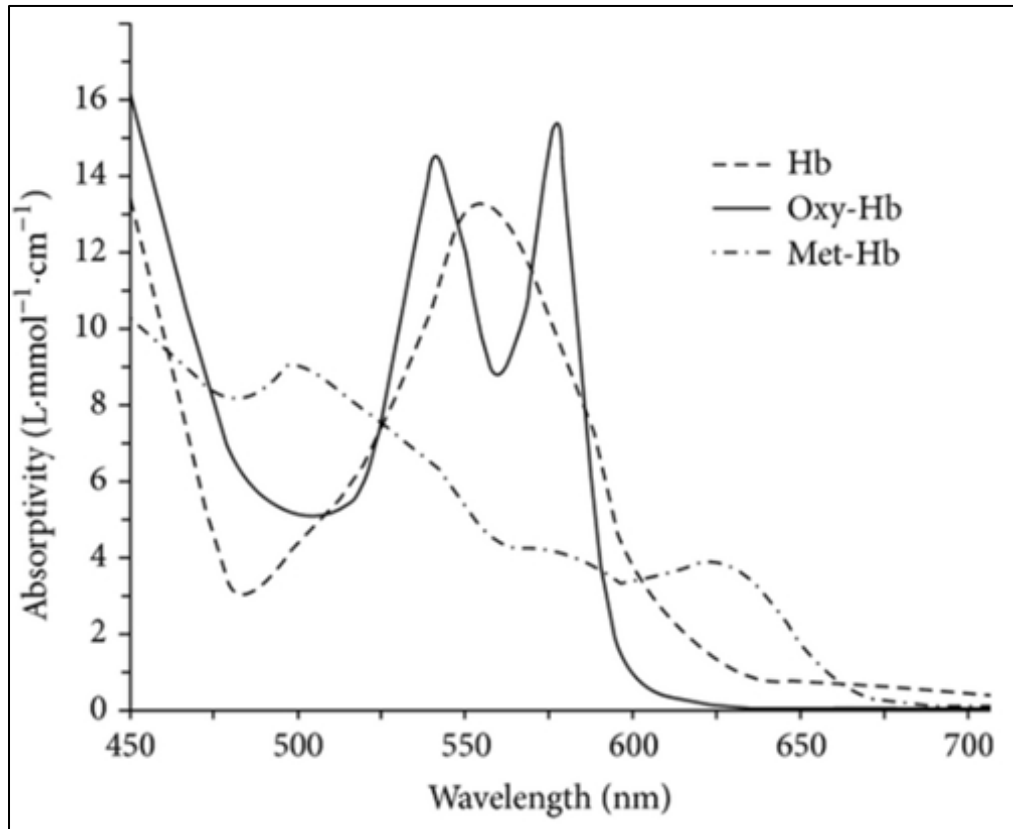


Figure 17: OxyHb and metHb absorbance curves from 450 - 700 nm (Giangreco, et al., 2013).

2.9 Glioblastoma

Glioma is a tumor occurring within the brain and spinal cord stemming from glial cells (Glioma, 2019). Glial cells are brain cells which support nerve cells (Glioma, 2019). There are three types of glial cells which can form into tumors, and the gliomas are classified by the type of glial cell that produced the tumor (Glioma, 2019). By knowing the glial cell which caused the glioma, it can help predict how the tumor will act over time and what treatments would be the most effective (Glioma, 2019). The three types of glial cells which form into gliomas are: astrocytomas, ependymomas, and oligodendrogliomas (Glioma, 2019). Astrocytomas gliomas include astrocytoma, anaplastic astrocytoma, and glioblastoma (Glioma, 2019). Anaplastic ependymoma, myxopapillary ependymoma, and subependymoma are categorized as ependymomas gliomas (Glioma, 2019). Lastly, oligodendrogliomas contain oligodendroglioma, anaplastic oligodendroglioma, and anaplastic oligoastrocytoma (Glioma, 2019). For the purpose of this paper, only glioblastoma will be expanded upon. For more information about astrocytomas, ependymomas, and oligodendrogliomas see references ‘Glioma: Astrocytoma’ (Glioma: Astrocytoma, 2019), ‘Brain tumor: Ependymoma’ (Brain tumor: Ependymoma, 2019), and ‘Glioma: Oligodendroglioma’ (Glioma: Oligodendroglioma, 2019), respectively.

Glioblastoma, or glioblastoma multiforme (GBM), is classified by the World Health Organization (WHO) as a grade IV glioma. It is the most common and lethal brain tumor in adults and accounts for 45% of all malignant brain tumors (GBM agile: A revolutionary new adaptive trial platform, 2019). The median survival rate upon diagnosis is about one to two years, and 95% die within five years (GBM agile: A revolutionary new adaptive trial platform, 2019). Different forms of treatment are surgery, radiation,

chemotherapy, tumor treating fields, and targeted drug therapy (Glioma: Glioblastoma, 2019). However, a cure is not often possible for GBM. Due to consistent poor prognoses for patients with this aggressive and persistent brain tumor, the hopes of developing new and more effective treatments are being explored.

It was stated that cancer stem cells (CSCs) could be the reason that GBM is violent and relentless (Lathia, et al., 2015). The ability to self-renew and give rise to a differentiated progeny is the definition of a CSC (Lathia, et al., 2015). Their functional characteristics are they can generate a tumor when transplanted for a second time into a body containing cellular heterogeneity and progeny with fluctuating degrees of self-renewal capabilities (Lathia, et al., 2015). The term ‘stem cell’ does not imply the cells formed from altered stem cells, because there is evidence that multiple cell types are susceptible to form cancerous cells (Lathia, et al., 2015). Efforts to identify and isolate CSCs have been difficult. Surface markers, like SOX2, CD133, and CD44, have been used to identify CSCs, which is then coupled with cytometry to separate them. This method of isolation has contributed to the research progress of CSCs (Duan, et al., 2013).

It is known that CSCs thrive in stressful conditions, such as hypoxia, low glucose, inflammation, oxidative stress, and acidic stress (Schonberg, et al., 2015). For all these situations, iron metabolism enables the effects and growth of CSCs (Schonberg, et al., 2015). A direct source of CSC resistance to therapy and tumorigenicity may be uncovered by exploiting the abnormal iron regulation within these combinations of conditions within tumors (Schonberg, et al., 2015). It was hypothesized that CSCs in GBM search out iron within regulatory functions within the body typically for the liver and specific regions of the brain, like choroid plexus, for the transferrin consumption and excretion, which

increases the intracellular iron concentrations of CSCs (Schonberg, et al., 2015). Transferrin (TF) is the primary iron storage protein and iron metabolism within the body (Brem, et al., 2006).

An important observation made by Schonberg, et al., was within an *ex vivo* transplant model and a 3D reconstruction of TF co-localization of a tumor cell surface, demonstrated that more than 20-fold higher amount of TF were bound to CSCs than non-CSCs in the same conditions. Also, an increased level of transferrin receptors (TfRs) was detected (Schonberg, et al., 2015). The prime path for iron uptake necessitates ferric iron (Fe^{3+}) to bind to TF and attach to TfRs on the cell membrane. Many cancers, such as bladder, breast, glioma, leukemia, lung, and lymphoma, express abnormally high quantities of TfRs, which in turn suggests that tumor cells display a high demand for iron (Schonberg, et al., 2015). From this information, it is apparent that TfR activity plays a part in tumor growth (Schonberg, et al., 2015). Iron bound to hemoglobin is one of the most common types of iron within the human brain (Brem, et al., 2006). The upregulated iron trafficking in GBM CSCs indicate they may possess intrinsic magnetic potential, which means CSCs exhibit nearly paramagnetic properties (Brem, et al., 2006). Through CTV, MDM, cytosmears, and fluorescent staining, it was investigated if CSCs could be differentiated and separated from other types of brain progenitor cells. Further explanation of the materials used for these experiments are described in Section 3.5.1.

2.10 Giddings Velocity Profile

When separating out viable RBCs for use in transfusions, scaling up the process from small amounts of blood, ~15 mL to 1 L, is always being explored. An idea which was considered was to couple magnetic separation with a temperature gradient being applied to

the sample suspension. J. Calvin Giddings developed a temperature gradient velocity profile, which would facilitate separation between two species by means of natural convection. For example, when a pot of water is placed on a stove top to boil, the water at the bottom heats up causing the density to drop. It then rises to the top of the pot, while the cooler water, with a higher density, moves to the bottom to replace it. Figure 18 represents an example of a velocity profile within a thermogravitational column.

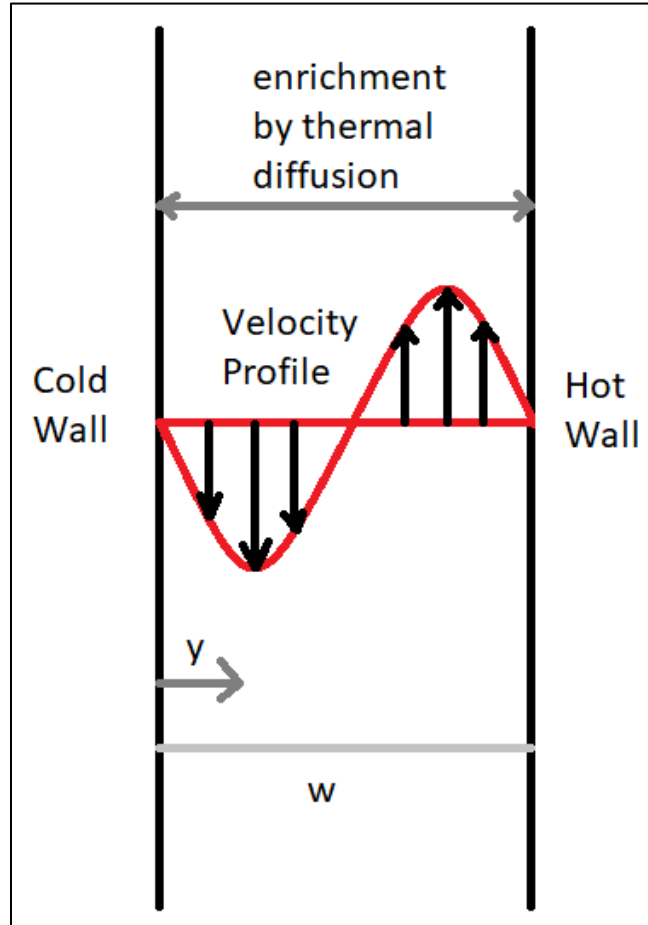


Figure 18: Representation of the Giddings velocity profile with a temperature gradient within the fluid (Giddings, 1991).

This velocity profile, $v(y)$, can be calculated from Equation 2.35.

$$v(y) = \frac{\rho \gamma g w^2 \Delta T}{12 \eta} \frac{y}{w} \left(1 - \frac{y}{w}\right) \left(1 - \frac{2y}{w}\right) \quad (2.35)$$

Here ρ is the density, γ is the thermal expansion coefficient, g is the gravitational constant of 9.81 m/s^2 , ΔT is the temperature difference between the hot wall and the cold wall, η is the viscosity of the fluid, y is the distance from the cold wall, and w is the width of the channel. Parameters ρ , γ , and η were evaluated for the fluid at the cold wall. Decreasing the viscosity of the fluid, having a larger temperature difference between the hot and cold walls, and increasing the channel thickness would increase convective flow to facilitate separation (Giddings, 1991).

CHAPTER III

MATERIALS AND METHODS

3.1 Determination of the Magnetophoretic Driving Force for the Cell Tracking

Velocimetry Magnet Assembly

3.1.1 Materials

Polystyrene (PS) particles of 2.7 μm nominal diameter were synthesized in Professor Shlomo Margel's Laboratory in the Department of Chemistry at Bar-Ilan University located in Ramat Gan, Israel in 2000 (Moore L. R., et al., 2000). They were originally measured to have a radius of $1.35 \pm 0.02 \mu\text{m}$, as evaluated by a sub-micron particle analyzer (model N4MD, Coulter Electronics Ltd., Luton, UK), and a volumetric susceptibility of -8.21×10^{-5} (SI units). These were kept in a powder form and stored at room temperature. Their radius was re-evaluated upon reconstitution in buffer solution with a Beckman-Coulter Multisizer 4e by Mitchell Weigand in Dr. Jeffrey Chalmers Lab at The Ohio State University in Columbus, OH, to have a mean radius of $1.42 \pm 0.02 \mu\text{m}$. The particles were tested in a 0.5 M Magnevist in MDM buffer solution. MDM buffer is a mixture of 0.1% weight/volume Pluronic F-68 (Sigma Aldrich), 2 mM EDTA (Sigma Aldrich), and 0.02% weight/volume Sodium Azide (NaN_3) (Sigma Aldrich) in 100 mL of 10 \times PBS (Phosphate Buffer Solution) free of calcium and magnesium (Cleveland Clinic

Main Campus Media Core Services). A Vortex Genie-2 (Scientific Industries, Bohemia, NY) was operated to mix the particles, MDM buffer, and Magnevist.

Two three-way Hamilton valves were utilized, intended to be chemically inert, with plug type 'T', with polytetrafluoroethylene (PTFE) and Kel-F flow path, rated for 100 psig. Male chromatography fittings ($\frac{1}{4}$ -28 \times 1/16") were used with poly ether ether ketone (PEEK) tubing (1/16" OD \times 0.02" ID; Upchurch Scientific) to connect to the square borosilicate glass channel (1.4 mm OD \times 1.0 mm ID; VitroCom #8100). Figure 19 is an image of the assembly itself. Approximately 2 cm of 1/16" ID silicone tubing was utilized to interface the PEEK tubing to the glass channel and wrapped with 28 AWG bare copper wire to secure the seal. Phar-Med (LS-16, Saint-Gobain) was placed over the silicone tubing and secured with 4" wire ties to minimize oxygen transport to the sample within the tubing. Connected to the Hamilton valves were two 5 mL B-D disposable, plastic syringes by means of a $\frac{1}{4}$ -28 male-to-female Luer adaptors from Upchurch Scientific. These materials were utilized to facilitate flow of the sample solution during experiments.

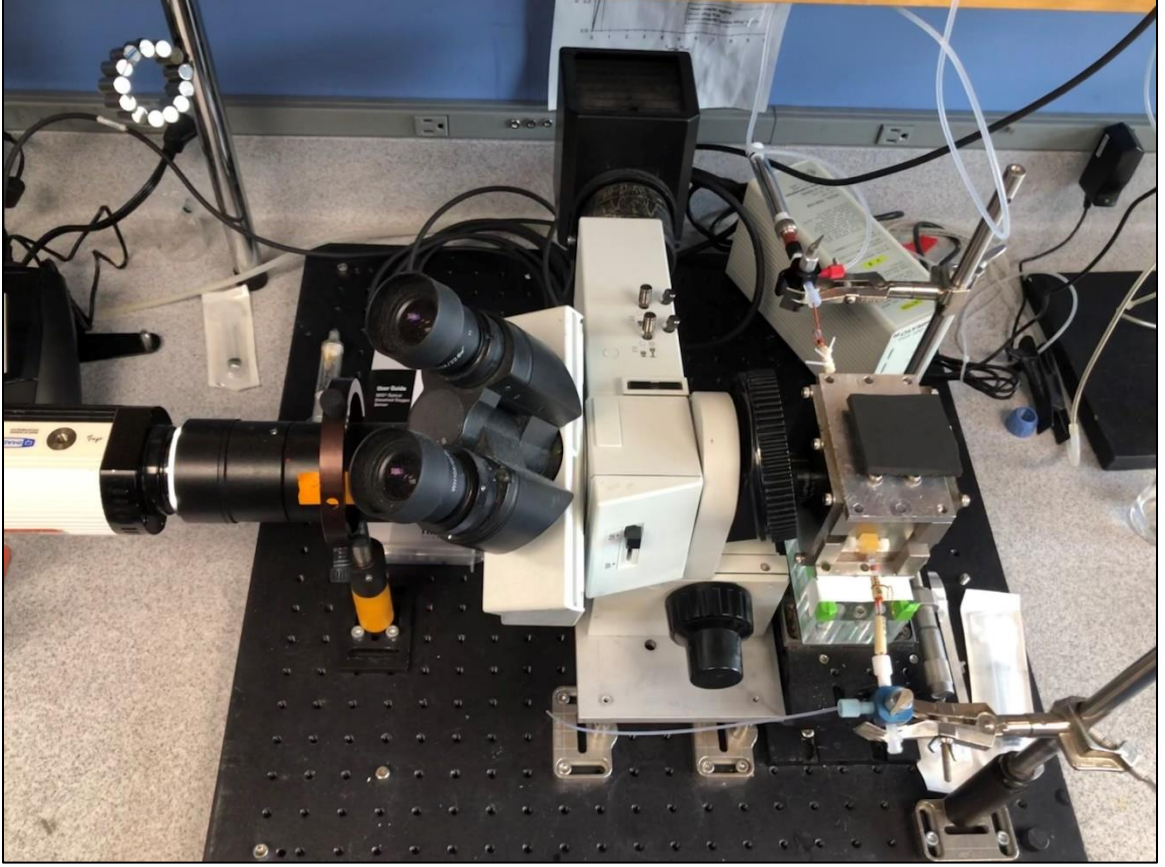


Figure 19: Picture of the CTV system utilized for the S_m verification experiments.

For the CTV setup, a $5\times$ objective lens (LMPlanFl, Olympus, Japan), $3.3\times$ photo eyepiece (U-PMTVC, Olympus, Japan), and CCD camera (Retiga 200R, QImaging, Canada) were used to capture the images of the particle motion within the magnetic field through the Video Savant 4 software (Xue, et al., 2019). This software allows the user to select the region of interest (ROI), gain, exposure time, frame rate, number of images in a set, and the image file type (*.RAW). The PC utilized was a Dell OptiPlex 980 with an Intel Core I7 280 GHz processor, 8.0 GB RAM, and 64-bit Win7 Pro OS. The camera and the computer are connected by firewire (IEEE 1394) cable to a firewire card installed in the PC.

A solution with a well-defined magnetic susceptibility ($\Delta\chi$) was utilized, made up of polystyrene beads, Magnevist®, and magnetic deposition microscopy (MDM) buffer. Magnevist is a gadolinium magnetic resonance imaging (MRI) contrast agent made by Bayer AG (Magnevist®, 2017), and its systematic name is gadopentetate dimeglumine ($C_{28}H_{54}GdN_5O_{20}$), which has a similar volumetric, magnetic susceptibility to gadolinium at 7.58×10^{-5} (SI) (Lide, 2005). Due to the paramagnetic susceptibility of the Magnevist, the diamagnetic PS particles should move away from the magnet indicating a significant diamagnetic component relative to the Magnevist/MDM buffer solution. Equation 2.12 was used to determine the magnetic susceptibility of the solution, difference between the Magnevist and the MDM buffer, which is similar to water at -9.035×10^{-6} (SI).

3.1.2 Methods

To begin, 1 g of PS particles was weighed and added to a 15 mL Falcon tube (Fisher Scientific) with 10 mL of MDM buffer. Then 40 μ L of the PS particles were pipetted into a 15 mL Falcon tube (Fisher Scientific), followed by 5 mL of Magnevist, and 5 mL of MDM buffer for a concentration of $\sim 100,000$ PS particles/mL. The solution was then vortexed on the Genie-2 for 15 – 30 seconds at the highest setting of 10 at room temperature to ensure the solution was well-mixed. Next, part of the solution was drawn into a 5 mL syringe and it was attached to the Luer adaptors connected to the Hamilton valve on one end of the CTV channel. An empty syringe was attached to the Hamilton valve on the opposite side of the channel. This is displayed by the schematic in Figure 20.

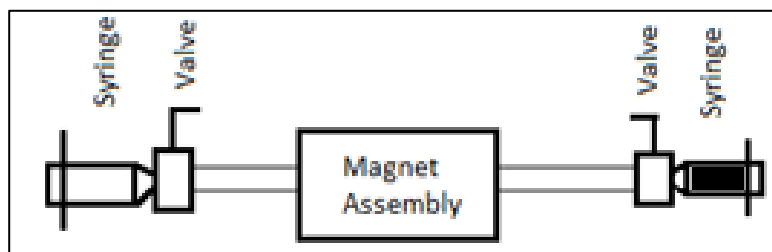


Figure 20: Schematic of the empty syringe on the left and full syringe on the right attached to the Hamilton valves.

The Hamilton valves were turned to allow for the sample to be pushed through the channel to the empty syringe. About 0.2 mL of sample was pushed through the channel over a time frame of 3 seconds, the Hamilton valves were closed to stop fluid flow, and it was given 30 seconds of relaxation time before recording the motion of the particles. Next, the record button in the Video Savant software was pressed to begin recording for 60 frames at a frame rate of 1 second, totaling a minute of acquisition time. Once the recording was completed, the images were reviewed to ensure the particle's motion were uniform in velocity and direction, and they were saved according to the nomenclature specified by the CTV logbook as set one. This process was repeated 11 times, over a time span of 25 – 30 minutes, for a total of 12 sets for the FOV position at a designated distance of 4 mm from the edge of the magnet. The additional three positions, 4.5, 5, and 5.5 mm from the edge of the magnet, as seen in Figure 21, were tested through the same procedure to verify the S_m value for the system.

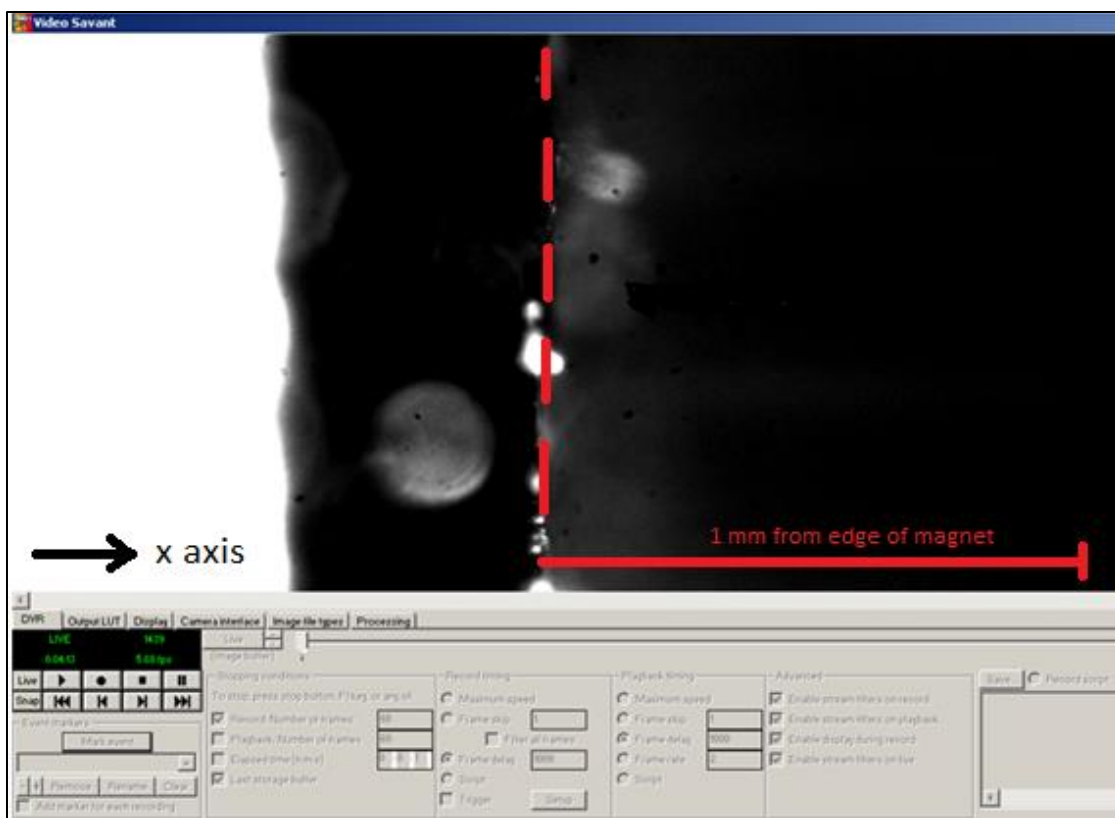


Figure 21: Edge of the CTV magnet in the center of the FOV within Video Savant.

3.1.3 MSB-Auto Methods to Measure the Magnetic Susceptibility of the MDM Buffer and Magnevist Solution

To ensure the magnetic susceptibility found in literature was accurate for MDM buffer and Magnevist, the solutions were verified with the MSB-Auto. Each experiment began by measuring an empty MSB Auto tube in order to account for the magnetic susceptibility of the tube itself, displayed in Figure 9. Next, the MSB Auto machine was turned on and given time to tare to zero before placing the empty tube into the measuring slot. Once the empty tube was measured, the range button was pressed to scale the value shown on the screen by a multiple of ten, to go from the 10^{-4} V range to the 10^{-5} V range. The unit V is used to represent the volumetric magnetic susceptibility in CGS units, cm^3/mol or cm^3/g . The range button is pressed again to scale the value to the 10^{-6} V range,

and finally one last time to scale to the 10^{-7} V range. The value displayed on the screen, was the value recorded as the volumetric, magnetic susceptibility. This was repeated four times, for a total of five readings for the empty tube. Next, the 50/50 mixture of the MDM buffer and Magnevist solution was tested. About 200 μ L was pipetted into the empty tube, which was just measured, to reach a height of about 1.5 cm from the bottom of the tube. Measurements for the solution were obtained the same way as the empty tube, but the range button was only pressed twice instead of three times due to an overflow error when it was pressed a third time. Just like the empty tube, the solution sample was measured for a total of five readings. This procedure was also completed for pure Magnevist, pure MDM buffer, 0.25 mL of Magnevist in MDM buffer, 0.125 mL of Magnevist in MDM buffer, 0.0625 mL of Magnevist in MDM buffer, and 0.03125 mL of Magnevist in MDM buffer.

3.2 Spectrophotometry

3.2.1 Materials

A 5 mL tube of whole blood with a pink top was obtained from the Pathology Lab at the Cleveland Clinic Main Campus Hospital. The pink top tube contains dipotassium ethylenediaminetetraacetic acid (K_2EDTA) to prevent the blood from coagulating until it can be tested by the Pathology Lab. The Institutional Review Board (IRB) regulations were followed for these samples to protect the rights and welfare of the person whose blood was used (Cleveland Clinic IRB #10-1064: EXEMPT. Magnetophoretic Cell Sorting and Analysis, P.I.: Maciej Zborowski). This blood was used to make metHb (made with 1 \times PBS and sodium nitrite, $NaNO_2$) and oxyHb to be tested within the spectrophotometer. Samples were placed in a 1.5 mL acrylic cuvette from VWR International (Radnor, Pennsylvania) to be measured in the Beckman Coulter DU® 730 Spectrophotometer (Brea, California).

Specifications for the spectrophotometer are in Appendix A, Table XI, while an image of the spectrophotometer and cuvette are displayed below.

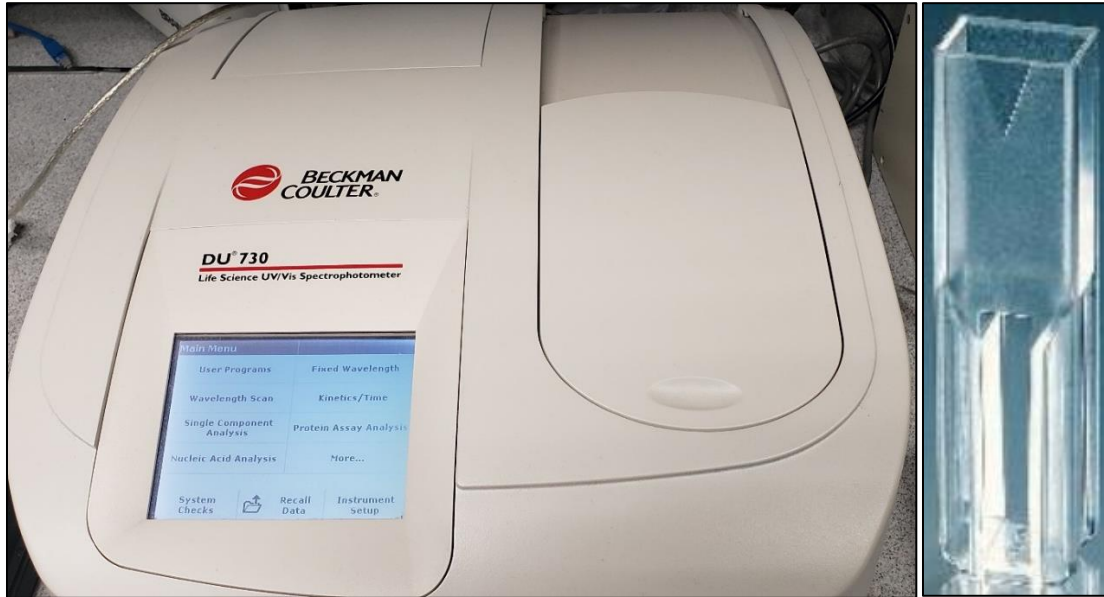


Figure 22: Spectrophotometer by Beckman Coulter and cuvettes by VWR utilized for the spectrophotometer experiments.

The samples were washed with 1×PBS, made from 10×PBS and MilliQ water (double deionized water, Cleveland Clinic, LRI), in 15 mL Falcon tubes (Fisher Scientific) in the Beckman Coulter Allegra™ 6R Centrifuge (Brea, California). The last material utilized for these experiments was distilled water obtained from the house line at the Cleveland Clinic, LRI building.

3.2.2 Methods

Before samples were made, 1 L of 1×PBS was made by mixing 100 mL of 10×PBS (Cleveland Clinic Media Core) and 900 mL of MilliQ water in a 1 L Pyrex bottle. Next, metHb was prepared by mixing 0.0119 g of NaNO₂ with 10 mL of 1×PBS in a 15 mL Falcon tube. This was then mixed with the Vortex Genie-2 at the highest setting to ensure the solution was well mixed. After, 50 µL of whole blood was added to the mixture and set into an incubator at 37°C for 30 minutes to allow for the RBCs to convert to metHb. While

the metHb was forming, 50 μ L of whole blood was added to another 15 mL Falcon tube with only 10 mL of 1 \times PBS to create oxyHb. Then, the oxyHb sample was washed with 1 \times PBS three times at 1,500 rpm for 5 minutes to guarantee all the white blood cells, platelets, and other residual components from the whole blood were removed from the sample. After each wash, the supernatant was removed and discarded in the biological waste container. When the metHb sample was done incubating, it was also washed the same as the oxyHb sample. Once the samples were ready to be tested, 1 mL of distilled water was pipetted into two cuvettes, and then 0.3 mL of the oxyHb was added to one and 0.3 mL of the metHb was added to the other. One cuvette was measured in the spectrophotometer at a time over the range of 500 – 700 nm. The spectrums for each sample and concentration calculations completed utilizing Equations 2.32 – 2.34 are displayed and discussed in Chapter 4.

3.3 Modifications made to the Cell Tracking Velocimetry System for the Deoxygenation of Red Blood Cells

Before experiments of magnetophoresis of RBCs at different deoxygenation levels could begin, the CTV system utilized to determine S_m had to be modified. A schematic of the original setup is in Figure 23. In order to modify the system, tubing had to be connected to allow for gas flow into the deoxygenation vessel and for sample flow from the vessel to the syringes for image acquisition. Therefore, Figure 23 was modified to account for these needed changes and the schematic of the system is found in Figure 24 and an image of the setup is in Figure 25 with a closeup image of the magnet assembly in Figure 26. For more information about each component, refer to Section 3.1.1 and 3.4.1.

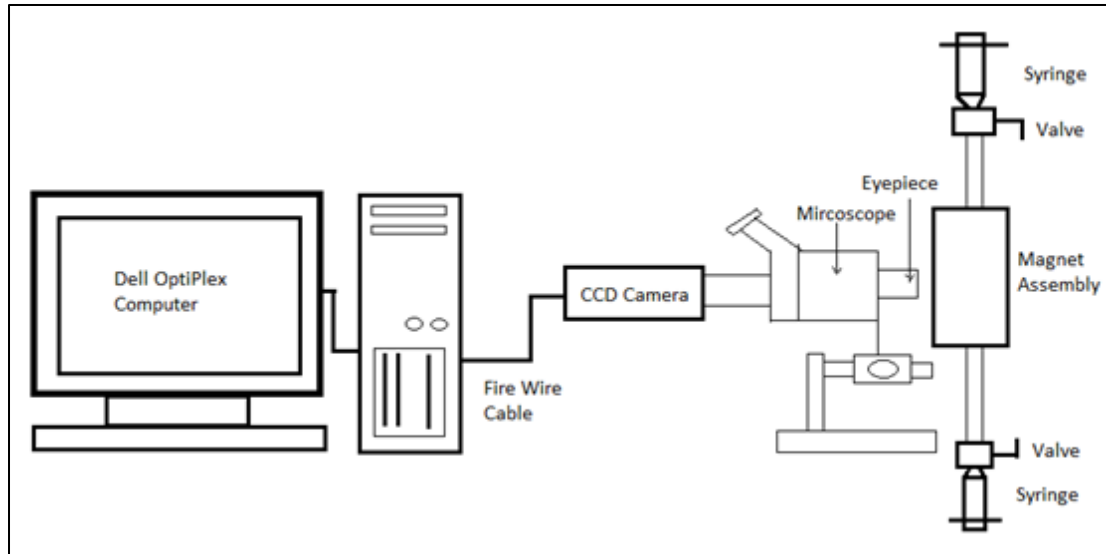


Figure 23: Adapted schematic of original CTV setup (Xue, et al., 2019).

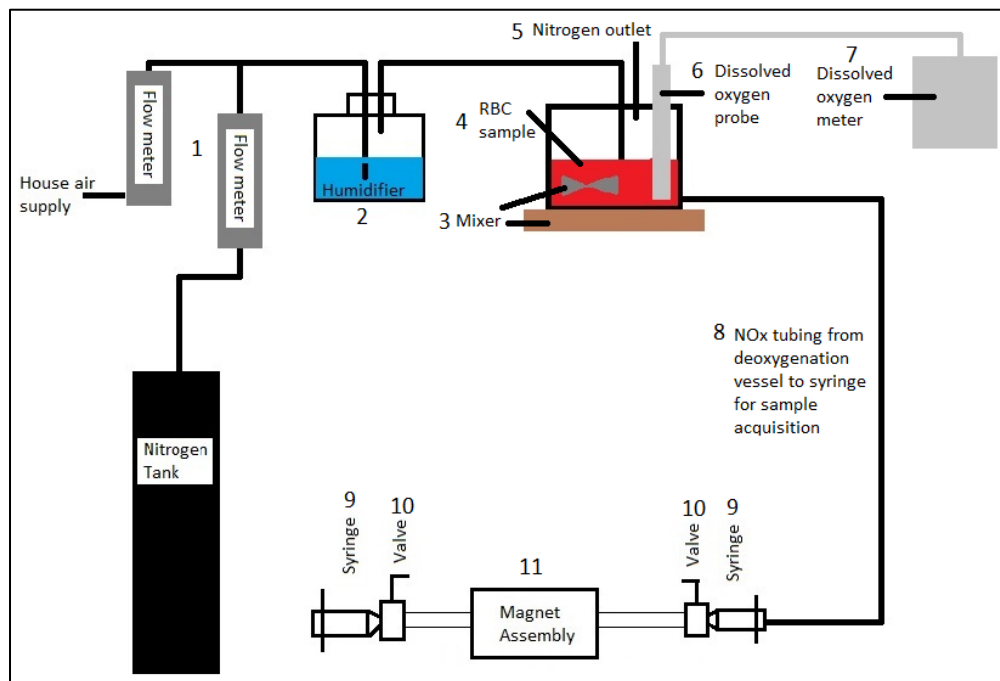


Figure 24: Modified CTV setup for the deoxygenation of RBC experiments (Xue, et al., 2019). 1) Flow meters utilized to regulate the compressed air and compressed N₂ to the system. 2) Humidifier to wet the gases. 3) Stir bar placed in the deoxygenation vessel and the Fisher Scientific Lab Disc Magnetic Stirrer placed under the vessel to ensure the system is well-mixed. 4) Deoxygenation vessel and sample solution inside it. 5) N₂ bleed-off tubing. 6) RDO® Rugged Dissolved Oxygen (DO) Sensor and Orion Star A213 Dissolved Oxygen Meter. 7) NOx tubing connecting the deoxygenation vessel to the syringes for sample measurement. 8) Mk V magnet connecting the syringes with the sample to the glass channel which runs through the magnet assembly itself to the other syringe. 9) PEEK tubing connecting the syringes with the sample to the glass channel which runs through the magnet assembly itself to the other syringe. 10) 10 mL glass syringes (made by Hamilton) which protects the sample from oxygen penetration.

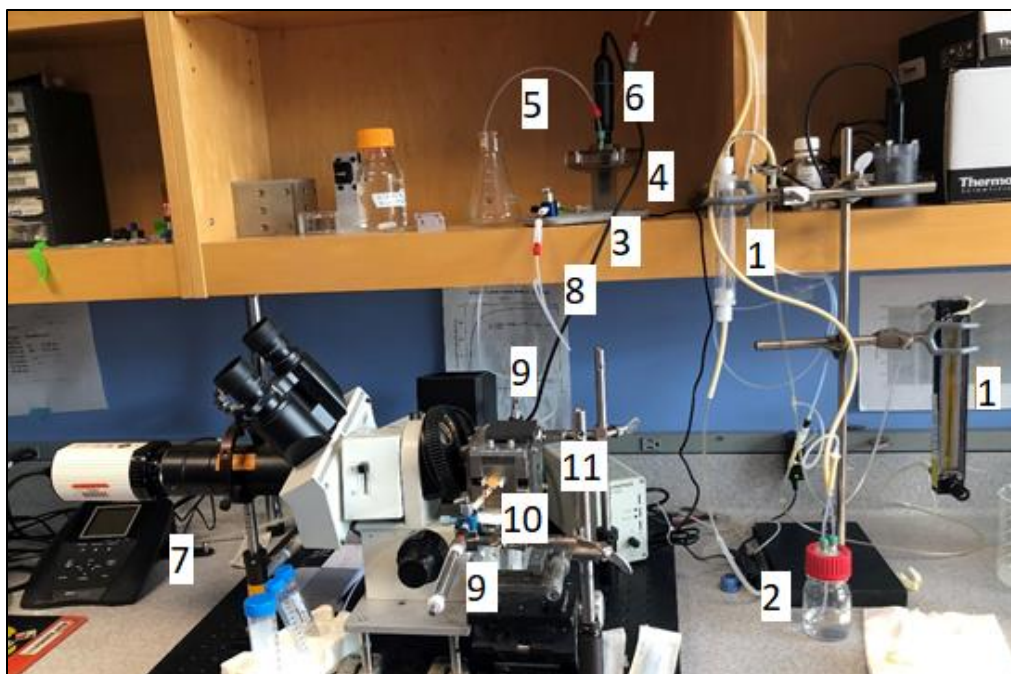


Figure 25: Full CTV setup for deoxygenation experiments.

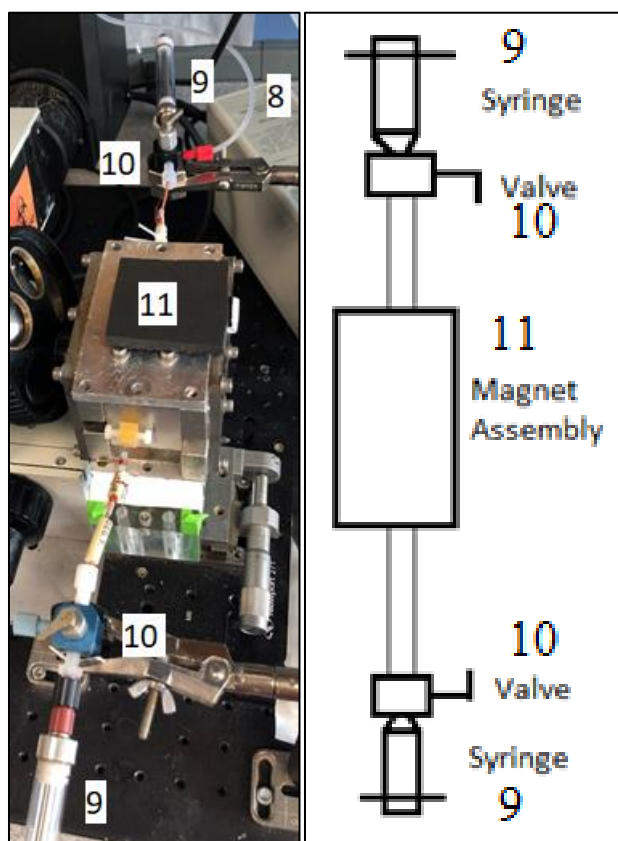


Figure 26: Magnet assembly with glass syringes, and Hamilton valves.

Previous experiments analyzing the magnetic mobility of fully deoxygenated RBCs completed by Dr. Wei Xue, (Xue, 2016) utilized a different DO probe and meter. For the experiments done here, the RDO[®] Rugged Dissolved Oxygen sensor (Thermo Scientific, Waltham, MA) and Orion Star A213 Dissolved Oxygen Meter (Thermo Scientific, Waltham, MA) were used. Specifications and dimensions of the probe are in Appendix A, Tables XIV and XV, respectively, while specifications for the meter are in Appendix A, Table XVI. Figure 27 below displays images of the meter and probe.



Figure 27: Left: Orion Star A213 dissolved oxygen meter from Thermo Scientific. (Component number 7 in Figure 25)
Right: Orion™ RDO[®] Rugged Dissolved Oxygen sensor from Thermo Scientific. (Component number 6 in Figure 25)

Along with the new DO probe and meter, a new deoxygenation vessel was designed to meet the required minimum immersion depth of the probe to measure the dissolved oxygen saturation of the sample solution. This was completed within SolidWorks, developed by Dassault Systèmes, in collaboration with Principal Research Engineer, Lee

Moore at the Lerner Research Institute at the Cleveland Clinic Main Campus, and 3D-printed. Rob Geszler operated a PolyJet printer (Stratsys, Eden Prairie, MN) with VeroClear resin, which is optically translucent with ABS-like mechanical properties to 3D-print the vessel. A schematic of the new deoxygenation vessel is shown in Figure 28 with the dimensions in Table II. This design allowed for a sample volume of more than 50 mL, while maintaining the required 40 mm minimum immersion depth for the probe.

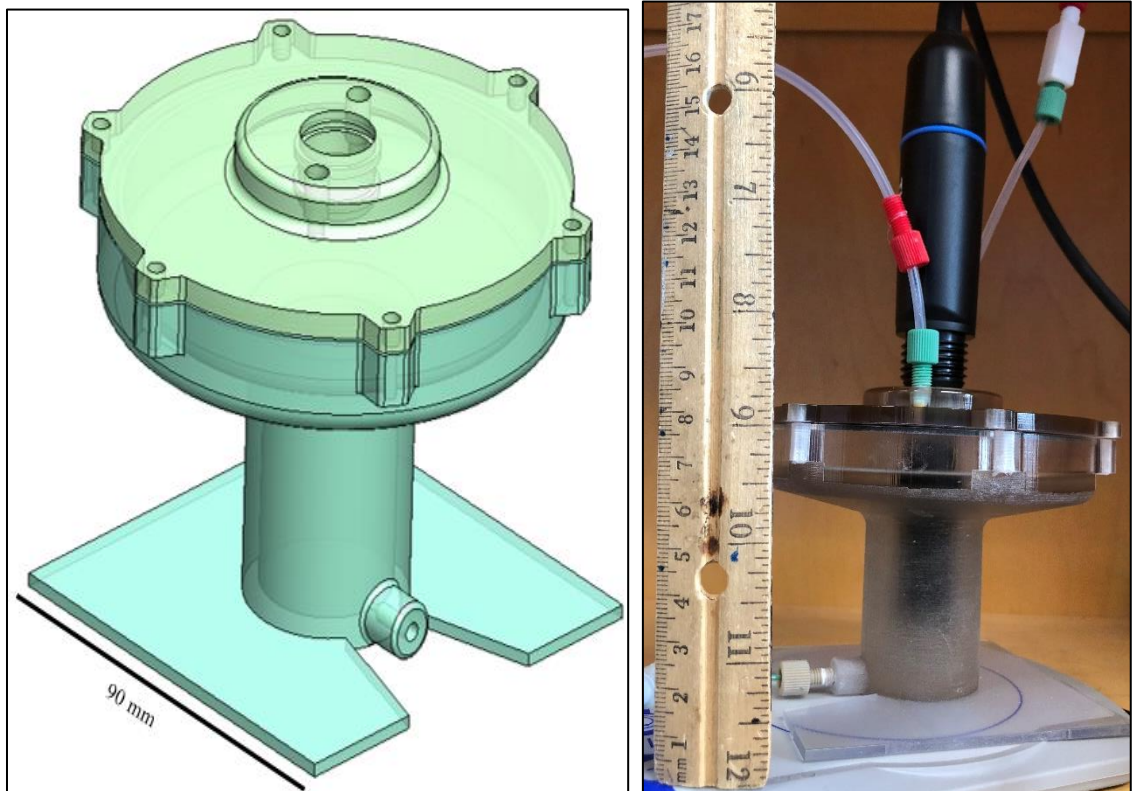


Figure 28: A schematic (left) and image (right) of the 3-D printed deoxygenation vessel (part of component numbers 3, 4, 5, and 6 in Figure 25).

Table II: Dimensions of the deoxygenation vessel designed in collaboration with Lee Moore.

Deoxygenation Vessel Dimensions		
Parameter	Value	Units
Overall Height	77	mm
Lower Half Height	40	mm
Lower Half Inner Diameter	29	mm
Upper Half Height	14.3	mm
Upper Half Inner Diameter	91	mm
Overall Volume	110	cm ³

3.4 Red Blood Cell Deoxygenation

3.4.1 Materials

To begin an experiment a 5 mL tube of whole blood with a pink top was obtained from the Pathology Lab at the Cleveland Clinic Main Campus Hospital, as described in Section 3.2.1. Again, these samples followed the Institutional Review Board (IRB) regulations to protect the rights and welfare of the person's whose blood was used (Cleveland Clinic IRB #10-1064: EXEMPT. Magnetophoretic Cell Sorting and Analysis, P.I.: Maciej Zborowski).

The modified CTV apparatus displayed in Figure 25 shows the components of the system labeled with a number for easy identification. The flow meters are labeled by #1. The one connected to the compressed nitrogen (N_2) tank from Praxair was an Oakton™ Gildmont™ Shielded laboratory Direct-Reading Flowmeter (Fisher Scientific, Hampton, NM), while the flow meter connected to the compressed air from the Cleveland Clinic Main Campus house source, was a Bel-Art™ SP Scienceware™ Riteflow™ Mounted Flowmeter (Fisher Scientific, Hampton, NM). An image of these flow meters is in Figure 29. The specifications for each meter are in Appendix A, Table's XII and XIII, respectively. The humidifier was labeled with #2, which is a 100 mL Pyrex bottle with a lid allowing for gas flow in and out, contained 40 mL, or less, of water to aerate the gases to eliminate water removal from the cells and the system to avoid the cells dying due to increased osmotic pressure. Number 3 denoted the stir bar and plate to ensure the sample solution within the vessel was well-mixed. The rest of the components used for these experiments were described above in Section 3.3. How the sample solutions were prepared will be described in Section 3.4.3.

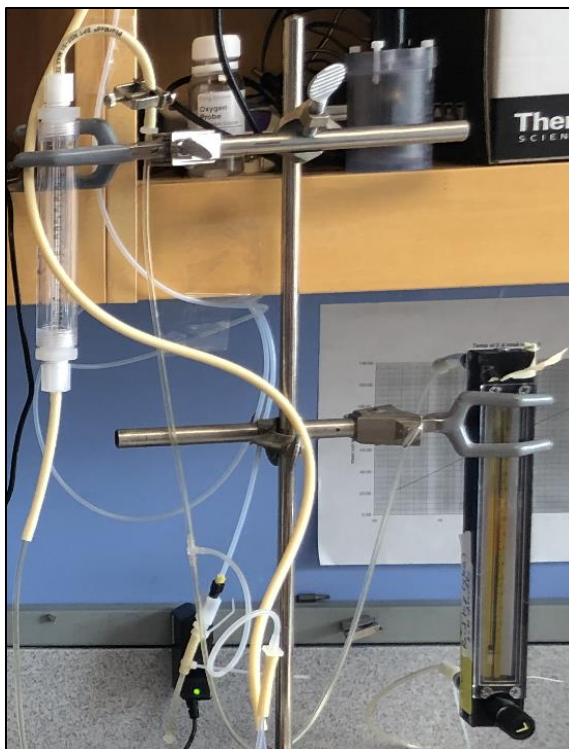


Figure 29: Flow meters utilized within the deoxygenation system. (Components 1 from Figure 25)

3.4.2 Methods for Calibrating the Dissolved Oxygen Probe and Meter

Before experiments could be completed, the DO probe and meter were calibrated for 100% saturated with air and 0% saturated with air. Instructions to complete the calibration steps were found in the manual for the DO meter (Orion star™ A213 dissolved oxygen benchtop meter, 2015). The probe was placed through the hole in the lid of the deoxygenation vessel and a stir bar was placed at the bottom of the vessel. NOx tubing connected the compressed air flow to the flow meter to the humidifier and into the 90 mL of distilled water in the deoxygenation vessel. First, the meter was turned on and the initial reading of O₂ concentration in mg/L, temperature units of °C, and percent O₂ saturation were recorded. Next, the stir bar was turned on to about 30 – 40 rpm and the compressed air flow was turned on to the 100 mark, corresponding to about 14 mL/min. On the meter display, the ‘fl’ key corresponded to calibration. This button was pressed, and four

calibration options were given: 'Air', 'Water', 'Manual', and 'Set Zero'. The 'Air' option was selected. After, the 'Start' selection was pressed and calibration began. When the percent saturated value reached 100% and stabilized, which corresponded to 160 mmHg, 8.05 mg/L at 22.5 °C, calibration was completed and logged in the meter.

For these experiments, since the percent saturated readings go below 10% saturation, about 17 mmHg, the 'Set Zero' calibration was completed. This was completed in the same fashion as the 100% calibration was done, but instead of bubbling compressed air into the deoxygenation vessel, N₂ was utilized. The N₂ flow was given about an hour to allow for the vessel to be evacuated of air. After about an hour of N₂ flow, the 'fl' calibration button was again pressed. This time the 'Set Zero' option was selected, and then 'Start' was pressed. Once the percent saturated point was at 0.1% and stabilized, or 0.01 mg/L at 24.9 °C, calibration stopped, and the meter logged 0.1%, 1.7 mmHg, as the 0% saturation value.

3.4.3 Methods for Deoxygenation Experiments

After obtaining a blood sample the morning of an experiment, 1 mL of whole blood is removed and pipetted into a 15 mL Falcon tube. This sample was then centrifuged at 1,500 rpm for 5 minutes at room temperature in the Beckman Coulter Allegra™ 6R Centrifuge. While centrifugation was being completed, 90 mL of 1×PBS (phosphate buffer solution) was added to the deoxygenation vessel. Once centrifugation is completed, the Falcon tube is removed and the supernatant, containing platelets, white blood cells, and residual K₂EDTA, was pipetted into the biological waste. Next, 18 µL of the pelleted RBCs were pipetted into the 90 mL of 1×PBS in the deoxygenation vessel, which was estimated to be 100,000 RBCs/mL based on the 5 billion RBCs/mL concentration of whole blood. A

stir bar was placed in the bottom of the vessel and the lid, with the DO probe through the center, was screwed on. The vessel was positioned on the magnetic plate to turn the stir bar, and it was turned on. Next, the DO meter was turned on to obtain the initial reading from the sample solution and it was recorded. The salinity of the solution was set to 8.9% within the DO meter to account for the salt content in the 1×PBS and RBCs. After the initial reading was taken, the compressed air flow was turned on to flood the sample solution with air to reach the 100% saturated point of the experiment, 160 mmHg.

Once the system stabilized at or above 100% saturated, the three-way Hamilton valve, labeled A in Figure 30, was turned to allow the sample to flow into the CTV system. Valve B was turned to allow the sample to flow through the channel to valve C and be drawn into the glass syringe. After flushing the channel with 2 mL of sample, it was disposed of in the waste container connected to valve C. Following the same procedure, another milliliter was flushed through the system and disposed of. Next, 2 mL of solution was drawn into the system for data acquisition, and valve A was turned to no longer allow sample from the vessel to flow into the CTV system. The sample was then drawn and infused between the two syringes attached to the channel.

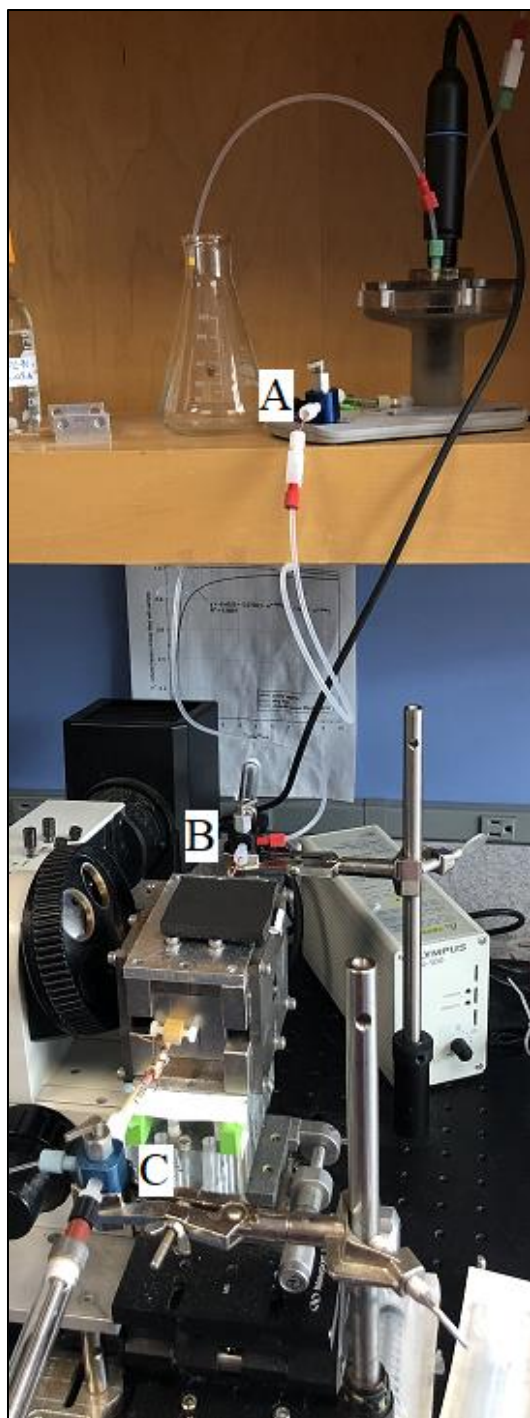


Figure 30: Deoxygenation system set up labeling the three three-way Hamilton valves.

To obtain a sample set, about 0.2 mL of sample was pushed into the channel and given two minutes of relaxation time. Once the two minutes were over, the record button in the Video Savant software was pressed to begin recording the frame-by-frame motion

of the cells within the channel at a frame rate of two seconds until 60 frames was reached, for a total of two minutes of recording time. The images were reviewed to ensure that cell motion was uniform in velocity and direction, and then they were saved according to the nomenclature specified by the CTV Logbook as set one. This procedure was repeated seven times for this 2 mL sample at 100% oxygenated at room temperature, which took ~30 – 35 minutes to complete. After eight sets were completed, the protocol was repeated for the nine remaining oxygenation levels. The specified oxygenation levels tested for a single experiment are in Table III. Experiment #1 took about 9 hours to complete. This was the average amount of time it took for each experiment, not including retrieving the blood sample and preparation. Experiments 1 – 5 were completed in this fashion by starting at 100% oxygenated and decreasing to as close to 0% oxygenated as possible, typically 0.1%, 1.7 mmHg or 0.01 mg/L.

Table III: Theoretical oxygenation levels for one experiment to determine if CTV is capable to detect differences in the magnetic mobility of RBCs.

Theoretical Oxygenation Levels for one Experiment at Room Temperature			
Partial Pressure of O ₂ , mmHg	Concentration of O ₂ , mg/L	O ₂ Saturation, %	Elapsed Time, mins
160	8.35	100	23
60	3.14	37.5	76
40	2.09	25	50
30	1.57	18.75	50
25	1.31	15.63	48
20	1.05	12.5	78
15	0.79	9.38	49
10	0.53	6.25	58
5	0.26	3.13	61
0.1	0.01	0.1	50

3.4.4 Methods of Analysis

Recorded images saved through the Video Savant software were renamed to be analyzed through ImageView, a custom image analyzing software for internal use only, created at The Ohio State University in Dr. Jeffrey Chalmers' Lab in the Chemical Engineering Department. The first image from the first set being analyzed was selected, then the processing button is pressed. Figure 31 displays the CTV parameters within the imaging software which were adjusted to track the particle frame-by-frame. After the position was traced, the distance the particle traveled was calculated from an average velocity over five frames divided by the frame rate specified in the Video Savant software (one second for the S_m verification and the glioma experiments and two seconds for the RBC deoxygenation experiments). Therefore, on average a single cell susceptibility measurement is repeated five times over the length of the cell trajectory (Xue, et al., 2019).

Set, Frame & Timing Information			Image Information			
	Set	Settling	Magnetic	Width	Height	Bit Depth
Start	1	1	0	1200	500	8
End	8	60	0	Binning Mode	1	1
Interval (ms)		2000	100	Exposure (ms)	100	
				Gain	1	Offset
						0
Particle Identification			Magnetic Field Information			
Min	4	Aspect ratio	3	Gauss	1	
Max	100	Threshold	75	Current (A)	5	
				Temperature (F)	50	
Particle Tracking			Calibration Information			
Max Distance	0.100		Binning Mode	1 x 1		
Error Control 1	0.010		X	10 (mm)	6519 pixels	
Error Control 2	0.050		Y	10 (mm)	6519 pixels	
Minimum Tracking Frame Numbers			Operation			
Settling	10		Don't save images			
Magnetic	3		<input checked="" type="checkbox"/> Average	<input checked="" type="checkbox"/> Purge Files		
			<input checked="" type="checkbox"/> Subtract	<input checked="" type="checkbox"/> Merge Files		
			<input checked="" type="checkbox"/> Centralis	<input type="checkbox"/> Batch Proc		
			<input checked="" type="checkbox"/> Tracking			
			<input checked="" type="checkbox"/> Velocity			
			OK			

Figure 31: Parameters changed in ImageView to ensure particles are tracked accurately. Under the 'Set, Frame, & Timing Information' Section 1) 'Settling End' is set to the corresponding number of sets being analyzed 2) 'Settling End' indicates the amount of images taken, or frames, per set 3) 'Settling Interval (ms)' is changed to the frame rate specified in Video Savant in milliseconds. In the 'Particle Identification' Section 4) 'Min' indicates the minimum number of pixels a particle will occupy at a given time 5) 'Threshold' brightens the images when it is reduced and dims the images when it is increased. Section 'Minimum Tracking Frame Numbers' 6) 'Settling' represents the consecutive number of frames a particle must be tracked to be counted in the average. 'Image Information' 7) 'Width' and 'Height' are also specified in Video Savant before the images are recorded. In the 'Calibration Information' Section 8) the number of pixels in 10 mm wide and 10 mm tall are specified, and for the 5× objective lens 6,519 pixels correspond to 10 mm. Lastly, the 'Operation' Section 9) all the boxes are checked besides the 'Batch Proc' box.

Within ImageView, all repeats in a set were analyzed at once, which created a .txt file with all the information from the analysis. From there, the file is opened in Excel as a delimited file and run through two Macros developed by two visiting students from The Ohio State University by the names of Aaron Richardson and Masa Nakamura (Nakamura,

et al., 2001). Over the years, the Macros have been modified to what they are today by Mr. Lee Moore, Dr. P. Stephen Williams, and Dr. Seungjoo Haam between 2005 – 2012. The first Macro, ‘sorter2’, organized the information into a recognizable format to be run through the second Macro, ‘Step1’. Upon completion of running the Macros, the mean, median, mode, standard deviation, variance, 95% confidence limits, and coefficient of variance for the magnetic mobility and the sedimentation velocity are provided. Also, three graphs for both the magnetic mobility and the sedimentation velocity are created with wide binning, middle binning, and narrow binning. The raw magnetic and sedimentation velocities are located on the second sheet labeled ‘DATA-1’ in columns B and C in the Excel file, where the magnetic velocity is labeled ‘u_avg’ and the sedimentation velocity is ‘v_avg’. The final version of the Excel file is then saved into the CTV results file on the computer. This method of analysis was completed for the S_m verification study, the deoxygenation of RBC experiments, and the glioma experiments.

3.4.5 Analysis of S_m Verification Experiments

Utilizing Equations 2.10 through 2.20 in Sections 2.6.1, an Excel file was created to calculate S_m for the four positions identified in Section 3.1.2.

3.4.6 Analysis of RBC Deoxygenation Experiments

A MATLAB code generated by Robert Royer and modified by Dr. Maciej Zborowski and me in 2018-2019, was then utilized to obtain more information from the Excel files and representative graphs for the RBC deoxygenation experiments. The MATLAB code is in Appendix B in its entirety. To begin, the ‘Run’ button in the MATLAB ‘Live Editor’ section was pressed, and the file explorer window popped up. Here the Excel file to be analyzed was selected, and the magnetic and sedimentation

velocities from page 'DATA-1' in the Excel file were extracted. First, the data was utilized to create a scatter plot of the sedimentation velocity versus the magnetic velocity including marginal histograms of the count of particles at specific locations. The points graphed on the scatter plots were completed utilizing a color-coding system, indicating where the most particles fell on the plot and the color bar with the high volume (yellow) and low volume (blue) color scheme located to the right of the sedimentation velocity histogram. Next, k-mean clustering was utilized to partition the sample group into two different clusters with similar data points and discover underlying patterns within the dataset (Garbade, 2018).

Once the clusters were identified, they were plotted on the sedimentation versus magnetic velocity scatter plot with cluster 1, identified by red points and cluster 2, identified by blue points, and their center of masses were labeled by black dots in the groups. Each group was graphed separately in the same manner as the whole dataset was first graphed in the color-coded scatter plot with histograms. The magnetic histograms were then fitted to a gaussian model to determine the peak (a_1), the mode (b_1), and the standard deviation (c_1) for each cluster. The gaussian fit equation utilized is found in Equation 3.1 below. The last graph generated in the MATLAB code was a combination of the original magnetic histogram from the whole dataset in a blue stair-type graph with a black line corresponding to the sum of cluster 1 and 2's gaussian curves, the light purple line graphing subset 1's gaussian, and the red line plotting subset 2's gaussian. To compare the functionality of the gaussian curve fitting code in MATLAB, a Welch's t-test for unequal variances and unequal sample sizes was coded. This statistical analysis is an adaptation of the Student's t-test; however, it is more reliable for samples with unequal variances and/or unequal sample sizes, which is present in the experiments being analyzed.

$$f(x) = a_1 e^{-\left(\frac{x-b_1}{c_1}\right)^2} \quad (3.1)$$

The last part of the MATLAB code compiles key points from data analysis into an Excel file. Original magnetic and sedimentation velocities were put into the sheet labeled ‘All’. Points within cluster 2 were put into a sheet labeled ‘A’ for subset A, while points in cluster 1 were located in the sheet labeled ‘B’. The center of masses for each cluster and their standard deviation were in sheet ‘CENTS’. Gaussian coefficients for subset A were put in sheet ‘GaussA’ and subset B were put in sheet ‘GaussB’. Welch’s t-test results were stored in sheet ‘Ttest’ with a p-value equal to 0.95. This included the alpha-value, the number of points, mean, and standard deviation of each cluster, along with the degrees of freedom denoted as ν , the t statistic as $tval$, and the 1-tail t-distribution denoted as ‘tail1’ and the 2-tail t-distribution denoted as ‘tail2’. Equation’s 3.2 and 3.5 demonstrate how the degrees of freedom and the t statistic were calculated for the Welch’s t-test, respectively. The sample variance is denoted as s , sample size is N , and \bar{X} is the sample mean. The last sheet in the Excel file generated from the MATLAB code provides the upper and lower confidence limits of both subsets for the t-test and the gaussian curve fitting.

$$\nu = \frac{\left(\frac{s_1^2}{N_1} + \frac{s_2^2}{N_2}\right)^2}{\frac{s_1^4}{N_1^2 \nu_1} + \frac{s_2^4}{N_2^2 \nu_2}} \quad (3.2)$$

$$\nu_1 = N_1 - 1 \quad (3.3)$$

$$\nu_2 = N_2 - 1 \quad (3.4)$$

$$tval = \frac{\overline{X_1} - \overline{X_2}}{\sqrt{\frac{s_1^2}{N_1} + \frac{s_2^2}{N_2}}} \quad (3.5)$$

Reduction of the data gathered from the MATLAB code was the last step when analyzing the results. The gaussian coefficients of subset A and B at each oxygenation level for one experiment were compared, where gaussian 1 was defined as the magnetic velocity closest to zero and gaussian 2 was the one farthest from zero. This varies between cluster 1 and 2 for each oxygenation level. The b-values, or the mode of the gaussian, were then plotted versus the oxygenation level they were measured at, with error bars corresponding to the c-values, standard deviation of the mode. Next, the b-values were normalized from 0 to 1 and graphed versus the oxygenation state with a best fit line consistent with the Hill equation describing the cooperative binding scheme of oxygen to hemoglobin. In Equation 3.6, Y is the normalized b-value, which is described further below.

$$Y \equiv \frac{y_0 - y}{y_0} \quad (3.6)$$

From the stated hypothesis, Y follows the Hill equation specified in Equation 3.7 of the order n and constant parameter k' , where variable x is the experimental pO_2 value

$$Y = \frac{x^n}{k' + x^n} \quad (3.7)$$

Equation 3.7 is algebraically manipulated to convert it to have a linear relationship between some closed-form functions of Y and x in Equations 3.8 through 3.10.

$$k'Y + x^nY = x^n \quad (3.8)$$

$$x^n = \frac{k'Y}{1-Y} \quad (3.9)$$

$$n\log(x) = \log(k') + \log\left(\frac{Y}{1-Y}\right) \quad (3.10)$$

Equation 3.8 can be further simplified to Equation 3.9 by introducing variable Z and redefining the constant k' in Equation 3.10.

$$Z \equiv \frac{Y}{1-Y} \quad (3.11)$$

$$k \equiv -\log(k') \quad (3.12)$$

The desired result, presented in Equation 3.13, is the linear relationship between the function of the experimentally measured b-value, $\log(Z)$, and the function of the independently varied experimental value of pO_2 , $\log(x)$.

$$\log(Z) = n\log(x) + k \quad (3.13)$$

For these equations, Y is the fractional saturation of oxygen bound to the hemoglobin, n is the Hill coefficient also known as the slope of the regression line of the linearized Hill equation, which corresponds to Z in Equation 3.11, and k is 10 raised to the negative value of the y-intercept from the regression line of the linearized Hill equation. For Equation 3.6, y_0 is the maximum b-value in an experiment (one experiment corresponds to sets at 160 mmHg to 0 mmHg) minus the minimum b-value and y is the original b-value minus the minimum b-value (Weiss, 1997). The Hill parameters n and k were determined by the usual method of least-square fitting of a straight line to the experimental data of $\log(Z)$ on $\log(x)$, whose significance was calculated by the linear regression analysis. For normal blood, parameter n ranges from 1.5 – 2.5 for $pO_2 < 30$ mmHg and reaches the saturation value of 2.7 at about 30 mmHg (Dash, et al., 2016). From here, conclusions were drawn to

determine if the hypothesis was correct about CTV being able to differentiate RBC subfractions differing in oxygenation levels.

3.5 Glioma Progenitor Cell Experiments

3.5.1 Materials

The glioma cell cultures were provided by Soumya Turaga, a graduate student in Dr. Justin Lathia's lab at the Cleveland Clinic, LRI. Originally, three different cultures were tested, 3T3 (control), GL26, and GL261, which were all murine models which were cultured for more than 20 passages. The 3T3 control were simply neural stem cells, while GL26 and GL261 were forms of glioblastoma/ependymoblastoma (Oh, et al., 2014). Preclinical testing of immunotherapeutic approaches for GBM have been most extensively completed on the GL261 model (Oh, et al., 2014). The GL261 and GL26 models are similar, but the GL26 tumors present greater necrosis and vascularity as well as being hemorrhagic (Oh, et al., 2014). All these cells were cultured in RPMI (Roswell Park Memorial Institute) 1640 media (ThermoFisher Scientific, Waltham, MA) supplemented with 10% fetal bovine serum and 1% penicillin/streptomycin, which was also provided by Soumya. The last material supplied by Soumya in Dr. Lathia's lab was 4% PFA (paraformaldehyde, made by Soumya Turaga at Cleveland Clinic, LRI) fixative to secure the cells onto the Mylar slide after MDM was completed, as well as after a cytosmear was generated within the cytopsin.

The MSB-Auto described in Section 2.3 and the CTV components defined in Section 3.1.1 were applied to the glioma experiments to validate the MATLAB analysis. Shandon Cytospin 3 (Thermo Fisher Scientific, San Francisco, California), displayed in Figure 32, was used to create cytosmeears of the glioma cells. Specifications for the

instrument are in Appendix A, Table XVII (Cytospin: Cell Preparation System Operator Guide, 1997). Components needed for the cytospin were the stainless steel Cytoclip™ slide clip, a microscope slide with a circle where the sample is released onto the slide, and a disposable Cytofunnel® with a sample chamber and filter card (Cytospin: Cell Preparation System Operator Guide, 1997). The method of how the sample was prepared and put together with the Cytoclip™, microscope slide, and Cytofunnel® will be described in Section 3.5.2.



Figure 32: Shandon Cytospin 3 (Thermo Fisher Scientific, San Francisco, CA) used to create cytosmears of glioma cultures (Cytospin: Cell Preparation System Operator Guide, 1997).

The MDM magnet described in Section 2.6.2 was also used to determine if magnetic separation is possible between CSCs and other brain cells. The magnet assembly was made up of three sizes of neodymium-iron-boron 42 MG Oe energy blocks (Applied

Magnet, Plano, TX). The steel yokes and aluminum supports were put together at the Cleveland Clinic, LRI. The two interpolar gaps had a width of 1.6 mm each and the maximum magnetic field intensity between these gaps in the 0y direction was measured to be $B_y = 0.475$ T. Five flow channels, each 6.3 mm wide and 15 mm long, were cutout into a 0.25 mm thick rubber spacer. The rubber spacer was squeezed between a 0.13 mm thick, poly-l-lysine coated Mylar sheet, acting as a microscopy substrate slide, and a polycarbonate manifold. The orientation and components in the assembly are displayed in Figure 33.

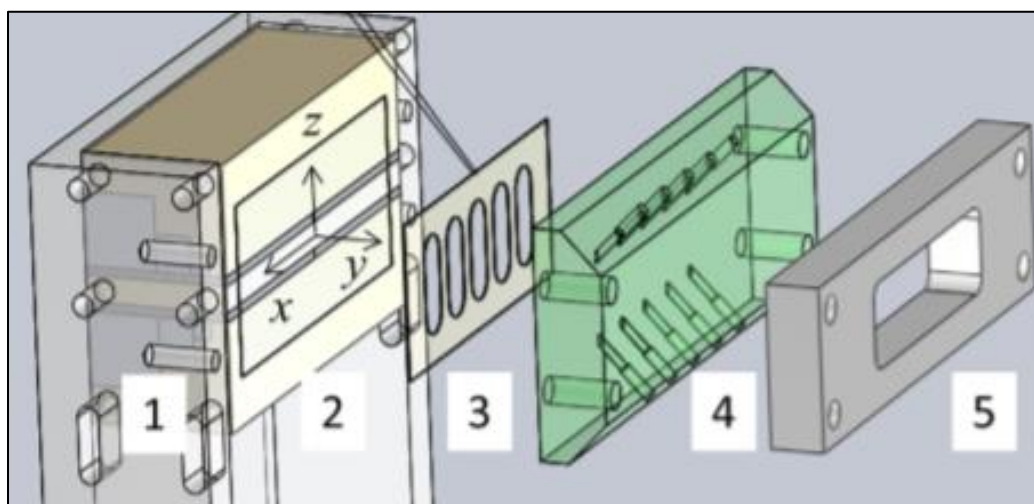


Figure 33: Magnet assembly (Buck, et al., 2014).

To facilitate sample flow through the channel, FEP, 0.508 mm inner diameter \times 1.59 mm outer diameter tubing (Zeus Industrial Products, Orangeburg, SC) was threaded through the manifold on both the top and bottom. While syringes were connected to the tubing leaving the top of the manifold, they were attached to the kd Scientific Legato 210P multi-syringe pump, displayed in Figure 34 and specifications in Appendix A, Table XVIII. Within the pump, flow rates could be specified and programed, allowing for controlled and

precise fluid flow in the channels. The flow rates utilized for the glioma experiments will be described in Section 3.5.2.



Figure 34: Legato 210P multi-syringe pump adaptor from kd Scientific (Holliston, MA) utilized in MDM (Legato 210/210P Syringe Pump, 2016).

3.5.2 Methods

First, the RPMI media utilized to culture the cells was tested with the MSB-Auto, applying the same procedure described in Section 3.1.3, to ensure the media did not present any magnetic properties which could be absorbed by the cells and inadvertently make them magnetic. Also, distilled water and MilliQ water were both measured to verify the magnetic susceptibility of the RPMI media was not statistically significantly different from water. The statistical analysis is in Section 4.4.

The morning of an experiment, a sample was received from Soumya containing about 1,000,000 cells/mL of solution. About 10,000 cells were needed for a cytosmear, 100,000 cells for each of the five MDM channels, 50,000 cells for Countess, and 1,000,000 cells/mL for CTV. The 50,000 cells for Countess were removed first to give to the Cleveland Clinic LRI FlowCore to determine the size and viability of the cells. From experiment to experiment, the amount of sample removed from the original 1,000,000 cells/mL solution for each test varied due to the number of cells Soumya was able to provide. Next, five 1.5 mL sample vials were prepared for MDM. The 20,000 cells for two cytosmeares were then pipetted into a 1.5 mL sample vial, which also contained excess RPMI media. The remaining of the cells were utilized for CTV.

MDM was the test which took the most amount of time to complete. Therefore, this was the first to start running. To begin, the Mylar slide was cut to size to cover the five channels, and the bottom right corner was cut diagonally, as seen in Figure 35, to know which channel was located where on the slide. Next, ten pieces of tubing was cut about 10 inches long. The tubing was then pulled at one end with plyers to thin it out to be able to thread it into the manifold. Once all ten pieces of tubing were in the manifold, the excess tubing on the inside of the manifold was cut off to provide a smooth surface for the rubber spacer and Mylar slide to sit. After the rubber spacer and Mylar slides were in place on the manifold, all three pieces were sandwiched together with the magnet assembly. The order was the magnet assembly, Mylar slide, rubber spacer, then the manifold threaded on four bolts sticking out of the outer edges of the magnet assembly. Next, the platen was placed next to the manifold on the bolts and screws were tightened to create an airtight seal within the channels and to ensure no sample would leak out once fluid flow began.

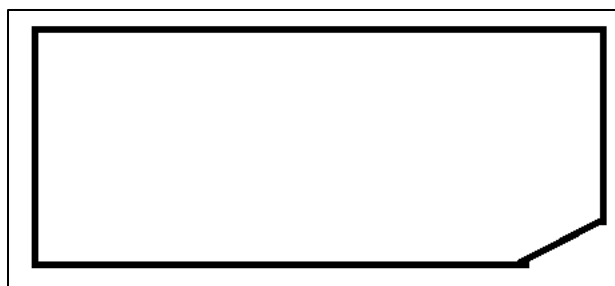


Figure 35: Schematic of a Mylar slide, 25 mm \times 75 mm, used within MDM as a microscope slide, cut on the bottom right corner to determine the locations of the channels.

When the magnet was assembled, the tubing at the top of the manifold needed to be connected to the syringes using a male chromatography fittings ($\frac{1}{4}$ -28 \times $\frac{1}{16}$ "') and $\frac{1}{4}$ -28 male-to-female Luer adaptors from Upchurch Scientific. The adaptors were a modification from the original Hamilton valves utilized for the process, due to complications of not every channel drawing up sample when the pump was turned on. Once the syringes were connected to the tubing, they were secured to the pump. About 1 mL of MDM carrier solution was placed in a 1.5 mL sample vial and placed at the bottom of each channel with the tubing placed inside the solution. On the pump, program Nina_C was selected to first determine which channels were withdrawing and infusing sample properly, and to coat the inside surfaces of the tubing and Mylar slide. The different pump programs utilized for the glioma experiments are listed in Table IV. About 10 minutes later, the carrier solution was withdrawn into the syringe and infused back into the sample vial, and the vials were switched out for the glioma samples. Program Nina_U was selected.

Table IV: Pump programs implemented by Nina Smith.

MDM Pump Programs				
Program Name	Withdraw/Infuse	Rate, mL/min	Volume, mL	Time, min
Nina_C	Withdraw	0.2	0.8	4.0
	Infuse	0.2	0.7	3.5
Nina_U	Withdraw	0.026	0.7	26.92
Nina_D	Infuse	0.03	0.6	20.0
Nina_M_U	Withdraw	0.13	0.6	4.62
Nina_M_D	Infuse	0.13	0.6	4.62

While waiting for MDM to finish, two cytosmears were created, one for PFA, the fluorescent fixative, and one for HEMA fixative. First, the 20,000 cells were split into two 1.5 mL sample vials with RPMI media. After the samples were prepared, the Cytoclip™, microscope slide, and the disposable Cytofunnel® were put together as displayed in Figure 36. Two of these combinations were prepared, with the microscope slide indicating which sample would be fixed with HEMA solution and which would be fixed with PFA. Next, 0.3 mL of the sample solutions were pipetted into the disposable Cytofunnel®. Both Cytoclip's™ were taken over to the Cytospin 3 and placed on opposite sides of the centrifuge to keep the system at equilibrium. The machine was then turned on and program number 2 was selected, which was preprogrammed.

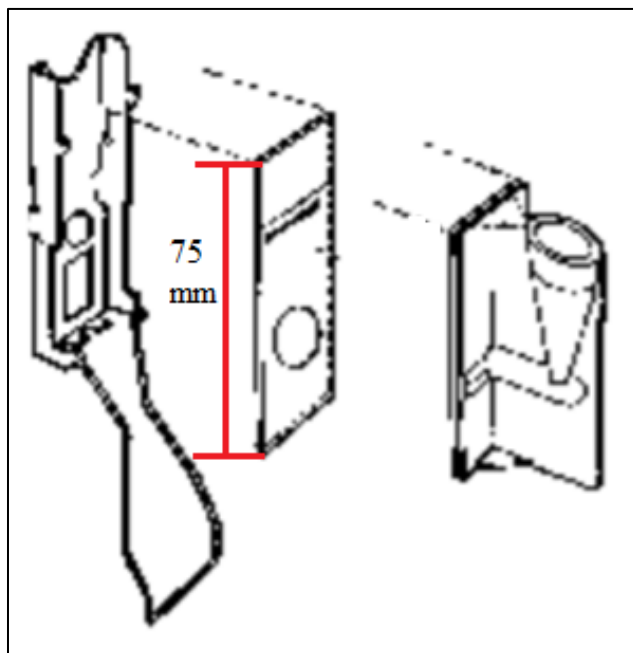


Figure 36: Schematic of how the Cytoclip™ slide clip, the microscope slide, and the disposable Cytofunnel® are put together to be placed into the cytospin (Cytospin: Cell Preparation System Operator Guide, 1997).

After 5 minutes, the cytospin stopped and the samples were removed. The disposable Cytofunnel® was removed and thrown away in the biological waste bin, while the Cytoclip's™ were placed back into the Cytospin 3, and the machine turned off. The

slide marked HEMA fixative was first dunked into the light blue HEMA solution five times, then five times in the red HEMA solution, and lastly five times in the purple HEMA solution. The slide was then left in the open to dry. Next, about 50 μ L of PFA was dropped on the cells within the circle on the slide marked PFA. The PFA was left on the cells for 15 minutes, and then it was washed off by dunking the slide in 1 \times PBS five times. The slide was then placed inside the refrigerator at 4°C until Soumya was able to fluorescently stain the cells. Once the HEMA slide was dry, a cover slide was placed over top of the slide to be taken to ImageCore to be imaged.

After the cytosmears were finished and while the MDM experiment was still running, the sample for CTV was prepared. The CTV procedure described for the S_m verification experiments was mimicked. A sample concentration of about ~100,000 cells/mL was drawn up into a 5 mL syringe. The syringe was attached to the Luer adaptors connected to the Hamilton valve on one end of the CTV channel, while an empty syringe was attached to the Hamilton valve on the opposite side of the channel. Then the valves were turned to allow for about 0.2 mL of the sample to be pushed through the channel to the empty syringe over a time span of about 3 seconds. Next, the valves were closed to stop fluid flow, and the cells were given about 30 seconds of relaxation time before the motion of the cells was recorded. After, the record button in the Video Savant software was pressed to begin recording for 60 frames at a frame rate of 1 second, totaling a minute of acquisition time. The images were reviewed once the recording was complete to ensure the cells moved in a uniform velocity and direction. The images were saved according to the nomenclature specified by the CTV logbook as set one. This process was repeated 7 times, for a total of 8 sets over a time span of 20 – 25 minutes. The methods of analysis for the glioma

experiments imitated those for the deoxygenation experiment described in Section 3.4.4 and 3.4.6. The part not completed, was for the analysis of the gaussians with the Welch t-test through the data reduction with the Hill equation.

Once the MDM program Nina_U was completed, program Nina_D was run. After it was done, the sample vials at the bottom of the tubing was switched out for vials containing 1 mL of PFA. PFA was drawn into the syringes at the top utilizing program Nina_M_U, and the PFA was left sitting in the channels for 15 minutes to allow for the cells to be fixed to the Mylar slide. When the 15 minutes was up, program Nina_M_D was run, so all the PFA was removed from the tubing and channels back into the sample vials. Once this was completed, the system was carefully disassembled. The syringes were removed from the pump holding location and the tubing connected to the top of the manifold was detached. The tubing at the bottom of the manifold was then disconnected and taken out of the sample vial. The sample vial was then closed to ensure none of the sample would spill. The tubing, syringes, and the samples were then discarded in the biological waste. Next, the magnet assembly was taken apart first by removing the screws and the platen. The Mylar slide was peeled off the rubber spacer and placed off to the side to confirm it was not contaminated. All the adaptors, rubber spacer, and the manifold were cleaned using 70% alcohol and bleach. Lastly, the Mylar slide was taped to a glass slide and stored in the refrigerator at 4°C until Soumya was able to stain the cells.

3.6 Exploration of the Effects of a Temperature Gradient on the Separation of Red Blood Cells

To begin, theoretical calculations were completed for water at 0°C as the cold wall and 40°C for the hot wall, to determine if applying a temperature gradient to the MDM

system would facilitate separation of the viable RBCs. The local water velocity profile in a thin channel bounded by a ‘cold wall’ (0°C) and a ‘hot wall’ (40°C), due to temperature-related changes in the local water density and in the absence of imposed volumetric flow, were calculated from Equation 2.35 (Giddings, 1991). The numerical values of water density, ρ , the water thermal expansion coefficient, γ , the width of the channel, w , the temperatures of the ‘hot wall’ and ‘cold wall’, °C, and the water viscosity, η , are listed in Table V. The local water velocity, $v(y)$, was calculated as a function of y , which was the distance from the ‘cold wall’. The maximum value of the local water velocity induced by the temperature difference between the ‘hot’ and ‘cold’ walls was compared to the known RBC sedimentation velocity in order to determine if it was large enough to affect the RBC sedimentation by entrainment in the falling or rising layer of water in the channel. The results are presented as a plot of $v(y)$ on y in Section 4.5.

Table V: Constants utilized to create Figure 74 Giddings velocity profile.

Giddings Velocity Profile Parameters		
Parameter	Value	Units
Width of Channel	0.25	mm
Density	998	kg/m ³
Thermal Expansion Coefficient	2.07×10^{-4}	1/K
Dynamic Viscosity	1.00×10^{-3}	Pas (Ns/m ²)
Cold Wall Temperature	0	°C
Hot Wall Temperature	40	°C

Once calculations were completed, computational modeling was begun through a cross-platform finite element analysis solver and multiphysics simulation software called COMSOL Multiphysics 5.3. Before modeling could be completed with the MDM assembly, tutorials for different types of fluid flow were completed. One example was erosion within a pipe elbow due to particle contamination. It demonstrated how to setup

the single-phase turbulent fluid flow physics within COMSOL, which were needed to complete the simulations. From there, the geometry of the pipe was drawn, which is similar to how geometries are drawn in SolidWorks. Next, the physics were defined further for the model, which was where the turbulent flow entering and exiting the pipe and the inlet velocity of the fluid were specified. Then the fluid material was defined as water, and the pipe mesh was applied, which distributes the stresses of the flow through the pipe for a more realistic representation of the fluid flow. After, a study was computed to determine the fluid velocity streamlines and the points within the pipe which experience the most pressure. Due to the limitations of the version of COMSOL accessible, the contamination particles were not able to be added to the simulation to finish the tutorial.

Once the tutorial was completed, modeling for the temperature gradient began utilizing the same physics from the pipe tutorial, single-phase turbulent fluid flow. First, the MDM magnet assembly, originally designed in SolidWorks and provided by Lee R. Moore, was imported into the COMSOL software utilizing an .STL file, allowing for a more accurate theoretical model. Initially, meshing was attempted with the whole magnet assembly, but this caused the program to take a few hours to complete. Therefore, the geometry was cut from the whole assembly to just one channel within the assembly. Figure 37 displays the whole assembly and just one channel of the assembly. Next, the fluid was specified as water and the inlet and outlets were specified. Last, the velocity and pressure profiles were generated for water flowing through the single channel.

Multiple attempts were completed to ensure the fluid was flowing through the tubing of the manifold into the channels. The second attempt was done by extruding an inlet and outlet from the tubing, which is present in the single channel assembly of Figure

37. Attempt number three, tubing was drawn through the manifold holes to the channel itself. The last attempt, the tubing walls were selected as boundaries to facilitate fluid flow. These simulation results will be further discussed in Chapter IV – Results and Discussion.

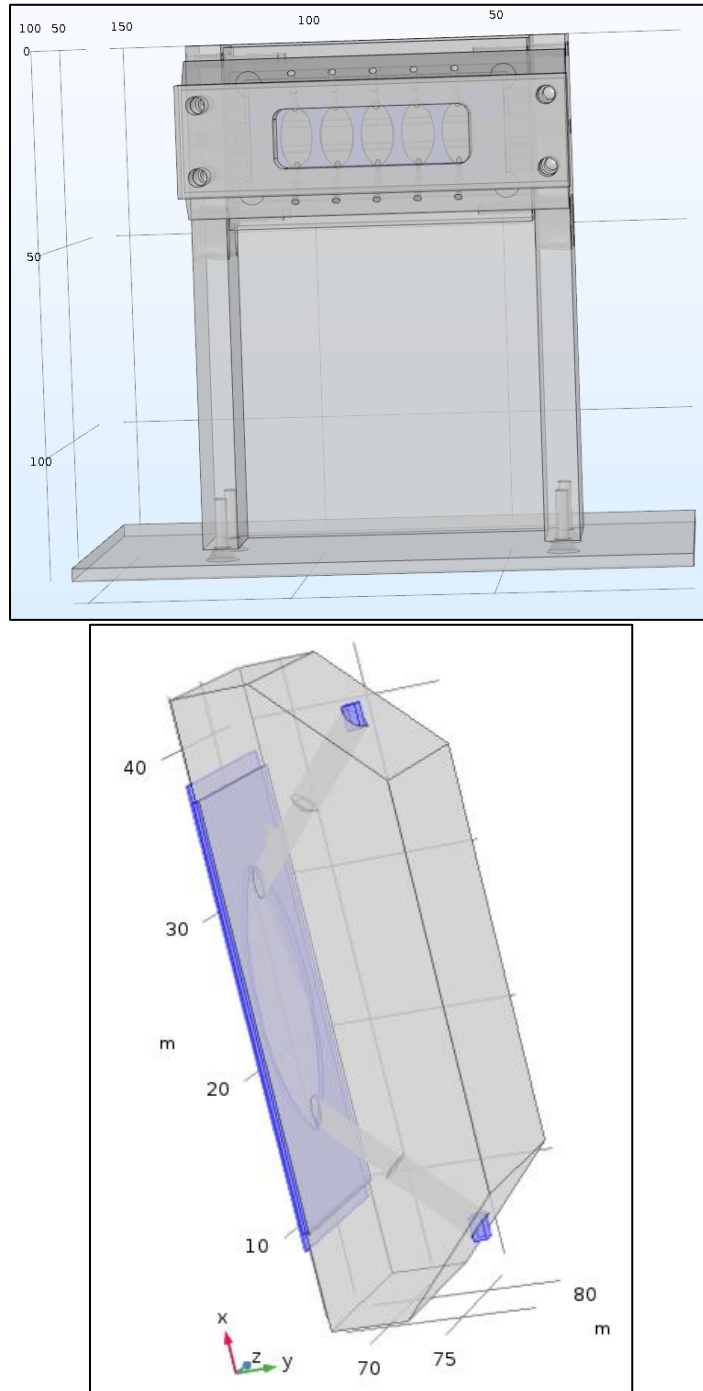


Figure 37: Above: Full MDM magnet assembly. Below: One channel of the assembly.

CHAPTER IV

RESULTS AND DISCUSSION

4.1 S_m Verification Results

The objective of this experiment was to validate the S_m value of the Mk V magnet assembly to ensure the particles are exposed to a uniform magnetic field when carrying out experiments on CTV. To begin calculations, Equation 2.20 in Section 2.6.1 was utilized to convert the mean magnetophoretic mobility ($\text{mm}^3/\text{T-A-s}$) to the mean magnetic velocity (mm/s), utilizing the current S_m value of 365 T-A/mm^2 (Xue, et al., 2019). Next, $\Delta\chi$ of the solution was calculated from Equation 2.12, with the assumption that MDM buffer has the same magnetic susceptibility as water, and the solution was measured by the MSB-Auto, described in Section 3.1.3. The theoretical volumetric, magnetic susceptibility of water is -7.19×10^{-7} (CGS), which corresponds to -9.035×10^{-6} (SI) (Zborowski, et al., 2003). The 50/50 Magnevist and MDM buffer solution was measured to have a magnetic susceptibility of 6.77×10^{-5} , in SI units, but it was calculated to be 7.58×10^{-5} (SI), which is a 10.68% difference between the two values. Then, these values were used to evaluate Equation 2.15 to obtain an S_m value, where the particle diameter and viscosity of the solution were kept constant for the calculations. These results are presented in Figure 38.

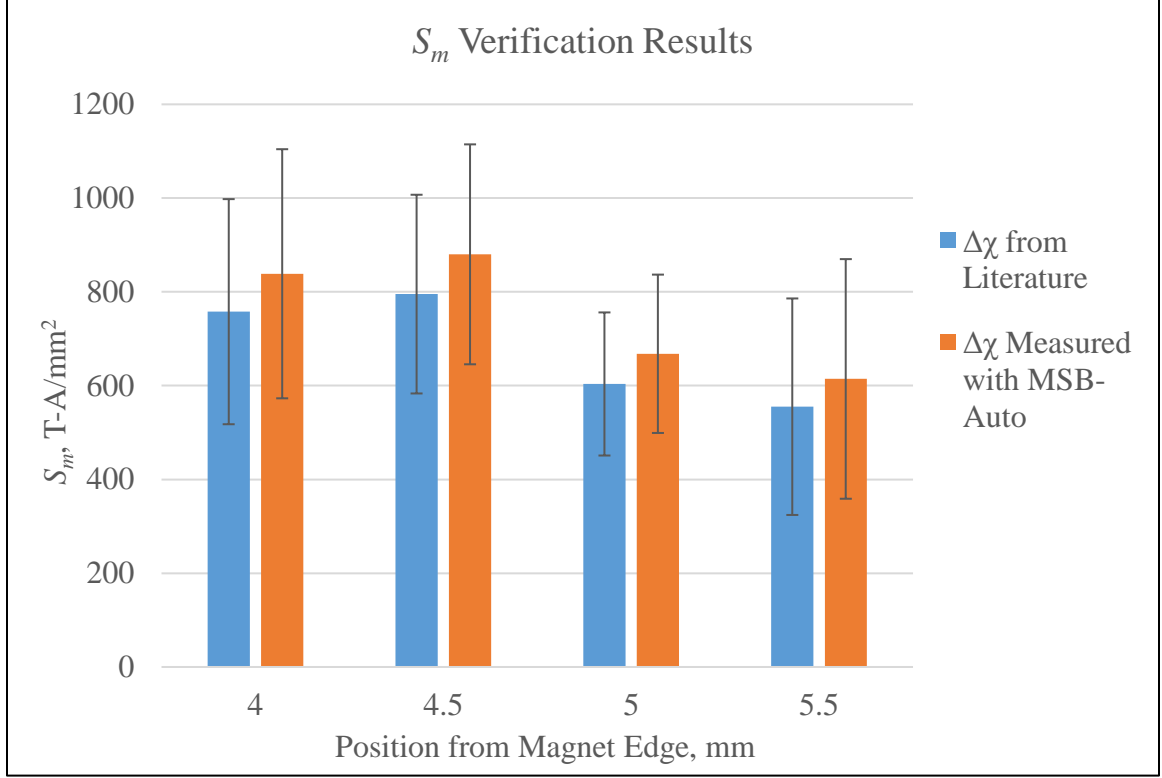


Figure 38: Results to determine the FOV location and the value of S_m .

In Figure 38, the highest S_m value is located at 4.5 mm away from the edge of the magnet. Figure 11, of the theoretical model for the Mk V magnet, also indicates around 4.5 mm away from the edge of the magnet, the S_m value is the highest. However, the experimental values for S_m are much higher than the original 365 T-A/mm² (theoretical) 795 ± 212 T-A/mm² ($\Delta\chi$ from literature) and 880 ± 235 T-A/mm² ($\Delta\chi$ measured by MSB-Auto). The potential sources of irregularity are discussed in Section 4.6.

4.2 Spectrophotometry Results

Specific aim number two was to determine the concentration levels of metHb and oxyHb within samples through spectrophotometry. As described in Section 3.2.2, the spectrum of two samples were measured over a wavelength range of 500 – 700 nm. The results are displayed in Figure 39 below. Around wavelength 577 nm, oxyHb rises steeply into a second peak. At wavelength 630 nm, a small peak is seen in the metHb curve. Also,

around 560 nm, both the oxyHb and metHb curves dip into a trough, indicating the presence of hemichromes, or unstable hemoglobin, within the samples.

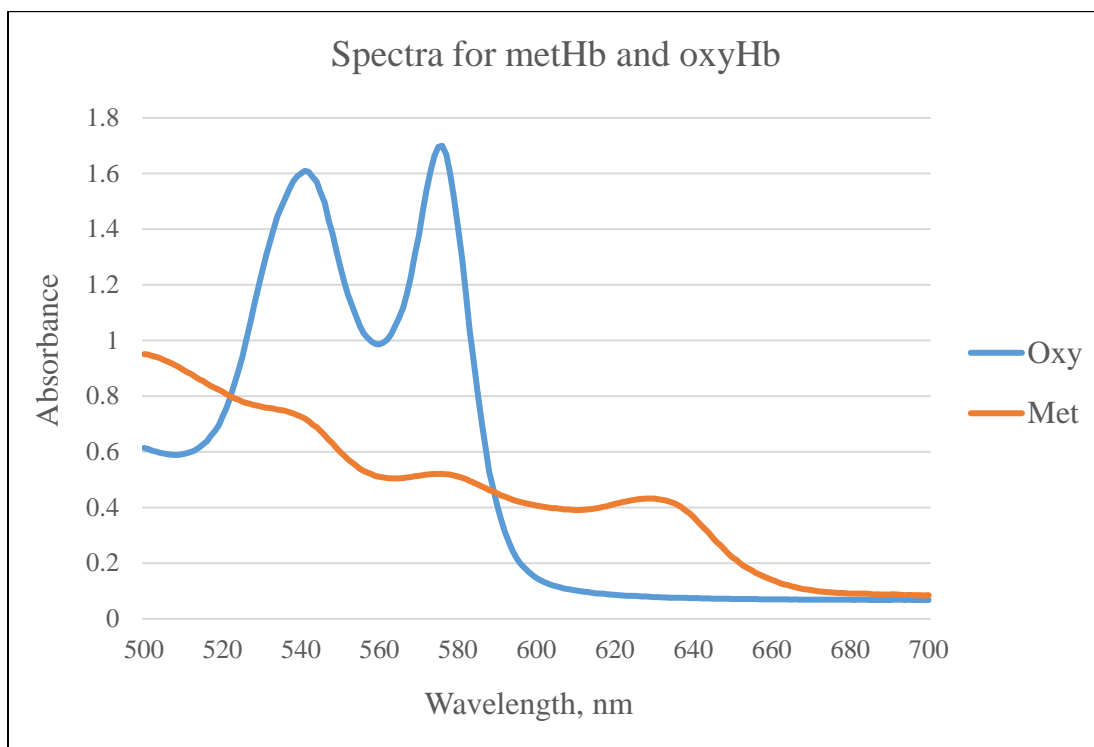


Figure 39: Results from running spectrophotometry on the oxyHb and metHb samples over a range of 500 - 700 nm.

Following the experiments, post-processing calculations were completed to determine the concentration of oxyHb, metHb, and hemichromes in the samples utilizing Equations 2.32 through 2.34. The results are displayed in Table VI and will be discussed in Section 4.7. Due to the high error associated with pipetting small amounts of the sample's multiple times and the accuracy of the spectrophotometer absorbance readings, the values of the oxyHb concentration in the metHb sample and hemichrome concentration in the oxyHb sample are below zero, however they are within the standard deviation. The suitable concentration for oxyHb and metHb for spectrophotometry measurements are 40 μ M per heme group (Winterbourn, 1990).

Table VI: Concentrations calculated from Equations 2.32-2.34 to obtain the concentration of oxyHb, metHb, and hemichrome within the samples analyzed by spectrophotometry.

Concentration Results Calculated with Winterbourn's Equations						
Type	A560	A577	A630	[oxyHb], μM	[metHb], μM	[hemi], μM
metHb	0.51	0.52	0.43	-0.36 ± 0.45	119.13 ± 0.45	0.422 ± 0.45
oxyHb	0.99	1.67	0.08	107.70 ± 1.03	16.42 ± 1.03	-1.0 ± 1.03

4.3 Deoxygenation of Red Blood Cell Results

The purpose of the deoxygenation of RBC experiments was to determine if CTV is capable of distinguishing different RBC subfractions when the levels of oxygenation were varied. Analysis began by running the Excel Macros described in Section 3.4.4 to obtain the magnetic mobility and sedimentation velocity results using CTV. The magnetic mobility versus the $p\text{O}_2$ for Experiments 1 and 2 are shown in Figures 40 and 41, respectively. These graphs demonstrate that as the $p\text{O}_2$ level decreases, the magnetic mobility of the RBCs increases.

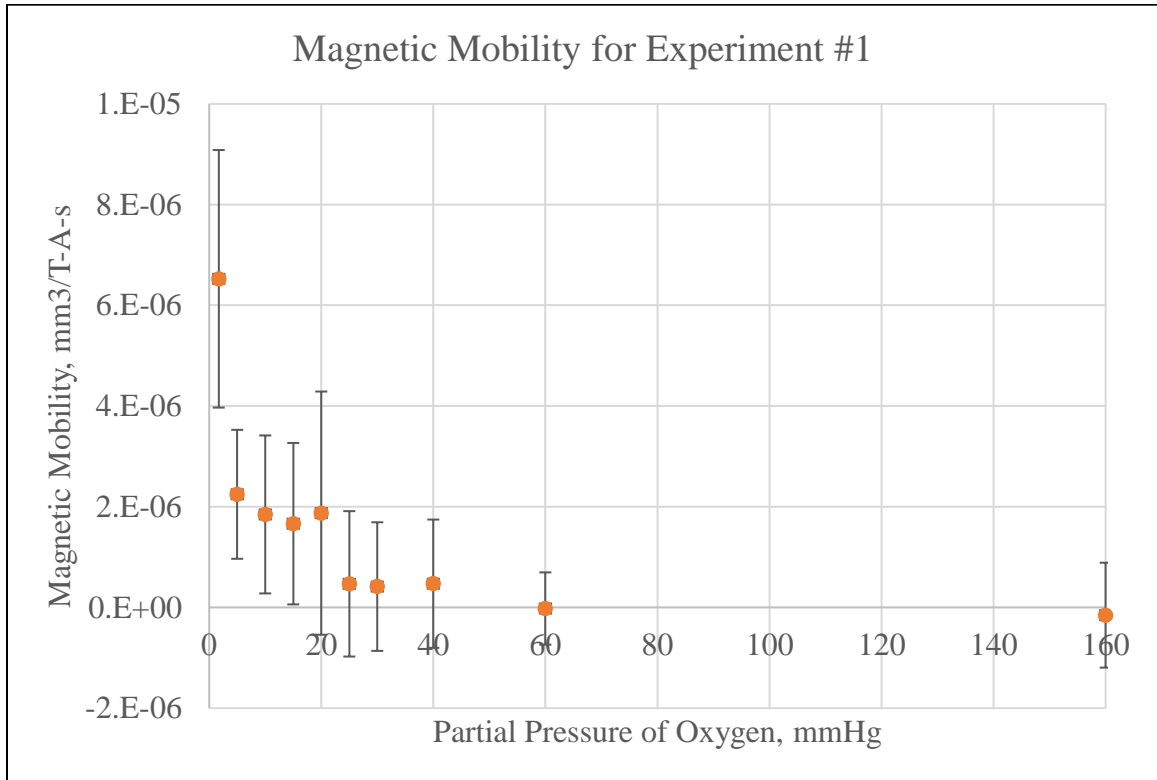


Figure 40: Magnetic mobility versus the $p\text{O}_2$ level for Experiment #1.

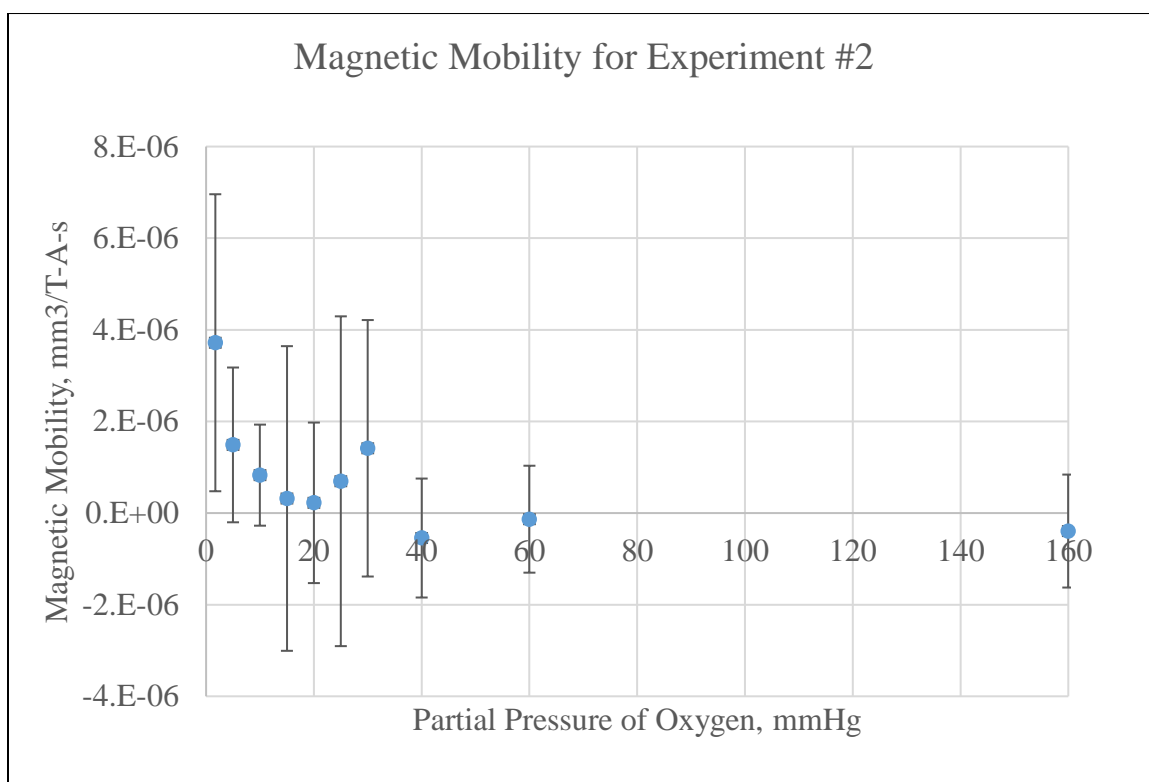


Figure 41: Magnetic mobility versus the pO₂ level for Experiment #2.

These results were then run through the MATLAB code, which generated a variety of graphs. Also, the original magnetic mobility and sedimentation velocity data, the original data split into cluster's 1 and 2, the Gaussian coefficients for the separate clusters, and Welch's t-test information was printed to a different Excel file to be further analyzed against the Hill equation.

4.3.1 Results Generated through the MATLAB Code for Experiment #1

The MATLAB code generated nine plots when analyzing the data for one oxygenation level. For the purpose of this study, only three were analyzed: 1 – the overall color coded dataset with the magnetic and sedimentation velocity histograms, the left graph in Figure 42, 2 – the original data split into two clusters based on the k-means clustering method, the right graph in Figure 42, and 3 – the Gaussians of the two clusters (red and

light purple curves) overlaid on the original magnetic velocity histogram (light blue stairs-type), and the sum of the cluster Gaussians (black), the top graph in Figure 43. As mentioned before, the red curve in the top graph in Figure 43 corresponds to cluster 2, and the light purple curve correlates to cluster 1. These three figures are the results of the pO_2 level at 160 mmHg for Experiment #1. The bottom graph in Figure 43, was created by Dr. Maciej Zborowski through Maple, is the theoretical behavior of an RBC when it is fully oxygenated.

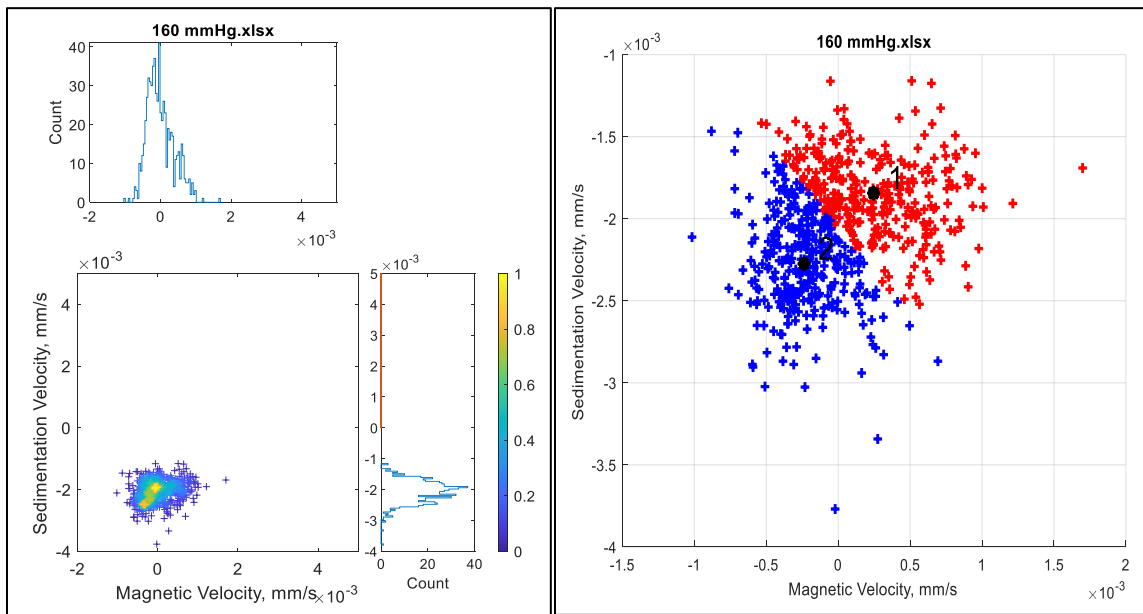


Figure 42: MATLAB graphs generated for the 160-mmHg oxygenation level in Experiment #1. On the left is the whole dataset with histograms and to the right are the two clusters generated by the k-mean clustering method.

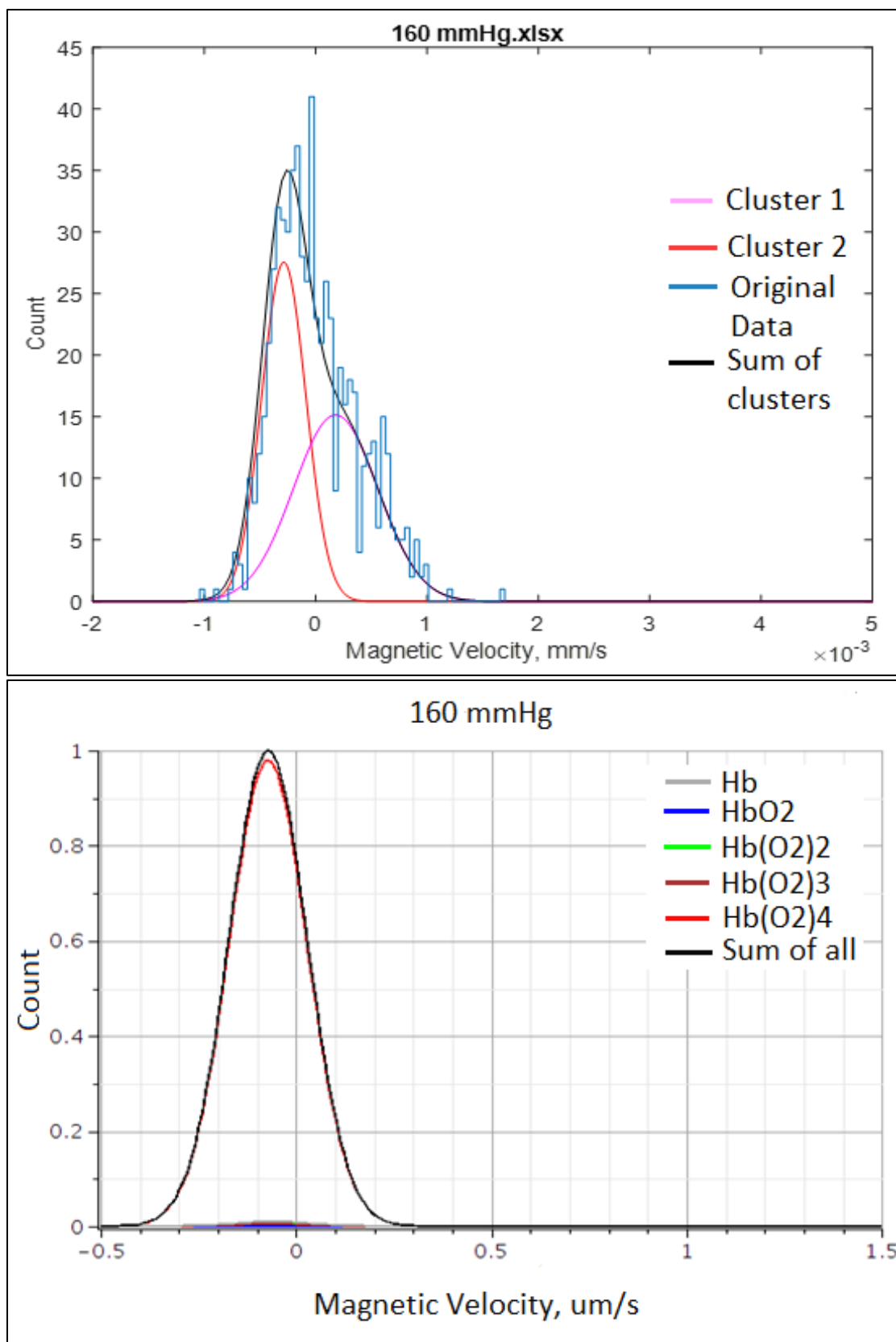


Figure 43: Above: Gaussian curves for the k-mean clusters for Experiment #1 at 160 mmHg. Below: Graph created in Maple for RBC behavior at 160 mmHg predicted from the Adair equation.

When comparing the taller gaussian peak to the left (red curve) in the top graph of Figure 43 and the gaussian peak in the bottom graph in Figure 43, they are both slightly to the left of zero. As the oxygenation level decreased during Experiment #1, the RBC's magnetic velocity increases, as demonstrated in Figures 42 – 61. Again, at each oxygenation level, the experimental motion of an RBC (graphs from MATLAB) were compared to the theoretical motion predicted from Adair's Equation 2.25 (graphs created in Maple).

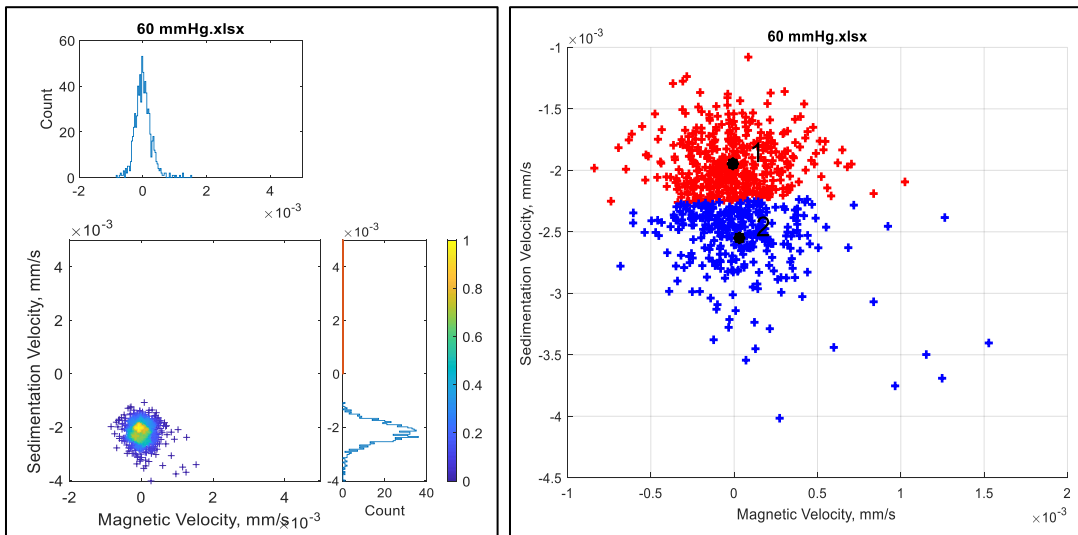


Figure 44: MATLAB graphs generated for the 60-mmHg oxygenation level in Experiment #1. On the left is the whole dataset with histograms and to the right are the two clusters generated by the k-mean clustering method.

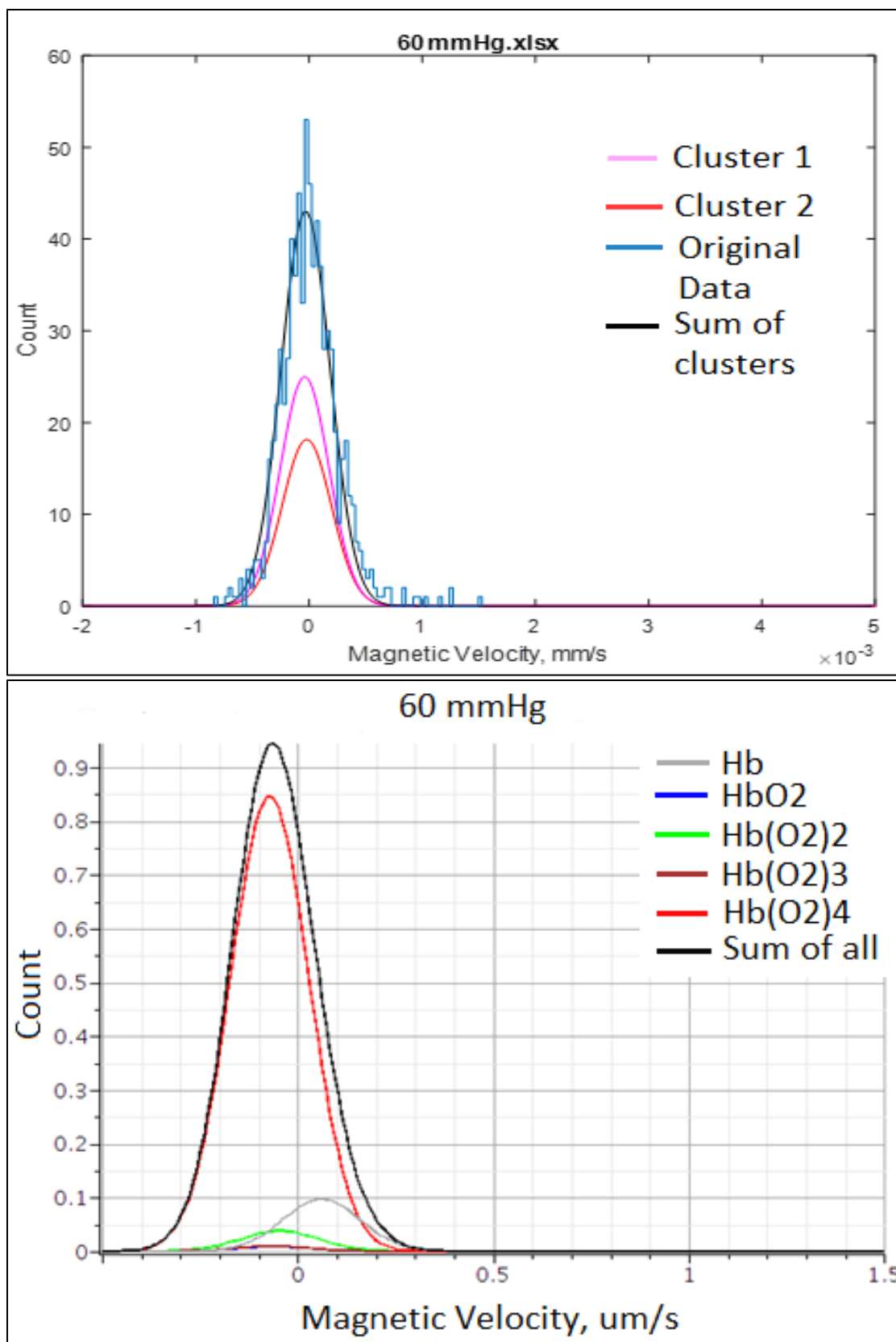


Figure 45: Above: Gaussian curves for the k-mean clusters for Experiment #1 at 60 mmHg. Below: Graph created in Maple for RBC behavior at 60 mmHg predicted from Adair equation.

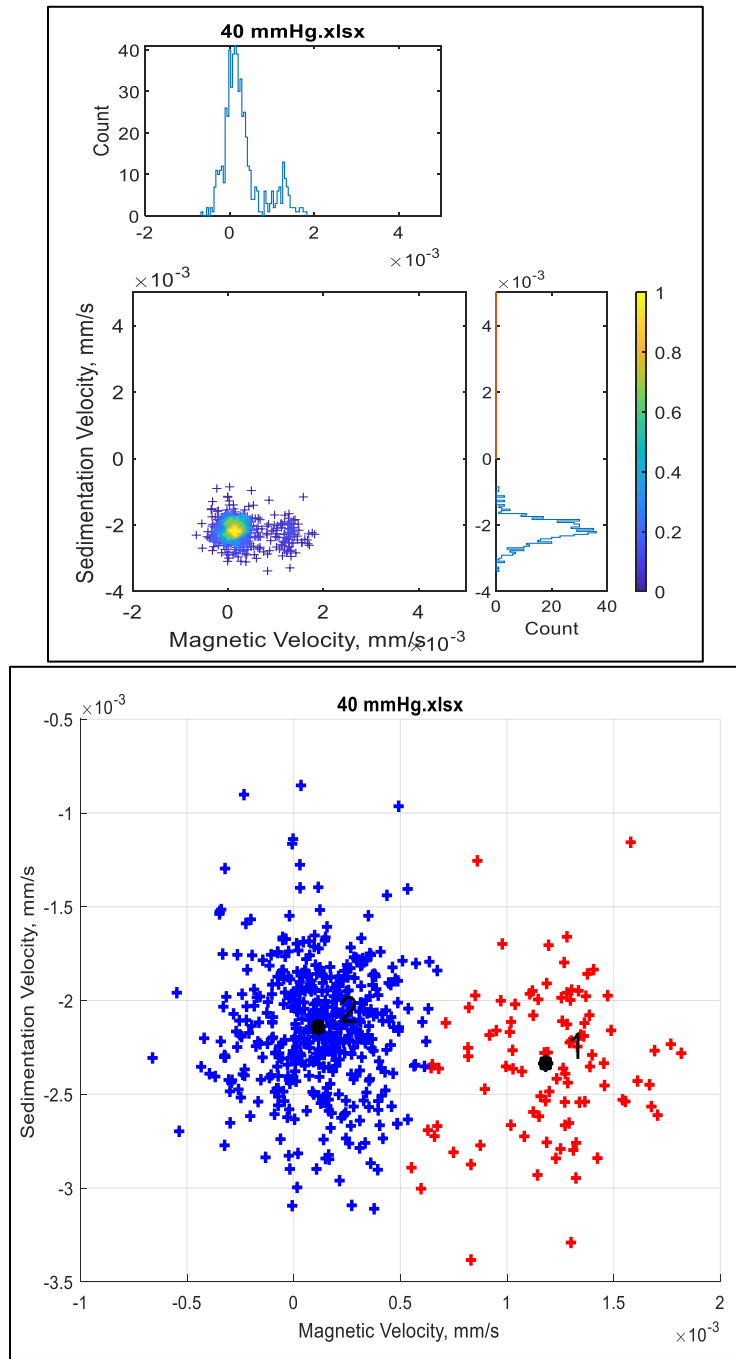


Figure 46: MATLAB graphs generated for the 40-mmHg oxygenation level in Experiment #1. On the top is the whole dataset with histograms and to the bottom are the two clusters generated by the k-mean clustering method.

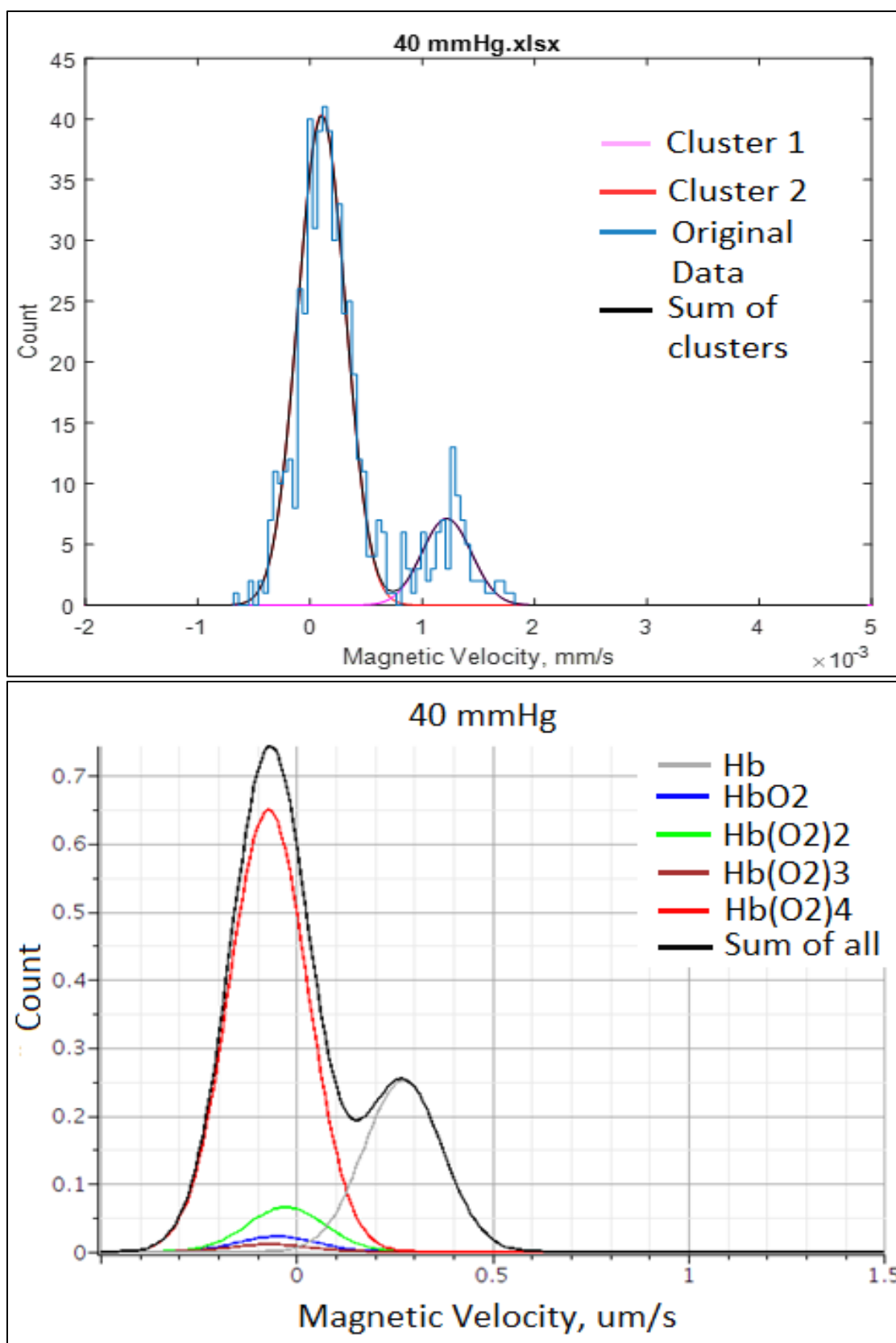


Figure 47: Above: Gaussian curves for the k-mean clusters for Experiment #1 at 40 mmHg. Below: Graph created in Maple for RBC behavior at 40 mmHg predicted from Adair equation.

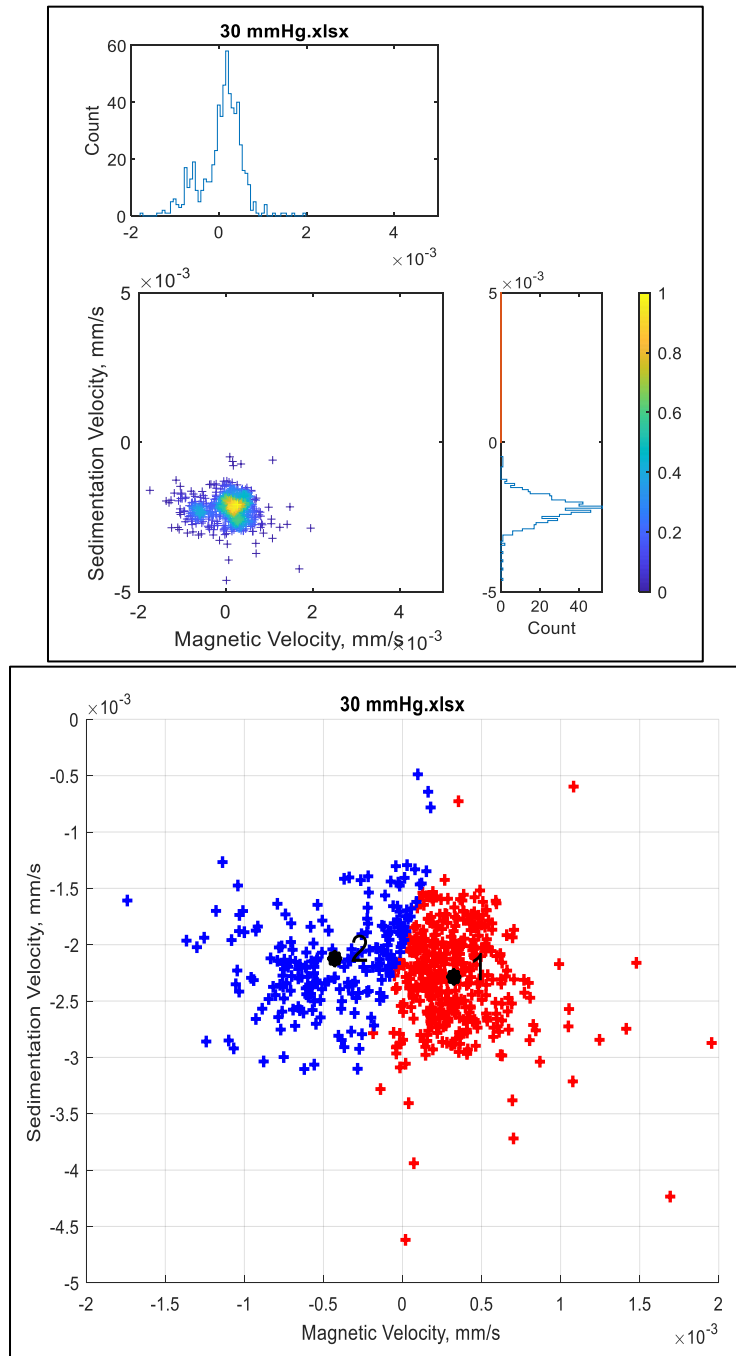


Figure 48: MATLAB graphs generated for the 30-mmHg oxygenation level in Experiment #1. On the top is the whole dataset with histograms and to the bottom are the two clusters generated by the k-mean clustering method.

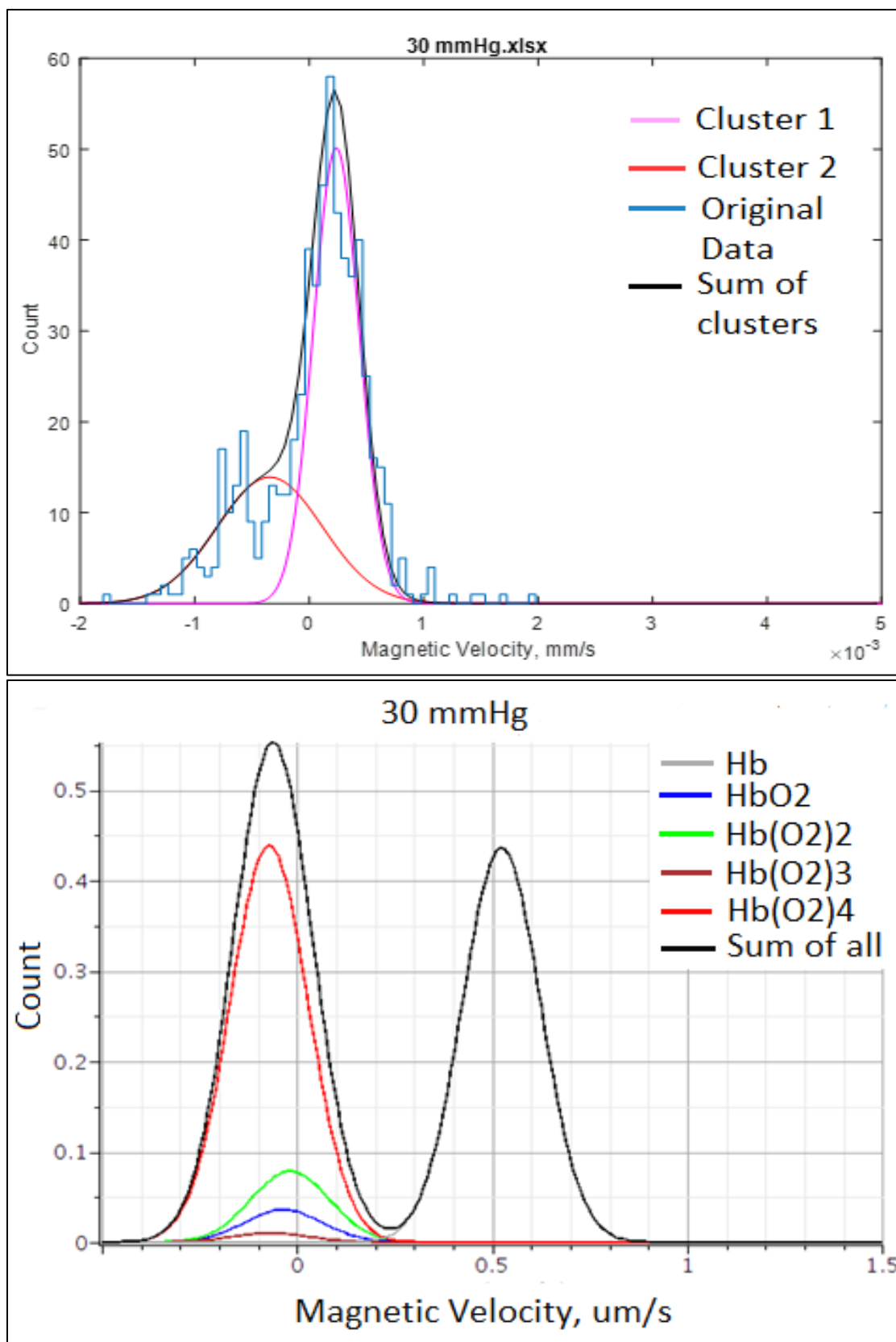


Figure 49: Above: Gaussian curves for the k-mean clusters for Experiment #1 at 30 mmHg. Below: Graph created in Maple for RBC behavior at 30 mmHg predicted from Adair equation.

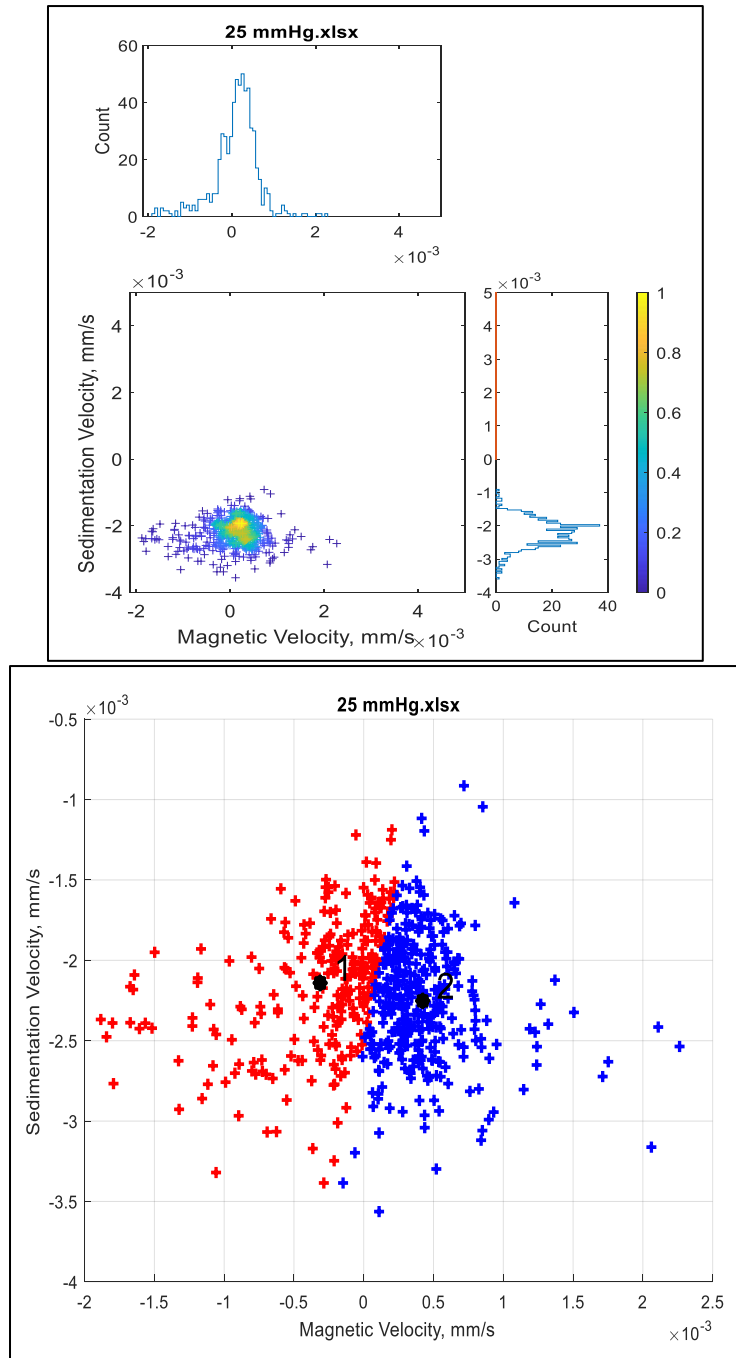


Figure 50: MATLAB graphs generated for the 25-mmHg oxygenation level in Experiment #1. On the top is the whole dataset with histograms and to the bottom are the two clusters generated by the k-mean clustering method.

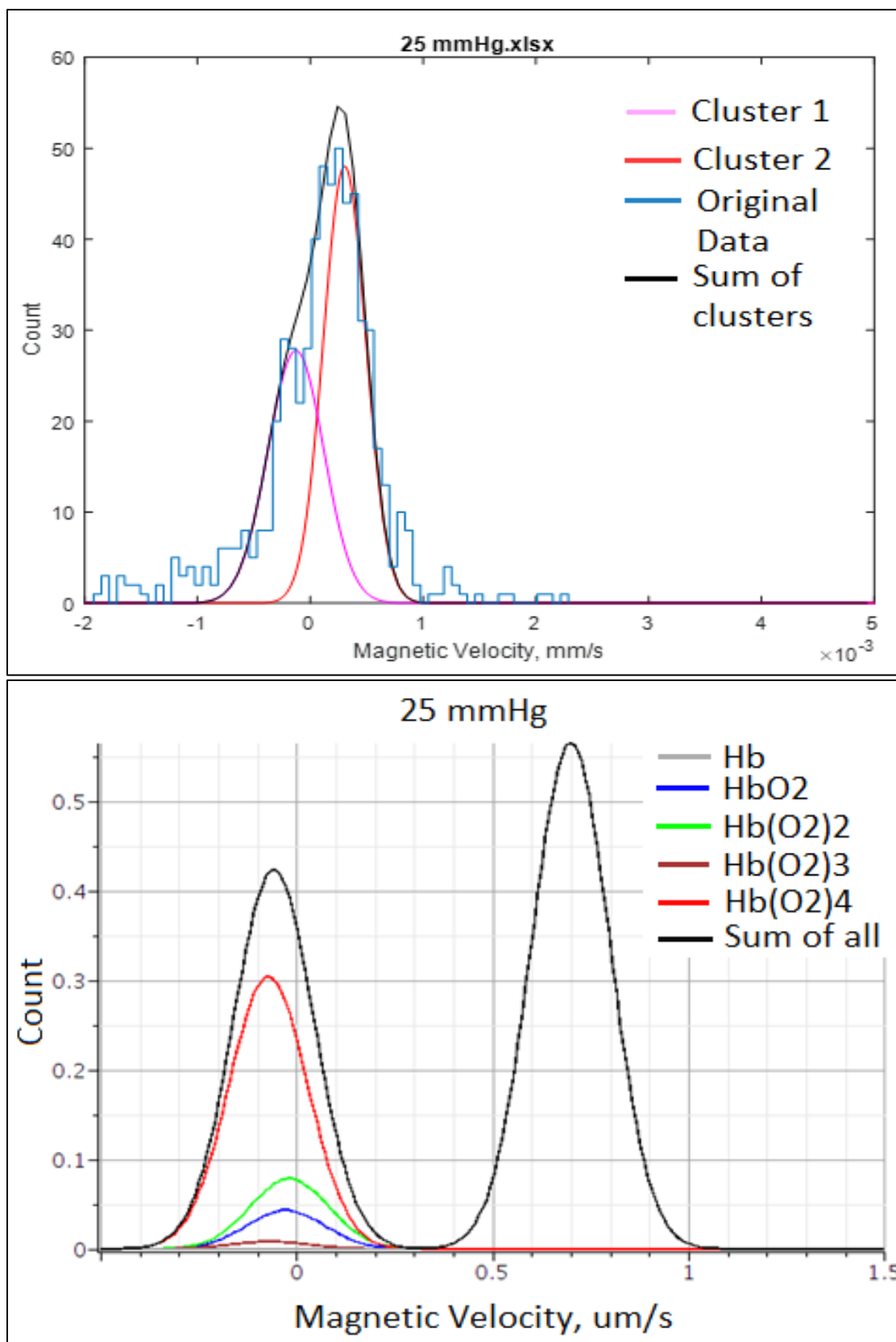


Figure 51: Above: Gaussian curves for the k-mean clusters for Experiment #1 at 25 mmHg. Below: Graph created in Maple for RBC behavior at 25 mmHg predicted from Adair equation.

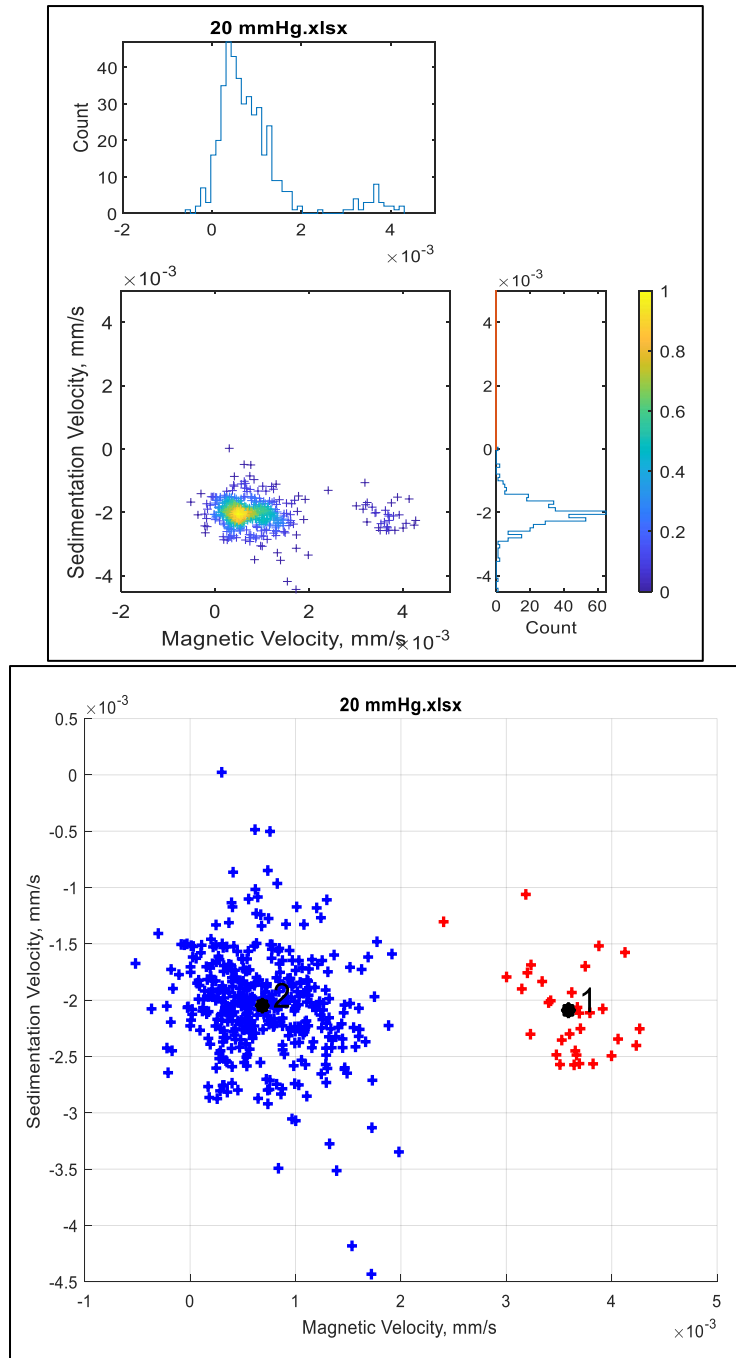


Figure 52: MATLAB graphs generated for the 20-mmHg oxygenation level in Experiment #1. On the top is the whole dataset with histograms and to the bottom are the two clusters generated by the k-mean clustering method.

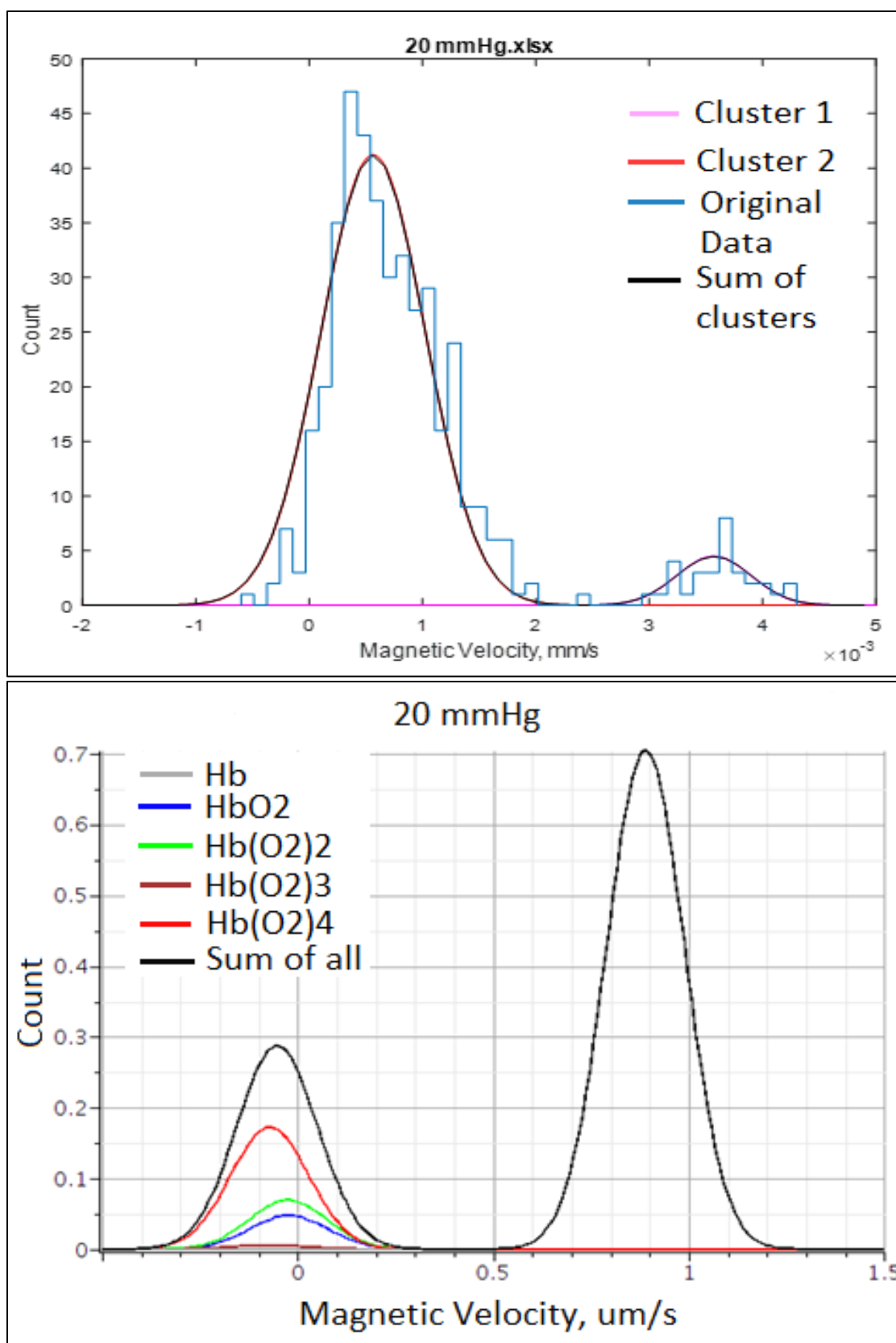


Figure 53: Above: Gaussian curves for the k-mean clusters for Experiment #1 at 20 mmHg. Below: Graph created in Maple for RBC behavior at 20 mmHg predicted from Adair equation.

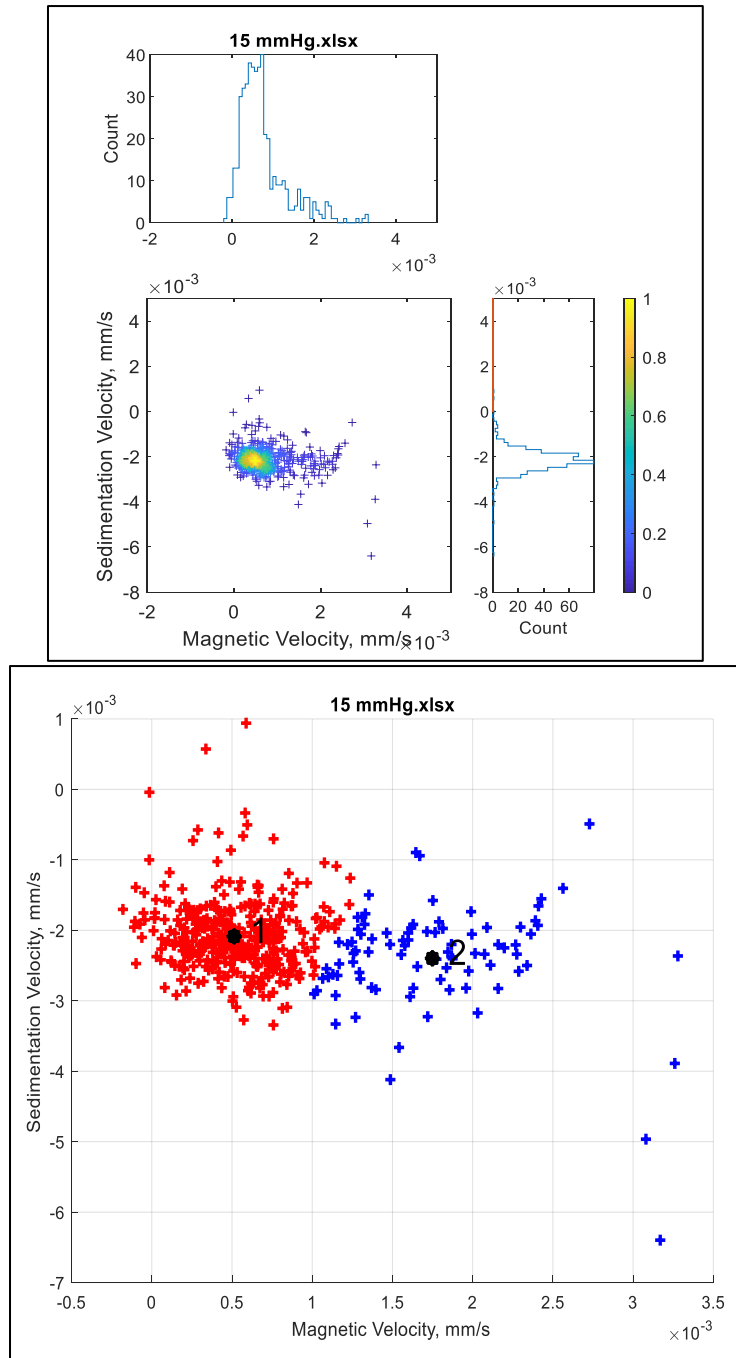


Figure 54: MATLAB graphs generated for the 15-mmHg oxygenation level in Experiment #1. On the top is the whole dataset with histograms and to the bottom are the two clusters generated by the k-mean clustering method.

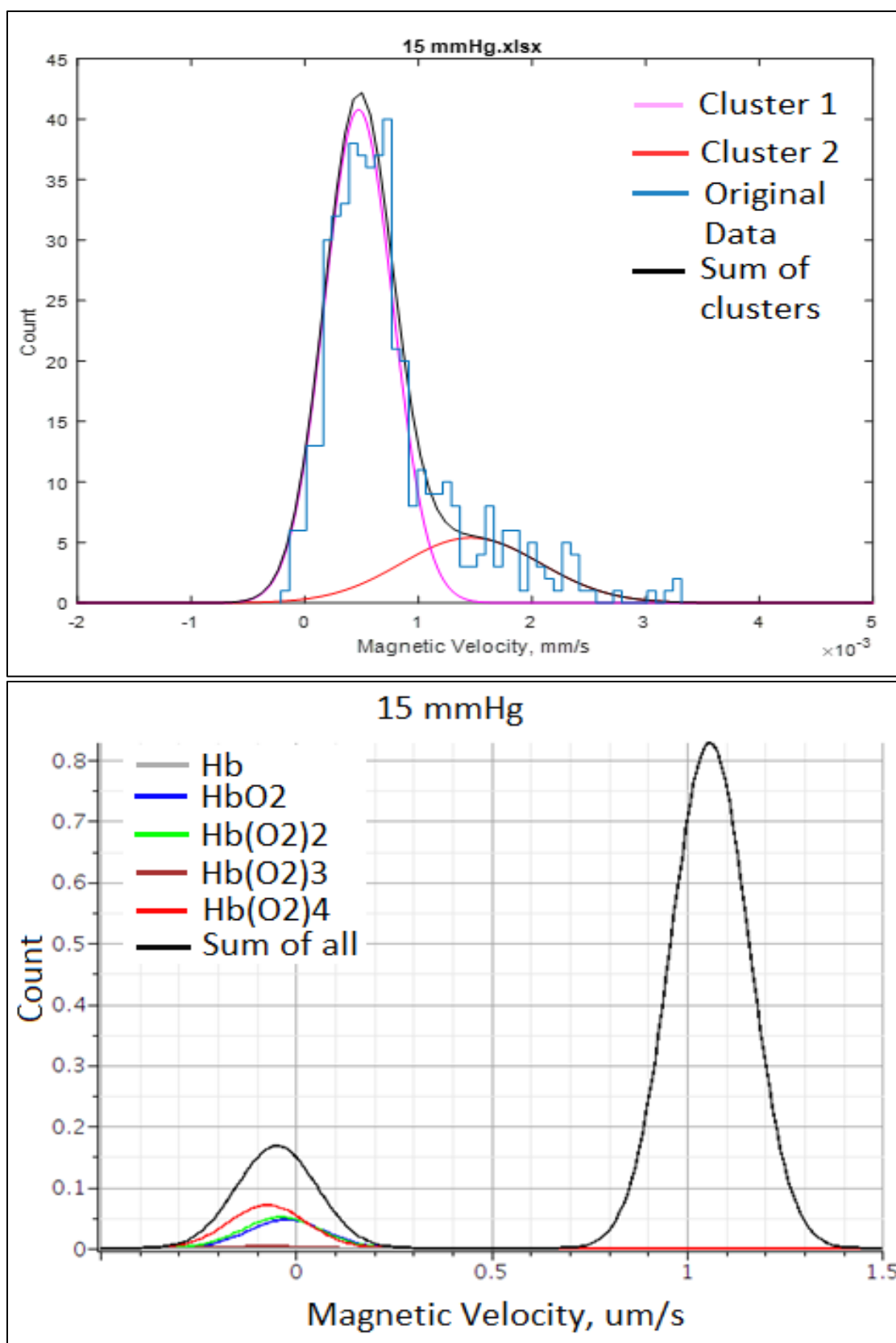


Figure 55: Above: Gaussian curves for the k-mean clusters for Experiment #1 at 15 mmHg. Below: Graph created in Maple for RBC behavior at 15 mmHg predicted from Adair equation.

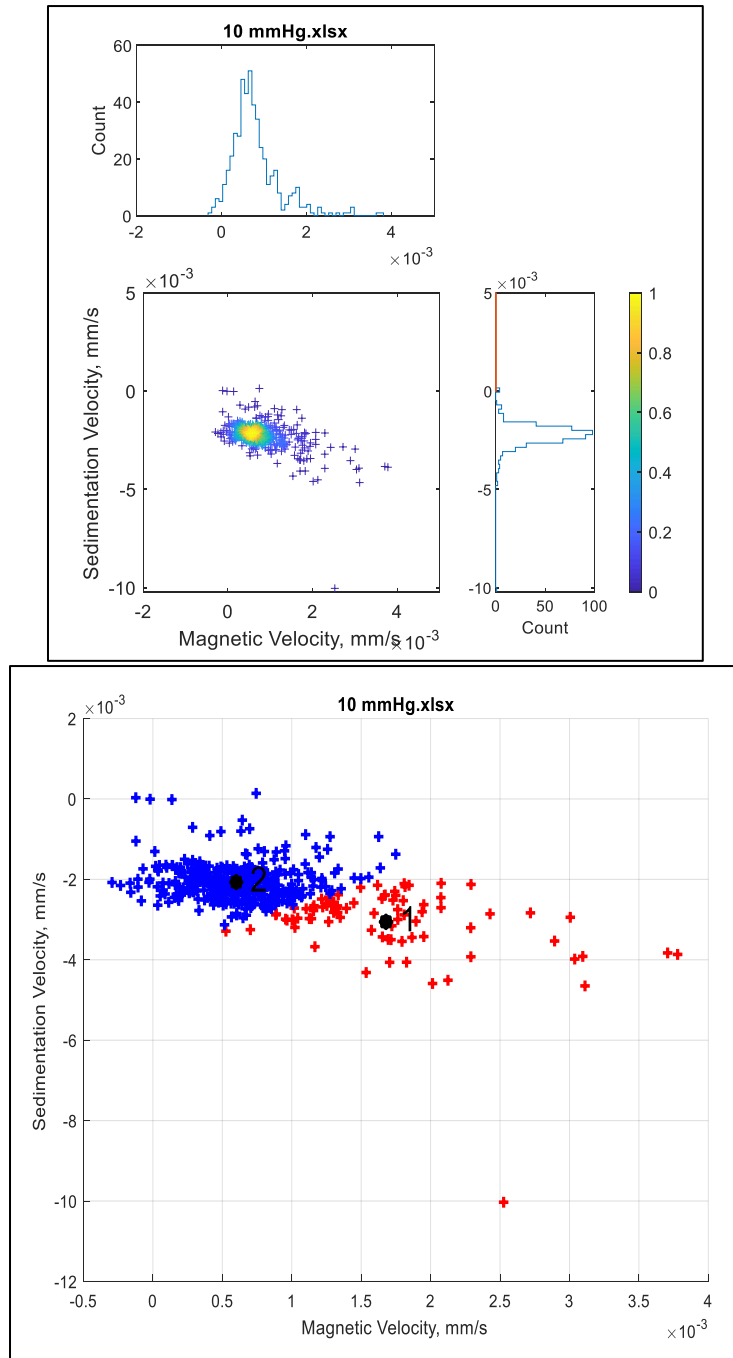


Figure 56: MATLAB graphs generated for the 10-mmHg oxygenation level in Experiment #1. On the top is the whole dataset with histograms and to the bottom are the two clusters generated by the k-mean clustering method.

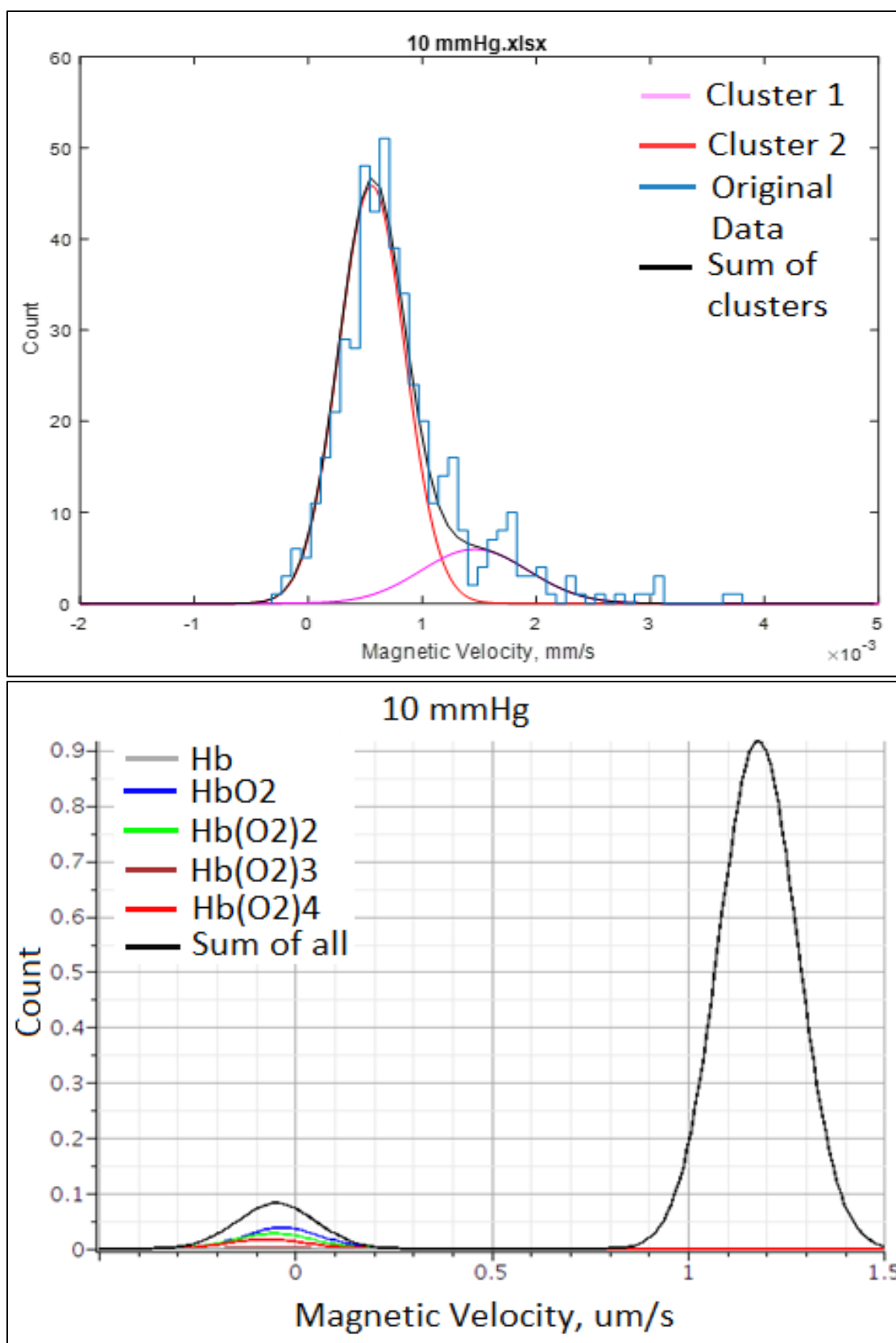


Figure 57: Above: Gaussian curves for the k-mean clusters for Experiment #1 at 10 mmHg. Below: Graph created in Maple for RBC behavior at 10 mmHg predicted from Adair equation.

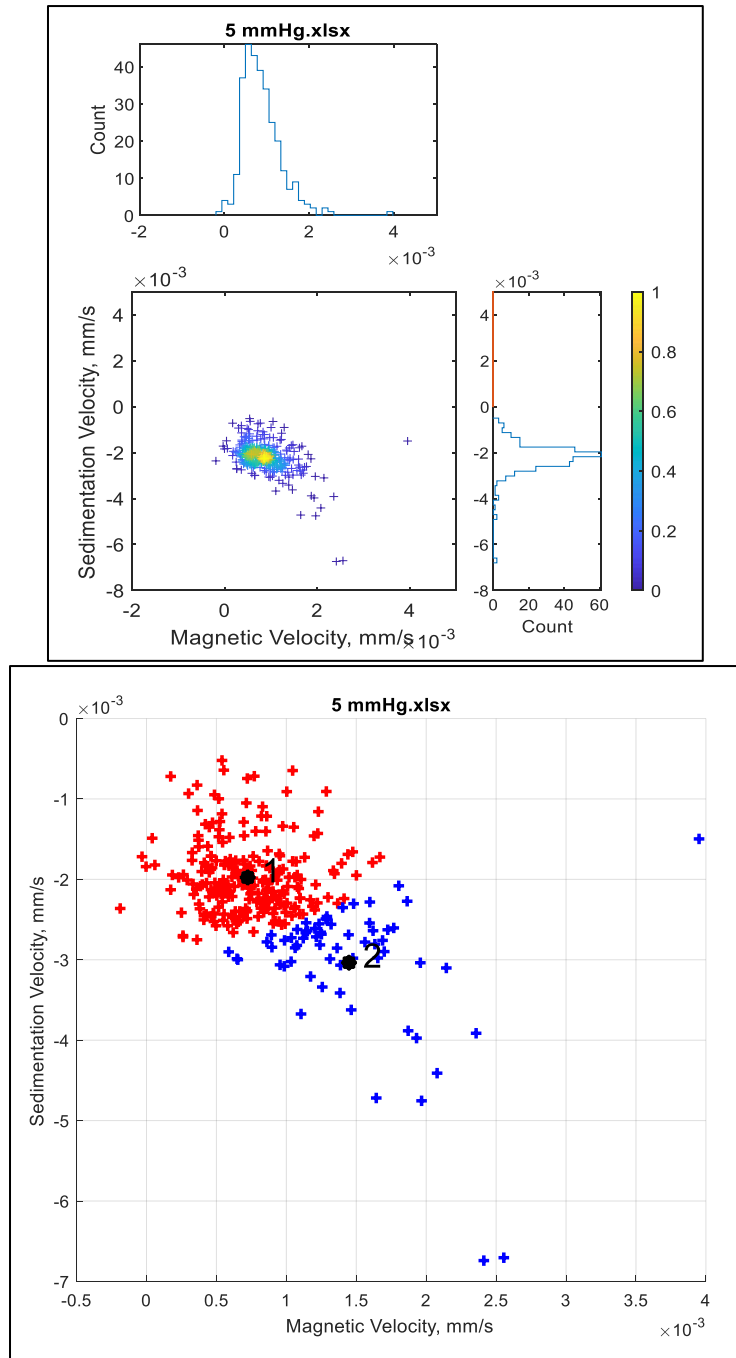


Figure 58: MATLAB graphs generated for the 5-mmHg oxygenation level in Experiment #1. On the top is the whole dataset with histograms and to the bottom are the two clusters generated by the k-mean clustering method.

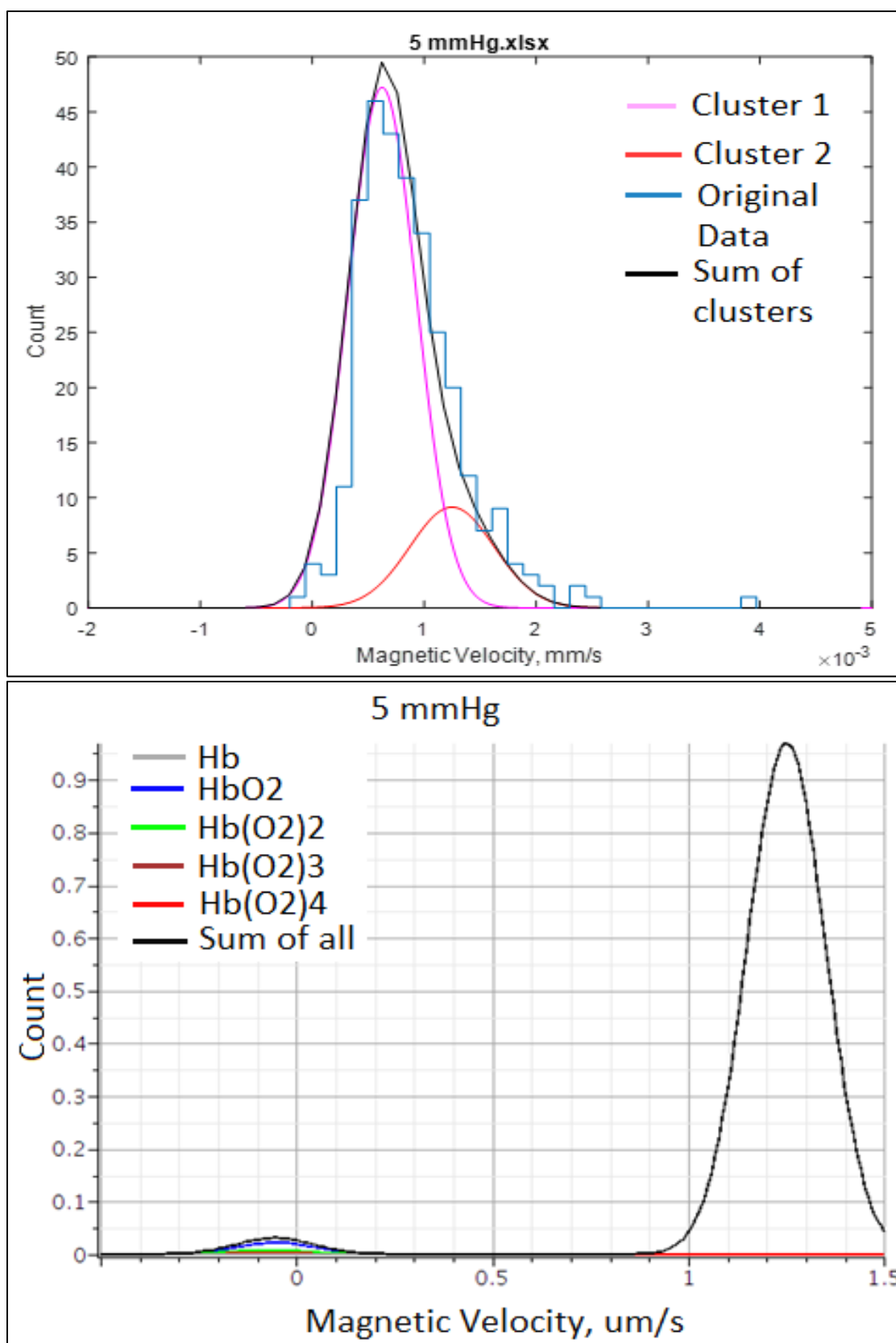


Figure 59: Above: Gaussian curves for the k-mean clusters for Experiment #1 at 5 mmHg. Below: Graph created in Maple for RBC behavior at 5 mmHg predicted from Adair equation.

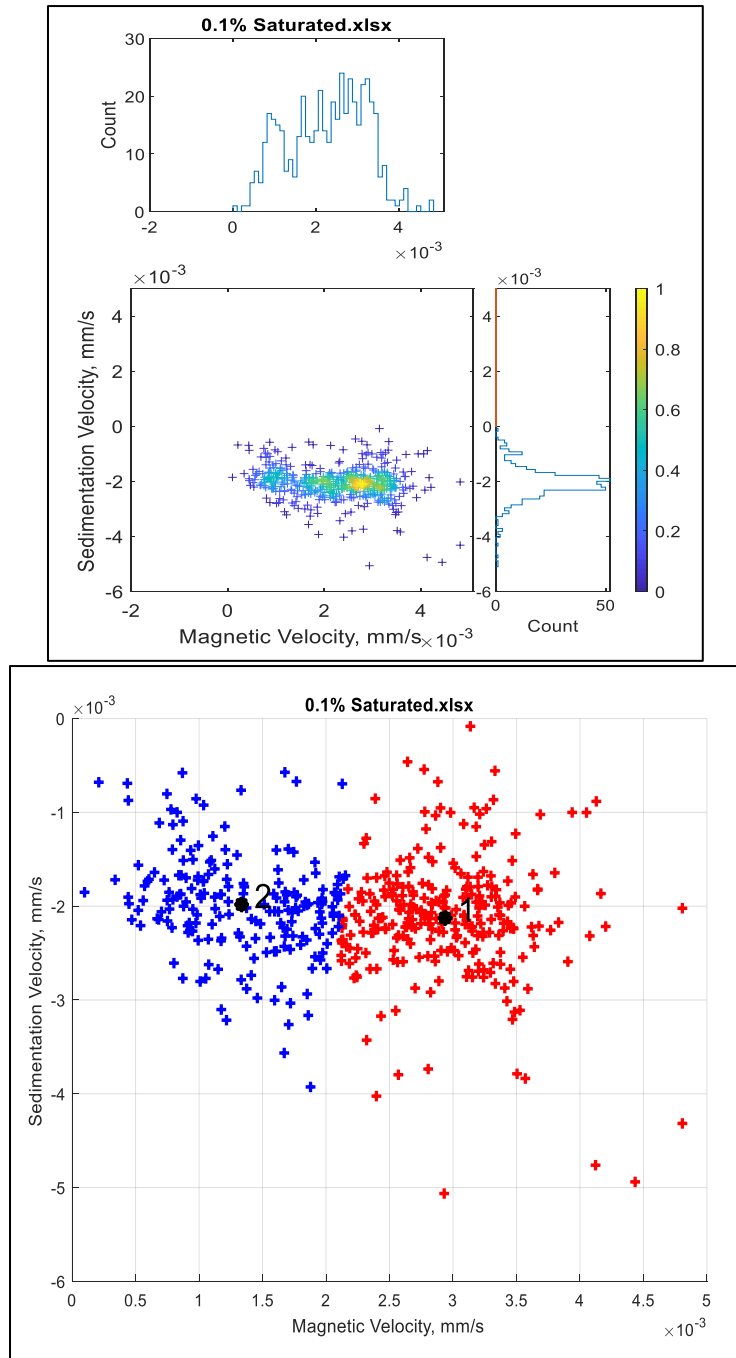


Figure 60: MATLAB graphs generated for 0.1% O_2 saturation level in Experiment #1. On the top is the whole dataset with histograms and to the bottom are the two clusters generated by the k-mean clustering method.

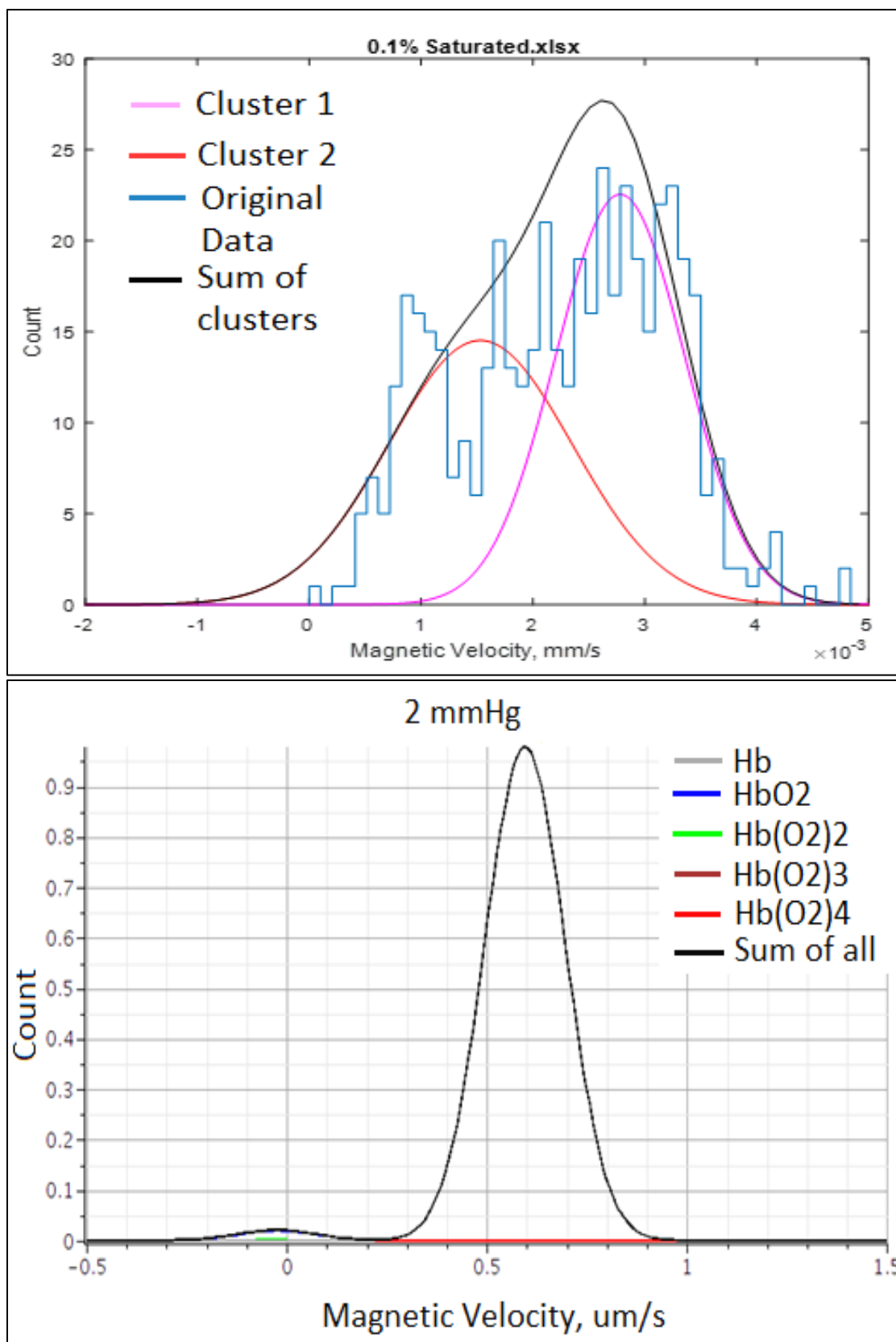


Figure 61: Above: Gaussian curves for the k-mean clusters for Experiment #1 at 0.1% O₂ saturation level. Below: Graph created in Maple for RBC behavior at 0.1% O₂ saturation level predicted from Adair equation.

Comparing the top graphs in Figure 43 (160 mmHg) and Figure 61 (about 1.7 mmHg, or 0.1% saturation) confirms that at lower oxygenation levels (high spin hemoglobin molecules, unpaired electrons) the magnetic velocity of an RBC is greater than at higher oxygenation levels (low spin hemoglobin molecules, covalently bonded to O₂). When relating the experimental graphs to the theoretical graphs for 60-30 mmHg, the peaks of the gaussians move comparably well with each other. However, for 25 mmHg and lower, the experimental graphs indicate the existence of fewer magnetic cells than the theoretical graphs display. Also, Figure 61 demonstrates the possible presence of varying oxygenated subfractions of RBCs due to the widespread distribution of the data. The graphs for Experiment #2 are below in Figures 62 – 71. Comparing the gaussian curves from Experiment #1 to the gaussian curves from Experiment #2, there is a clear pattern seen in the magnetic velocities while decreasing the pO₂ between these two experiments. Due to limitations of the MATLAB code, analysis of Experiments 3 – 5 were not available at this time.

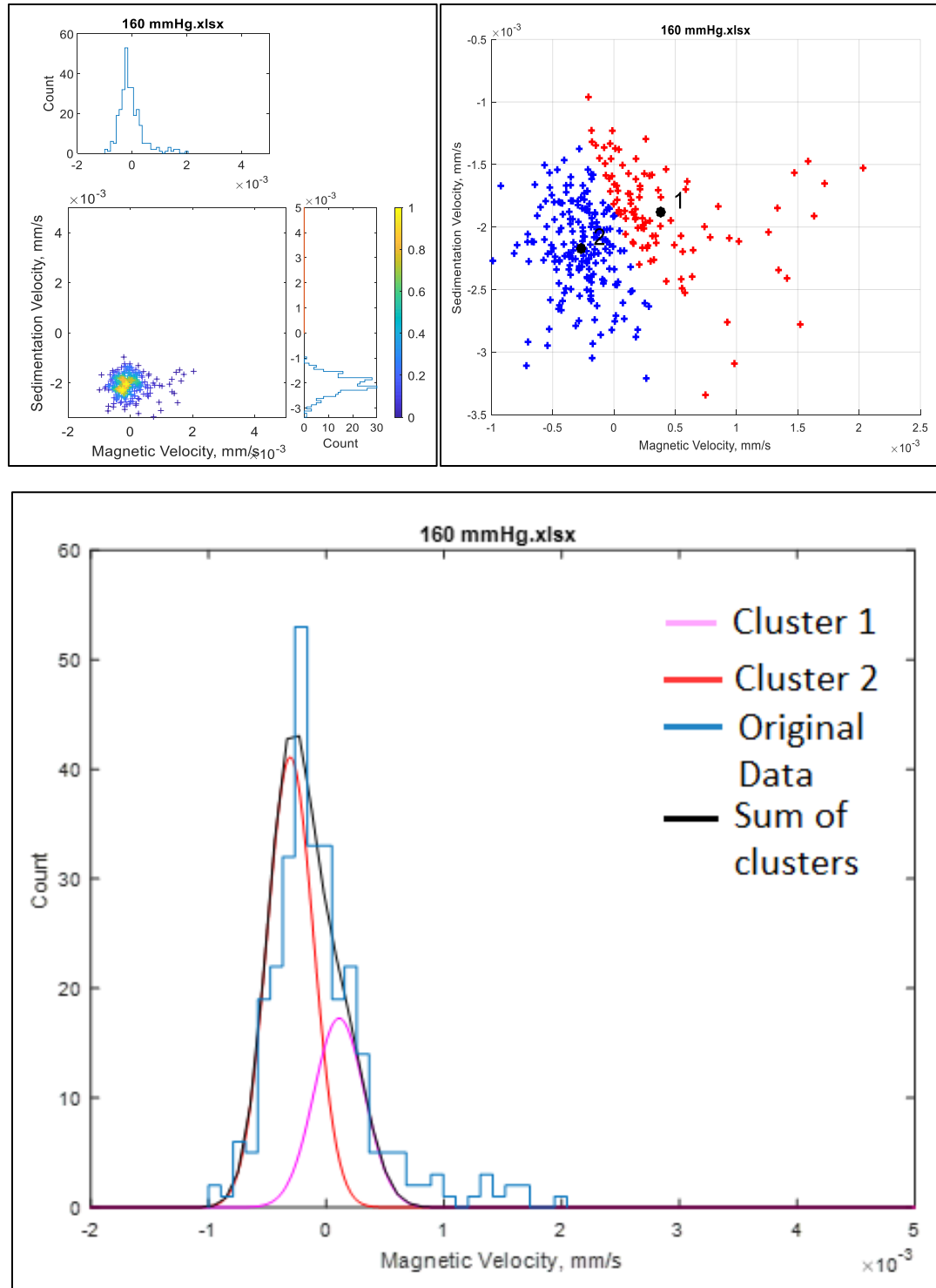


Figure 62: MATLAB graphs generated for 160 mmHg oxygenation level in Experiment #2. Top Left: Whole dataset with histograms. Top Right: Two clusters generated by the k-mean clustering method. Below: Gaussian curves for the k-mean clusters.

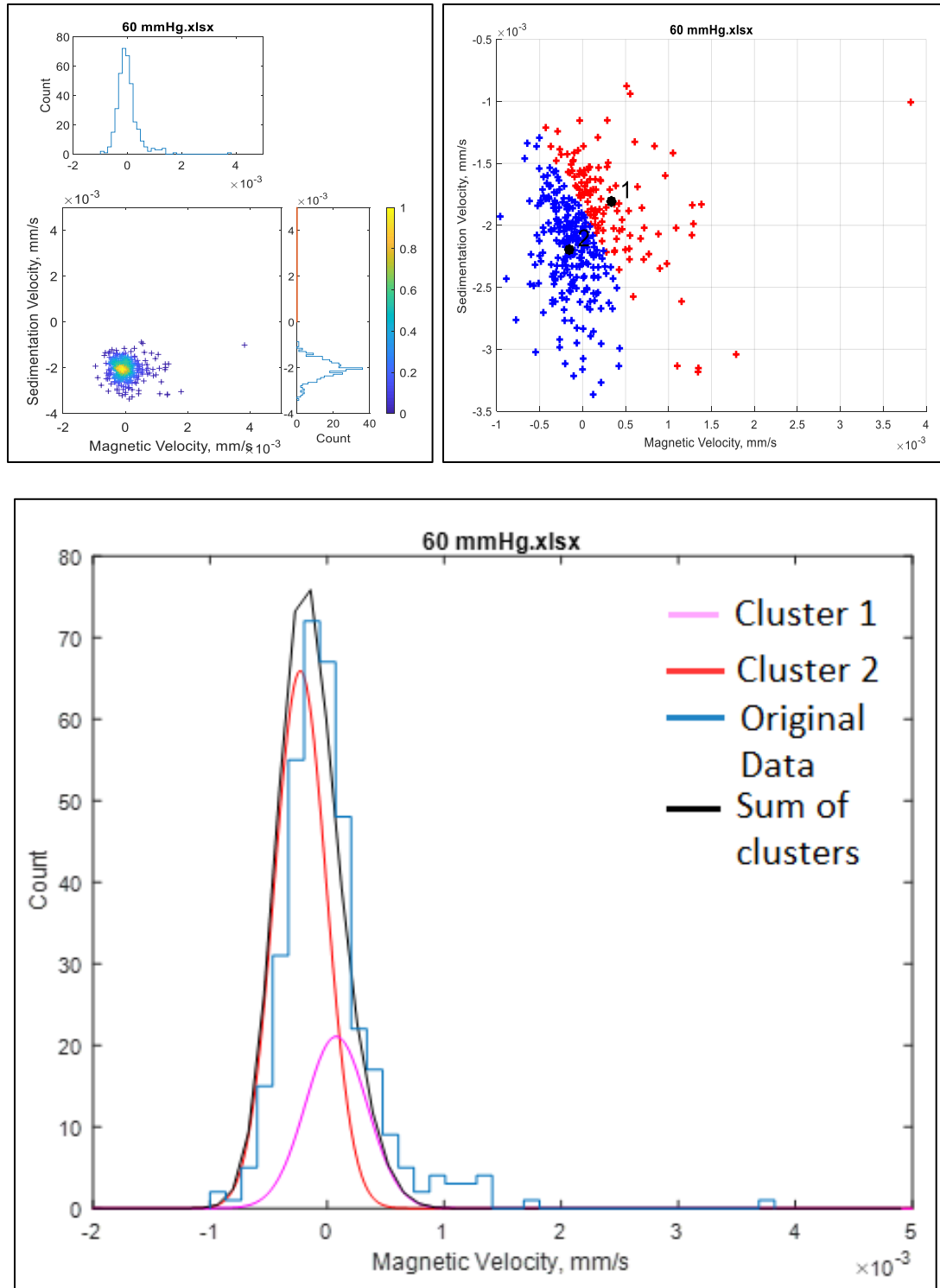


Figure 63: MATLAB graphs generated for 60 mmHg oxygenation level in Experiment #2. Top Left: Whole dataset with histograms. Top Right: Two clusters generated by the k-mean clustering method. Below: Gaussian curves for the k-mean clusters.

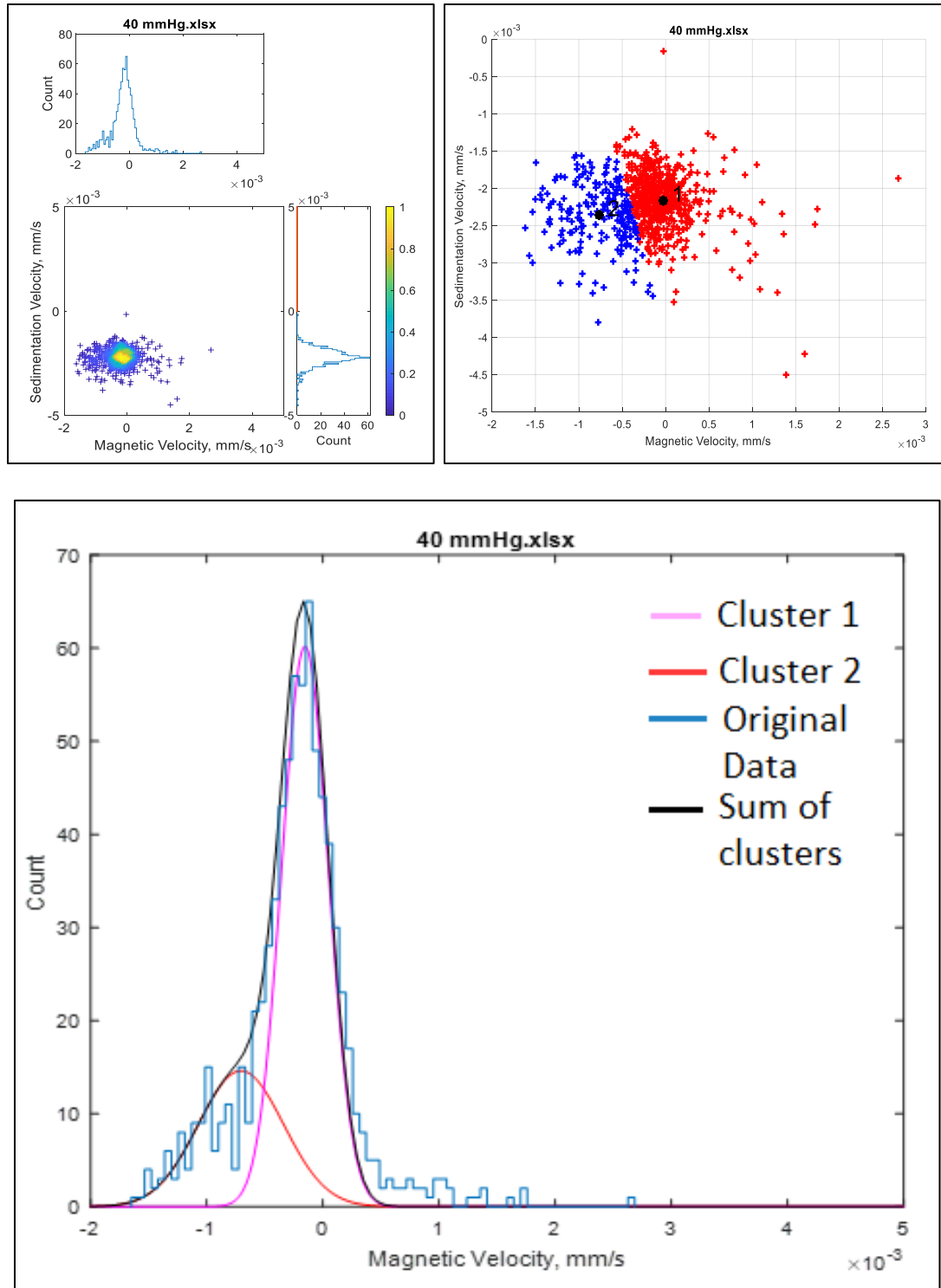


Figure 64: MATLAB graphs generated for 40 mmHg oxygenation level in Experiment #2. Top Left: Whole dataset with histograms. Top Right: Two clusters generated by the k-mean clustering method. Below: Gaussian curves for the k-mean clusters.

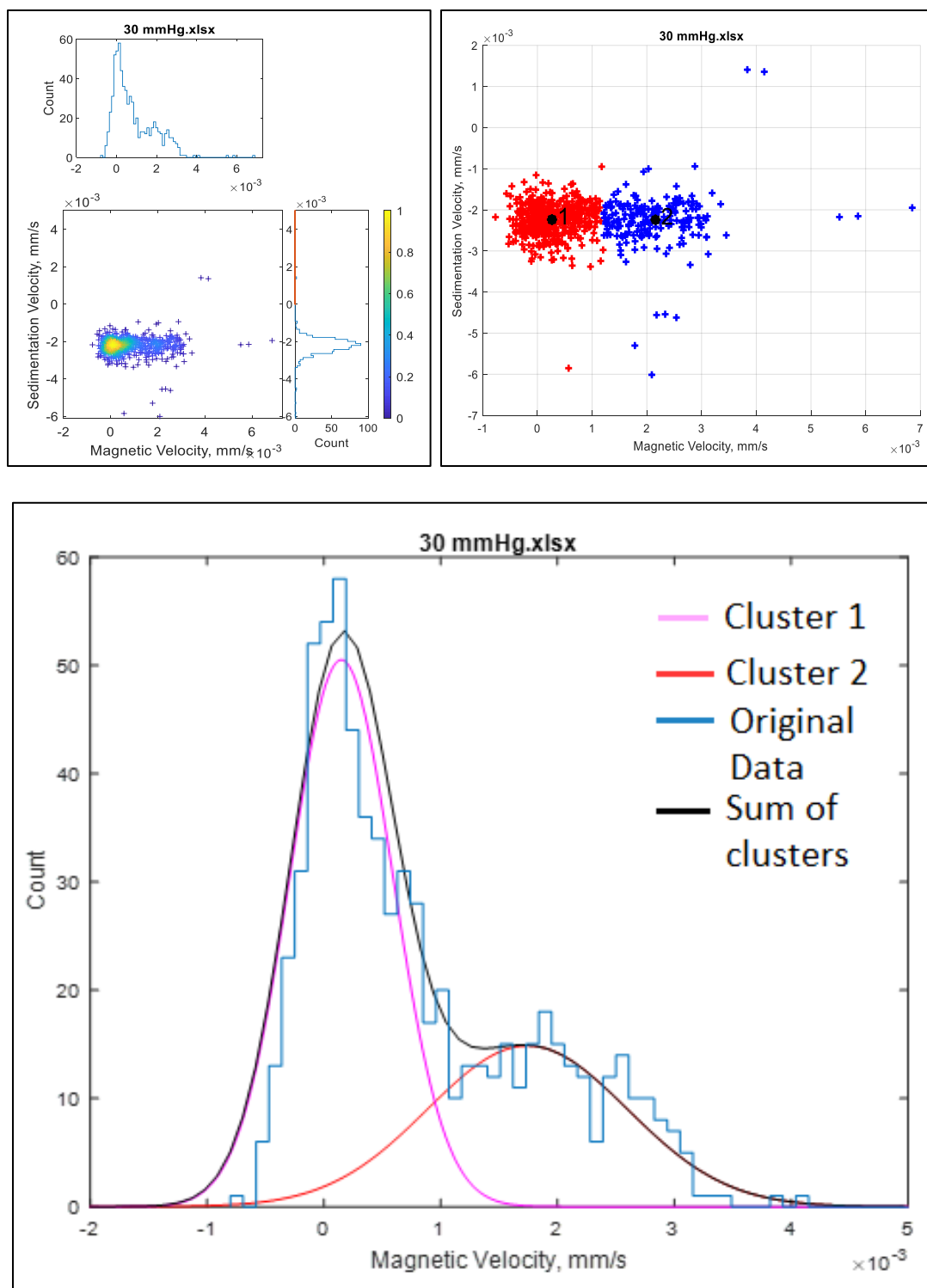


Figure 65 MATLAB graphs generated for 30 mmHg oxygenation level in Experiment #2. Top Left: Whole dataset with histograms. Top Right: Two clusters generated by the k-mean clustering method. Below: Gaussian curves for the k-mean clusters.

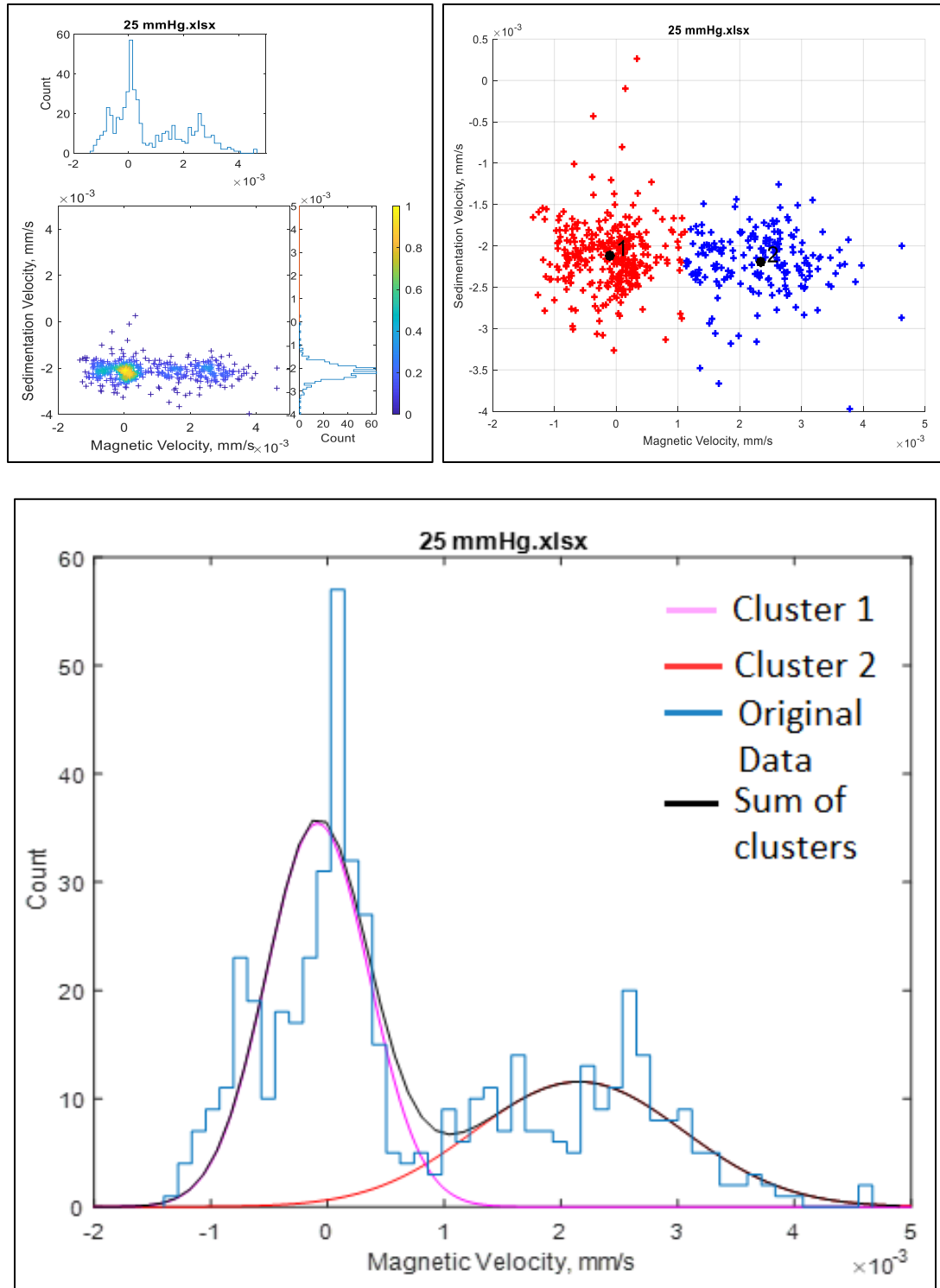


Figure 66 MATLAB graphs generated for 25 mmHg oxygenation level in Experiment #2. Top Left: Whole dataset with histograms. Top Right: Two clusters generated by the k-mean clustering method. Below: Gaussian curves for the k-mean clusters.

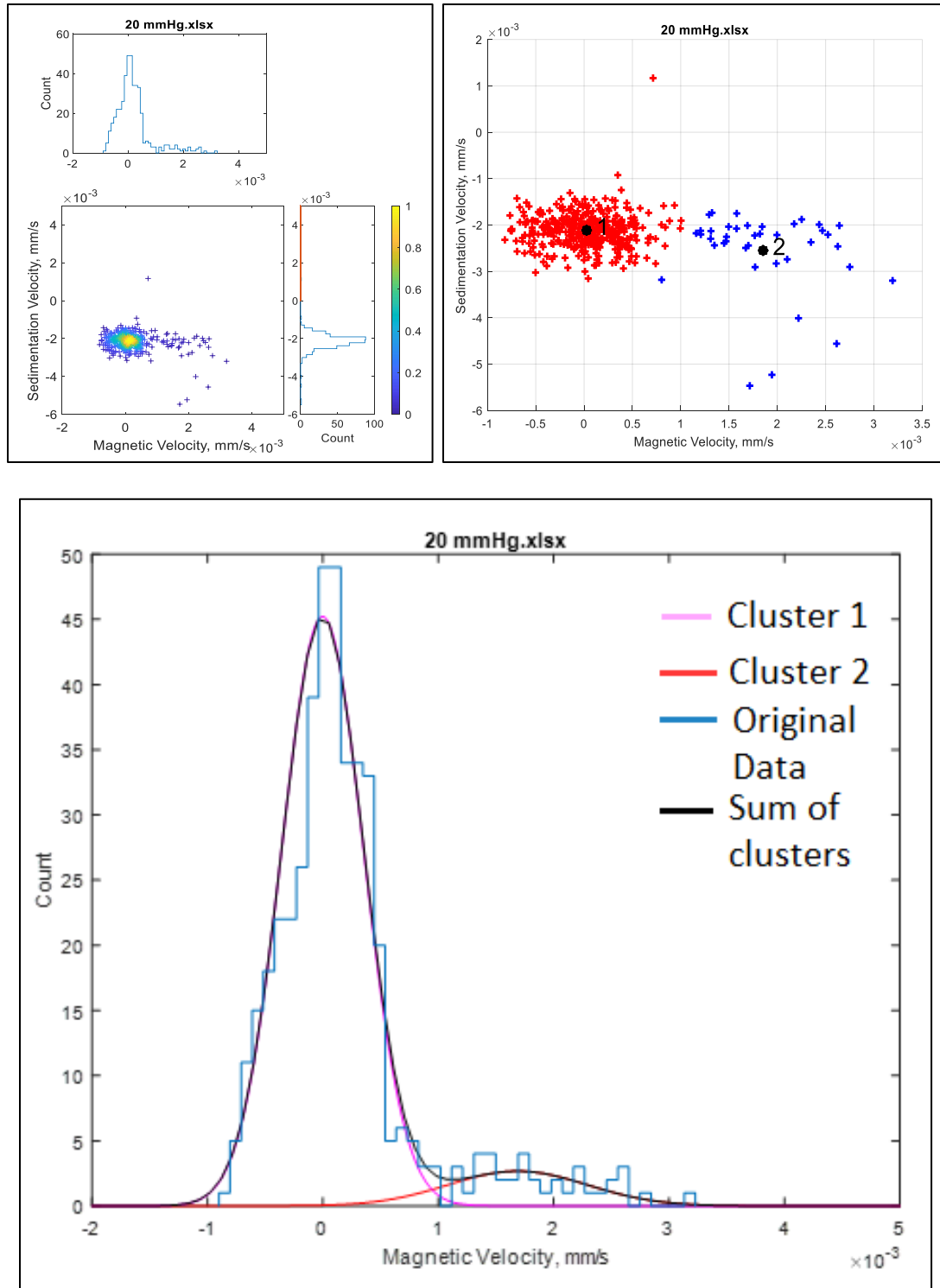


Figure 67: MATLAB graphs generated for 20 mmHg oxygenation level in Experiment #2. Top Left: Whole dataset with histograms. Top Right: Two clusters generated by the k-mean clustering method. Below: Gaussian curves for the k-mean clusters.

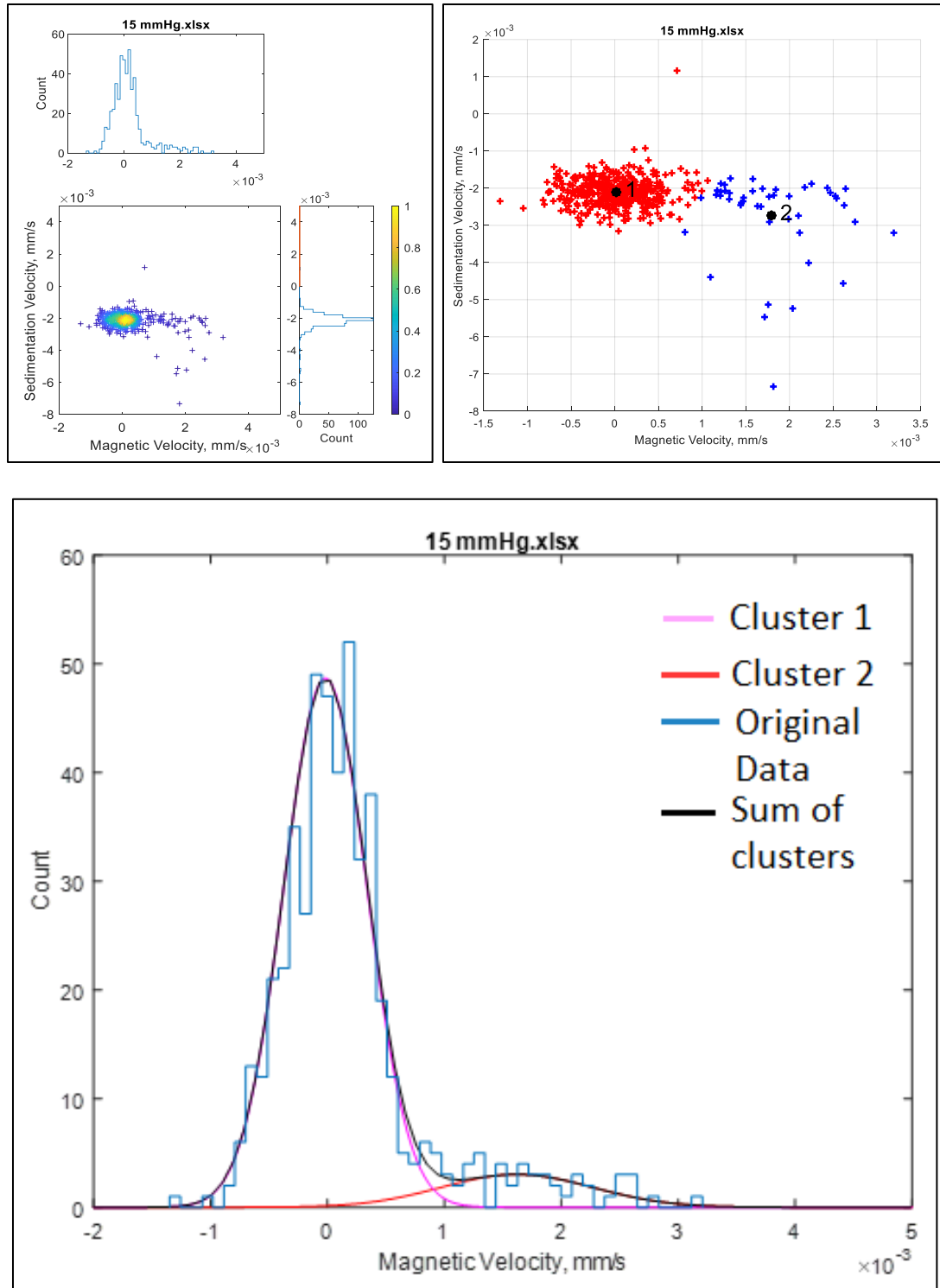


Figure 68: MATLAB graphs generated for 15 mmHg oxygenation level in Experiment #2. Top Left: Whole dataset with histograms. Top Right: Two clusters generated by the k-mean clustering method. Below: Gaussian curves for the k-mean clusters.

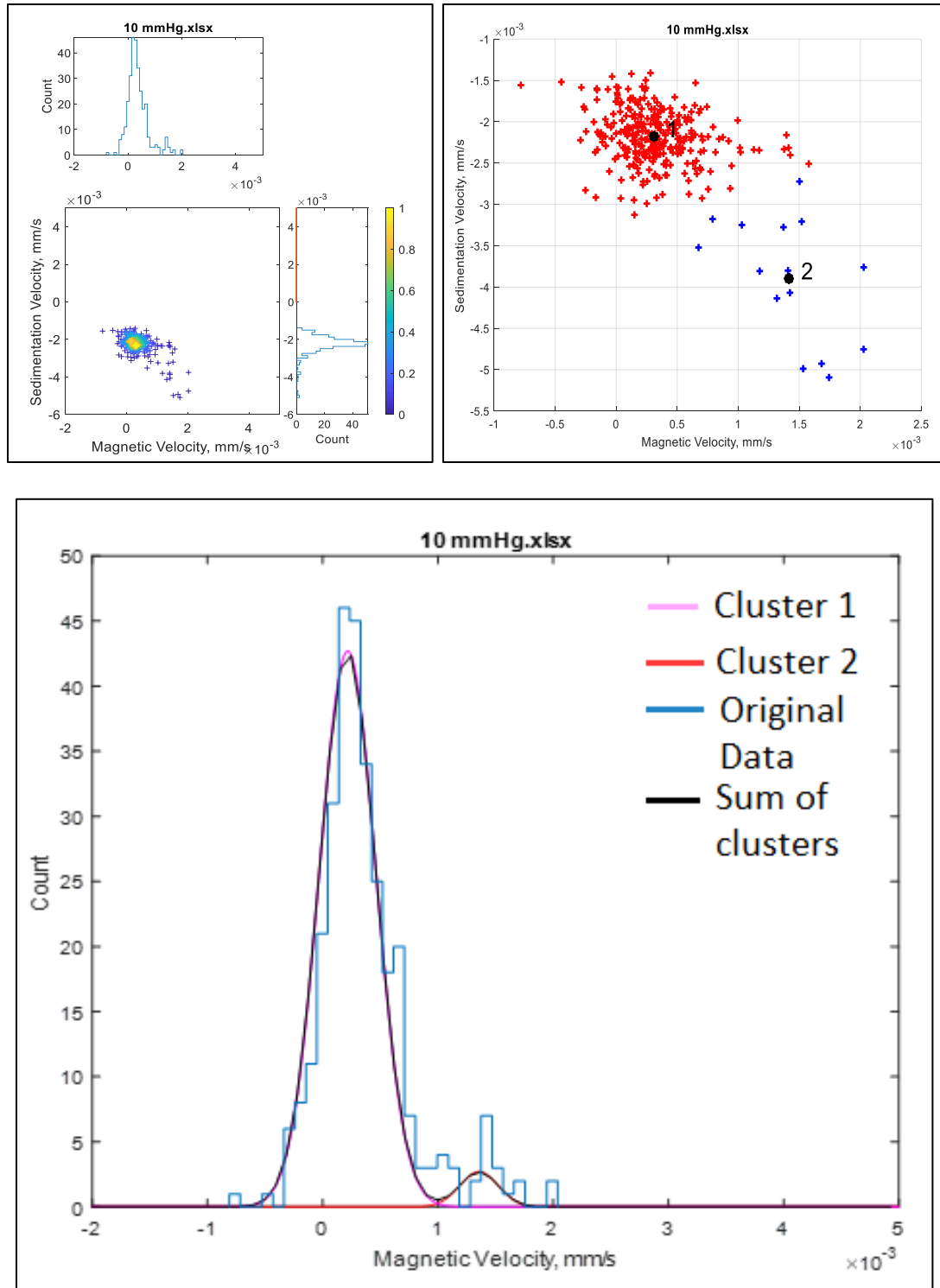


Figure 69: MATLAB graphs generated for 10 mmHg oxygenation level in Experiment #2. Top Left: Whole dataset with histograms. Top Right: Two clusters generated by the k-mean clustering method. Below: Gaussian curves for the k-mean clusters.

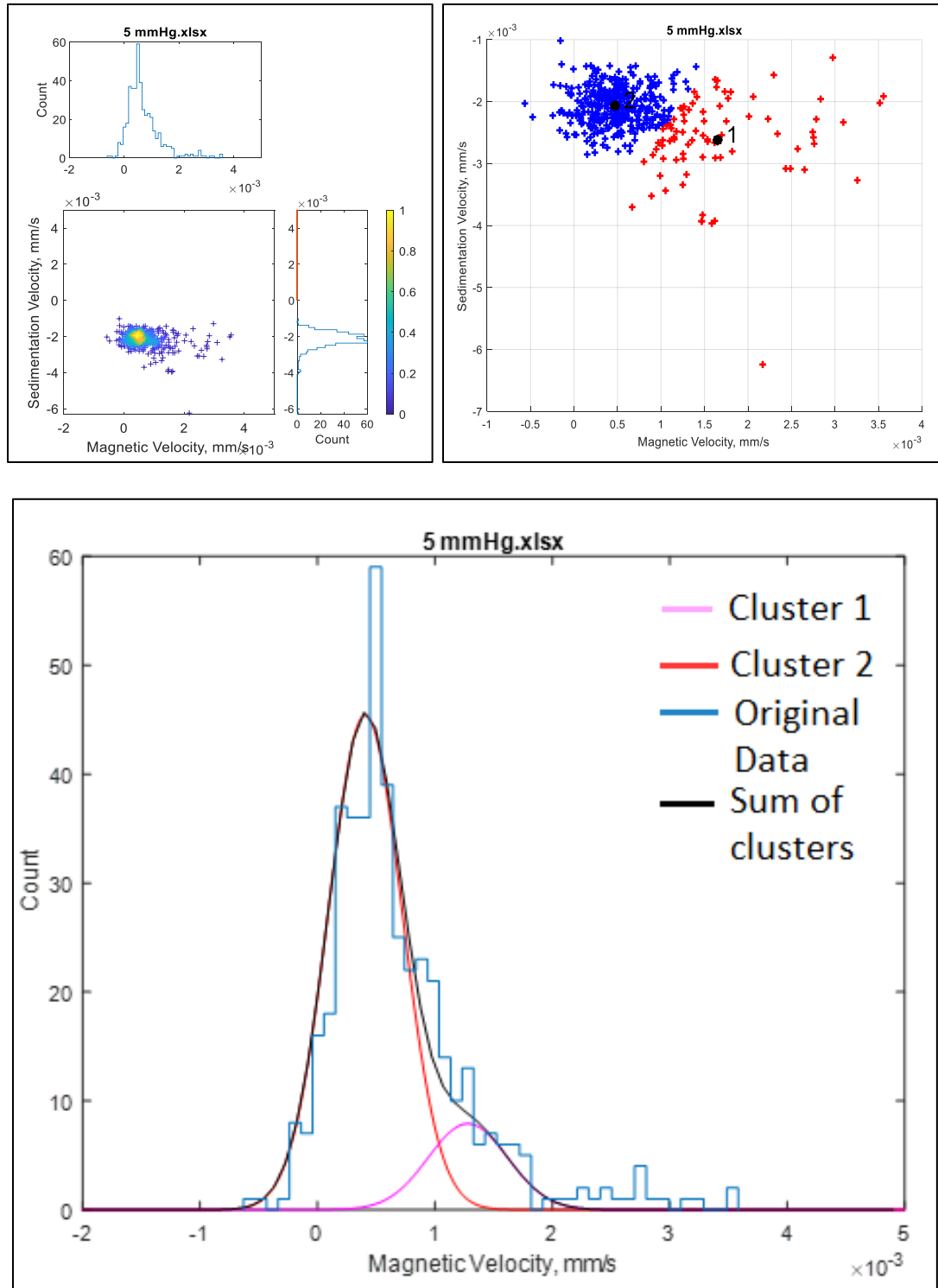


Figure 70: MATLAB graphs generated for 5 mmHg oxygenation level in Experiment #2. Top Left: Whole dataset with histograms. Top Right: Two clusters generated by the k-mean clustering method. Below: Gaussian curves for the k-mean clusters.

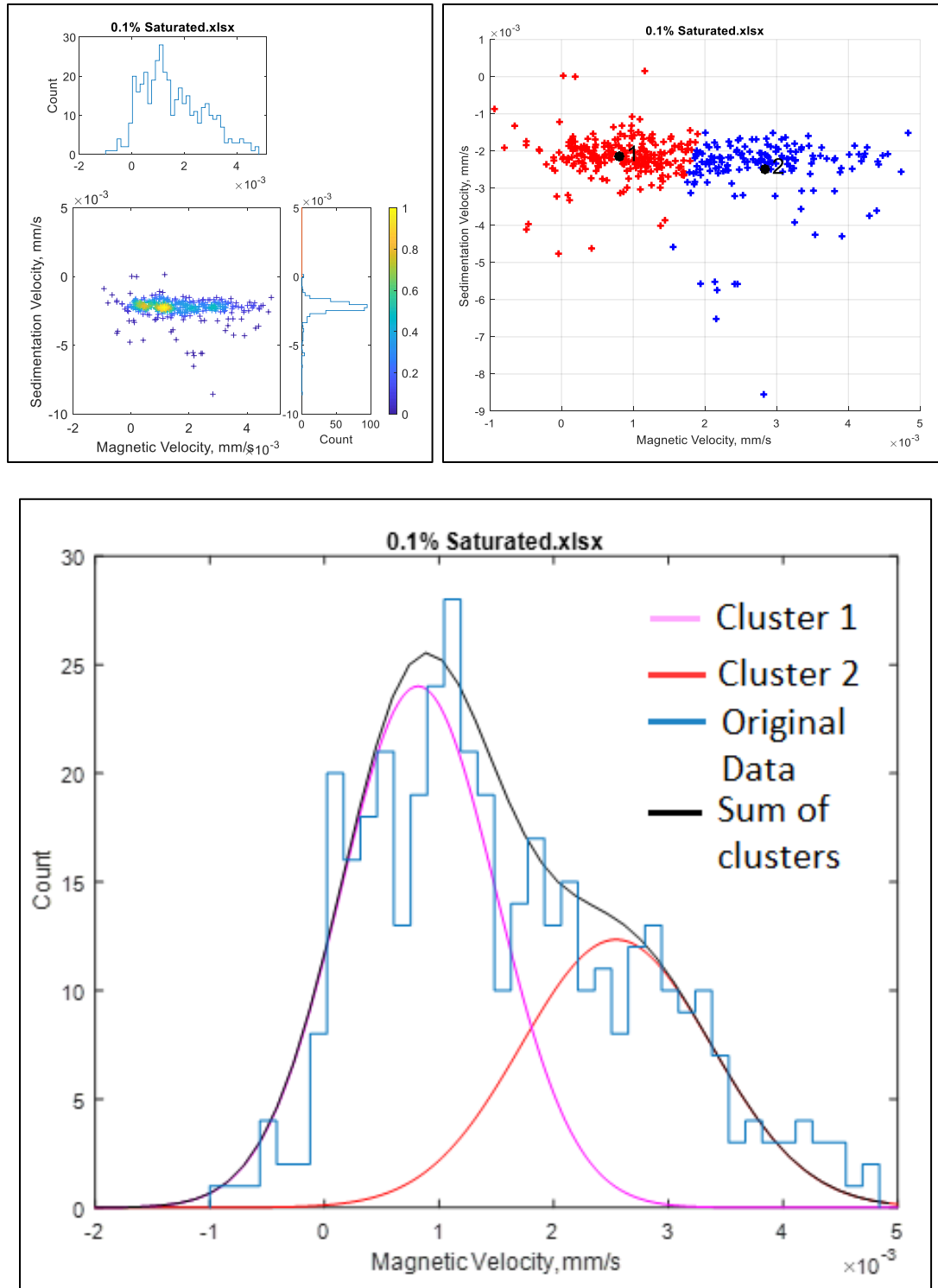


Figure 71: MATLAB graphs generated for 0.1% O_2 oxygenation level in Experiment #2. Top Left: Whole dataset with histograms. Top Right: Two clusters generated by the k-mean clustering method. Below: Gaussian curves for the k-mean clusters.

4.3.2 Gaussian Fit Results Compared to the Hill Equation

Once each oxygenation level was evaluated through MATLAB, the Gaussian coefficients generated for the two clusters, specified by the k-mean clustering method, were utilized to create six graphs per experiment. The first graph, Figure 72, is the magnetic velocity mode values in mm/s (b gaussian coefficients) versus the partial pressure of O₂ for Gaussian 1 for Experiment #1, with error bars representing the standard deviation. Figure 73 is the same plot; however, it represents the values for Gaussian 2. As mentioned before, Gaussian 1 is comprised of the clusters with b-values closest to zero, which varied in cluster from oxygenation level to oxygenation level. This convention for Gaussian 1 and 2 is represented in Figures 72 and 73. Gaussian 1 does not have a b-value higher than about 1.5×10^{-3} mm/s, whereas Gaussian 2's highest b-value was around 3.5×10^{-3} mm/s. The same graphs for Experiment #2 are in Figures 74 and 75.

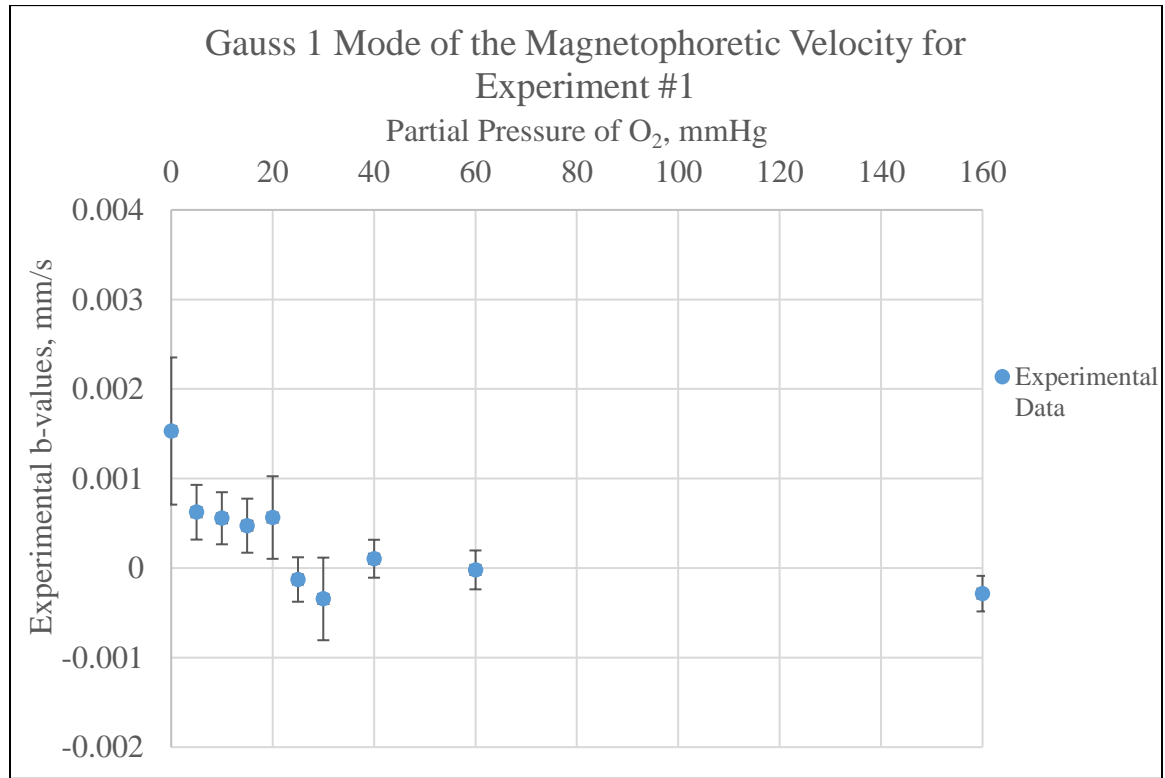


Figure 72: Gaussian 1 magnetophoretic velocity mode for Experiment #1.

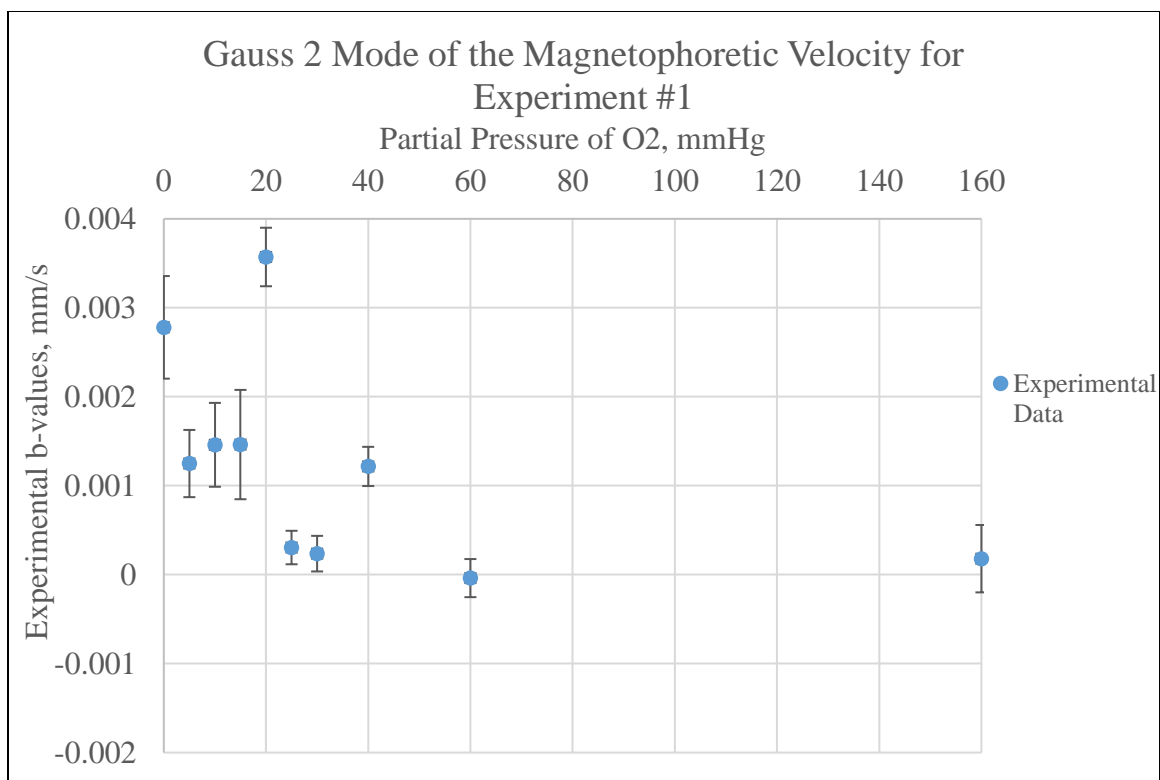


Figure 73: Gaussian 2 magnetophoretic velocity mode for Experiment #1.

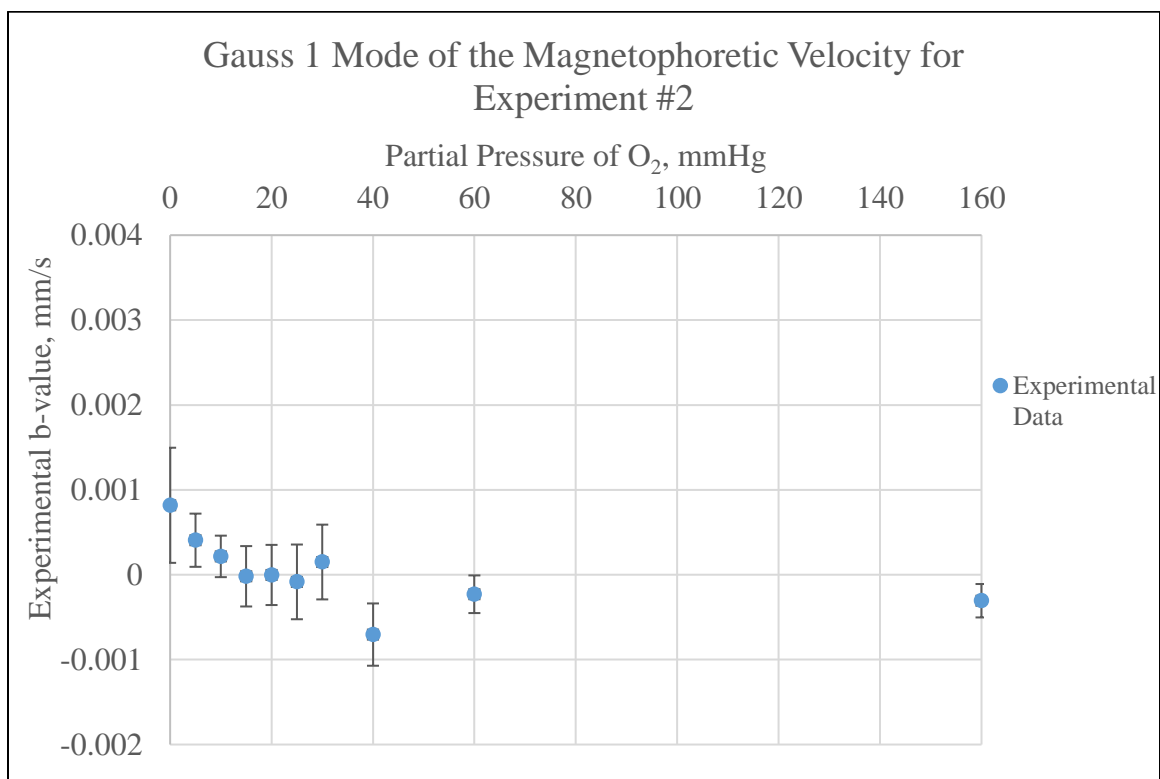


Figure 74: Gaussian 1 magnetophoretic velocity mode for Experiment #2.

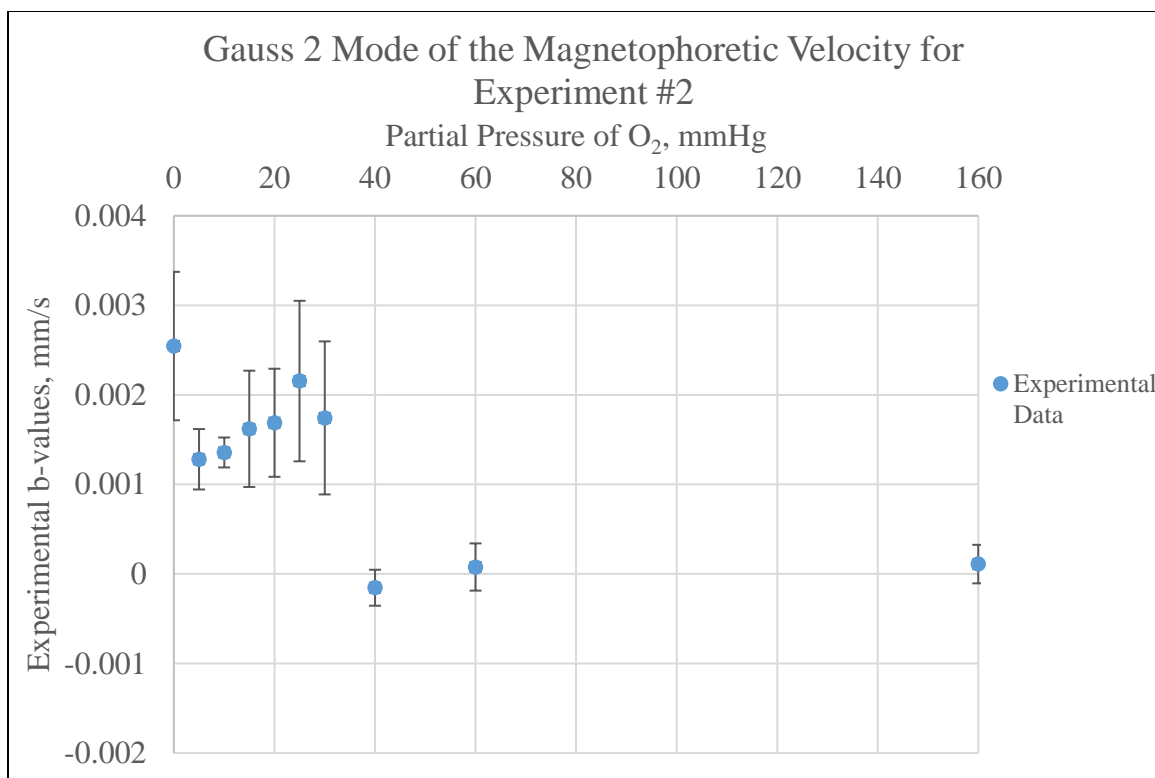


Figure 75: Gaussian 2 magnetophoretic velocity mode for Experiment #2.

The next graph produced with the MATLAB gaussian coefficients was the normalized b-values versus partial pressure of O₂, along with the Hill equation curve fitted for the experimental data. The fitted curve was generated through the ‘Regression’ option within the ‘Data Analysis’ section of Excel to obtain the slope (n) and intercept (k). Also, a linear regression of the $\log(Z)$ values versus the $\log(x)$ values calculated from Equations 3.10 and 3.13 were made through the ‘Regression’ option. Figures 76 and 77 represent the data in Gauss 1 for Experiment #1, while Figures 78 and 79 are the same graphs, but for the data within Gauss 2 in Experiment #1. The corresponding graphs for Experiment #2 are Figures 80 – 83.

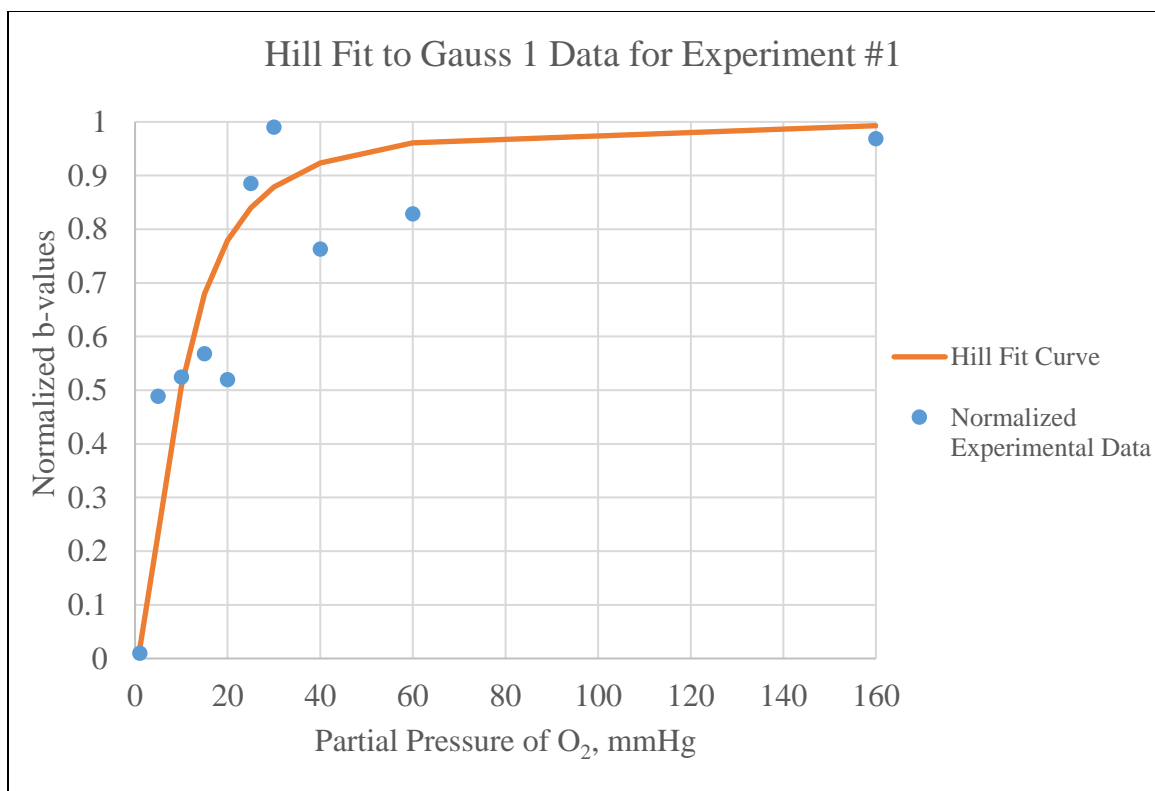


Figure 76: Hill curve for the Gauss 1 data for Experiment #1. Normalized experimental b-values graphed with a fitted Hill curve generated by the regression of the experimental values

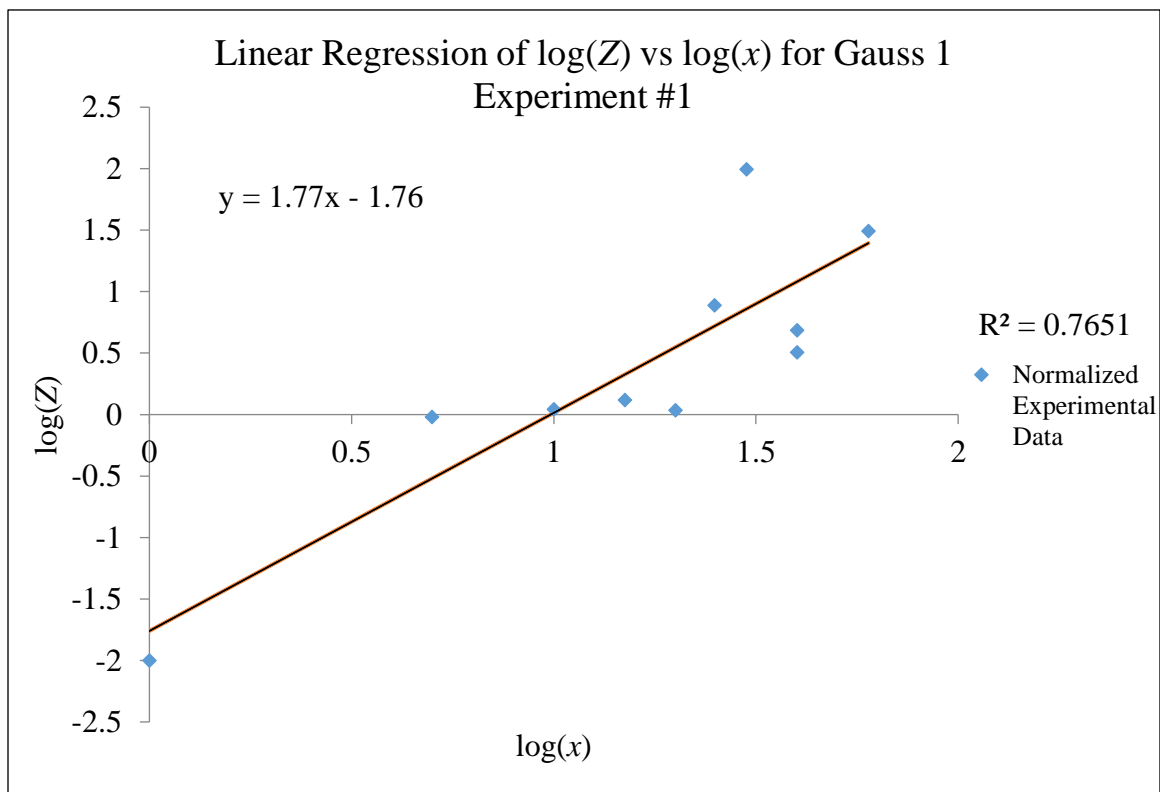


Figure 77: Linear regression of Gauss 1 data for Experiment #1. Regression was completed for the normalized log(Z) and log(x) experimental values.

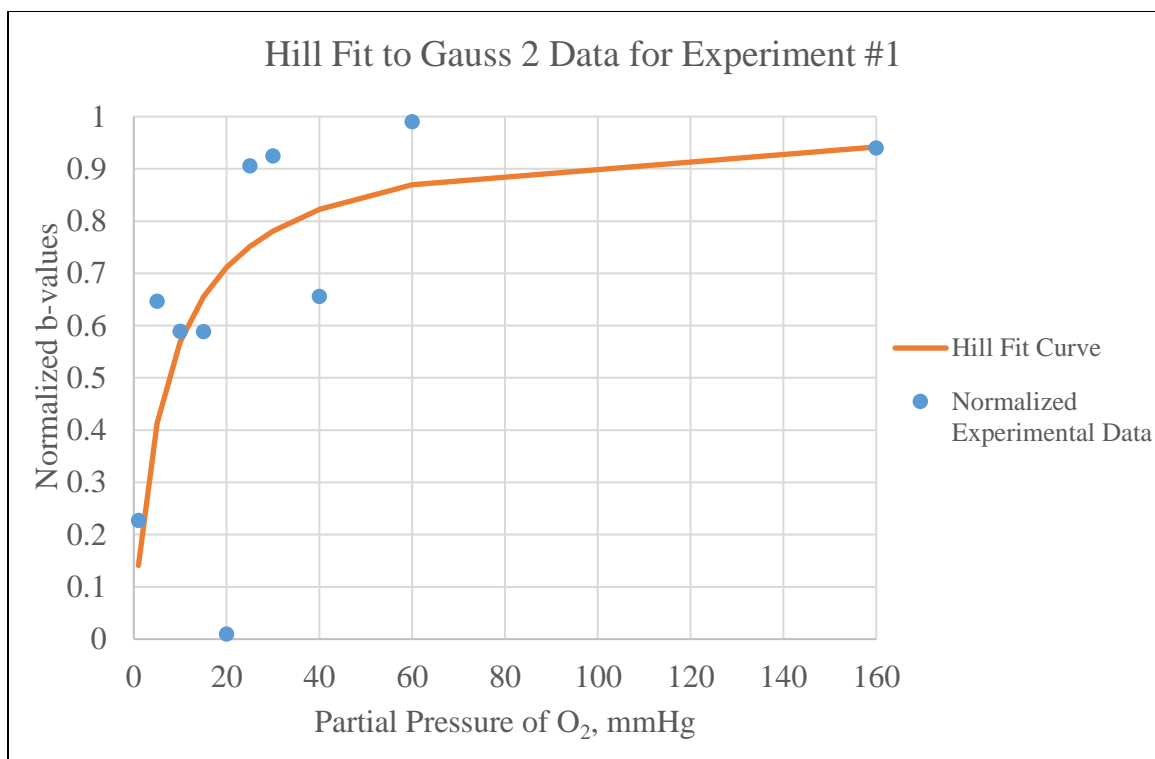


Figure 78: Hill curve for the Gauss 2 data for Experiment #1. Normalized experimental b-values graphed with a fitted Hill curve generated by the regression of the experimental values.

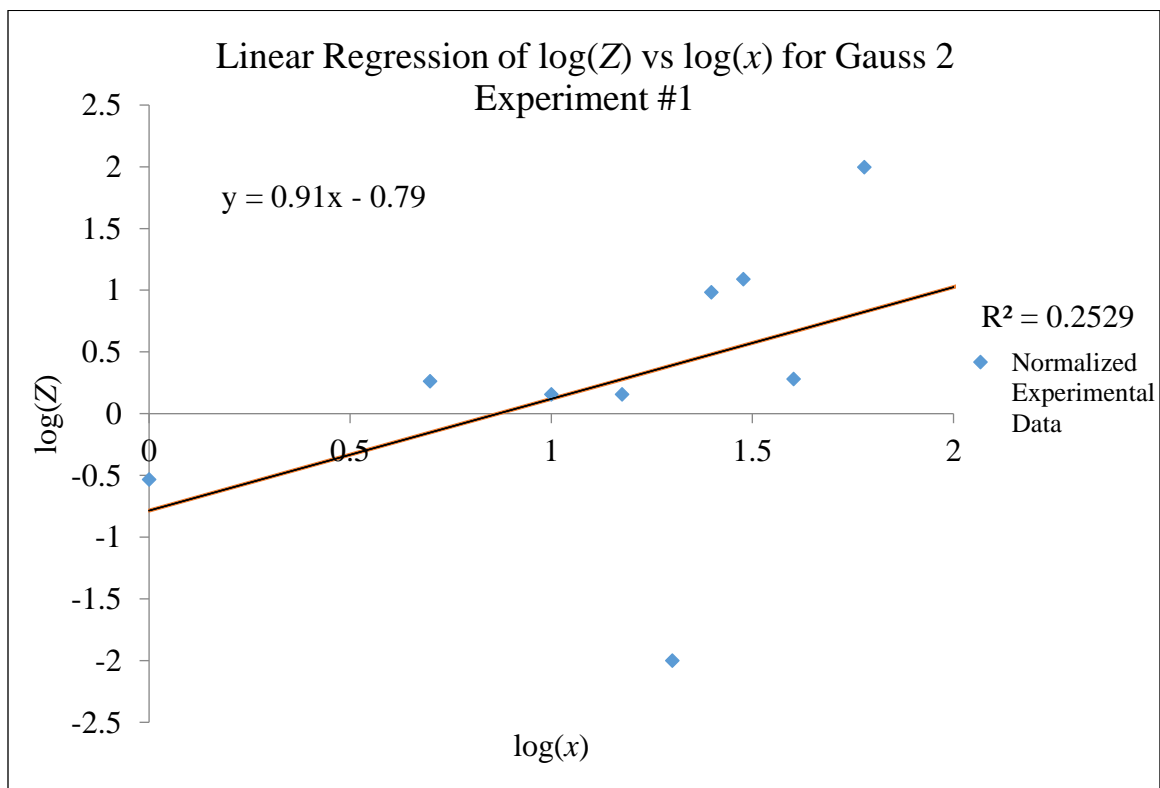


Figure 79: Linear regression of Gauss 2 data for Experiment #1. Regression was completed for the normalized $\log(Z)$ and $\log(x)$ experimental values.

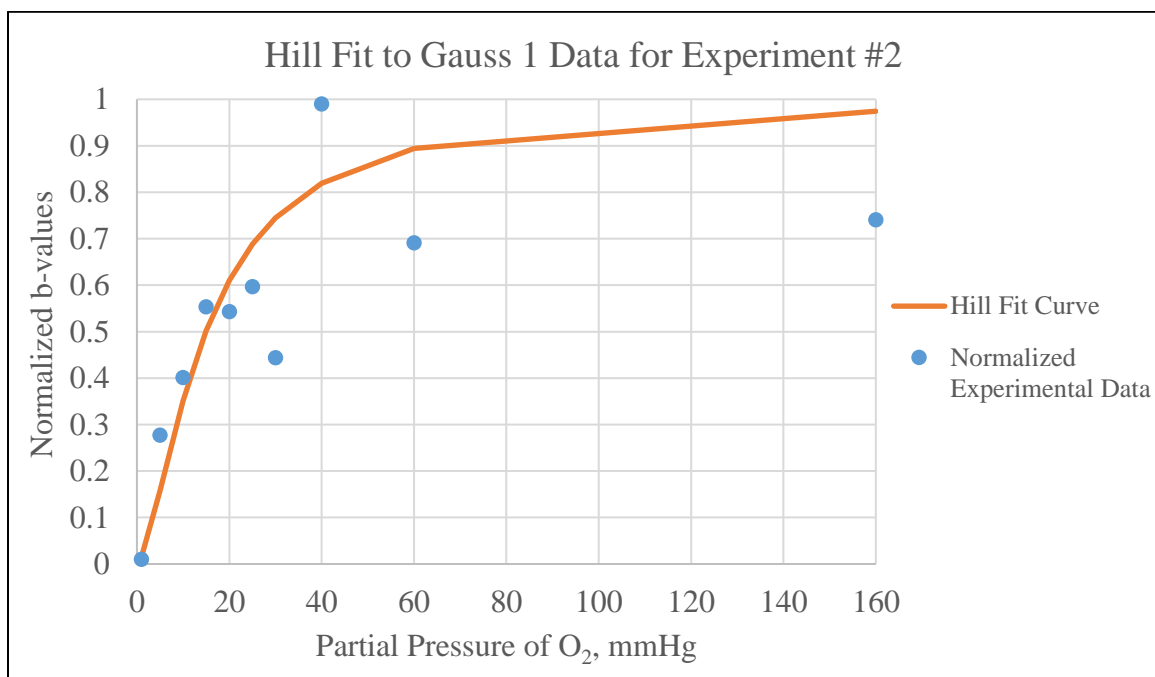


Figure 80: Hill curve for the Gauss 1 data for Experiment #2. Normalized experimental b-values graphed with a fitted Hill curve generated by the regression of the experimental values

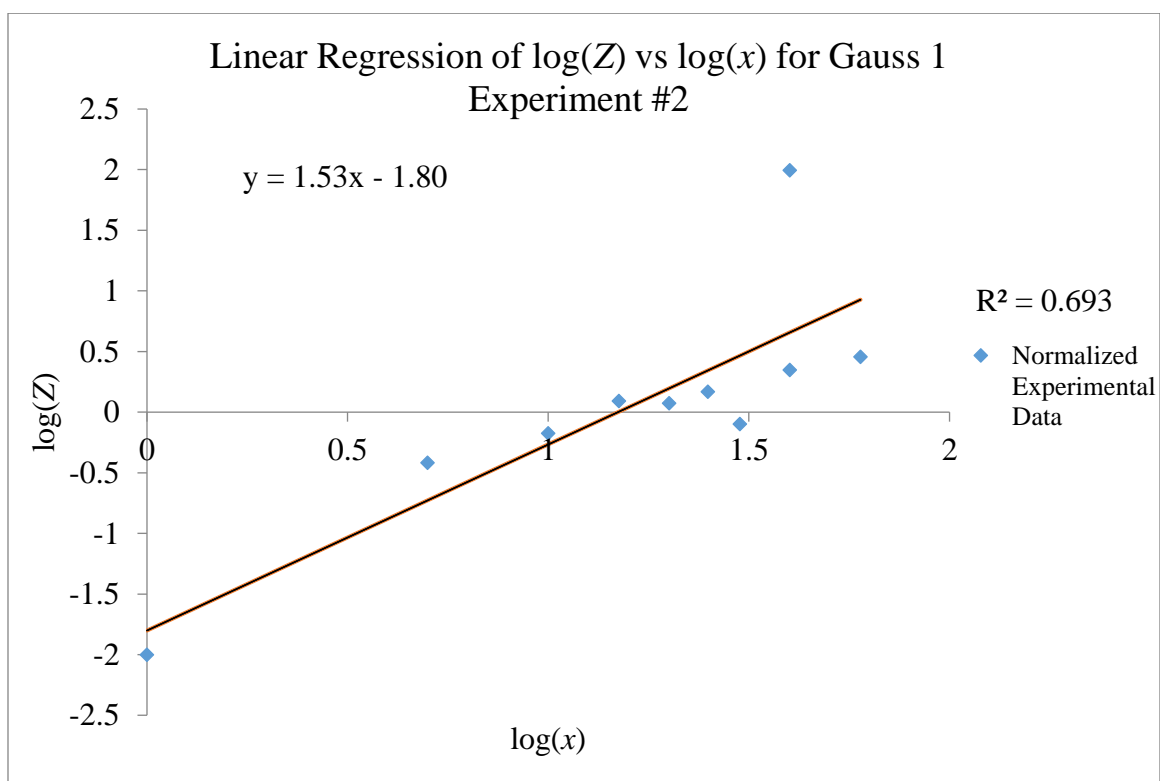


Figure 81: Linear regression of Gauss 1 data for Experiment #2. Regression was completed for the normalized $\log(Z)$ and $\log(x)$ experimental values.

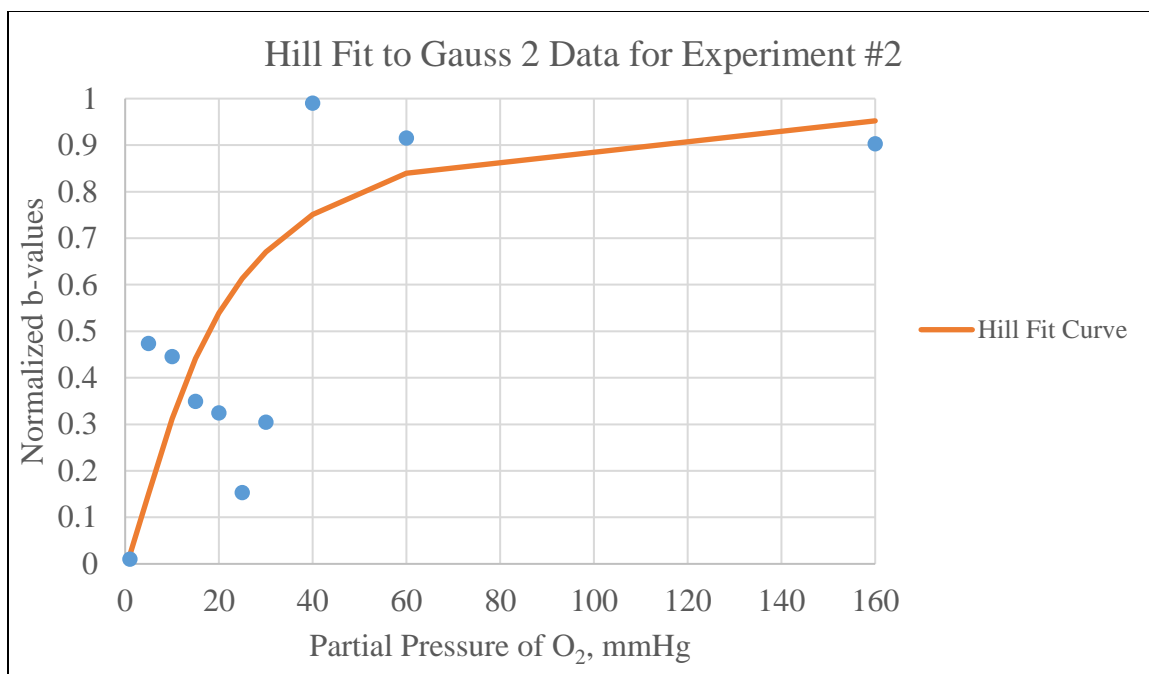


Figure 82: Hill curve for the Gauss 2 data for Experiment #2. Normalized experimental b-values graphed with a fitted Hill curve generated by the regression of the experimental values.

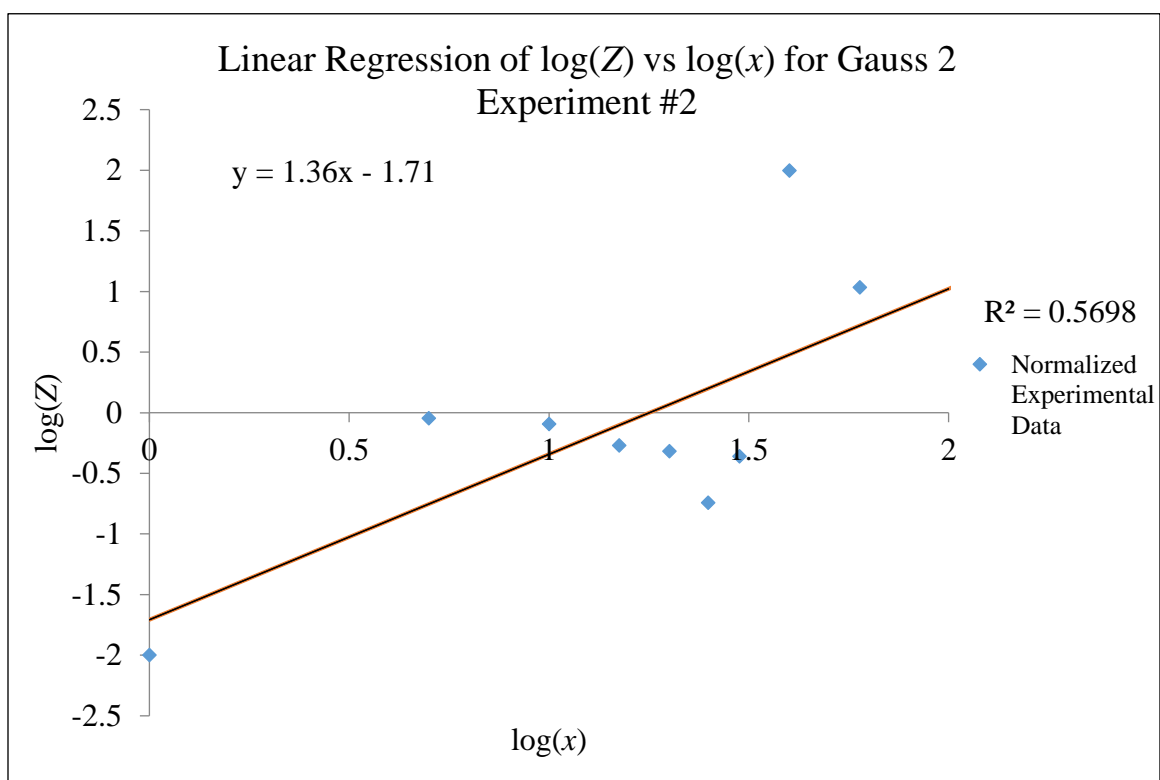


Figure 83: Linear regression of Gauss 2 data for Experiment #2. Regression was completed for the normalized $\log(Z)$ and $\log(x)$ experimental values.

The specific values from these graphs, which are important in determining whether the Hill equation is a representative model for the deoxygenation of RBC experiments, are the slope (n) and intercepts (k) for the linear regression graphs, Figures 77, 79, 81, and 83. These values for Experiments 1 and 2 are summarized in Table VII below. Compared to common practice of setting $n = 2.7$ in literature, the values obtained through experiments, found in Table VII, were on average 65.53% lower.

Table VII: Regression line information for both Gaussians in Experiments 1 and 2.

Regression Line Slope and Intercept Information					
Experiment	Gaussian	Slope, n	Intercept, k	Slope P Value	Intercept P Value
1	1	1.77 ± 0.35	-1.76 ± 0.45	9.2×10^{-4}	4.6×10^{-3}
	2	0.91 ± 0.55	-0.79 ± 0.76	0.14	0.33
2	1	1.53 ± 0.36	-1.8 ± 0.47	2.8×10^{-3}	5.0×10^{-3}
	2	1.36 ± 0.41	-1.71 ± 0.58	0.01	0.02

4.4 Results for Glioma Experiments

The specific aim for the glioma experiments was to determine the magnetic properties of the GL261 cell cultures provided by Dr. Justin Lathia's lab at the Cleveland Clinic, and to validate the CTV data post-processing capabilities utilized in the deoxygenation of RBCs. First, the RPMI media was evaluated to determine if it possessed any magnetic properties. Then, cytosmeareds were created to image the cells. Next, the magnetophoretic mobility was analyzed through CTV, and lastly, the ability to isolate CSCs was explored with MDM.

To ensure the RPMI media did not present magnetic properties, and the magnetic susceptibility was similar to that of water, the mean magnetic susceptibility values measured with the MSB-Auto were compared through a t-Test assuming unequal variances

for the means. The results from the t-Test between RPMI and MilliQ water are displayed in Table VIII and the results from RPMI and distilled water are in Table IX.

Table VIII: Results of the t-Test between RPMI media and MilliQ water to determine how similar the magnetic susceptibilities are between the two with five measurements for each.

t-Test: Two-Sample Assuming Unequal Variances		
Statistical Parameter	χ of RPMI Media	χ of MilliQ Water
Mean	-9.31×10^{-6}	-9.32×10^{-6}
t Stat	0.047	
t Critical two-tail	2.57	

Table IX: Results of the t-Test between RPMI media and distilled water to determine how similar the magnetic susceptibilities are between the two with five measurements for each.

t-Test: Two-Sample Assuming Unequal Variances		
Statistical Parameter	χ of RPMI Media	χ of Distilled Water
Mean	-9.31×10^{-6}	-9.10×10^{-6}
t Stat	-0.73	
t Critical two-tail	2.78	

Upon reviewing the results of the statistical analysis, the t-stat value between RPMI and MilliQ water is 0.047, which is between the positive and negative values of the t-critical two-tail values, -2.571 and 2.571. Also, the t-stat value for RPMI and distilled water, -0.726, is between -2.776 and 2.776, t-critical two-tail values. This information indicates that the RPMI media does not have magnetic properties.

Due to time constraints of this project, none of the PFA fixed slides generated through cytospin and MDM were fluorescently stained to be imaged. However, four cytosmears created utilizing HEMA fixative were imaged, which are displayed in Figures 84-87. All the images were taken utilizing the same microscope within the ImageCore at the Cleveland Clinic LRI, at the same magnification of 40 \times with a 15 μ m scale bar in the bottom right corner.

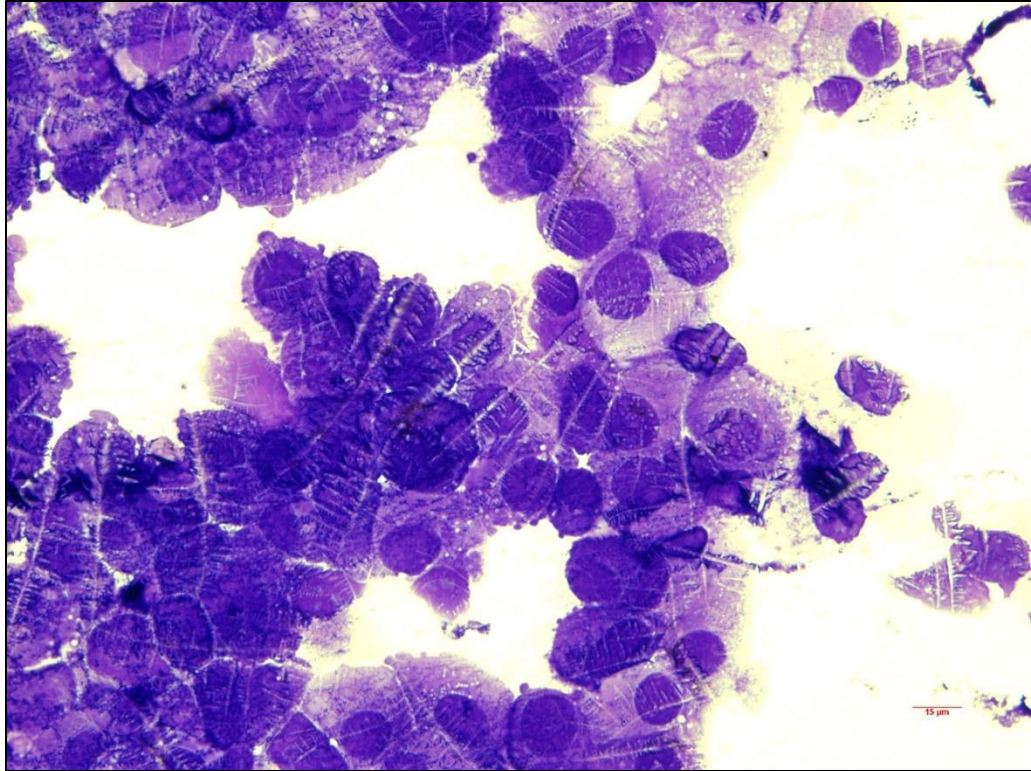


Figure 84: Image of GL261 fixed with HEMA solution, imaged at 40× magnification on November 19, 2018.

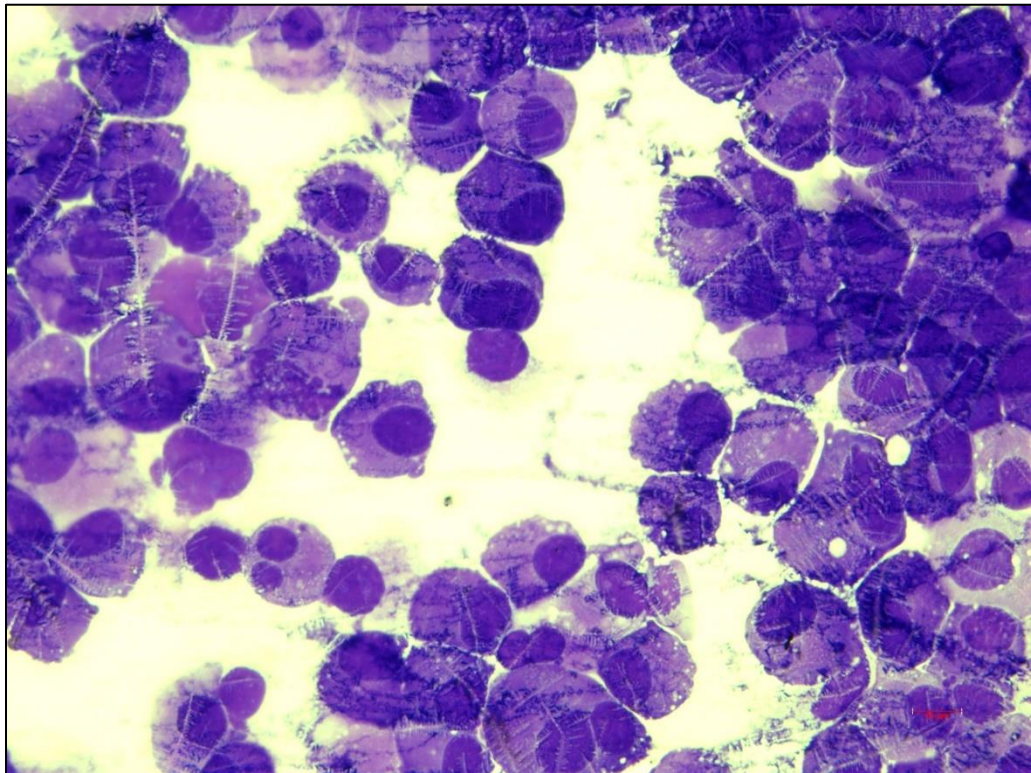


Figure 85: Image of GL261 fixed with HEMA solution, imaged at 40× magnification on November 30, 2018.

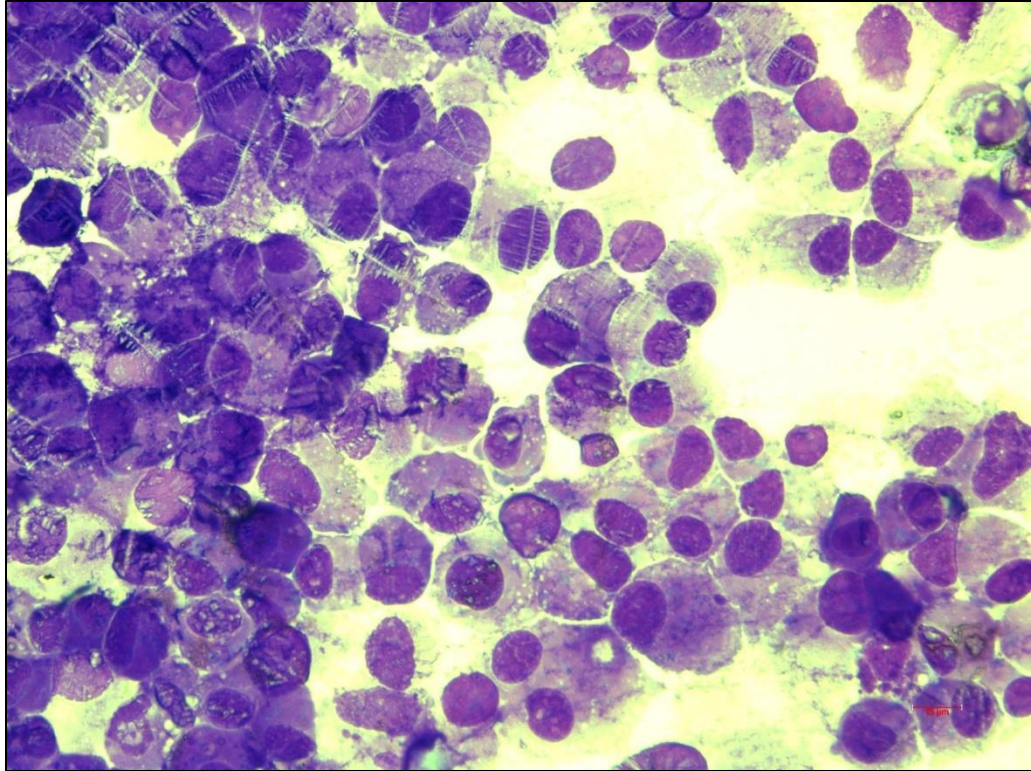


Figure 86: Image of GL261 fixed with HEMA solution, imaged at 40× magnification on December 5, 2018.

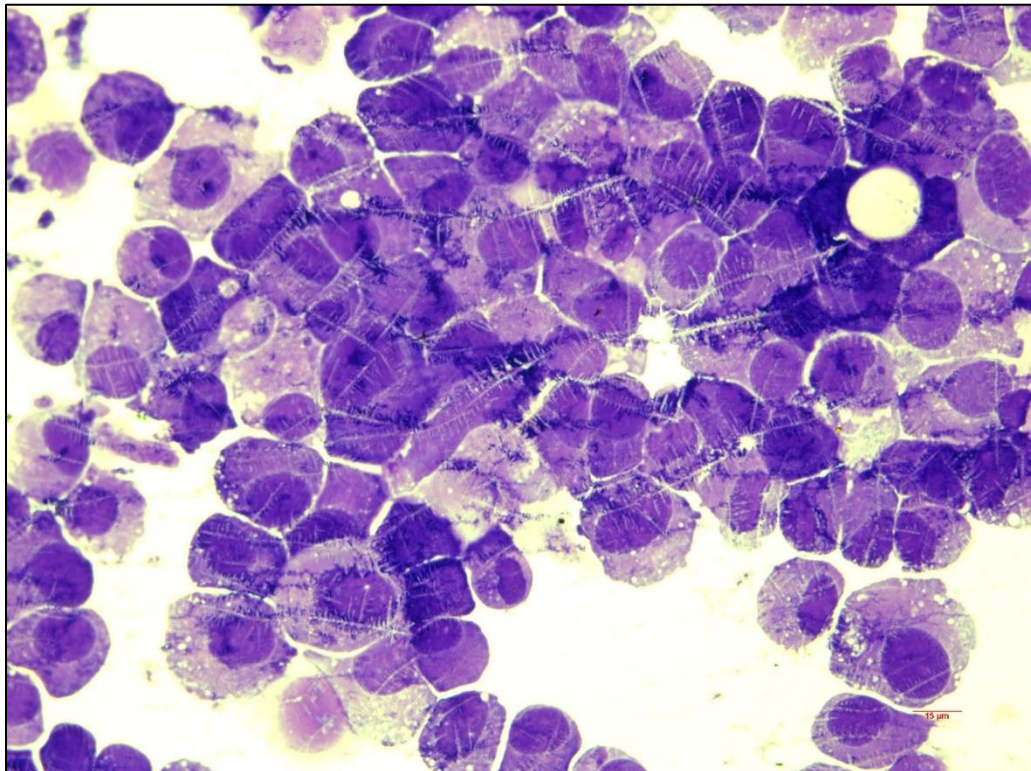


Figure 87: Image of GL261 fixed with HEMA solution, imaged at 40× magnification on December 14, 2018.

As mentioned in Section 3.5.2, the procedure for analyzing the CTV results for the glioma experiments followed the same procedure as the analysis for the deoxygenation experiments. A total of 12 glioma experiments were completed for the GL261 and 3T3 cultures, and were analyzed with the MATLAB program found in Appendix B. These 12 experiments were analyzed utilizing the k-mean clustering concept described in Section 3.4.6 to differentiate bands of cells within a sample. Each experiment was run through the MATLAB code two or three times with modifying the code to have the data be split into two clusters and three clusters. Results from experiments completed on December 5th and 20th, 2018 for GL261 are presented below in Figures 88 – 91. As seen in Figures 89 and 91, the MATLAB code can differentiate between two subsets of cells within a sample. The remainder of the results are in Appendix C.

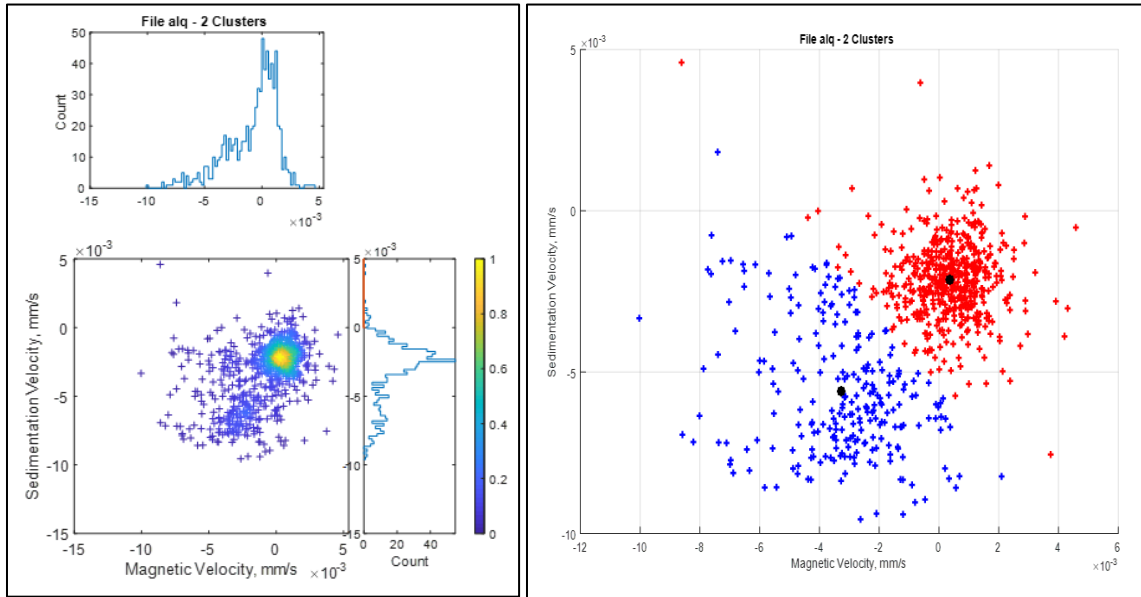


Figure 88: Left: Scatter plot of original data obtained December 5, 2018. Right: Scatter plot of original data split into two clusters.

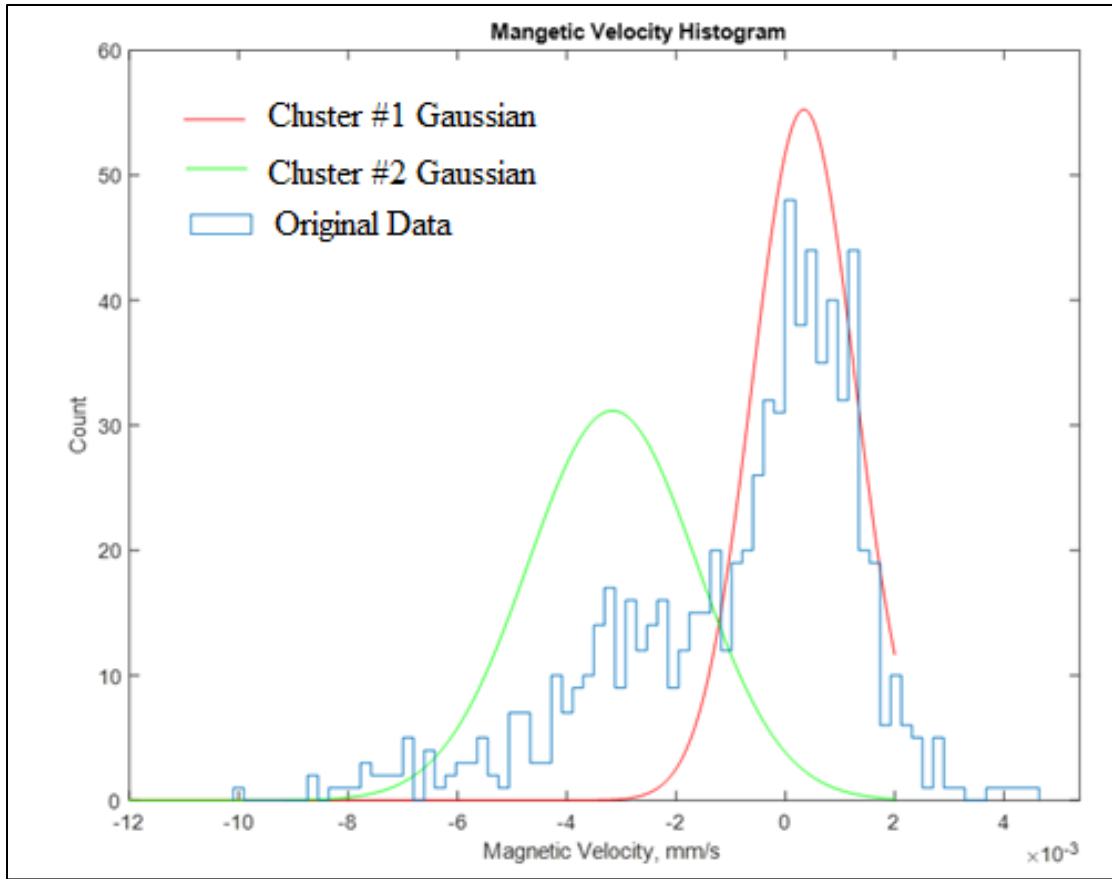


Figure 89: Gaussian plot of the two clusters presented in Figure 88.

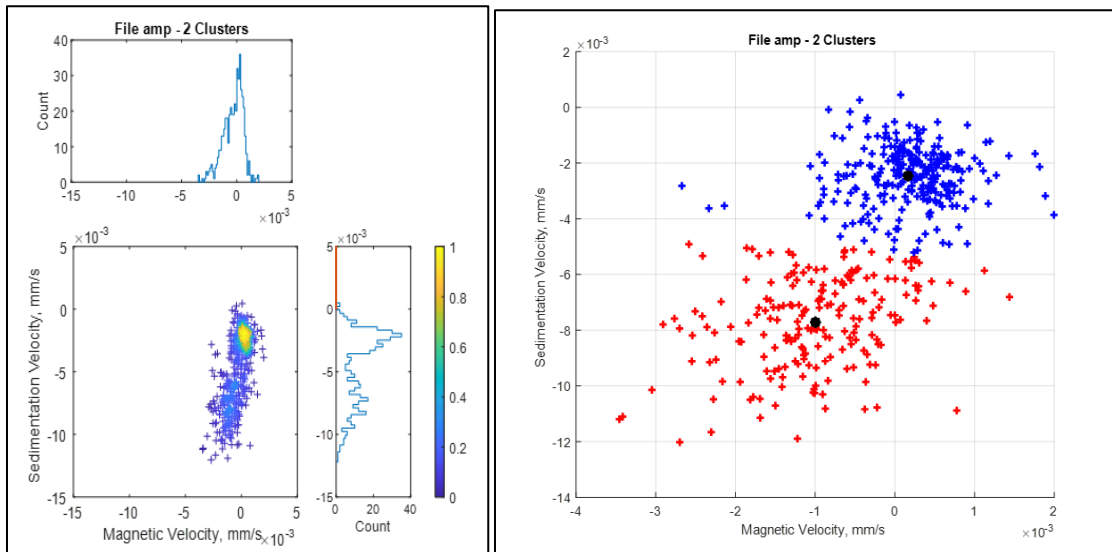


Figure 90: Left: Scatter plot of original data obtained December 20, 2018. Right: Scatter plot of original data split into two clusters.

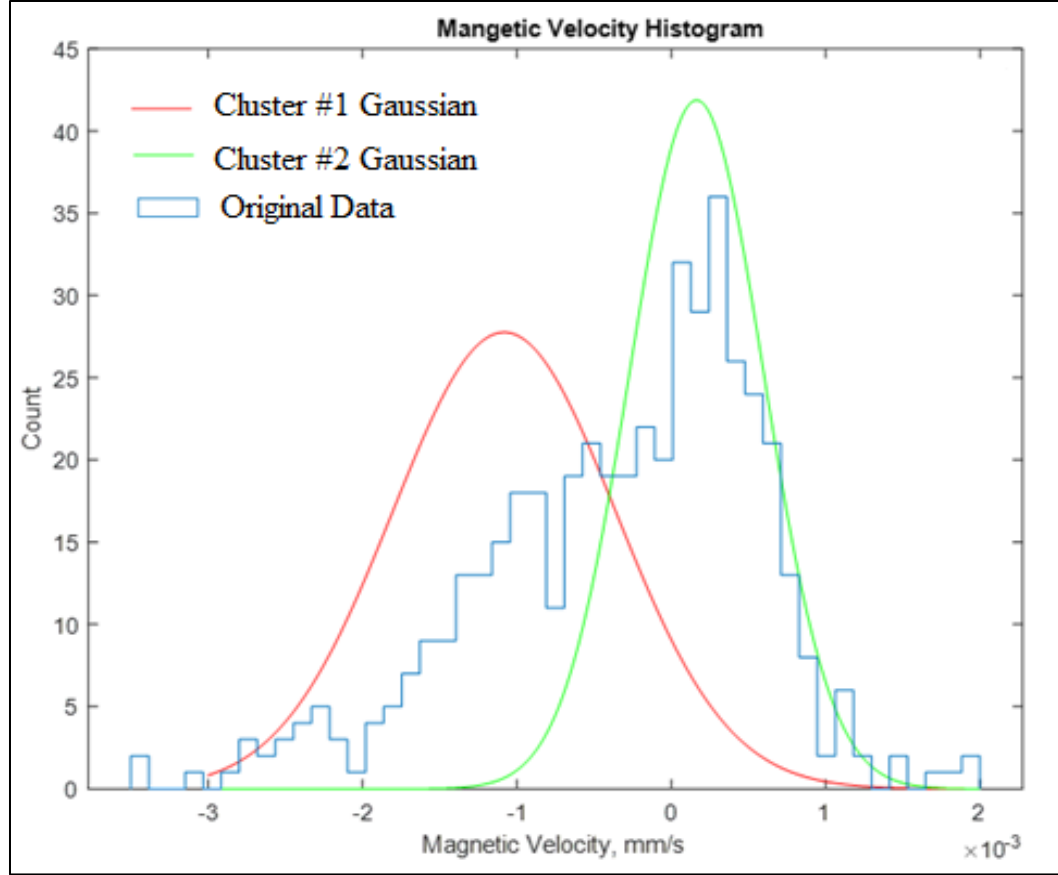


Figure 91: Gaussian plot of the two clusters presented in Figure 90.

4.5 Results for Temperature Gradient Exploration

The main purpose of these calculations was to determine if applying a temperature gradient to the MDM assembly would enhance RBC magnetic separation. Figure 92 depicts the velocity profile, which was calculated from Equation 2.35, and varying the width by 0.01 mm increments until 0.25 mm, which is the width of the MDM channel. The slowest velocity reached about $-40.5 \mu\text{m/s}$ at 0.05 mm from the cold wall and the fastest velocity was about $40.5 \mu\text{m/s}$ at a distance of 0.2 mm from the cold wall.

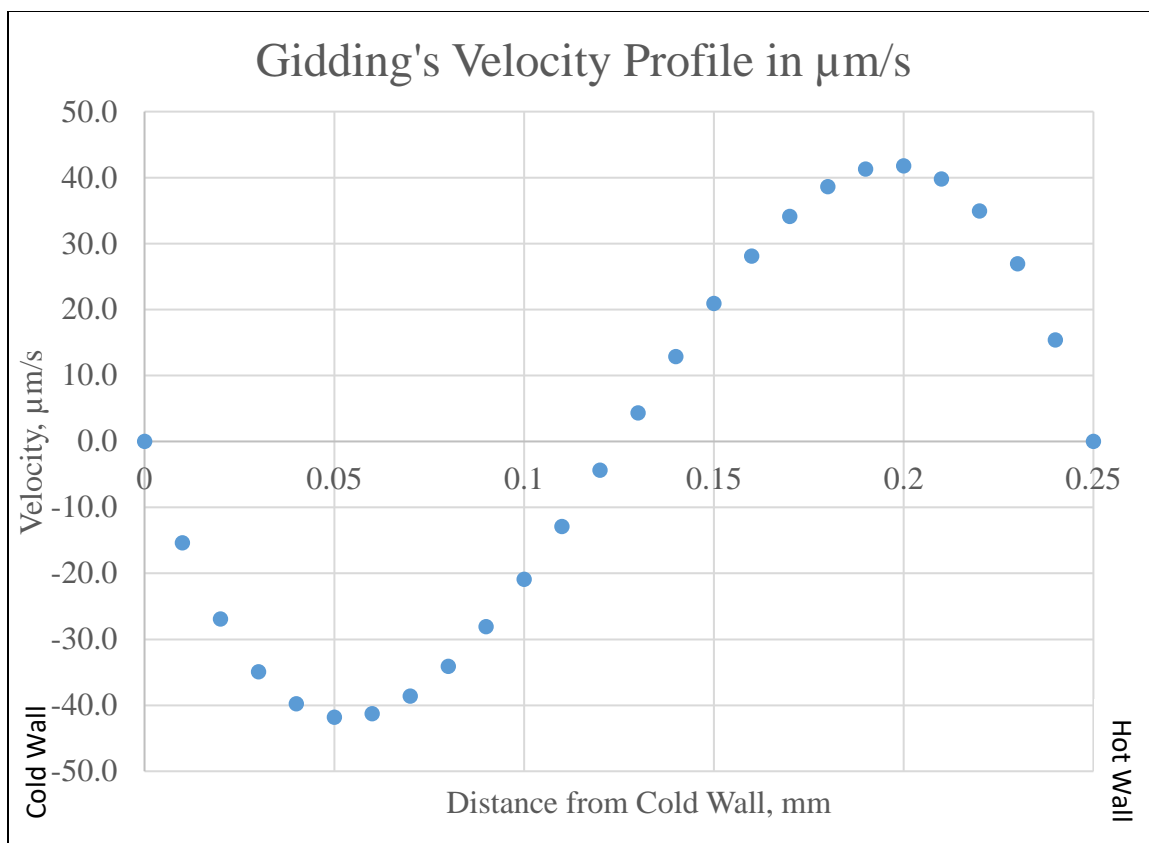


Figure 92: Giddings velocity profile calculated within Excel.

The COMSOL simulations of the velocity profile were completed next. Figure 93 displays the results from attempt number one described in Section 3.6. The fastest velocity was obtained at the outlet, which is the location of the syringe pump, at about $4 \times 10^{-5} \text{ m/s}$. The highest pressure was located at the inlet at about $2.55 \times 10^{-6} \text{ Pa}$.

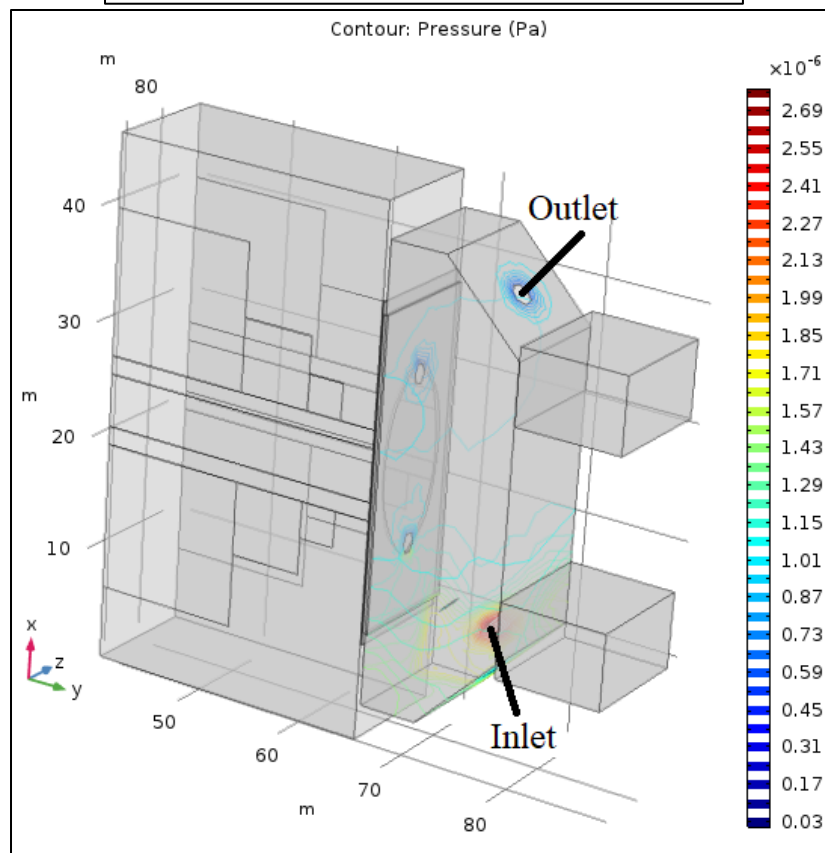
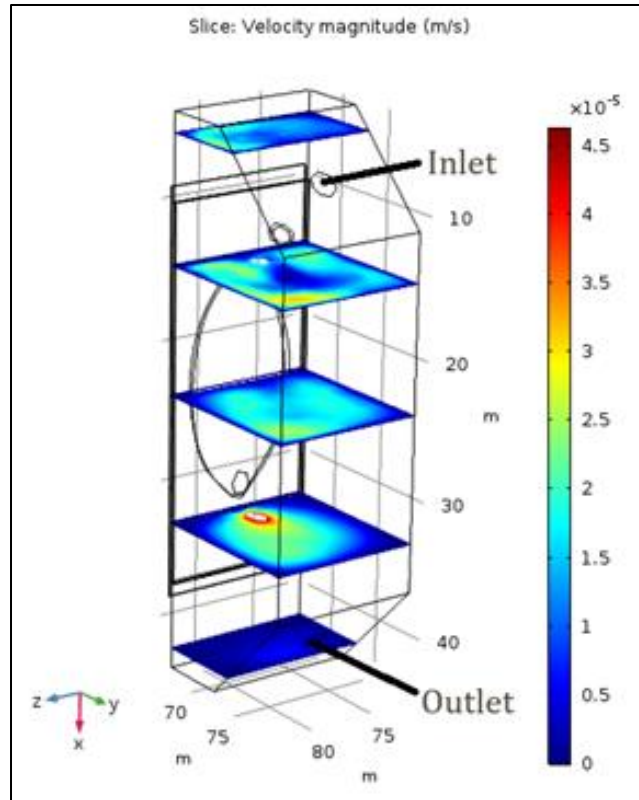


Figure 93: Above: Velocity profile through the manifold generated with COMSOL. Below: Pressure contours through the manifold with COMSOL.

4.6 Discussion for S_m Verification

Over 30 experiments were completed to verify the S_m value, utilizing different concentrations of Magnevist and varying the position over a wider range and imaging at smaller increments. The results presented in Section 4.1 in Figure 38, utilizing the 2.7 μm PS particles and a 50/50 mixture of MDM buffer and Magnevist solution, verified the location within the FOV with the highest S_m value and the least variability within the FOV was positioned about 4.5 mm from the edge of the magnet. This confirmed the position in Figure 11. However, when comparing the S_m values experimentally acquired to the model value, the experimental value is almost 1.4 times higher. This did not confirm which value for S_m should be utilized when completing CTV.

There are a few discrepancies which could cause the S_m value to be as high as the results presented in Figure 38. The major issue could have been with the particle size. Equation 2.15 demonstrates that the S_m value and the particle diameter are inversely proportional, increasing S_m if the particle diameter is small. Therefore, if there were aggregates within the sample solution, causing the particle size to be larger than what was reported, then the S_m value would drop significantly. For example, if the diameter was actually 4.0×10^{-3} mm, then the S_m value would be about 400 T-A/mm². Another difference could be the Video Savant and ImageView software are not tracking particles, but groups of particles. This could be caused by too high of a particle concentration within the sample and would cause the magnetophoretic mobility of the particles appear to be greater than they actually are.

4.7 Discussion for the Spectrophotometer Experiments

The spectrum results for wavelengths of 500 – 700 nm in Figure 39 closely resemble the theoretical curves of oxyHb and metHb in Figure 17. Also, the characteristics described by Winterbourn within her paper at wavelengths 560, 577, and 630 nm were closely reflected (Winterbourn, 1990). Upon analysis utilizing Equations 2.32 – 2.34, the concentration of oxyHb within the metHb sample was determined to be negligible, along with the concentration of metHb found within the oxyHb sample. The concentrations which were calculated agree with the spectrum presented in Figure 39 of the results.

4.8 Discussion for the Deoxygenation of Red Blood Cells

The results obtained through the MATLAB code and the Hill curve fitting analysis both suggest that for Experiments 1 and 2, RBCs behave similarly to the theoretical models from a pO_2 at 0.1 mmHg to 160 mmHg. Also, for the points below 30 mmHg, the magnetophoresis data indicated significant admixtures of partially oxygenated RBCs. These results are in agreement with the Hill model, which demonstrates fully oxygenated RBCs dominate within the mixture from 160 mmHg until 30-40 mmHg, where partially oxygenated RBCs become noticeable. This is displayed in Figure 94 below.

This work has demonstrated that the current CTV equipment, modified for the purpose of the deoxygenation of RBCs, is capable of determining both parameters, n and k , that underlie the two-parameter Hill model. The values of those parameters, determined by RBC magnetophoresis, are comparable to the literature values for normal blood determined spectrophotometrically (Dash, et al., 2016). As stated by Dash, when the Hill parameter n is set to 2.7, between oxygen saturation levels of 30% to 98%, Equation 2.27 is utilized. Any saturation levels above or below this range, the equation is inaccurately

applied (Dash, et al., 2016). However, the current CTV equipment and the RBC deoxygenation protocols did not provide the highest precision needed for the determination of Adair parameters described in Section 2.7. It is technically plausible that such precision could be achieved in the future with the further refinement of the CTV high magnetic field assembly and more precise control over the RBC deoxygenation process.

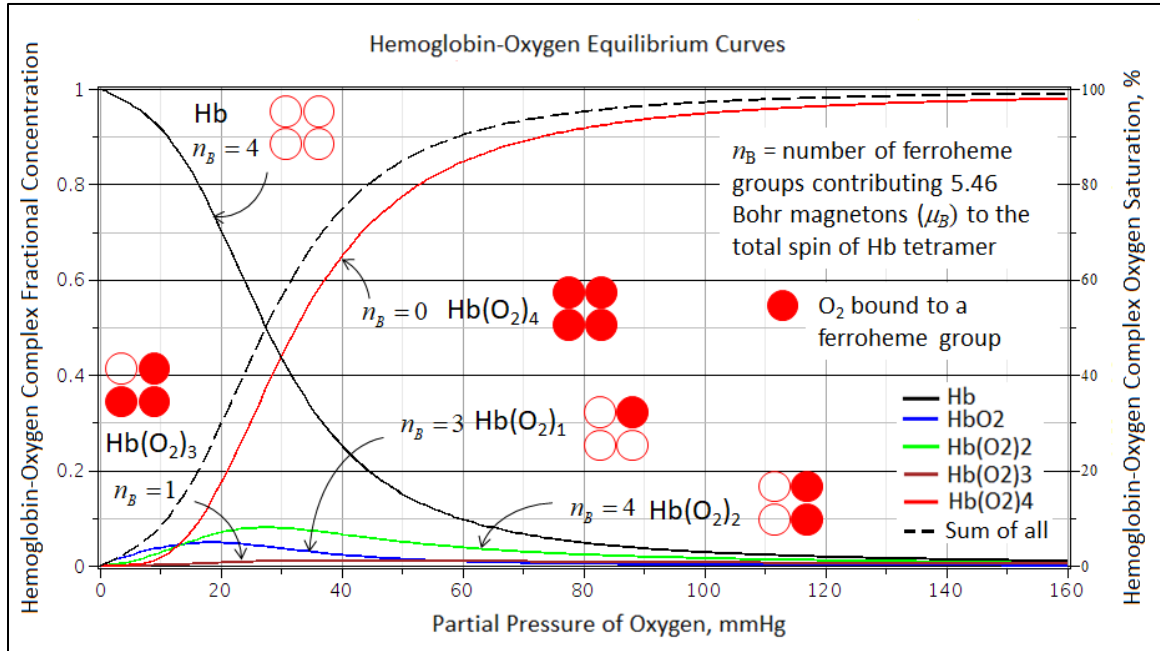


Figure 94: Model of Adair's equation generated in Maple by Dr. Zborowski. Indicates singly-, doubly-, triply-, fully oxygenated, and fully deoxygenated RBC behavior at different partial pressures of O₂. Graph of the fractional concentrations of five hemoglobin-O₂ complexes (left axis), and the corresponding hemoglobin-O₂ equilibrium curve (right axis) as a function of pO₂ calculated from the Adair equation. Symbols n_B describe the number of heme groups that contribute to the paramagnetic dipole moment of the hemoglobin-O₂ complex.

Analysis of the Hill curve slope values provide a measure of the cooperative binding of O₂ to the Fe²⁺ ferrous ion, Figure 2. Values of $n > 1$ indicates when one O₂ molecule is bond to the hemoglobin it is easier for the next O₂ molecule to bind, positively cooperative binding. When $n < 1$, negative cooperative binding occurs, meaning if one O₂ molecule is bond, then then next molecule will have a more difficult time to bind. Lastly, for $n = 1$ noncooperative (completely independent) binding exists, therefore, binding is independent of the pO₂ (Weiss, 1997). From these definitions of n , it was determined that

for both Experiments 1 and 2, there is a slight indication of positive cooperative binding of O₂ to hemoglobin based on the n values for the fitted gaussian distributions. Based on the p-values of the slope and intercepts for the regression lines and the R^2 values being below 0.8, the experimental data is said to be significantly different from the regression line.

4.9 Discussion for the Glioma Experiments

The results for the original scatter plot for the experiment completed on December 5, 2018, there are two clusters seen in the histograms for the magnetic velocity and the sedimentation velocity. When the data was analyzed with the MATLAB code, Figure 89 displays the two clusters of cells seen in the magnetic velocity histogram in Figure 88. The results for the experiment completed on December 20, 2018 has a similar trend with the magnetic and sedimentation velocity histograms showing signs of two clusters of cells in each, Figure 91. Figures 89 and 91 demonstrate that there is a cluster of cells within the sample which are more magnetic than the others in the sample. When looking at the right plots in Figures 88 and 90, the clusters which are more magnetic, also sediment out of the solution at a slower rate than the less magnetic clusters. Upon reviewing the results of the statistical analysis, the t-stat value between RPMI and MilliQ water is 0.047, which is between the positive and negative values of the t-critical two-tail values, -2.571 and 2.571. Also, the t-stat value for RPMI and distilled water, -0.726, is between -2.776 and 2.776, t-critical two-tail values. This information indicates that the RPMI media does not have magnetic properties. The cytosmeears generated provide a reference to compare to the MDM slides to determine if the MDM can isolate CSCs from cancer cells.

4.10 Discussion for the Temperature Gradient Exploration

As seen in Section 4.5 in Figure 92, the maximum value obtained for the velocity profile created in Excel was large enough to affect the RBC sedimentation by entrainment in the falling or rising layer of water in the channel. However, due to limited knowledge of how the COMSOL Multiphysics program works, and the limited time allotted to complete the modeling, the attempts completed to obtain the velocity profile within the channel were not successful. The results presented in Figure 93 of the velocity profile and the pressure contours were in the manifold, not the channel. The remainder of the attempts did not provide any results.

CHAPTER V

CONCLUSION AND RECOMMENDATIONS

5.1 Conclusions and Recommendations: S_m Verification Experiments

The location from the edge of the magnet which produces the highest magnetic energy density gradient (S_m) with the least variation in the magnitude over the FOV for the Mk V magnet assembly was confirmed to be 4.5 mm. However, the value for S_m is still in question due to the 140% difference from the values obtained through experiments compared to the theoretical value generated through software. Therefore, the original value of 365 T-A/mm² will be utilized until further research is completed.

In the future, more experiments should be done at the confirmed 4.5 mm distance from the edge of the magnet. When completing these studies, it is recommended to change the mixture of Magnevist and MDM buffer from 50/50, to 25/75 while keeping the PS particles the same. When a lower concentration of Magnevist is utilized, for example 0.5/99.5 mixture ratio of Magnevist to MDM buffer, the smaller particle would have a lower velocity due to the viscous drag force being proportional to velocity of the particle. This allows for the Video Savant imaging software to capture the motion of the PS particles, without them moving too fast to be tracked. Lastly, decreasing the frame delay

would permit for the fast-moving PS particles to be tracked in more images as well as capturing the slower-moving particles before they sediment to the bottom of the channel.

5.2 Conclusions and Recommendations: Spectrophotometry

From the results obtained from the spectrophotometry experiments, it was concluded that metHb sample was fully converted to metHb, while the oxyHb sample was saturated with O₂. This demonstrates that spectrophotometry is a reliable reference model for RBC magnetophoresis. Recommendations for the future are to complete in process testing for the RBC deoxygenation experiments in the spectrophotometer to verify Winterbourn's spectra for oxyHb and deoxyHb (surrogate metHb).

5.3 Conclusions and Recommendations: Red Blood Cell Deoxygenation Experiments

The RBC magnetophoretic analysis indicates the fully oxygenated RBCs dominant in the sample until the pO₂ reaches about 30-40 mmHg. As indicated by the graphs generated from Adair's equation by Dr. Zborowski in Maple, below this point is when the partially oxygenated RBC, containing a significant fraction of high-spin hemoglobin, come into consideration. These results agree with what is known about cooperative binding between the pO₂ values of 0 – 30 mmHg, that the fully oxygenated RBCs dominate until this range is reached. Therefore, in order to study the RBC sample for its composition in partially oxygenated hemoglobin, such a study needs to be focused on the low range of 0-30 mmHg. These results provided important insights into the opportunities and limitations of the new technique of magnetophoretic RBC analysis. This information also confirms the hypothesis that the magnetic susceptibility of RBCs does follow the same cooperative binding dependence on pO₂ as determined spectrophotometrically.

The experiments of the deoxygenation of RBCs provided a basis for future studies. It is recommended that more research be done for pO_2 from 30-0 mmHg to determine if singly-, doubly-, triply-, and fully oxygenated and deoxygenated RBCs are able to be identified in this region in accordance with the Adair model. When completing future experiments, instead of varying the pO_2 from 160 mmHg to 0 mmHg as was done for the experiments presented in this paper, start with 0 mmHg and go up in oxygenation until 160 mmHg. Testing blood that was stored for 42 days (from Dr. Mark Yazer at the University of Pittsburgh, collaborator on the project) for differences in the RBC magnetically induced velocity dependence on pO_2 as compared to a freshly drawn blood sample is also a future research consideration. Another recommendation for the future, is to use a small amount of sample at each pO_2 level and test it within the spectrophotometer to confirm Winterbourn's spectra for oxyHb and deoxyHb (surrogate metHb).

5.4 Conclusions and Recommendations: Glioma Experiments

The results from the t-test determined that the mean magnetic susceptibility value for RPMI media was not statistically significantly different from the mean values of MilliQ water and distilled water. Therefore, it was concluded that the RPMI media does not present any magnetic properties which could be passed to the glioma cell causing them to be magnetic.

The conclusion drawn from the results presented in Section 4.4 about the CTV experiments, is that there may be two cell types within the GL261 culture samples provided from Soumya in Dr. Lathia's laboratory, but at this point in time the properties of the cells are unknown. To understand these results more, the cytosmears and MDM slides need to be fluorescently stained and imaged to determine if CSCs are more magnetic than the other

cells present within the sample, and if they are able to be isolated through MDM. Also, it is recommended to reanalyze the data through the MATLAB code to confirm the results obtained in the experiments presented here. However, the sensitivity of the CTV post-processing capabilities was validated based on the separation shown in the original scatter plots in Figures 88 and 90.

5.5 Conclusions and Recommendations: Temperature Gradient Exploration

The Giddings velocity profile generated in Excel confirmed that introducing a temperature gradient to the MDM channel would enhance the magnetic separation of RBCs. Therefore, COMSOL modeling progressed to determine a more realistic representation of the temperature gradient affects. Due to these results and discussion for the COMSOL modeling, no information was provided for the velocity profile within the channel. Also, the magnetic properties and the temperature gradient were not introduced to the simulation. Therefore, no information was gained by completing these trials within COMSOL. In the future it is recommended that someone with experience and knowledge of COMSOL Multiphysics completes further exploration of the effects of a temperature gradient applied to the MDM system.

REFERENCES

- Bel-Art riteflow aluminum mounted flowmeter; 150mm scale, size 4.* (1998). Retrieved March 2019, from Bel-Art H-B Instrument: SP Scienceware:
www.belart.com/bel-art-h40407-0215-riteflow-aluminum-mounted-flowmeter-150mm-scale-size-4.html.
- Borradaile, G. J. (1998). Magnetic susceptibility, petrofabrics and strain. *Tectonophysics*, 156, 1-20. doi:10.1016/0040-1951(88)90279-X
- Bostick, M. (2018). *What goes on inside a spectrophotometer?* Retrieved 2019, from Carolina: <https://www.carolina.com/teacher-resources/Interactive/what-goes-on-inside-a-spectrophotometer/tr41103.tr>
- Brem, F., Hirt, A. M., Winklhofer, M., Frei, K., Yonekawa, Y., Wieser, H.-G., & Dobson, J. (2006). Magnetic iron compounds in the human brain: a comparison of tumour and hippocampal tissue. *Journal of the Royal Society Interface*, 3, 833-841. doi:10.1098/rsif.2006.0133
- Buck, A., Moore, L. R., Lane, C. D., Kumar, A., Stroff, C., White, N., . . . Zborowski, M. (2014). Magnetic separation of algae genetically modified for increased intracellular iron uptake. *Journal of Magnetism and Magnetic Materials*, 380, 201-204. doi:10.1016/j.jmmm.2014.09.008
- Campbell, P. (1999). *Permanent magnet materials and their application*. Cambridge University Press.
- Cullity, B. D., & Graham, C. D. (2008). *Introduction to magnetic materials* (2 ed.). John Wiley & Sons, Inc. Retrieved May 2019, from www.gbv.de/dms/ilmenau/toc/497966662.PDF

- Cytospin: Cell Preparation System Operator Guide*. (1997). Retrieved 2019, from Thermo Fisher Scientific: <http://www.blockscientific.com/manuals/shandon-cytospin-3-operator-guide.pdf>
- D'Alessandro, A., Dzieciatkowska, M., Nemkov, T., & Hansen, K. C. (2017). Red blood cell proteomics update: is there more to discover? *Blood Transfusion*, 15, 182-187. doi:10.2450/2017.0293-16
- Dash, R. K., Korman, B., & Bassingthwaite, J. B. (2016). Simple accurate mathematical models of blood HbO₂ and HbCO₂ dissociation curves at varied physiological conditions: evaluation and comparison with other models. *European Journal of Applied Physiology*, 116, 97-113. doi:10.1007/s00421-015-3228-3
- Duan, J.-j., Qiu, W., Xu, S.-l., Wang, B., Ye, X.-z., Ping, Y.-f., . . . Yu, S.-c. (2013). Strategies for isolating and enriching cancer stem cells: Well begun is half done. *Stem Cells and Development*, 22, 2221-2239. doi:10.1089/scd.2012.0613
- Erythrocytes. (2013). In *Anatomy and Physiology*. WordPress. Retrieved May 6, 2019, from OpenTextbook: opentextbc.ca/anatomyandphysiology/chapter/18-3-erythrocytes/
- Fang, B., Zborowski, M., & Moore, L. R. (1999). Detection of rare MCF-7 breast carcinoma cells from mixtures of human peripheral leukocytes by magnetic deposition analysis. *Cytometry*, 36, 294-302.
- Four different kinds of magnetism*. (2016). Retrieved May 2019, from web.hep.uiuc.edu/home/serrede/P435/Lecture_Notes/Magnetism.pdf.

- Garbade, M. J. (2018). *Understanding k-means clustering in machine learning*. Retrieved May 2019, from Towards Data Science: towardsdatascience.com/understanding-k-means-clustering-in-machine-learning-6a6e67336aa1
- GBM agile: A revolutionary new adaptive trial platform*. (2019). Retrieved 2019, from National Foudation for Cancer Research: https://www.nfcr.org/gbm-agile/?gclid=EAIaIQobChMIImoy_2ru64wIVi5OzCh0dTQJLEAAYAiAAEgIwIPD_BwE#diseasem
- Giangreco, G. J., Campbell, D., & Cowan, M. J. (2013). *A 32-year-old female with AIDS, Pneumocytis jiroveci pneumonia, and methemoglobinemia*. Hindawi Publishing Corporation. doi:10.1155/2013/980589
- Giddings, J. C. (1991). *Unified Separation Science*. John Wiley & Sons, Inc. Retrieved 2019
- Haidas, S., Labie, D., & Kaplan, J.-C. (1971). 2,3-Diphosphoglycerate content and oxygen affinity as a function of red cell age in normal individuals. *Blood*, 38, 463-467. Retrieved May 2019, from <http://www.bloodjournal.org/content/38/4/463>
- Hemoglobin: portrait of a protein in action . (2012). In *Biochemistry* (7 ed.). W. H. Freeman and Company. Retrieved May 2019, from http://ocw.sogang.ac.kr/rfile/2013/course07-CHM1/biochemistry7e_ch07_20130620145200.pdf
- Hill equation - interactive graph*. (2014). Retrieved May 2019, from PhysiologyWeb: https://www.physiologyweb.com/calculators/hill_equation_interactive_graph.htm

- Hill, A. V. (1910). The possible effects of the aggregation of the molecules of haemoglobin on its dissociation curves. *The Journal of Physiology*, 40, 4-7.
Retrieved April 2019, from mathgeomsrv2.epfl.ch/teaching/oldCourses/2017-2018/MathematicalPhysiology/protected_files/articles/Hill.pdf
- Imai, K. (1994). Adair fitting to oxygen equilibrium curves of hemoglobin. *Methods in Enzymology*, 232, 559-576. Retrieved 2019
- Inglut, C., Kausch, K., Gray, A., & Landrigan, M. (2016). Rejuvenation of stored red blood cells increases oxygen release capacity. *Blood*, 128. Retrieved April 2019, from www.bloodjournal.org/content/128/22/4808
- Jin, X., Chalmers, J. J., & Zborowski, M. (2012). Iron transport in cancer cell culture suspensions measured by cell magnetophoresis. *Analytical Chemistry*, 84, 4502-4526. doi:10.1021/ac3004677
- Joshi, P., Jacobs, B., Derakhshan, A., Moore, L. R., Elson, P., Triozzi, P. L., . . . Zborowski, M. (2014). Enrichment of circulating melanoma cells (CMCs) using negative selection from patients with metastatic melanoma. *Oncotarget*, 5, 2450-2461. Retrieved 2019
- Joshi, P., Williams, P. S., Moore, L. R., Caralla, T., Boehm, C., Muschler, G., & Zborowski, M. (2015). Circular halbach array for fast magnetic separation of hyaluronan-expressing tissue progenitors. *Analytical Chemistry*, 87. doi:10.1021/acs.analchem.5b02431
- Kawabata, H., Yang, R., Hiramata, T., Vuong, P. T., Kawano, S., Gombart, A. F., & Koeffler, H. P. (1999). Molecular cloning of transferrin receptor 2 - a new

member of the transferrin receptor-like family. *Journal of Biological Chemistry*, 274, 20826-20832.

Lathia, J. D., Mack, S. C., Mulkearns-Hubert, E. E., Valentim, C. L., & Rich, J. N.

(2015). Cancer stem cells in glioblastoma. *Genes & Development*, 29, 1203-1217.

doi:10.1101/gad.261982.115

Legato 210/210P Syringe Pump. (2016). Retrieved 2019, from kd Scientific: Syringe

Pumps & Dispensers: <https://www.kdscientific.com/legato-210-210p-syringe-pump.html>

Lide, D. R. (2005). *CRC Handbook of Chemistry and Physics* (85 ed.). CRC Press.

Retrieved April 2019, from

<http://diyhpl.us/~nmz787/mems/unorganized/CRC%20Handbook%20of%20Chemistry%20and%20Physics%2085th%20edition.pdf>

Mader, S. (1997). *Inquiry into life* (8 ed.). The McGraw-Hill Inc. Retrieved April 2019

Magnetic susceptibility balances (MSB). (2005). Retrieved May 2019, from Johnson

Matthey: https://faculty.uca.edu/patrickd/chem3150/MSB1_Brochure.pdf

Magnetic susceptibility balances. (1930). Retrieved May 2019, from Sherwood

Scientific: [http://www.sherwood-](http://www.sherwood-scientific.com/Magnetic%20Susceptibility%20Balance%20Brochure.pdf)

[scientific.com/Magnetic%20Susceptibility%20Balance%20Brochure.pdf](http://www.sherwood-scientific.com/Magnetic%20Susceptibility%20Balance%20Brochure.pdf)

Magnevist®. (2017). Retrieved May 2019, from Bayer Pharmaceuticals:

[https://www.radiologysolutions.bayer.com/static/media/PDFs/2-2-1-](https://www.radiologysolutions.bayer.com/static/media/PDFs/2-2-1-3_Magnevist/Magnevist%20NDC%20Code%20One-sheet%20-%20Electronic%20Version.pdf)

[3_Magnevist/Magnevist%20NDC%20Code%20One-sheet%20-](https://www.radiologysolutions.bayer.com/static/media/PDFs/2-2-1-3_Magnevist/Magnevist%20NDC%20Code%20One-sheet%20-%20Electronic%20Version.pdf)

[%20Electronic%20Version.pdf](https://www.radiologysolutions.bayer.com/static/media/PDFs/2-2-1-3_Magnevist/Magnevist%20NDC%20Code%20One-sheet%20-%20Electronic%20Version.pdf)

- Matejak, M., Kulhanek, T., & Matousek, S. (2015). *Adair-based hemoglobin equilibrium with oxygen, carbon dioxide and hydrogen ion activity*.
doi:10.3109/00365513.2014.984320
- Moore, L. R., Mizutani, D., Tanaka, T., Buck, A., Yazer, M., Zborowski, M., & Chalmers, J. (2018). Continuous, intrinsic magnetic depletion of erythrocytes from whole blood with a quadrupole magnet and annular flow channel; pilot scale study. *Biotechnology and Bioengineering*, 115, 1521-1530. doi:10.1002/bit.26581
- Moore, L. R., Zborowski, M., Nakamura, M., McCloskey, K., Gura, S., Zuberi, M., . . . Chalmers, J. (2000). *The use of magnetite-doped polymeric microspheres in calibrating cell tracking velocimetry*. *Journal of Biochem Biophys Methods*.
Retrieved 2019
- Moore, L. R., Zborowski, M., Sun, L., & Chalmers, J. J. (1998). Lymphocyte fractionation using immunomagnetic colloid and a dipole magnet flow cell sorter. *Journal of Biochemical Biophysical Methods*, 37, 11-33.
- Nakamura, M., Zborowski, M., Lasky, L. C., Margel, S., & Chalmers, J. (2001). Theoretical and experimental analysis of the accuracy and reproducibility of cell tracking velocimetry. *Experiments in Fluids*, 30, 371-380.
doi:10.1007/s003480000211
- Oakton™ Gilmont™ shielded laboratory direct-reading flowmeters. (2006). Retrieved May 2019, from Fisher Scientific: <https://www.fishersci.com/shop/products/cole-parmer-gilmont-shielded-laboratory-direct-reading-flowmeters-4/p-179228>
- Oh, T., Fakurnejad, S., Sayegh, E. T., Clark, A. J., Ivan, M. E., Z., S. M., . . . Parsa, A. T. (2014). Immunocompetent murine models for the study of glioblastoma

immunotherapy. *Journal of Translational Medicine*, 12, 1-10. doi:10.1186/1479-5876-12-107

Orion star™ A213 dissolved oxygen benchtop meter. (2015). Retrieved May 2019, from Thermo Fisher Scientific:

<https://www.thermofisher.com/order/catalog/product/STARA2130>

Orion™ RDO™ dissolved oxygen probe. (2008). Retrieved May 2019, from Thermo Fisher Scientific:

<https://www.thermofisher.com/order/catalog/product/087010MD?SID=srch-srp-087010MD>

Pauling, L., & Coryell, C. (1936a). The magnetic properties and structure of the hemochromogens and related substances. *Proceedings of the National Academy of Sciences of the United States of America*, 22, 159-163. doi:10.1073/pnas.22.3.159

Pauling, L., & Coryell, C. D. (1936b). The magnetic properties and structure of hemoglobin, oxyhemoglobin and carbonmonoxyhemoglobin. *Proceeding of the National Academy of Sciences of the United States of America*, 22, 210-216. doi:10.1073/pnas.22.4.210

Permanent magnet guidelines. (1998). Retrieved May 2019, from

<https://www.intemag.com/images/MMPAPMG-88.pdf>

Schonberg, D. L., Miller, T. E., Wu, Q., Flavahan, W. A., Das, N. K., Hale, J. S., . . .

Rich, J. N. (2015, October). Preferential iron trafficking characterizes glioblastoma stem-like cells. *Cancer Cell*, 28, 441-455.

doi:10.1016/j.ccell.2015.09.002

- Sparrow, R. L. (2010). Red blood cell storage and transfusion-related immunomodulation. *Blood Transfusion*, 8, 26-30. doi:10.2450/2010.005S
- Staff, M. C. (2019, April). *Brain tumor: Ependymoma*. Retrieved 2019, from Mayo Clinic: <https://www.mayoclinic.org/diseases-conditions/ependymoma/cdc-20350144>
- Staff, M. C. (2019, April). *Glioma*. Retrieved 2019, from Mayo Clinic: <https://www.mayoclinic.org/diseases-conditions/glioma/symptoms-causes/syc-20350251>
- Staff, M. C. (2019, April). *Glioma: Astrocytoma*. Retrieved 2019, from Mayo Clinic: <https://www.mayoclinic.org/diseases-conditions/astrocytoma/cdc-20350132>
- Staff, M. C. (2019, April). *Glioma: Glioblastoma*. Retrieved 2019, from Mayo Clinic: <https://www.mayoclinic.org/diseases-conditions/glioblastoma/cdc-20350148>
- Staff, M. C. (2019, April). *Glioma: Oligodendroglioma*. Retrieved 2019, from Mayo Clinic: <https://www.mayoclinic.org/diseases-conditions/oligodendroglioma/cdc-20350152>
- The use of magnetite-doped polymeric microspheres in calibrating cell tracking velocimetry. (2000). *Journal of Biochemical and Biophysical Methods*, 44, 115-1130. doi:10.1016/S0165-022X(00)00085-3
- Understanding permanent magnets*. (2015). Retrieved May 2019, from Arnold Magnetic Technologies: spontaneousmaterials.com/Papers/CW2000.pdf
- User's guide: DU series 700 UV/Vis scanning spectrophotometer*. (2012, December). Retrieved 2019, from Beckman Coulter: https://physiology.case.edu/media/eq_manuals/eq_manual_beckman_du700_.pdf

- Water - density, specific weight and thermal expansion coefficient.* (2003). Retrieved 2019, from Engineering ToolBox: https://www.engineeringtoolbox.com/water-density-specific-weight-d_595.html
- Water - dynamic and kinematic viscosity.* (2004). Retrieved 2019, from Engineering ToolBox: https://www.engineeringtoolbox.com/water-dynamic-kinematic-viscosity-d_596.html
- Weiss, J. (1997). The hill equation revisited: uses and misuses. *FASEB Journal*, 11, 835-841. doi:10.1096/fasebj.11.11.9285481
- What is the magnetic hysteresis loop.* (2015). Retrieved May 2019, from Arnold Magnetic Technologies: https://www.arnoldmagnetics.com/wp-content/uploads/2017/10/FINAL_Tech-Library_Tech-Notes_Hysteresis-Loop.pdf
- Why patients receive blood transfusions.* (2019). Retrieved 2019, from American Red Cross: <https://www.redcrossblood.org/donate-blood/blood-donation-process/what-happens-to-donated-blood/blood-transfusions/reasons-transfusions.html>
- Williams, P. S., Carpino, F., & Zborowski, M. (2010, August). Characterization of magnetic nanoparticles using programmed quadrupole magnetic field-flow fractionation. *Philosophical Transactions of the Royal Society*, 368, 4419-4437. doi:10.1098/rsta.2010.0133
- Winslow, R., Swenberg, M., Berger, R., Shrager, R., Luzzana, M., Samaja, M., & Rossi-Bernardi, L. (1977). Oxygen equilibrium curve of normal human blood and its evaluation by adair's equation. *The Journal of Biological Chemistry*, 252, 2331-2337. Retrieved May 2019, from <https://www.ncbi.nlm.nih.gov/pubmed/849931>

- Winterbourn, C. C. (1990). Oxidative Reactions of Hemoglobin. *Methods in Enzymology*, 186, 265-272. Retrieved 2019
- Xue, W. (2016). *Measurements of cellular intrinsic magnetism with cell tracking velocimetry and separation with magnetic deposition microscopy*. Dissertation, The Ohio State University, Graduate Program in Chemical and Biomolecular Engineering, Columbus. Retrieved May 2019, from https://etd.ohiolink.edu/!etd.send_file?accession=osu1461231847&disposition=inline
- Xue, W., Moore, L. R., Nakano, N., Chalmers, J. J., & Zborowski, M. (2019). Single cell magnetometry by magnetophoresis vs. bulk cell suspension magnetometry by squid-mpms- a comparison. *Journal of Magnetism and Magnetic Materials*, 474, 152-160. doi:10.1016/j.jmmm.2018.10.108
- Zborowski, M., & Chalmers, J. J. (Eds.). (2007). *Magnetic cell separation* (1 ed., Vol. 32). Elsevier Science. Retrieved May 2019
- Zborowski, M., Chalmers, J. J., & Lowrie, W. G. (2016). Magnetic cell manipulation and sorting. *Microtechnology for Cell manipulation and Sorting*, 15-55. doi:10.1007/978-3-319-44139-9_2
- Zborowski, M., Chalmers, J., & Moore, L. R. (2003). *United States of America Patent No. 6557430*. Retrieved May 2019, from <https://patents.justia.com/patent/6557430>
- Zborowski, M., Fuh, C. B., Green, R., Sun, L., & Chalmers, J. J. (1995). Analytical magnetapheresis of ferritin-labeled lymphocytes. *Analytical Chemistry*, 67, 3702-3712. doi:10.1021/ac00116a014

Zborowski, M., Ostera, G. R., Moore, L. R., Milliron, S., Chalmers, J. J., & Schechter, A.

N. (2003). Red blood cell magnetophoresis. *Biophysical Journal*, 84, 2638-2645.

doi:10.1016/S0006-3495(03)75069-3

Zimmerman, P. A., Thomson, J. M., Fujioka, H., Collins, W. E., & Zborowski, M.

(2006). Diagnosis of malaria by magnetic deposition microscopy. *American*

Society of Tropical Medicine and Hygiene, 74, 568-572. Retrieved 2019

APPENDIX A: RELEVANT GRAPHS AND TABLES

Table X: Common forms of magnetic susceptibility designation, units, and conversion factors (Zborowski, et al., 2016).

Magnetic Susceptibility Common Forms and Conversion Factors				
Susceptibility Designation	Symbol	χ (CGS units)	χ (SI units)	Conversion factor from CGS to SI
Volume	χ	1	1	4π
Mass/Specific	χ_g	cm ³ /g	m ³ /kg	$4\pi/1000$
Molar	χ_N	cm ³ /mol	m ³ /mol or m ³ /kmol	$4\pi/10^6$ or $4\pi/1000$, respectively
One-gram-formula-weight	χ'_N	cm ³ /mol	m ³ /mol or m ³ /kmol	$4\pi/10^6$ or $4\pi/1000$, respectively

Table XI: Specifications for the Beckman Coulter spectrophotometer (User's guide: DU series 700 UV/Vis scanning spectrophotometer, 2012)

Beckman Coulter DU® 730 Specifications		
Parameter	Value	Unit
Operating Mode	Transmittance %, Absorbance, Concentration	
Source Lamp	Tungsten (visible), Deuterium (UV)	
Wavelength Range	190 - 1100	nm
Wavelength Accuracy	± 1 in 200 - 900 range	nm
Wavelength Resolution	Selectable - 0.1, 0.2, 0.5, 1.0, 2.0, 5.0	nm
Wavelength Calibration	Automatic	
Wavelength Selection	Automatic, based on mode selected	
Spectral Bandwidth	3	nm
Photometric Readout	-0.3 - 3.0 A, 0.1 - 100 %T	
Photometric Accuracy	± 0.005 A at 0 A - 0.5 A, 1% at 0.5 A - 2.0 A	
Photometric Linearity	<0.5% at 2.0 A, 1% at > 2.0 A	

Table XII: Specifications for the Oakton™ Gildmont™ Shielded laboratory Direct-Reading Flowmeter (Oakton™ Gildmont™ shielded laboratory direct-reading flowmeters, 2006).

Oakton™ Gildmont™ Shielded laboratory Direct-Reading Flowmeter Specifications		
Parameter	Range	Units
Flow Rate	0.002 - 1.1	mL/min
Accuracy	± 5 of reading	%
Repeatability	± 1 of reading	%
Maximum Temperature	65	°C

Table XIII: Specifications for the Bel-Art™ SP Scienceware™ Riteflow™ Mounted Flowmeter (Bel-Art riteflow aluminum mounted flowmeter; 150mm scale, size 4, 1998).

Bel-Art™ SP Scienceware™ Riteflow™ Mounted Flowmeter Specifications		
Parameter	Range	Units
Flow Rate	1.1 - 20.4	mL/min
Accuracy	± 5 of full scale	%
Repeatability	± 0.25 of full scale	%
Maximum Temperature	121	°C
Maximum Pressure	200	psig

Table XIV: Specifications for the RDO® Rugged DO sensor operated in the deoxygenation vessel for the deoxygenation of RBCs experiments (Orion™ RDO™ dissolved oxygen probe, 2008).

RDO® Rugged Dissolved Oxygen Sensor Specifications		
Parameter	Range	Units
Dissolved Oxygen Concentration	0 - 20	mg/L
Dissolved Oxygen Saturation	0 - 200	%
Dissolved Oxygen Concentration Accuracy	±0.1 mg/L up to 8 mg/L	mg/L
	±0.2 mg/L up from 8 to 20 mg/L	mg/L
Dissolved Oxygen Concentration Resolution	0.01	mg/L
Temperature	0 - 50	°C
Temperature Accuracy	±0.3	°C
Minimum Immersion Depth	40	mm

Table XV: Dimensions for the RDO® Rugged DO sensor used in the deoxygenation vessel for the deoxygenation of RBCs experiments (Orion™ RDO™ dissolved oxygen probe, 2008).

RDO® Rugged Dissolved Oxygen Sensor Dimensions		
Parameter	Value	Units
Sensor Tip Length	70	mm
Overall Sensor Length	190	mm
Sensor Tip Diameter	16	mm
Maximum Sensor Diameter	33	mm

Table XVI: Specifications for the Orion Star A213 DO Benchtop meter utilized for the deoxygenation of RBCs experiments (Orion star™ A213 dissolved oxygen benchtop meter, 2015).

Orion Star A213 DO Benchtop Meter Specifications		
Parameter	Range	Units
Concentration	0 - 50	mg/L
Concentration Resolution	0.01/0.1	mg/L
Concentration Relative Accuracy	±0.1 mg/L up to 8 mg/L	mg/L
	±0.2 mg/L up from 8 to 20 mg/L	mg/L
Saturation	0 - 500	%
Saturation Resolution	0.1/1	%
Saturation Relative Accuracy	±2 % saturation ≤ 200 %	%
Temperature	0 - 50	°C
Temperature Resolution	0.1	°C
Temperature Relative Accuracy	±0.1	°C

Table XVII: Specifications and dimensions of the Shandon Cytospin 3 (Cytospin: Cell Preparation System Operator Guide, 1997).

Shandon Cytospin 3 Specifications		
Parameter	Value	Units
Operating Speed Range	200 - 2,000	rpm
Height	215	mm
Height Clearance	560	mm
Width	385	mm
Width Clearance	405	mm
Depth	495	mm
Depth Clearance	556	mm
Weight	18	kg

Table XVIII: Specifications of the Legato 210P multi-syringe pump (Legato 210/210P Syringe Pump, 2016).

Legato® 210/210P Syringe Pump Specifications		
Parameter	Value	Units
Accuracy	± 0.35	%
Minimum Syringe Size	0.5	µL
Maximum Syringe Size	140	mL
Minimum Flow Rate for 0.5 µL Syringe	3.06	pL/min
Maximum Flow Rate for 140 mL Syringe	215.8	mL/min
Minimum Step Rate	27.5	sec/µstep
Maximum Step Rate	26	µsec/µstep
Minimum Pusher Travel Rate	0.36	µm/min
Maximum Pusher Travel Rate	190.8	mm/min

APPENDIX B: MATLAB CODE FOR ANALYZING CTV RESULTS – 4/17/2019

Authors: Robert Royer, Dr. Maciej Zborowski, and Nina Smith

Select CTV macro file

Program will pull data from the 'DATA-1' sheet to build plots

```
clear
[file,path] = uigetfile('*.xlsx');
cd(path);
x = xlsread(file,'DATA-1','B:B');
y = xlsread(file,'DATA-1','C:C');
x = -x;                      %% Magnet is flipped over
y = -y;                      %% Makes sedimentaion rate below zero
x1 = x;                      % stores gated data
y1 = y;                      % stores gated data
x2 = x1;                     % stores original data
y2 = y1;                     % stores original data
lx=length(x)
ly=length(y)
lx1=lx;
ly1=ly;
minX=min(x)
maxX=max(x)
minY=min(y)
maxY=max(y)
%xlimLo=min(minX,minY);
%xlimHi=max(maxX,maxY);
%ylimLo=xlimLo;
%ylimHi=xlimHi;
xlimLo=-0.002
xlimHi=0.005
ylimLo=xlimLo
ylimHi=xlimHi
minX1=min(x)
maxX1=max(x)
minY1=min(y)
maxY1=max(y)
```

Scatter plot with marginal histograms

Position is defined by [x y xlength ylength]

position is determined by the bottom-left corner

```
binN=10                      % average number of histogram counts per bin
Nbins = floor(lx1/binN)      % number of histogram bins is 1/binN of sample
size
binX=((maxX1-minX1)/Nbins)    % bin length
```

```

figure1 = figure('Name',sprintf('file name is
%s',file),'NumberTitle','off');
axes1 = axes('Parent',figure1,'Position',[0.3 0.08 0.35 0.35],'Box','on');
hold(axes1,'on');
%axis 'equal'

% scatplot(x1,y1,'method',radius, N, number of filter coeffs., plot option
number, marker size)
% N square grid size, determines number of isolines
% 'method' = "circles", "squares", or "voronoi" (default)
% po number = 0 (no plot), 1 (scatter filtered), 2 (scatter & isolines
filter), 3 (as in 1 unfiltered), and 4 (as in 2 unfiltered)
% Example:
%scatplot(x1,y1,'circles',0.01,100,7,2,10)

scatplot(x1,y1)
pbaspect([1 1 1]);
xlabel('Magnetic Velocity, mm/s')
ylabel('Sedimentation Velocity, mm/s')
%xlim([minX1 maxX1])
%ylim([minY1 maxY1])
xlim([xlimLo xlimHi])
ylim([ylimLo ylimHi])
axis([xlimLo xlimHi ylimLo ylimHi])

colorbar('peer',axes1,'Position',[0.77 0.08 0.01 0.35])

axes2 = axes('Parent',figure1,'Position',[0.34 0.52 0.26 0.2],'Box','on');
hold(axes2,'on');
histogram(x1,Nbins,'DisplayStyle','stairs')
ylabel('Count')
title(file) %Changes depending on which file is being run

axes3 = axes('Parent',figure1,'Position',[0.63 0.08 0.133
0.35],'Box','on');
hold(axes3,'on');
histogram(y1,Nbins,'Orientation','horizontal','DisplayStyle','stairs')
pbaspect([1 3 1])
xlabel('Count')

linkaxes([axes1,axes2],'x')
linkaxes([axes1,axes3],'y')

```



```

histoP=histogram(x1,Nbins,'DisplayStyle','stairs');
hold off
clf

```

Histogram for full Set x1 using "histcounts" and "stairs" plot

```

clear N edgesN histoN
[Nx1,edgesN] = histcounts(x1,Nbins);
length(edgesN);
length(Nx1);
clf
histoN=stairs(edgesN(1:length(edgesN)-1),Nx1);    % vector "edges" and "N"
have to be same length for plotting
%hold on

```

K mean clustering analysis. Caution - assigns clusters differently each time it is run. Re-run to make sure that the plot displays properly.

K is the number of clusters in the data

```

K      = 2    % Cluster Number
KMI    = 10    % K-means Iteration

```

Concatenate x and y vectors horizontally to form F(N,2) array for cluster analysis

```

x0=x1;
y0=y1;
F=horzcat(x0,y0);
clf

CENTS = F( ceil(rand(K,1)*size(F,1)) ,:);    % Cluster Centers
DAL    = zeros(size(F,1),K+2);                % Distances and
Labels
CV      = '+r+b+c+m+yo+ob+om+ok+oysr+bs+cs+ms+ksy';    % Color Vector

for n = 1:KMI
for i = 1:size(F,1)
for j = 1:K
    DAL(i,j) = norm(F(i,:) - CENTS(j,:));
end
    [Distance, CN] = min(DAL(i,1:K));    % n1:K are Distance
from Cluster Centers 1:K
    DAL(i,K+1) = CN;                    % K+1 is Cluster
Label
    DAL(i,K+2) = Distance;              % K+2 is Minimum
Distance

```

```

end
for i = 1:K
    A = (DAL(:,K+1) == i);
    CENTS(i,:) = mean(F(A,:));
Centers
    NC = find(isnan(CENTS(:,1)) == 1);
    for Ind = 1:size(NC,1)
        CENTS(NC(Ind),:) = F(randi(size(F,1)),:);
    end
end
end
CENTS

```

Plot

```

clf
figure(1)
hold on

for i = 1:K
    PT = F(DAL(:,K+1) == i,:);
each cluster
    plot(PT(:,1),PT(:,2),CV(2*i-1:2*i),'LineWidth',2);
determined color and shape
    plot(CENTS(:,1),CENTS(:,2),'*k','LineWidth',7);
Plot cluster centers
    text(xlimHi/50+CENTS(i,1),xlimHi/50+CENTS(i,2),num2str(i),'FontSize',20)
end
xlabel('Magnetic Velocity, mm/s')
ylabel('Sedimentation Velocity, mm/s')
title(file)
hold off
grid on

```

**** Select index "i" for a Cluster selected as Subset B (exluded from Subset A)

```

iB=1;
PW = F(DAL(:,K+1) == iB,:);
F2=vertcat(PW);
x1b=F2(:,1);
y1b=F2(:,2);
lx1b=length(x1b)
ly1b=length(y1b)

```

Select Cluster(s) for Subset A, then plot it for easy reference.

```

clf
%figure(1);
hold on

```

```

%PU=zeros(1x1,2);
PU=[];
for i = 1:K
if i~=iB
    PT = F(DAL(:,K+1) == i,:); % Find points of
each cluster
    plot(PT(:,1),PT(:,2),CV(2*i-1:2*i),'LineWidth',2); % Plot points
with determined color and shape
    plot(CENTS(:,1),CENTS(:,2),'*k','LineWidth',7); % Plot cluster
centers

text(xlimHi/50+CENTS(i,1),xlimHi/50+CENTS(i,2),num2str(i),'FontSize',20);
    PU=vertcat(PU,PT);
end
end

hold off
grid on

%scatter(PU(:,1),PU(:,2),'c');
hold on
%scatter(PW(:,1),PW(:,2),'b');
hold off

```

Combine data vectors of clusters included in Subset A

```

F1=PU;
x1a=F1(:,1);
y1a=F1(:,2);
lx1a=length(x1a)
ly1a=length(y1a)
min(x1a)
max(x1a)

```

Scatter plot with marginal histograms for Subset A

Position is defined by [x y xlength ylength]

position is determined by the bottom-left corner

```

lx1(1) % full sample size (w/o outliers)
binA=lx1a % Subset A size
Nbins(1) % full sample histogram bin #
binXa=binX(1) % Subset A histogram bin size = full histogram
bin size
Abins=abs(floor((max(x1a)-min(x1a))/binXa))
CENTS1(1,1)=mean(x1a); % CENTS matrix expanded by addition of SD
columns

```

```

CENTS1(1,2)=std(x1a);          % CENTS matrix expanded by addition of SD
columns
CENTS1(1,3)=mean(y1a);        % CENTS matrix expanded by addition of SD
columns
CENTS1(1,4)=std(y1a);         % CENTS matrix expanded by addition of SD
columns

clear figure1
%figure1 = figure('Name','Figure');
figure1 = figure('Name',sprintf('file name is
%s',file),'NumberTitle','off');
axes1 = axes('Parent',figure1,'Position',[0.3 0.08 0.35 0.35],'Box','on');
hold(axes1,'on')
%axis 'equal'

% scatplot(x1a,y1a,'method',radius, N, number of filter coeffs., plot
option number, marker size)
% N square grid size, determines number of isolines
% 'method' = "circles", "squares", or "voronoi" (default)
% po number = 0 (no plot), 1 (scatter filtered), 2 (scatter & isolines
filter), 3 (as in 1 unfiltered), and 4 (as in 2 unfiltered)
% Example:
%scatplot(x1,y1,'circles',0.01,100,7,2,10)

scatplot(x1a,y1a)
pbaspect([1 1 1])
title('Subset A')
xlabel('u_mag, mm/s')
ylabel('v, mm/s')
xlim([minX1 maxX1])
ylim([minY1 maxY1])
%xlim([xlimLo xlimHi])
%ylim([ylimLo ylimHi])

colorbar('peer',axes1,'Position',[0.77 0.08 0.01 0.35])

axes2 = axes('Parent',figure1,'Position',[0.34 0.52 0.26 0.2],'Box','on');
hold(axes2,'on');
histogram(x1a,Abins,'DisplayStyle','stairs')
ylabel('Count')

axes3 = axes('Parent',figure1,'Position',[0.63 0.08 0.133
0.35],'Box','on');
hold(axes3,'on');

```

```

histogram(y1a,Abins,'Orientation','horizontal','DisplayStyle','stairs')
pbaspect([1 3 1])
xlabel('Count')

linkaxes([axes1,axes2],'x')
linkaxes([axes1,axes3],'y')
hold off

```

Scatter plot with marginal histograms for Subset B

Position is defined by [x y xlength ylength]

position is determined by the bottom-left corner

```

lx1(1) % full sample size (w/o outliers)
binB=lx1b % Subset A size
Nbins(1) % full sample histogram bin #
binXb=binX(1)
Bbins=abs(floor((max(x1b)-min(x1b))/binXb))
CENTS1(2,1)=mean(x1b); % CENTS matrix expanded by addition of SD
columns
CENTS1(2,2)=std(x1b); % CENTS matrix expanded by addition of SD
columns
CENTS1(2,3)=mean(y1b); % CENTS matrix expanded by addition of SD
columns
CENTS1(2,4)=std(y1b); % CENTS matrix expanded by addition of SD
columns

clear figure1
%figure1 = figure('Name','Figure');
figure1 = figure('Name',sprintf('file name is
%s',file),'NumberTitle','off');

axes1 = axes('Parent',figure1,'Position',[0.3 0.08 0.35 0.35],'Box','on');
hold(axes1,'on')
%axis 'equal'

% scatplot(x1,y1,'method',radius, N, number of filter coeffs., plot option
number, marker size)
% N square grid size, determines number of isolines
% 'method' = "circles", "squares", or "voronoi" (default)
% po number = 0 (no plot), 1 (scatter filtered), 2 (scatter & isolines
filter), 3 (as in 1 unfiltered), and 4 (as in 2 unfiltered)
% Example:
%scatplot(x1,y1,'circles',0.01,100,7,2,10)

```

```

scatplot(x1b,y1b)
pbaspect([1 1 1])
xlabel('u_mag, mm/s')
ylabel('v, mm/s')
title('Subset B')
xlim([minX1 maxX1])
ylim([minY1 maxY1])
%xlim([xlimLo xlimHi])
%ylim([ylimLo ylimHi])

colorbar('peer',axes1,'Position',[0.77 0.08 0.01 0.35])

axes2 = axes('Parent',figure1,'Position',[0.34 0.52 0.26 0.2],'Box','on');
hold(axes2,'on');
histogram(x1b,Bbins,'DisplayStyle','stairs')
ylabel('Count')

axes3 = axes('Parent',figure1,'Position',[0.63 0.08 0.133
0.35],'Box','on');
hold(axes3,'on');
histogram(y1b,Bbins,'Orientation','horizontal','DisplayStyle','stairs')
pbaspect([1 3 1])
xlabel('Count')

linkaxes([axes1,axes2],'x')
linkaxes([axes1,axes3],'y')
hold off

```

Histogram and Gaussian fit for Subset A using "histcounts" and "stairs" plot

```

clear N edges histoA
[NA,edgesA] = histcounts(x1a,Abins);
length(edgesA)
length(NA)
clf
histoA=stairs(edgesA(1:length(edgesA)-1),NA);    % vector "edges" and "N"
have to be same length for plotting
hold on

```

Gaussian fit for Subset A

```

xG=edgesA(1:length(edgesA)-1).';    % transpose rows to columns
yG=NA.';    % transpose rows to columns

```

```
options = fitoptions('gauss1', 'Lower', [0 xlimLo 0], 'Upper', [1000
xlimHi xlimHi]);
ff=fit(xG,yG,'gauss1',options)
```

Plot data and fit for Subset A

```
%plot(ff);
xlim([xlimLo xlimHi])
legend('off')
hold off
```

Fit parameters for Subset A

```
clear a1 b1 c1
coeff=coeffvalues(ff)
a1=coeff(1)
b1=coeff(2)
c1=coeff(3)
```

Confidence Intervals for Gaussian peak position fitted to Subset A

```
ci = confint(ff,0.95);
CIloA=ci(1,2)
CIhiA=ci(2,2)
```

Histogram for Subset B using "histcounts" function and "stairs" plot

```
%clear N edges
[NB,edgesB] = histcounts(x1b,Bbins);
length(edgesB)
length(NB)
clf
histoB=stairs(edgesB(1:length(edgesB)-1),NB); % vector "edges" and "N"
have to be same length for plotting
hold on
```

Gaussian fit for Subset B

```
xG=edgesB(1:length(edgesB)-1).'; % transpose rows to columns
yG=NB.'; % transpose rows to columns
options = fitoptions('gauss1', 'Lower', [0 xlimLo 0], 'Upper', [1000
xlimHi xlimHi]);
ff1=fit(xG,yG,'gauss1',options)
```

Plot data and fit for Subset B

```
%plot(ff1,'b')
xlim([xlimLo xlimHi])
legend('off')
hold off
```

Fit parameters for Subset B

```
clear a2 b2 c2
coeff=coeffvalues(ff1)
a2=coeff(1)
b2=coeff(2)
c2=coeff(3)
```

Confidence Intervals for Gaussani fit peak position for Subset B

```
ci = confint(ff1,0.95);
CIloB=ci(1,2)
CIhiB=ci(2,2)
```

Plot Subset A and B Gaussians, their sum & original (Subset A+Subset B) histogram

```
%xf=minX1:binX:maxX1;
xf=xlimLo:binX:xlimHi;
sumff=feval(ff,xf)+feval(ff1,xf);
plot(ff,'r')
hold on
plot(ff1,'m')
plot(xf,sumff,'k')
histogram(x1,Nbins,'DisplayStyle','stairs')
xlim([xlimLo xlimHi])
legend('off')
title(file)
xlabel('Magnetic Velocity, mm/s')
ylabel('Count')
hold off
```

Welch's t test (unequal variances and sample sizes)

```
N1=binA
Amean=mean(x1a) % use mean x1a for t statistic
Asd=std(x1a) % use SD x1a for t statistic

N2=binB
Bmean=mean(x1b) % use mean x1b for t statistic
Bsd=std(x1b) % use SD x1b for t statistic

v = ((Asd^2/N1+Bsd^2/N2))^2/((Asd^4/N1^2/(N1-1)+Bsd^4/N2^2/(N2-1)))
tval = ((Amean)-(Bmean)) / sqrt((Asd^2/N1+Bsd^2/N2))

tdist2T = @(t,v) (1-betainc(v/(v+t^2),v/2,0.5)); % 2-tailed t-
distribution
```



```

tdist1T = @(t,v) 1-(1-tdist2T(t,v))/2; % 1-tailed t-
distribution
tprob = 1-[tdist2T(tval,v) tdist1T(tval,v)]

```

Welch's t test CIs of the mean

```

alpha=0.05 % select parameter alpha (significance
level p)
fun = @(t) tdist2T(t,v)-(1-alpha); % function of t alone
xrange = 1e-6; % initial point (or range) for fzero
procedure

```

Subset A CIs of the mean

```

alpha
v=N1-1
tval0 = fzero(fun,xrange)
Amean
LCLA=Amean-Asd/sqrt(N1)*abs(tval0)
UCLA=Amean+Asd/sqrt(N1)*abs(tval0)

```

Subset B CIs of the mean

```

v=N2-1
tval0 = fzero(fun,xrange)
Bmean
LCLB=Bmean-Bsd/sqrt(N2)*abs(tval0)
UCLB=Bmean+Bsd/sqrt(N2)*abs(tval0)

```

Compare with Gauss fit CI's

```

CIloA
CIhiA
CIloB
CIhiB

```

Write to Excel

```

filename = 'C:\Users\adamm\Documents\Thesis\Analysis Data.xlsx';

sheet='A11'
xlswrite(filename,[x1 y1],sheet)

sheet='A'
xlswrite(filename,[x1a y1a],sheet)

sheet='B'
xlswrite(filename,[x1b y1b],sheet)

```

```

sheet='CENTS'
colHead = {'xM', 'SD', 'yM', 'SD'};
x1Range='B1'
rowHead = {'SubA'; 'SubB'};
y1Range='A2'
xlswrite(filename,colHead,sheet,x1Range)
xlswrite(filename,rowHead,sheet,y1Range)
xlswrite(filename,CENTS1,sheet,'B2')

sheet='GaussA'
Gcoeffs=coeffvalues(ff).';
colHead = {'Gauss coeffs'};
x1Range='B1'
rowHead = {'a'; 'b'; 'c'};
y1Range='A2'
xlswrite(filename,colHead,sheet,x1Range)
xlswrite(filename,rowHead,sheet,y1Range)
xlswrite(filename,Gcoeffs,sheet,'B2')

sheet='GaussB'
Gcoeffs=coeffvalues(ff1).';
colHead = {'Gauss coeffs'};
x1Range='B1'
rowHead = {'a'; 'b'; 'c'};
y1Range='A2'
xlswrite(filename,colHead,sheet,x1Range)
xlswrite(filename,rowHead,sheet,y1Range)
xlswrite(filename,Gcoeffs,sheet,'B2')

sheet='Ttest'
alphaN=alpha(1);
N1N=N1(1);
AmeanN=Amean(1);
AsdN=Asd(1);
N2N=N2(1);
BmeanN=Bmean(1);
BsdN=Bsd(1);
vN=v(1);
tvalN=tval(1);
tprobeN11=tprob(1,1);
tprobeN12=tprob(1,2);
Tcoeffs=[alpha;N1N;AmeanN;AsdN;N2N;BmeanN;BsdN;vN;tvalN;tprobeN11;tprobeN12]
colHead = {'Welch t test'};
x1Range='B1'
rowHead =
{'alpha'; 'N1'; 'Amean'; 'Asd'; 'N2'; 'Bmean'; 'Bsd'; 'v'; 'tval'; 'tail2'; 'tail1'}

```

```

y1Range='A2'
xlswrite(filename,colHead,sheet,x1Range)
xlswrite(filename,rowHead,sheet,y1Range)
xlswrite(filename,Tcoeffs,sheet,'B2')

sheet='CIs'
UCLAN=UCLA(1);
LCLAN=LCLA(1);
UCLBN=UCLB(1);
LCLBN=LCLB(1);
CIloAN=CIloA(1);
CIhiAN=CIhiA(1);
CIloBN=CIloB(1);
CIhiBN=CIhiB(1);
CITcoeffs=[UCLAN,LCLAN,UCLBN,LCLBN;CIhiAN,CIloAN,CIhiBN,CIloBN]
colHead = {'UCLA','LCLA','UCLB','LCLB'};
x1Range='B1'
rowHead = {'Ttest','Gauss fit'}
y1Range='A2'
xlswrite(filename,colHead,sheet,x1Range)
xlswrite(filename,rowHead,sheet,y1Range)
xlswrite(filename,CITcoeffs,sheet,'B2')

```

APPENDIX C: RESULTS GENERATED BY THE MATLAB CODE FOR THE GLIOMA EXPERIMENTS

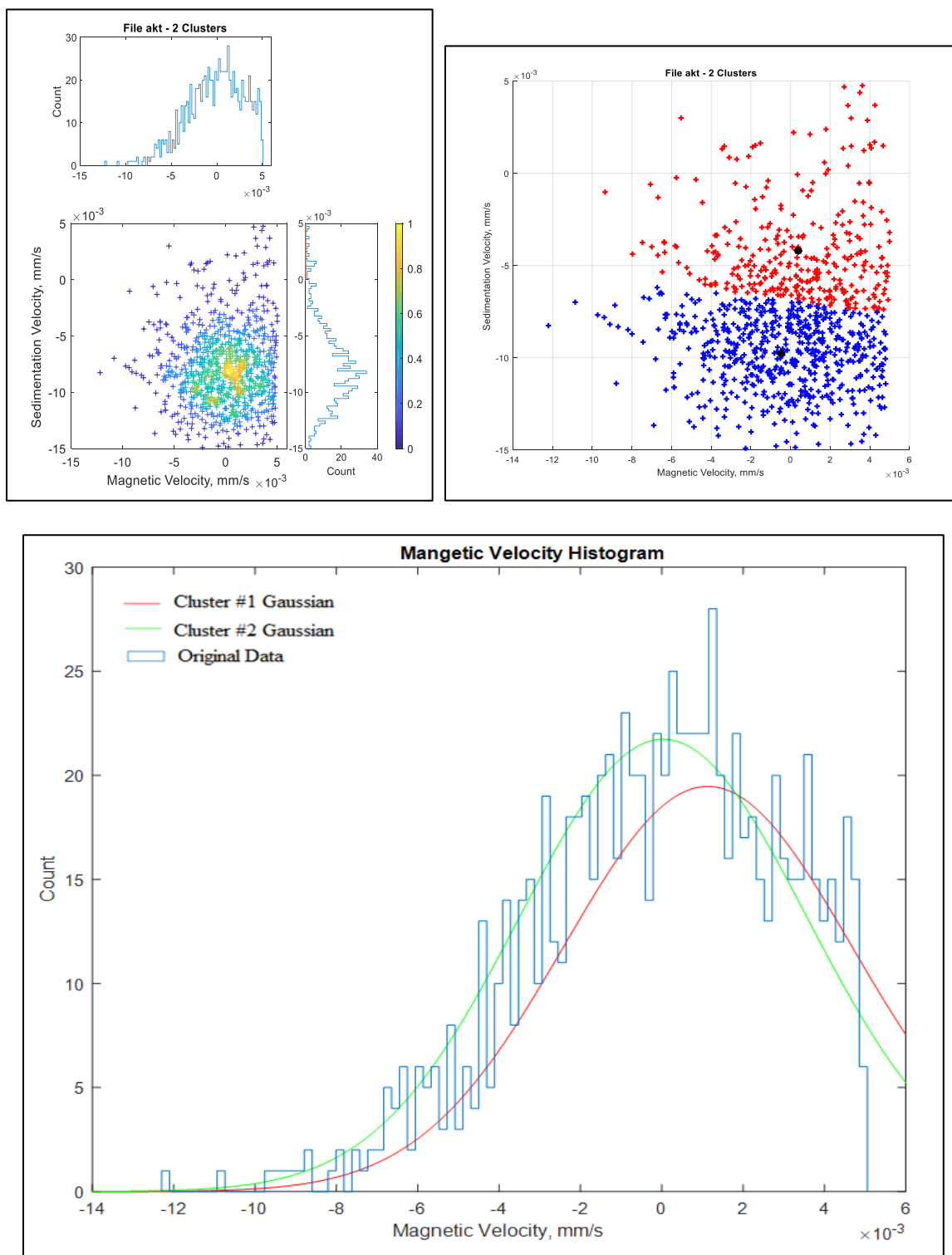


Figure 95: MATLAB results generated for 2 clusters the experiment completed by Matt Nagy for a GL261 on August 21, 2018.

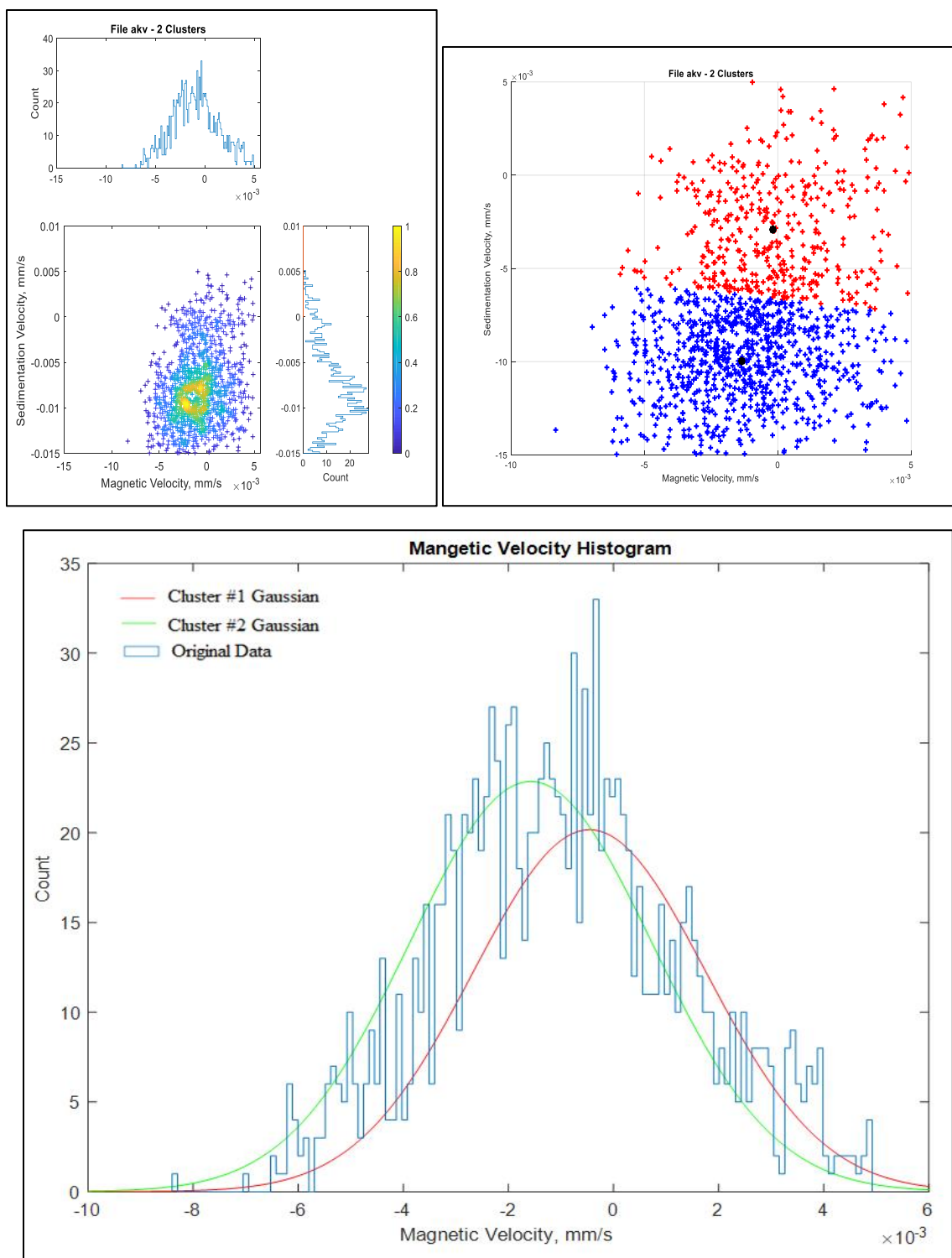


Figure 96: MATLAB results generated for 2 clusters the experiment completed by Matt Nagy for a GL261 on August 28, 2018.

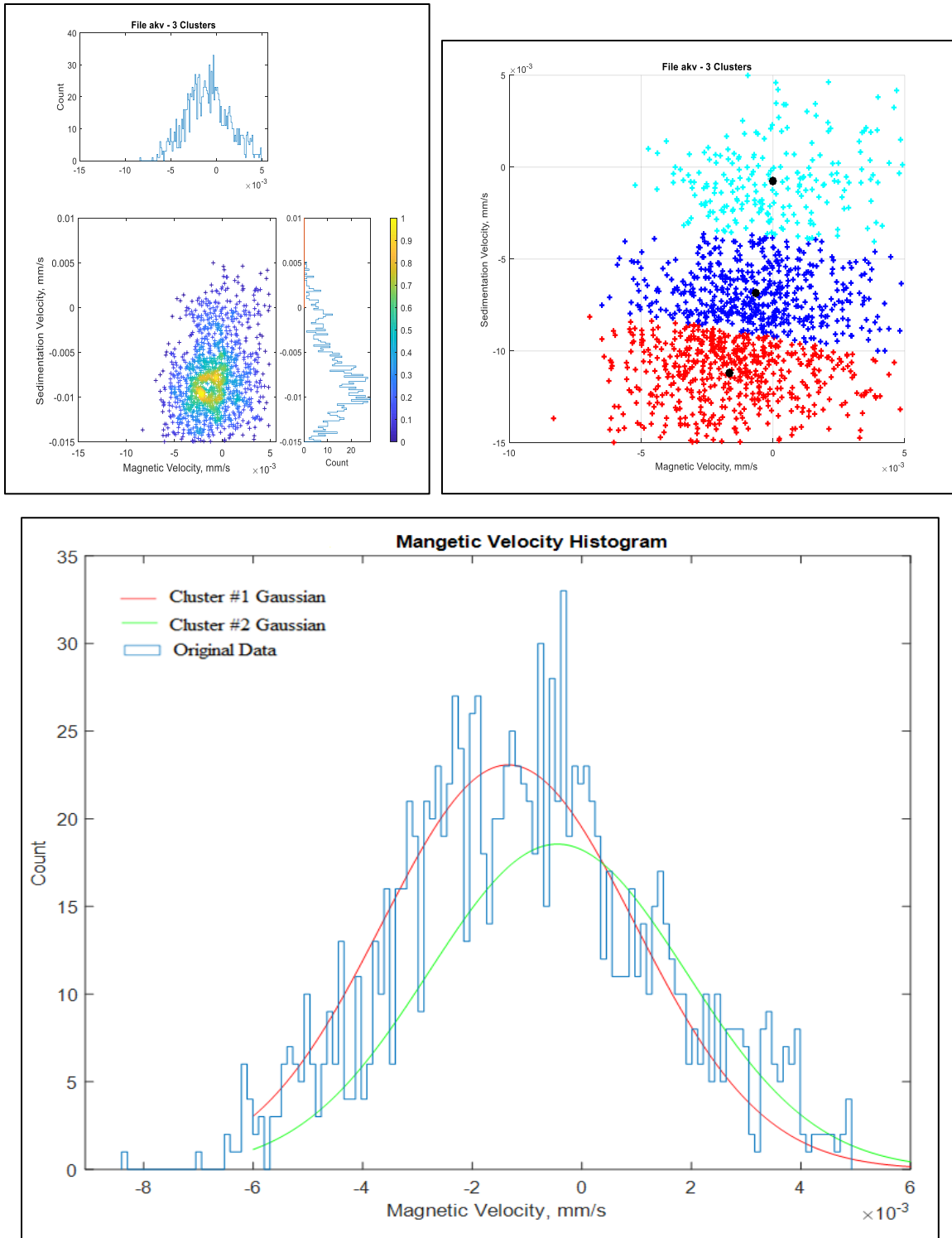


Figure 97: MATLAB results generated for 3 clusters the experiment completed by Matt Nagy for a GL261 on August 28, 2018.

The red and navy clusters were combined as cluster 1 while the light blue cluster was cluster 2.

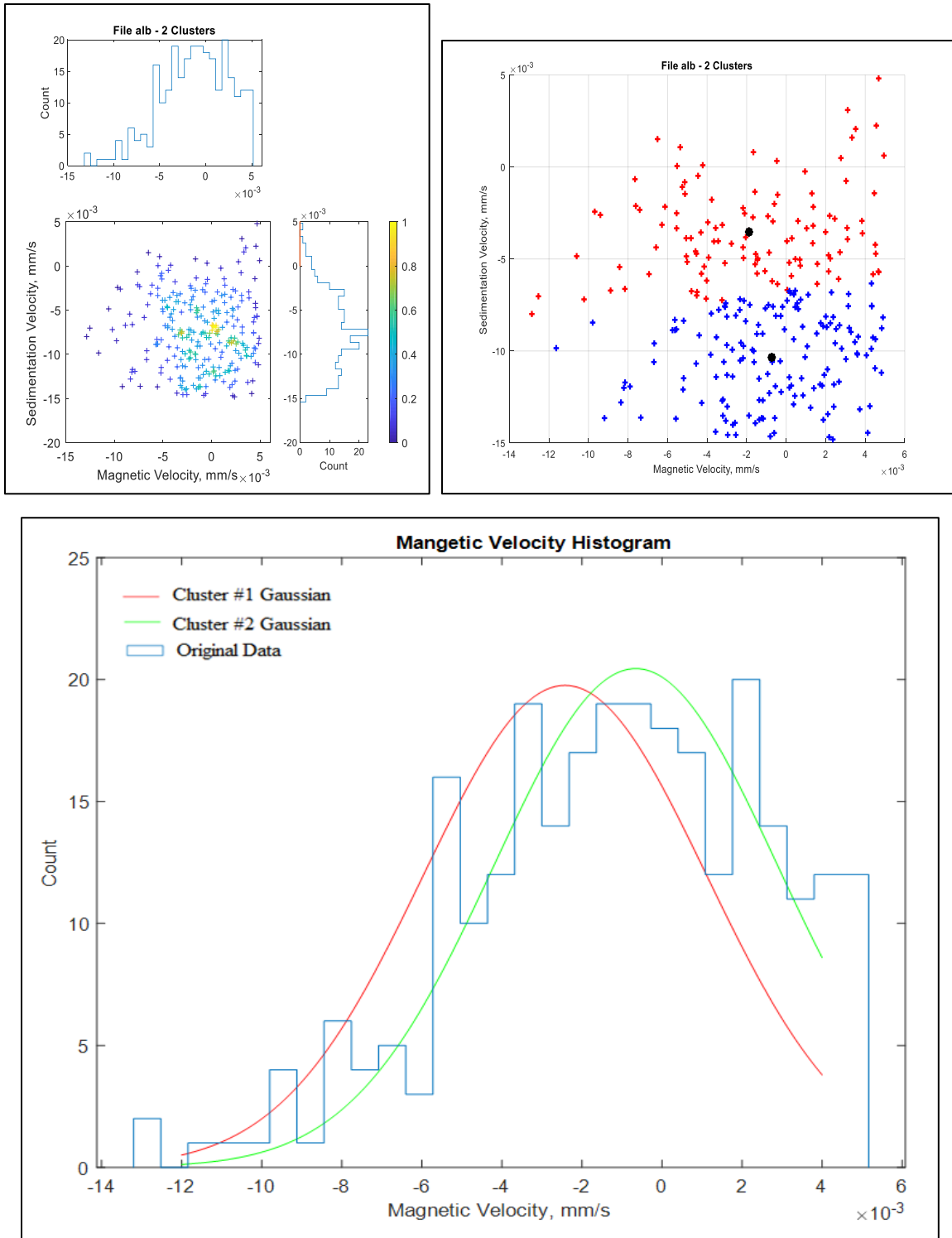


Figure 98: MATLAB results generated for 2 clusters the experiment completed for a GL261 on October 15, 2018.

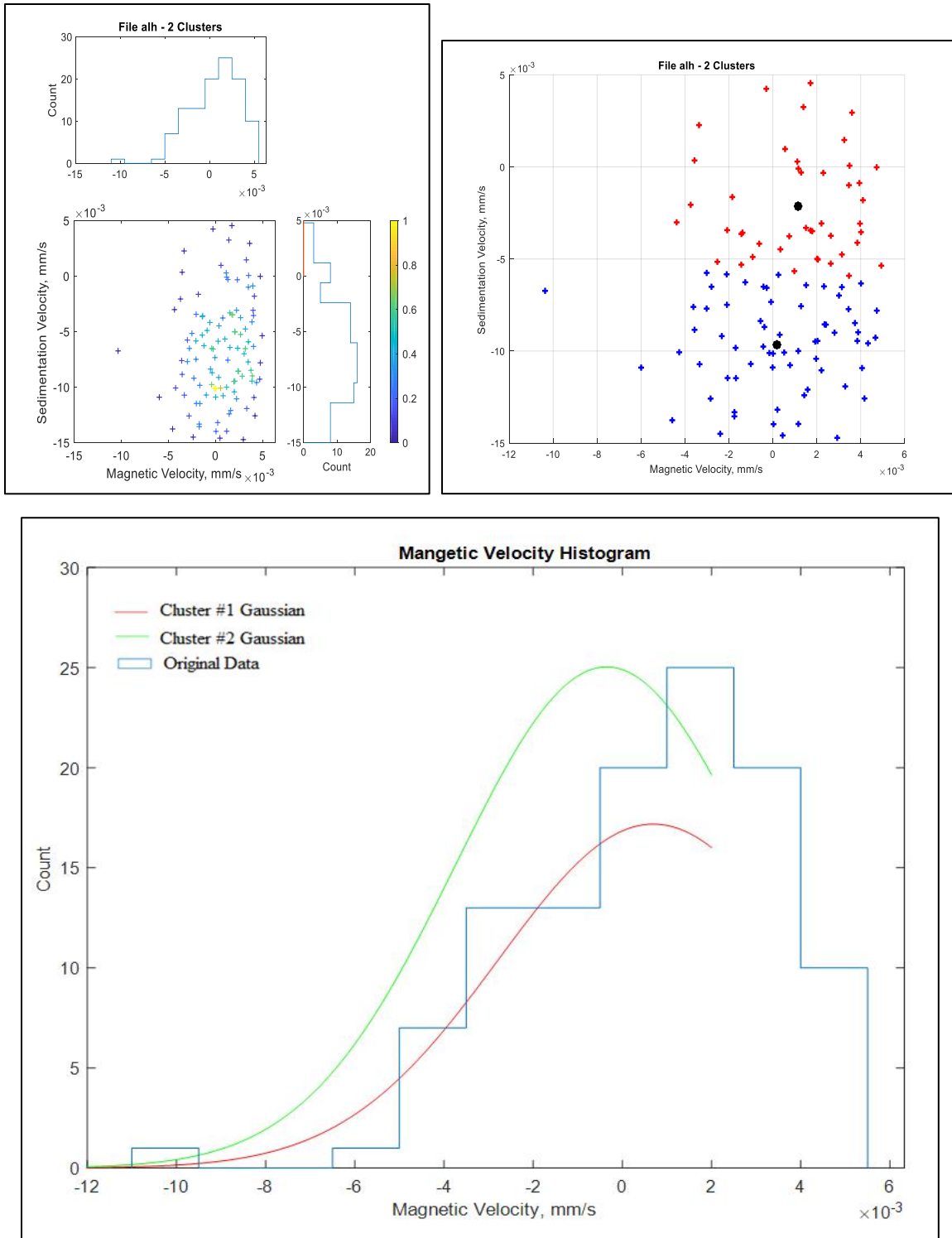


Figure 99: MATLAB results generated for 2 clusters the experiment completed for a GL261 on November 19, 2018.

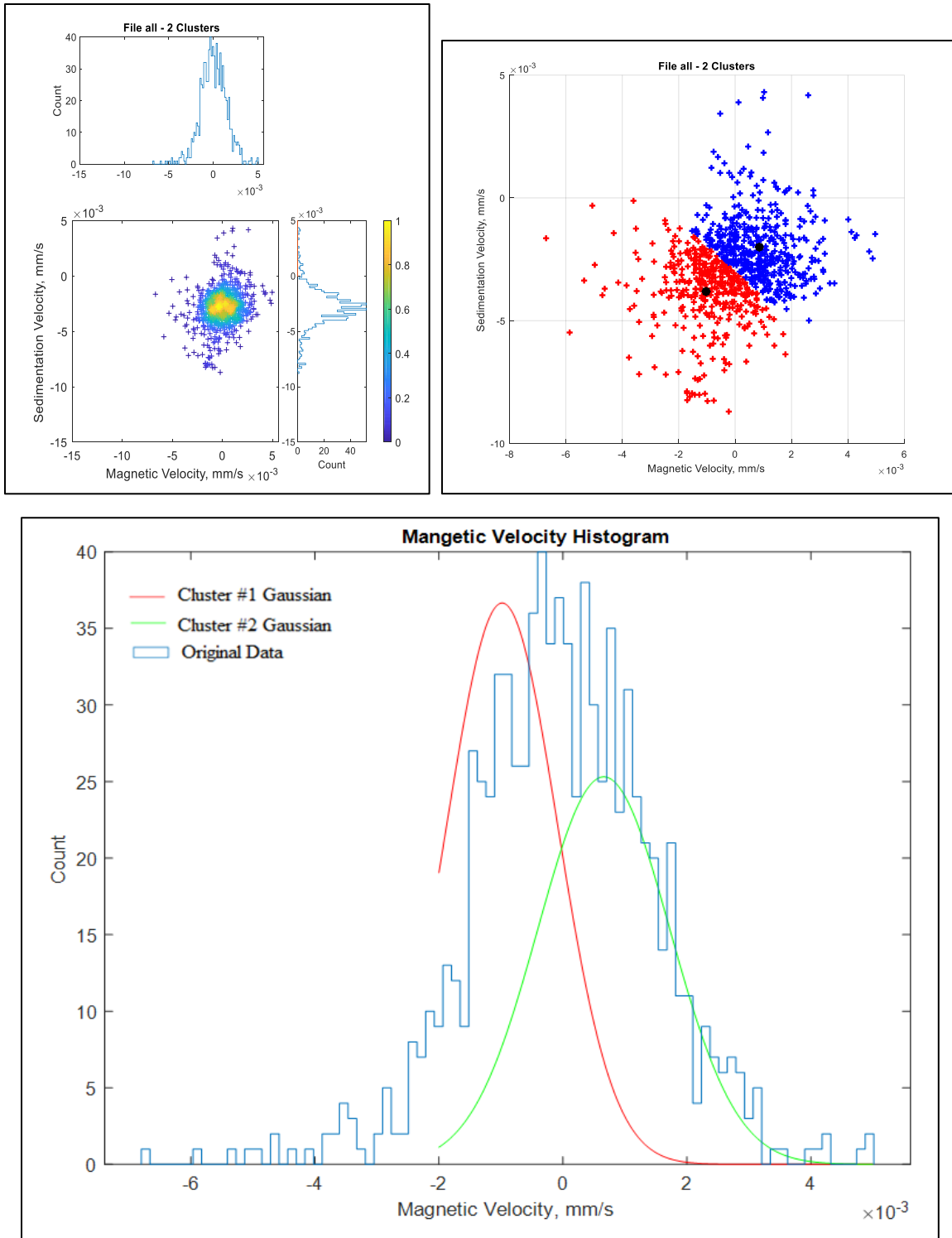


Figure 100: MATLAB results generated for 2 clusters the experiment completed for a GL261 on November 30, 2018.

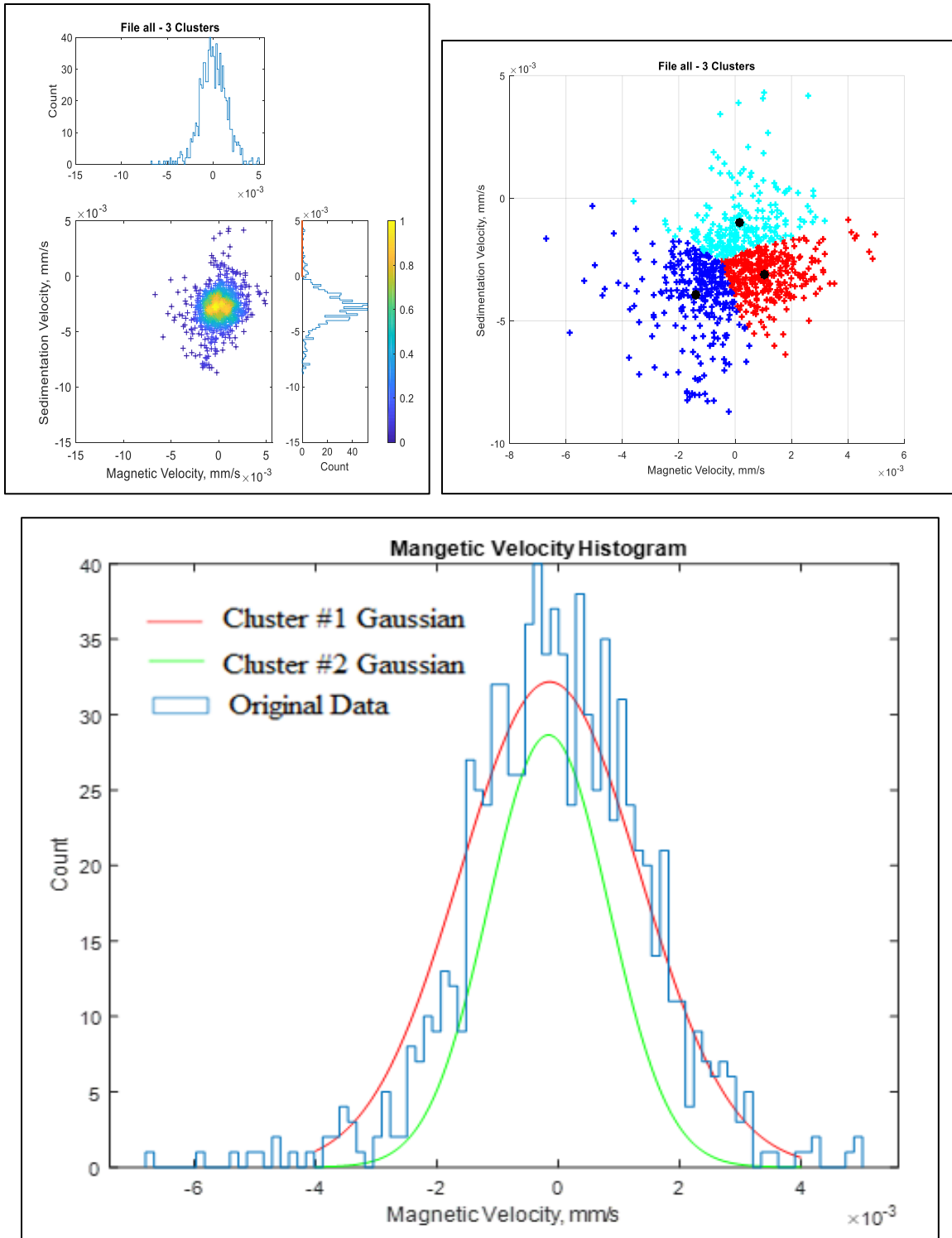


Figure 101: MATLAB results generated for 3 clusters the experiment completed for a GL261 on November 30, 2018. The red and navy clusters were combined as cluster 1 while the light blue cluster was cluster 2.

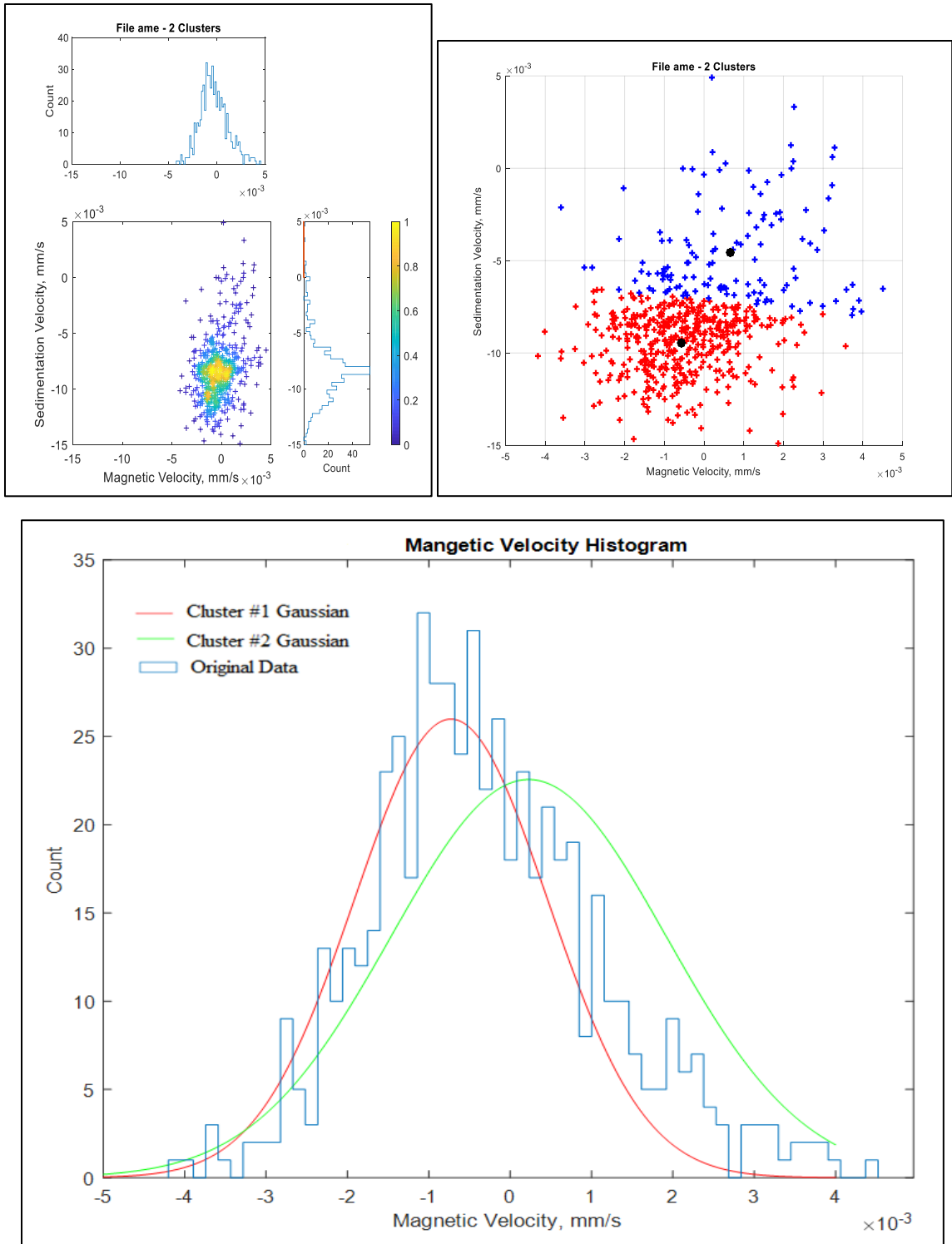


Figure 102: MATLAB results generated for 2 clusters the experiment completed for a GL261 on December 14, 2018.

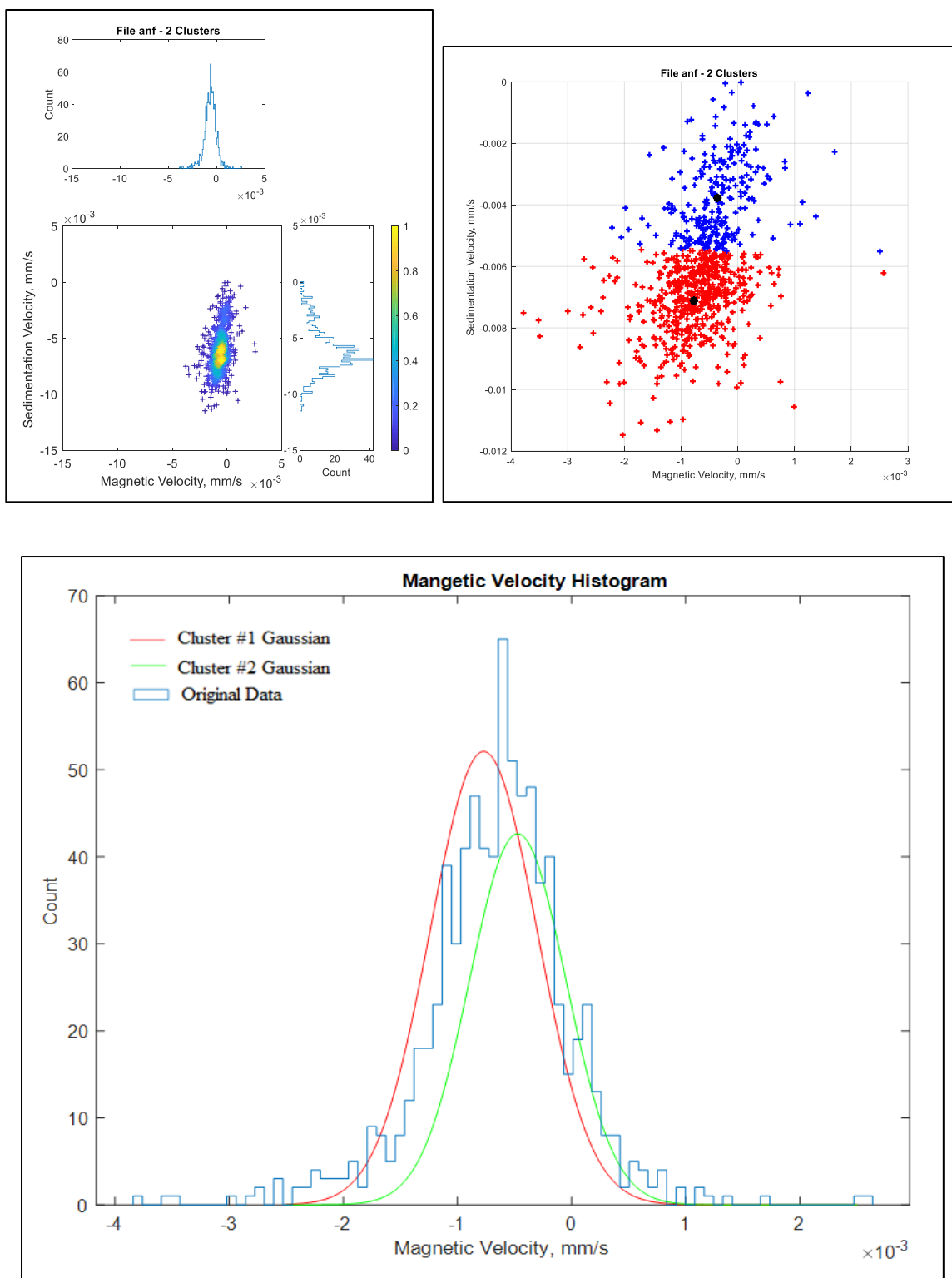


Figure 103: MATLAB results generated for 2 clusters the experiment completed for a GL261 on January 15, 2019.